Electrostatic Micro Walkers

Micro Electromechanics and Micro Tribology

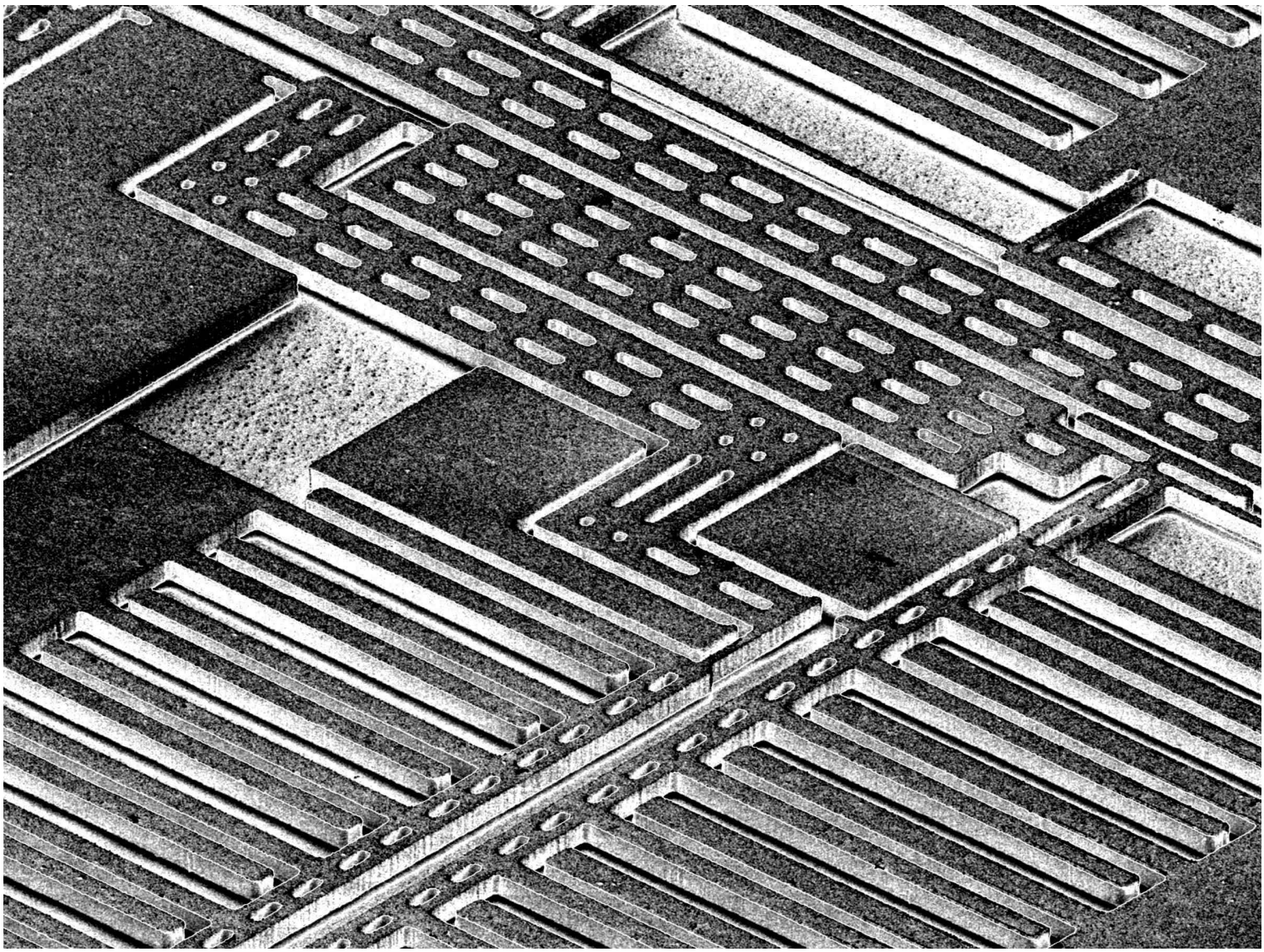

Niels Tas

Electrostatic Micro Walkers

Micro Electromechanics and Micro Tribology

Niels Tas

The Micro Walker Project:
The Research described in this thesis was carried out at the Micromechanical Transducers Group ('MicMec') of the MESA Research Institute, Faculty of Electrical Engineering, University of Twente. The Micro Walker project was a cooperative research with and was sponsored by Philips Research, Eindhoven, The Netherlands.

De promotiecommissie:

Voorzitter:

Prof. dr. H. Wallinga	Universiteit Twente

Secretaris:

Prof. dr. H. Wallinga	Universiteit Twente

Promotoren:

Prof. dr. M.C. Elwenspoek	Universiteit Twente
Prof. dr. ir. M.P. Koster	Universiteit Twente

Leden:

Prof. dr. ir. J.C. Compter	Technische Universiteit Eindhoven
Prof. dr. ir. P.J. French	Technische Universiteit Delft
Prof. dr. ir. P.P.L. Regtien	Universiteit Twente
Dr. D. Reynaerts	Katholieke Universiteit Leuven
Prof. dr. J.-Å Schweitz	Universiteit Uppsala
Prof. dr. ir. H.Tijdeman	Universiteit Twente

CIP-gegevens koninklijke bibliotheek, Den Haag:

Tas, Niels R.

Electrostatic Micro Walkers/ Niels R. Tas
[S.I. : s.n.]
Ph.D. Thesis University of Twente, Enschede, The Netherlands
ISBN 90-36514355
Subject headings: electrostatic/ micromotors / tribology

ELECTROSTATIC MICRO WALKERS

PROEFSCHRIFT

ter verkrijging van
de graad van doctor aan de Universiteit Twente
op gezag van de rector magnificus
prof. dr. F.A. van Vught
volgens besluit van het College voor Promoties
in het openbaar te verdedigen
op donderdag 20 april 2000 te 16:45 uur.

door
Niels Roelof Tas
geboren op 4 januari 1970
te Jutphaas

Dit proefschrift is goedgekeurd door de promotoren:

Prof. dr. M.C. Elwenspoek
Prof. dr. ir. M.P. Koster

Aan mijn ouders,
Albert en Sytske Tas - de Groot.

Contents

1

Introduction

The project reported in this thesis focuses on the development of linear micro-motors based on walking motion. From their potential application in data storage guiding specifications are derived: An output acceleration of a 1 mg load larger than 100 m / s^2, 10 nm resolution, reach larger than 10 μm, a driving voltage below 30 V and a maximum linear size smaller than 1 mm. The linear micromotors to be developed, will be based on variable capacitance electrostatic actuation and surface micromachining fabrication technology. Electrostatic motors have already been made in the 18th century. The first known variable capacitance motor has been built by Zipernowski in 1889. Different propulsion principles for linear micromotors have been found in literature: Inertial drive, elastic inertial drive, impact drive, traveling field surface drive, scratch drive, zigzag drive, transformation of rotary into linearly motion, and walking motion. The latter principle is implemented in the project. Controlled friction in clamp feet is necessary for walking. Therefore, microtribology is one of the main topics in this thesis. The focus is on shearing friction in elastic adhesive contacts. Questions to be answered in the project have been collected in section 1.7.

1.1 General Introduction

1.1.1 Motive For The Project

This thesis is the result of a five years cooperative project, in which Philips Research and the micromechanical transducers group from the MESA Research Institute participated. The motivation for the cooperation was for Philips the ability to study the potential of silicon micromachining techniques, for the fabrication of sub-mm sized sensors and actuators. For the micromechanical transducers group the cooperation meant a way to investigate the applicability of the available silicon micromachining techniques in an industrial environment.

1.1.2 Main Research Theme: Walking Motion in MEMS

At the start of the project it was decided to focus on the development of micro actuators with a large dynamic range (reach : resolution). Here one should think of sub-micron resolution and millimeter reach. Possible application for such actuators include:

- Positioning of a read/write head of a storage system.
- Accurate micro-assembly.
- Scanning probe systems like AFM.

The concept we had in mind at the start of the project, is to use some kind of walking motion to add small steps to obtain a large total stroke. Based on this the main research themes can be formulated:

1. Is it possible to implement walking motion in MEMS?

2. What performance is possible with walking motion in MEMS, in terms of resolution, reach and generated force?

1.1.3 Future Application in Datastorage

As the interest of Philips was mainly on the potential application in future data storage systems, we decided to focus on this application. One of the most important demands on the actuator moving a read/write head is that the acceleration of the head should increase. There are three main reasons why:

- Larger global acceleration decreases the access time.
- Increasing the angular velocity of the disk, without decreasing the dislocation of the bits with respect to the ideal track increases the local acceleration which is demanded for the tracking.
- Increasing the bit density by decreasing the track width and pitch demands a smaller deviation of the position of the head with respect to the track. In general this means that larger local accelerations are desired for the tracking.

Under certain conditions, down scaling of the actuator and the mass to be moved, will lead to larger acceleration: The force produced in an actuator is given by the product of a characteristic active area and the energy density in the active volume of the actuator. The energy density can be considered as a virtual pressure acting on the active area. For an n times smaller configuration, the mass to be moved decreases with n^3, while the active area decreases with n^2. Therefore, under the assumption of constant energy density, the produced force decreases with n^2 and the acceleration of the mass increases with a factor n. With the application in data storage in mind, guiding specifications for the micro actuators to be made, have been derived (table 1.1). The desired force is at least 0.1 mN, in order to accelerate a 1 mg element with 10 g = 100 m/s^2. This acceleration is enough to make the servo system almost insensitive for the (earth) gravitation, acting in any direction with respect to the displacement axis. It is also enough for axial and radial tracking in an audio CD system. The actuator should have a resolution of 10 nm, in order to access 100 nm pitched tracks in future high density storage systems. The total stroke of the actuator should be at least 10 μm, (arbitrary) based on the track pitch of an audio CD. Finally, the actuator should be able to function in a system fed by a 3V battery source. Using a 10-fold DC-DC converter (this is readily available), a 30 V source can be realized. This voltage is therefore chosen as the maximum driving voltage of the actuator. From spec. 4 and 5 it follows that an actuator with a large dynamic range (> 200) is desired. This supports the choice to concentrate on linear micromotors in which a large stroke is obtained by addition of small repeated motions.

1.1.4 Electrostatic Actuation

In an early stage of the project it was decided to concentrate on electrostatic actuators. The reason is that these actuators can be made from conductive silicon or polysilicon, and complete fabrication processes are available within the micromechanical transducers group. Within the project the use of thin deposited film of PZT has briefly been investigated [2], however the compatibility of the piezoelectric material with silicon micromachining is (still) problematic [3] .

Functional need	**Technical Interpretation**	**Technical specification**
1. Portable	Gravitation Insensitive	Output acceleration > 10 *g*
2. Fast tracking	Audio CD: Radial Tracking 22 nm in 0.1 ms ⇒ 0.9 *g* Axial Tracking 230 nm in 0.13 ms ⇒ 6 *g* [1]	Output acceleration > 6 *g*
3. Move read/write head	Capable of accelerating small lens, mirror or magnetic head with a 1 mg mass, up to 10 *g*	Output force > 0.1 mN
4. High Resolution	Access 100 nm pitched tracks in high density data storage system	10 nm resolution with simple (external) feedback control
5. Large stroke	Several times the track pitch of audio CD (1.6 μm)	Total stroke > 10 μm
6. Battery supply	3V source , use of DC-DC converter allowed.	Driving voltage < 30 V
7. Small size	Size of motor in the same order as the size of the mass to be moved	Max. linear size < 1mm,

Table 1.1: Guiding specifications for the linear motor design in this thesis.

1.2 Silicon Micromachining and Surface Micromachining Techniques

1.2.1 Silicon Micromachining

It was recognized in the beginning of the 1980's that silicon was increasingly being used as a construction material [4]. Peterson [4] mentioned the important features of silicon that make it valuable as a construction material: 1) Silicon is a high strength elastic material. 2) Almost defect free silicon is widely available due to its use for semiconductor production. 3) High precision processes based on photolithography on silicon wafers have been developed for IC fabrication, and are widely available. 4) These processes enable parallel fabrication of many devices on one silicon wafer. 5) Intimate integration of mechanisms and electronics is feasible, because both can be fabricated on one silicon wafer.

In the past years numerous silicon micromachined products have been developed: Pressure sensors [5, 6, 7], acceleration sensors [5, 8], inkjet nozzles (Hewlett Packard), microsieves [9], microflowns [10], microvalves [7], micromixers [7], flowsensors [7].

Traditionally, silicon micromachining is divided into bulk micromachining and surface micromachining. The main processes in bulk micromachining have been reviewed in the previously mentioned article of Petersen [4]. More up-to date overviews are given by Madou [11], and by Elwenspoek and Jansen [12].

In the actuator project described in this thesis, we have chosen to use surface micromachining, because complete process sequences for the fabrication of electrostatic actuators were available in the MESA cleanroom. These processes had been developed in the SLE-project (*SLE = Sacrificial Layer Etching)* [13, 14]. Basic surface micromachining process steps will be explained next.

1.2.2 Surface Micromachining

Micromechanical structures can be formed using IC-fabrication processes to deposited, pattern and etch thin films. An essential step in this so called surface micromachining process is the selective etching of sacrificial layers, in order to create movable parts. The first known surface micromachined device was the Resonant Gate Transistor [15], in which a high-Q resonator was made with a golden, vibrating cantilever beam as a gate electrode. The golden beam was released by means of sacrificial etching of a different metal, on which the gold layer was deposited. Later on, the same group [15] used metal surface micromachining to develop a magnetically driven micromotor [16]. It was in the 1980s that surface micromachining of polysilicon structures, using sacrificial etching of SiO_2 was increasingly employed. Various passive elements and mechanisms were realized, including springs, gear trains, joints, cranks, sliders **[**17, 18, 19**].** The first active structures were laterally driven resonators, activated by comb-drive, variable capacitance electrostatic actuators [20, 21]. With the successful development of rotary electrostatic micromotors [22, 23, 24, 25, 26**]**, surface micromachining proved its potential to realize electromechanical functions with the successful IC-technology.

Surface Micromachining Process Sequence

Figure 1.1 shows the most basic process sequence in surface micromachining. A sacrificial silicon oxide layer is grown on a substrate wafer. Often a phosphosilicate glass (PSG) is deposited as the sacrificial layer, because of its fast etch-rate in HF [19]. The polysilicon structural layer is deposited on top of the sacrificial layer, usually by LPCVD. For electric devices the polysilicon will be made conductive by doping with donor or acceptor atoms. It is possible to use the PSG sacrificial layer as a phosphorus dopant source [20]. Next, a thin top layer is deposited which serves as a mask for the etching of the polysilicon. In fig. 1.1 a silicon-dioxide mask is indicated, but other mask materials like metals may be used. In the next step the mask layer is patterned. This is done by means of photolithography, using a photo-sensitive resist layer. The pattern in the photoresist is transferred to the silicon-dioxide mask layer, either by Buffered HF or by Reactive Ion Etching (RIE). With the help of the patterned mask layer, the polysilicon is etched, usually by Reactive Ion Etching (RIE). Sacrificial layer etching of the silicon oxide in an HF-solution, frees the narrow structures by under-etching, and removes the mask layer. Wide structures remain anchored to the substrate. The process shown here is a very basic sequence. In practice more than one polysilicon layer is often used [27].

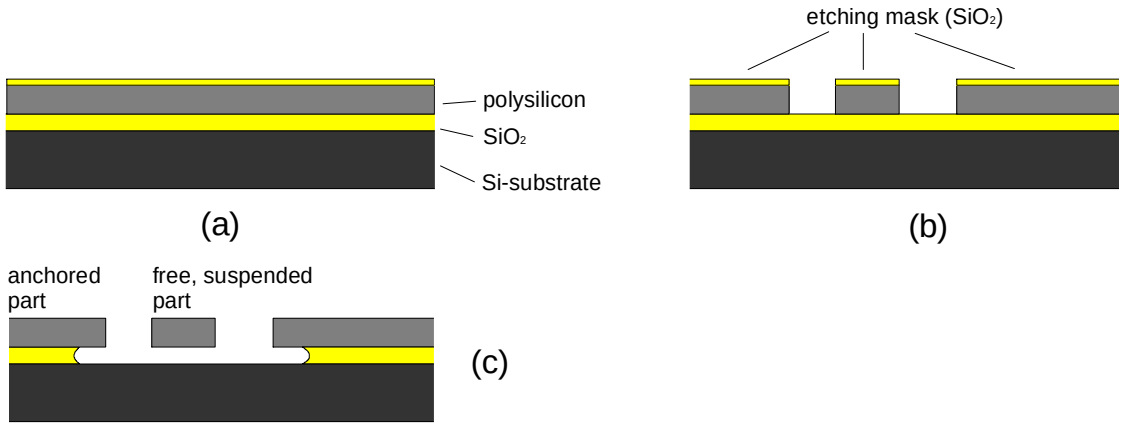

Figure 1.1: Basic steps in surface micromachining. A sacrificial silicon oxide layer is grown on a substrate wafer. The polysilicon structural layer is deposited on top of the silicon-dioxide. A thin top layer is deposited which serves as a mask for the etching of the polysilicon (a). Next the mask layer is patterned by photo-lithography Using the patterned mask layer the polysilicon is etched (b). Sacrificial layer etching frees the narrow structures by under-etching. Wide structures remain anchored to the substrate (c).

Anchoring is commonly done by etching a hole in the sacrificial layer before deposition of the polysilicon structural layer, thereby connecting the polysilicon to a lower layer which resists the sacrificial layer etching. Anchoring to a lower layer of conductive polysilicon is often made in order to equalize the voltage of the moving polysilicon and the lower layer (fig. 1.2). The lower layer then acts as an electrical shield, preventing the electrostatic forces from pulling released beams down to the substrate, due to a voltage difference between the beams and the substrate [23].

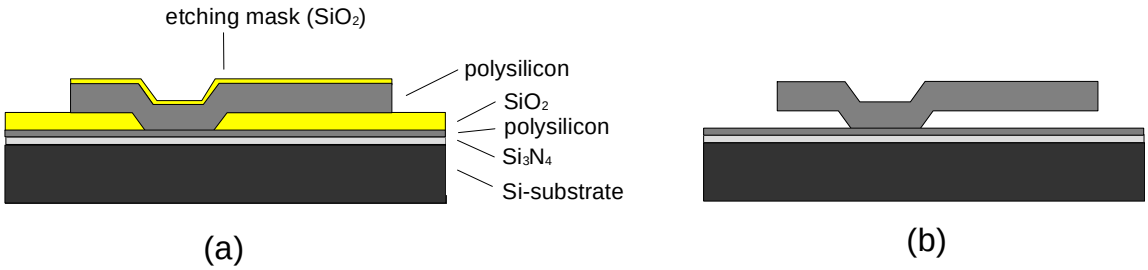

Figure 1.2: In order to anchor a structure to a lower polysilicon layer, a hole is etched in the sacrificial layer, prior to deposition of the structural polysilicon (a). After the sacrificial layer etch the anchored structure remains as shown in (b).

Due to the smoothness of the surface of the polished silicon wafers, the top surface of the sacrificial oxide in fig. 1.1 can be extremely smooth. This causes the bottom side of the deposited polysilicon to be smooth. Once the bottom side of released polysilicon parts touch the silicon substrate, either during fabrication or operation, large adhesion forces exist between the smooth surfaces, and the parts can permanently adhere to the substrate. This effect is often called stiction. It has been studied extensively within research groups employing surface micromachining [27, 28, 29, 30, 31, 32]. Because of the importance of stiction in microstructures, chapter 3 is devoted to this subject. Sources of stiction, and methods to reduce stiction are reviewed.

Surface Micromachining Design Rules in the MESA Clean Room
The designs that will be discussed are based on a surface micromachining process, in which the structural polysilicon layer has a maximum height of 5 μm. As a rule of thumb the maximum lateral size of elements should be less than 1 mm, in order to keep the deflection due to out-of plane bending caused by possible stress gradients, below 1 μm. The minimum lateral size of both gaps and beams is determined by the resolution of the photolithography. For both gaps and beams we work with a 2 μm resolution.

1.3 Electrostatic Motors

1.3.1 Definition of Motor

Following Mehregany [33] we define motors as actuators capable of unrestrained motion in at least one degree of freedom. In case of a linear motor, the motion will practically always be restrained by the size of the guidance. It is called a motor, if the generated stroke is created by an addition of small motions, which in principle can be repeated infinitely.

1.3.2 Brief History of Electrostatic Motors

The history of electrostatic motors goes back to the 18th century. Andrew Gordon constructed the motor known as the “electric bells”. Around the same time, Benjamin Franklin built his spark motors, which were able to generate a considerable power of ca. 0.1W [34]. The size of these motors was huge: The rotor was a disc with a diameter up to around one meter. The power density of these motors was therefore small, caused by the fact that in large air gaps the break-down electric field and therefore the energy density is small (in section 2.5 this will be explained in more detail). It is because of the low power density that electrostatic motors have not found wide-spread application. An improvement was made by Poggendorf [35], who constructed a so called corona motor. In the Franklin’s motor only the electrodes at the edge of the rotating disc were charged and contributed to the torque generation. In the corona motor sharp needles spray charge on a glass disc. Therefore, the whole disc surface became active in the torque generation. The variable capacitance motor, on which we focus in this thesis, was introduced by Zipernowski in 1889 [36]. In this type of motor, forces are generated by electrostatic attraction between oppositely charged (conductive) capacitor plates. For more details and references, we refer to Jefimenko [34], which gives an extensive overview of realized electrostatic motors.
Within Philips Research Laboratories, Bollée and coworkers have studied electrostatic motors in the 1960’s [37]. They constructed rotary electrostatic motors with a size in the order of 1-10 cm. Both synchronous variable capacitance and asynchronous induction motors were studied. Motors have been constructed using precision fabrication techniques. For a realized synchronous motor, Bollée reports an output power of 600 μW at 1 rev/s, driven by 200 V. Bollée expects that electrostatic motors become attractive if very small (sub-mm) motors are

constructed. The reason is that in electromagnetic motors, the amount of dissipation with respect to the consumed electric power becomes larger when motors become smaller. Small electrostatic motors suffer less from dissipation, because in these motors the electrical wires are much shorter, as no coils are needed. A second reason is that the breakdown electric field in air increases with decreasing electrode spacing. The energy density in small electrostatic motors can therefore come close to the energy density of electromagnetic motors (see section 2.5).

Starting in 1988, several electrostatic micromotors have been developed within MEMS-research groups. These include side drive motors [19, 38], top drive motors [25], outer-stator wobble motors [39, 40], outer-rotor wobble motors [33, 41] and lower-stator wobble motors [42]. In literature only a small number *linear* electrostatic motors has been found [43], [44, 45], [46, 47], [48]. They are part of the next section.

1.4 Propulsion Principles for Linear Micromotors

Realized linear micromotors which have been found in literature, include piezoelectric, and electrostatic motors, fabricated either by 'traditional' precision-mechanical, bulk- and surface micromachining fabrication processes. The micromotors presented below have been selected to illustrate different propulsion principles suited for linear micromotors. The survey includes a few rotary motors, because we think that their propulsion principle can be employed to generate linearly motion.

1.4.1 Inertial Drive

The inertial drive was presented in MEMS by Higuchi [49]. Fig. 1.3 shows the principle: A load with mass m_{load} is connected to the help mass m_{help}, by an actuator element. The load is pressed on to the substrate with a force F_{clamp}, which induces friction between them. The motor is actuated by rapid extension of the actuator (b). Both m_{load} and m_{help} are accelerated with a_l and a_h respectively. If the inertial force of m_{help} acting on m_{load} is larger than the friction force, than the load will shift leftward. In the next phase (c) the actuator generates a contraction force, and both masses are decelerated slowly. If this done subtle enough the inertial forces will be small compared to the friction force, and m_{load} will rest. Only m_{help} is decelerated with a_{help} pointed leftward. At the end of the contraction, the actuator suddenly generates and extension force, in order to turn the direction of movement of m_{help}. Due the mutual inertial forces, both m_{load} and m_{help} are accelerated outward, and we have returned to phase (b).

Higuchi [49] has successfully used this concept to move robot arms. The typical mass m_{help} is in the range of 1-10 g. Stacked piezos with a size of 2x3x10 mm^3 and a driving voltage < 150 V were used. Step-sizes generated were between several nanometers up to ten μm. The inertial drive has been improved by Ikuta et al. [50, 51] by including clamp actuators in order to control the friction between the moving load and the substrate or the guiding rail.

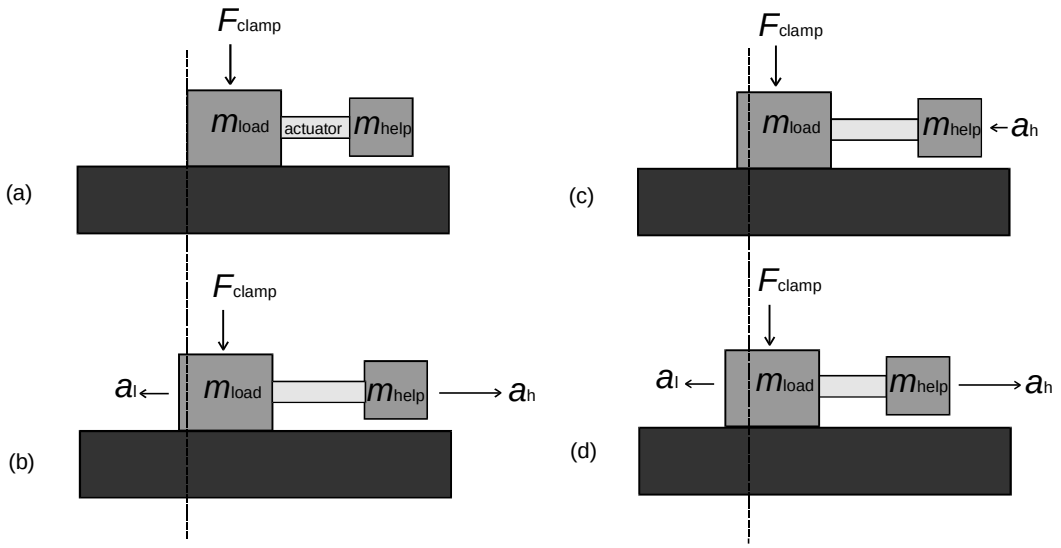

Figure 1.3: The load with a mass m_{load} is connected to a help mass m_{help} by an actuator element. (a) Initial rest position. The load is pressed on to the substrate with a constant force F_{clamp}.to generate friction (b) sudden expansion with large acceleration a_{load} and a_{help} of the load and the help masses respectively. The inertial force of m_{help} acting on m_{load} is larger than the friction between m_{load} and the substrate. Therefore the load shifts leftward (c) slow decceleration, m_{load} fixed by friction, m_{help} slowly moves back, (d) sudden stop, with a large acceleration of the masses. The inertial force acting on the load is larger than the friction, therefore the load shifts leftward and we have returned to phase (b).

1.4.2 Elastic Inertial Drive

This propulsion principle is based on the conversion of an oscillation, into directional motion. The conversion is accomplished by mechanical rectification using an elastic fin connected to the translator [52]. Figure 1.4 illustrates the principle. The configuration consists of a translator with mass m_1 which is in contact with the oscillating mass m_2 by means of the fin which is connected to m_1 by a hinge joint. The elastic deformation of the fin is represented by its rotation and by the spring k_1. The forces working on the translator m_1 are shown in fig. 1.3b. The translator is clamped onto the oscillating mass with a constant force F_{clamp}. Mass m_1 moves in the x-direction with a speed $v_{x1}(t)$. Mass m_2 is connected to the substrate by the spring k_2. The oscillation of m_2 is represented by its acceleration $a_{y2}(t)$. There are two forces working on the tip of the fin: The contact force $F_{21}(t)$ and the friction force F_f (t), which we assume to be proportional to $F_{21}(t)$ with the friction coefficient m. The mechanical rectification is based on variation of F_{21} and therefore of the friction force F_f, due to the oscillation of m_2. Assume that the resonance frequency $\sqrt{(k_2 / m_2)}$ is larger than the resonance frequency $\sqrt{(k_1 / m_1)}$. If $m_2 > m_1$ this means that $k_2 >> k_1$. It means that the mass m_1 is not able to follow the oscillation of m_2. As a result the spring k_1 is deflected. In the positive flank of a_{2y} the spring will be compressed, and F_{21} will be large. Because k_1 is placed obliquely, the compression of k_1 also induces acceleration of m_1 in x-direction. This acceleration is limited by the friction force, and is therefore proportional to F_{21}. During the negative flank of a_{2y} the spring k_1 extends so F_{21} will be smaller than in the positive flank. During the extension of k_1 the friction force will tend to decelerate m_1. Because F_{21} is smaller in the extension phase, the

decelerating friction force will be smaller than in the compression phase. Therefore, in the complete cycle there is a net acceleration of m_1 to the right.

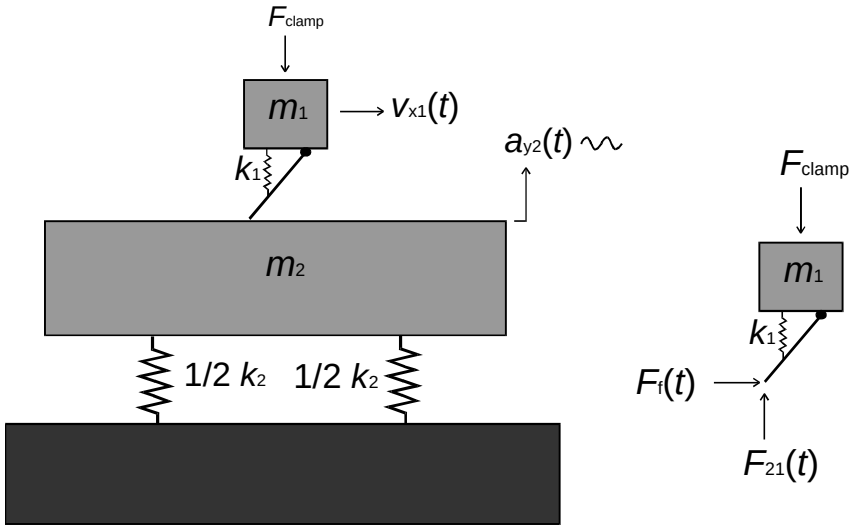

Figure 1.4: (a) The translator with mass m_1 is in contact with the oscillating mass m_2 by means of the fin which is connected to m_1 by a hinge joint. The elastic deformation of the fin is represented by the its rotation and by the spring k_1. Mass m_1 moves in the x-direction with a speed v_{x1}(t). Mass m_2 is connected to the substrate by a spring k_2. The oscillation of m_2 is represented by its acceleration a_{y2}(t). (b) The forces working on the translator m_1. The translator is clamped onto the oscillating mass with a constant force F_{clamp}. There are two forces working on the tip of the fin: The contact force $F_{21}(t)$ and the friction force $F_f(t)$.

The concept has been implemented by Racine et al. [53]. They built a hybrid rotation motor with a silicon micromachined oscillator, activated by a ZnO thin-film layer. The rotor was made by a laser cut metal film, with tilted flexures made by pressing in a mould. The size of the assembled motor was 6x6x1.5 mm^3. The motor driven by 10 V_{RMS} delivered a free rotational speed up to 200 rpm, and a torque of 50 nNm. A similar motor with a PZT thin film actuation has been realized by Muralt et al. [54]. The use of PZT in stead of ZnO results in a three times higher speed per Volt, and a factor two larger torque per Volt [54].

1.4.3 Impact Drive

Impact-driven microactuators were first presented by Lee et al. [55]. In their design the slider was driven by impact of a flexure connected to a resonating mass-spring system. This system is almost similar to the inertial elastic drive presented in the previous section. The difference is that the flexure is connected to the resonating mass. Daneman [56] created microvibromotors driven through stiff, oblique impact by resonating masses (fig. 1.5). The resonators are actuated by electrostatic comb-drives [20, 21, 57]. In resonance, the maximum produced electrostatic force is amplified, roughly by the resonator quality factor. For laterally driven microstructures the quality factor can be as high as 100 in air [56, 59]. In order to create impact, at least 4 driving cycles at the resonance frequency were needed. To obtain repeatable steps, 6 driving cycles were applied for each step. The typical measured step-size was in the order of 0.3 - 0.4 μm, at a driving voltage of 50 Vdc and 12.5 Vac (p-p)

superimposed [56]. Slider velocities over 1 mm/s, and displacements of the slider up to 100 μm have been reached. The value of the generated forces have not been reported, but they were large enough to overcome the (adhesive) static friction of the slider with the substrate and the flange. The linear microvibromotors have been successfully employed to position a micromachined mirror in a laser-to-fiber coupler system [60].

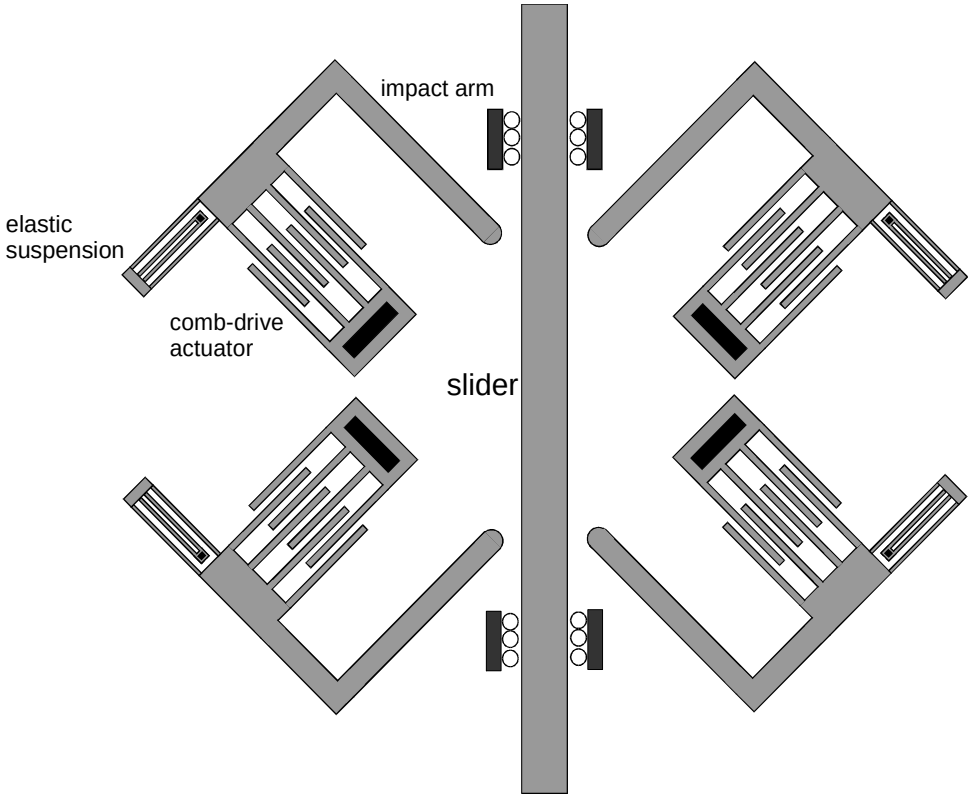

Figure 1.5: Top view of a impact driven linear motor, by Daneman et al. [54]. This so called microvibromotor consists of a slider which is driven by oblique impact of resonating impact arms. The resonators are driven by comb-drive actuators. The motor contains four drive units, two for each driving direction.

1.4.4 Zigzag Drive

The zigzag concept has been proposed by Anderson et al. [61] in 1991. Koga et al. [62] have implemented the concept, using (bulk) micromachining of Pyrex and silicon wafers, and anodic bonding to join the glass and silicon parts. The principle of operation is illustrated in fig. 1.6 the motor consists of a (grounded) translator and four stator electrodes, two in the upper stator plate and two in the lower stator plate. By making the zigzagging motion illustrated in fig. 1.6, small steps are made. For small angles g / l, the leftward movement x of the translator as defined in fig. 1.6a, is given by $g \cdot y$ / l - y^2 / 2l, with y the upward movement, l the translator length, and g the gap. Due to the large transformation ratio (leftward movement : upward movement), the generated lateral force can be much larger than the normal attractive forces between the stator electrodes and the translator.

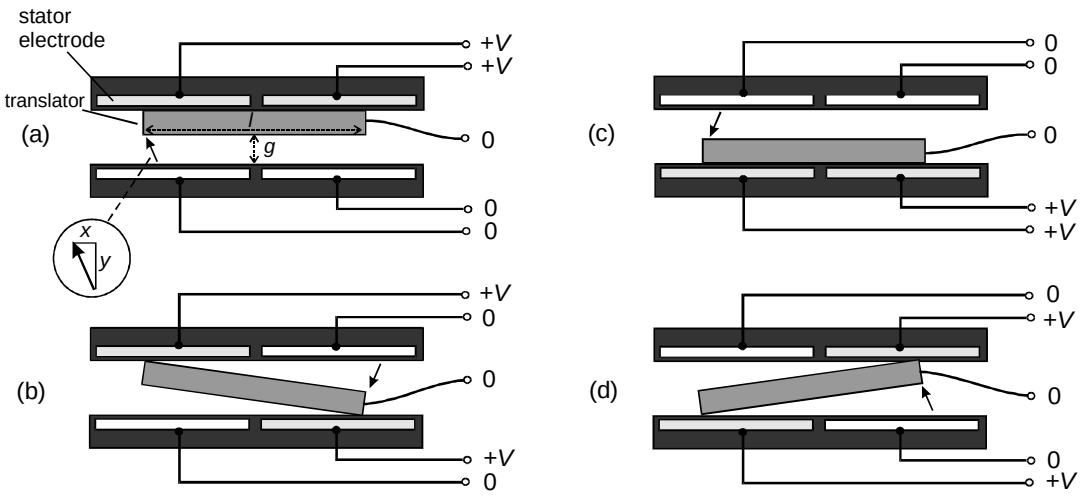

Figure 1.6: Principle of operation of the zigzag drive. It consists of a translator with a length l "zigzagging" in a channel, between four electrodes. Electrostatic forces are generated by applying a voltage difference between the grounded slider and the stator electrodes. The cycle is as follows: (a) The translator is attracted by both upper electrodes. (b) One of the lower electrode attracts the back of the translator. The translator rotates around the front contact line, and the back slightly moves forward. (c) The front is attracted by the lower front electrode. Rotation is around the back contact line, so the front moves forward (d) The back moves to the upper back electrode and moves forward. Finally the front moves upward (a) and the cycle is completed. For $g << l$, the leftward movement x of the translator equals $gy / l - y^2 / 2l$, with y the upward movement from (d) to (a), l the length of the translator, and g the gap (maximum value of y).

The dimensions of the fabricated motors is 6 x 7 x 1.2 mm [62]. Motors have been tested successfully. They were operated at 80-250 V, and could travel ±1 mm at a speed of 0.3 mm/s. At 250 V the produced force is in the order of 0.1 mN. This is smaller than what can be calculated from the large transformation ratio and the (normal) electrostatic forces. Probably, the lateral force is limited by the friction force in the stator-translator contact, which will be in the order of the normally acting electrostatic forces.

1.4.5 Traveling Field Surface Drive

Egawa and Higuchi [63] introduced their multi-layered electrostatic film actuator in 1990. This first version was an electrostatic pulse driven induction motor. It is propulsed by electrostatic forces between charges on the stator electrodes, and induced charges on the highly resistive slider surface. Therefore, it has been called the image charge stepping actuator. By moving the voltage pattern on the stator electrodes, the slider is dragged and pushed by the electrostatic forces. Fig. 1.7 shows the principle of operation. Initially, a charge distribution is induced on the resistive layer by applying a voltage pattern on the stator electrodes (fig. 1.7b). Next, the voltage pattern at the stator electrodes is shifted to the right (fig. 1.7c). The attractive electrostatic forces force the slider to shift to the right, to the next equilibrium position (fig. 1.7d). Stage (c) and (d) can indefinitely be repeated. After shifting the voltage pattern three times, the initial voltage pattern returns. These actuators have some attractive features: Because the slider does not contain electrodes which have to be contacted, there are no wires or (conductive) sliding contacts needed between the slider and the outside world. Furthermore, due to the repulsive forces at the start of the propulsive phase no bearings

are needed, as the propulsive forces reduce the friction sifgnificantly. In the realized motors, the stator electrodes and the translator surface coating were applied on PET films with a thickness of about 100 μm. Copper electrodes were plated on the stator to create the electrodes. The translator was coated with highly resistive layer [48, 63] either an anti-static agent [48], a resin [63] or polyurethane mixed with carbon particles [63]were used. For proper operation the resistivity of the translator surface was chosen around 10^{14} [Ω/square] [48, 63]. In order to increase the break-down field strength, the actuator was mounted in a package filled with dielectric fluid (Fluorinert, by 3M).

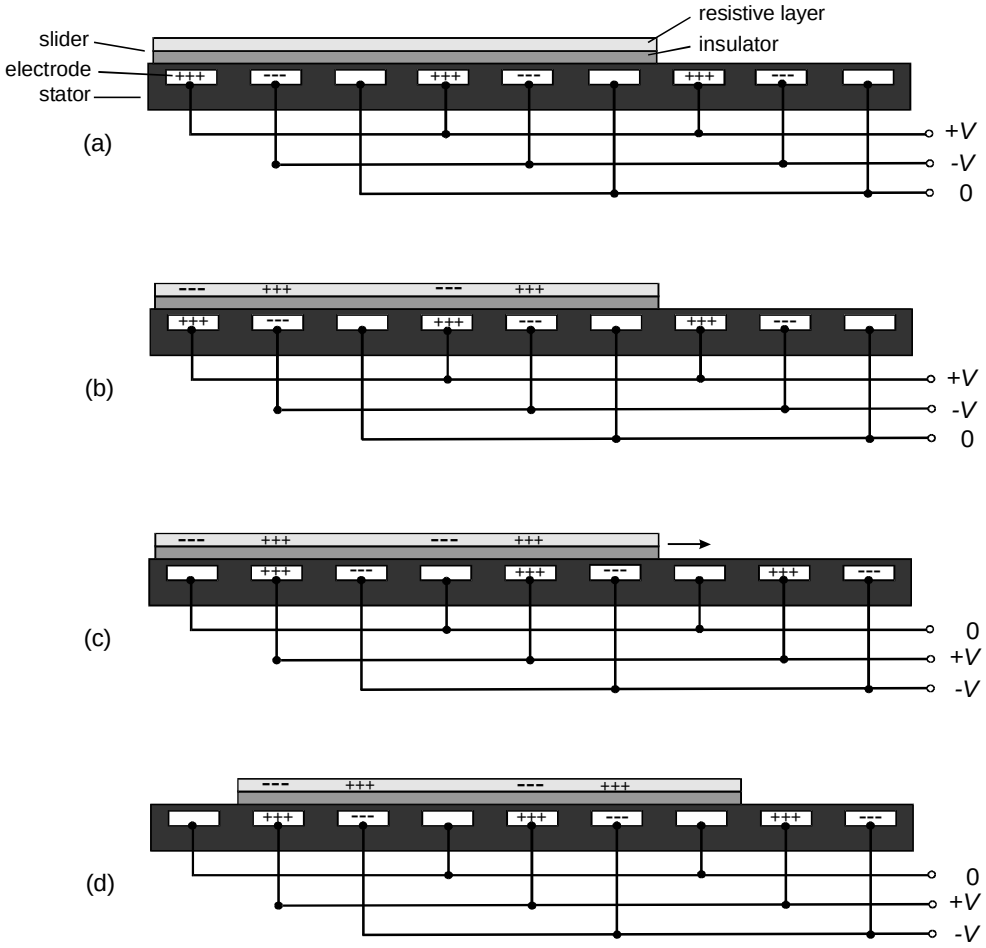

Fiure 1.7: (a) Cross section of the traveling field inductive surface drive motor. The motor consists of a stator with electrodes, and a slider with two layers: An insulating layer and a highly resistive top layer, in which a charge distribution can be induced by the electric field generated by applying a voltage pattern to the electrodes. The principle of operation is as follows: Image charge is induced on the resistive layer by applying a voltage pattern on the stator electrodes (b). Next, the voltage pattern at the stator electrodes is shifted to the right (d). The attractive electrostatic forces force the slider to shift to the right, to the next equilibrium position (d). Stage (c) and (d) can indefinitely be repeated. After shifting the voltage pattern three times, the initial voltage pattern returns.

Several design optimizations have been published, for example the optimal stator-translator electrode spacing compared to the electrode pitch, in order to obtain maximum force generation [63], the introduction of 18 μm glass balls between the stator and the slider to reduce friction [64], and special electrode design which reduces the force ripple [65].

With the pulse driven induction motor a maximum force of 8 N and a power to weight ration of 5W/kg have been reached, using a driving voltage of 800 V. The motor weighs 110 g and consists of 40 stacked layers. The outer dimensions are 20 x 14 x 50 mm^3 [64].
Niino [64, 66] introduces three other driving principles for the film actuators: ac-driven induction, pulse-drive variable capacitance, and ac-driven variable capacitance motors [64]. The variable capacitance motors have the advantage of a larger power generation, and the disadvantage of larger complexity due to the necessary of electrodes on and electrical connections to the slider [64].

1.4.6 Scratch Drive

This propulsion principle is invented by Akiyama [44, 45], and has been implemented as an electrostatic, surface micromachined motor. The operation principle of the scratch drive actuator (SDA) is illustrated in fig. 1.8. The SDA consists of a thin (1 - 2 μm) polysilicon plate, with a so called bushing at one end of the plate (fig.1.8a,d). Fig. 1.8a-c illustrates the stepping cycle. In the activated state (fig. 1.8a) the plate is attracted to the lower electrode (substrate). As the actuation voltage switches from positive in negative, the plate relaxes shortly (fig 1.8b). This causes the bushing to rotate. Because the friction between the bushing and the insulator is higher than between the plate and the substrate the bushing does not slide, and the center of rotation is the line where the bushing touches the insulator. Therefore, the result of this movement is that the plate shifts slightly forward (fig. 1.8b). The plate is pulled down again, and the bushing slides forward. Next, the state of fig. (1.8a) is reached again and the cycle can be repeated.

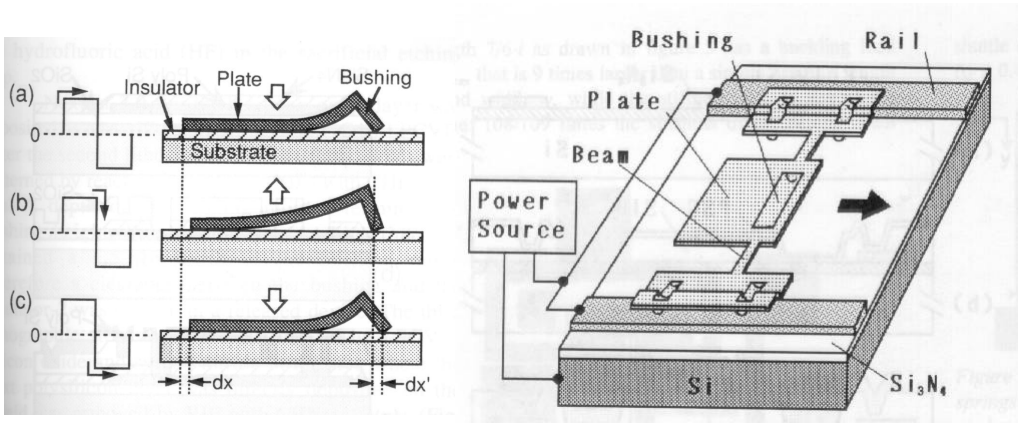

(a), (b), (c) (d)

Fig. 1.8 (from Akiyama [44,45]): Operation principle of the Scratch Drive Actuator. Starting from the activated stage (a), the plate is released shortly while the driving voltage switches polarity (b). In this relaxation the bushing-insulator contact remains fixed, and the plate slides slightly forward. In the next activation (c) the plate is pulled down onto the insulator, and the bushing is forced to rotate and to slip slightly forward. Next, this sequence is repeated. (d) Shows the electrical connections. The driving voltage is applied between the whole moving structure and the substrate.

In tested SDA's the length of the plate is between 50 and 80μm, and bushing height is around 1.5 μm [44, 67]. The step-size increases with increasing driving voltage, and lies between 10 and 100 nm, for driving voltages between 40 V and 200 V. Measured speeds range between 5

and 80 μm/s, at driving frequencies between 100 and 1000 Hz [44, 67]. The maximum measured force is 63 μN at ± 112 V pulse peak voltage [67]
A problem with the SDA is that the operation principle is not fully understood. In particular, it is not clear why during the relaxation of the plate, the friction in the bushing-insulator contact is larger than in the plate-insulator contact. As a result it is not clear to if there are critical parts in the structure. For example the shape of the bushing edge touching the insulator might be important to obtain the desired frictional behavior. Also it is difficult to predict whether or not wear in the bushing-insulator contact can cause malfunction. Despite these problems the SDA has become popular in the MEMS society, because of its simple geometry and the compatibility with standardized surface micromachining processes, such as the Multi-User MEMS processes (MUMPs) offered by MCNC [68]. Nice examples of application of the SDA are the lifting of a polysilicon plate to create suspended inductors and variable capacitors [69], and the integrated assembly of XYZ-stages for optical scanning and alignment [70].

1.4.7 Transformation of Rotary Motion to Linearly Motion

Transformation of rotary into linearly motion is a concept which is often employed in macro-actuators. An example is the car with a combustion motor: Linear motion of the cylinders is transformed into rotary motion by the crankshaft, and the rotary motion is transformed into linearly motion by the wheels. This principle has successfully been tested by Legtenberg et al. [71, 72] in micromechanics, who coupled a rotary wobble motor and a gear rack (fig. 1.9). The advantage of this concept is that infinite motion can easily be generated by a rotary motor. The disadvantage is that if a gearwheel and rack are used for the transformation, there will be back lash. This might be avoided if frictional contact is used for the transformation.

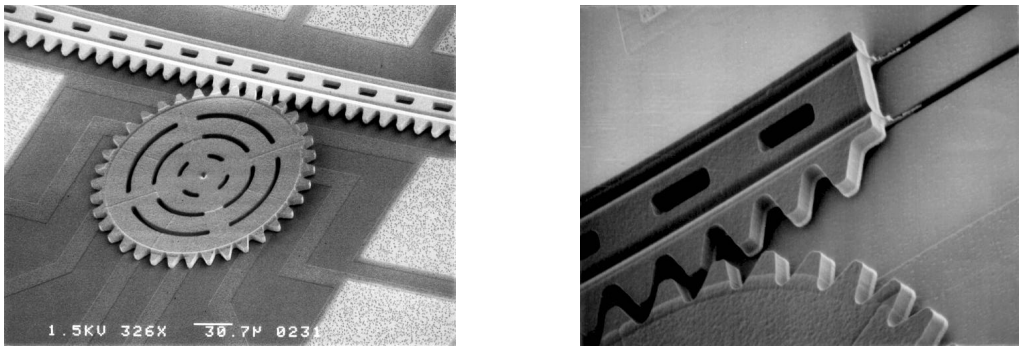

(a) (b)

Fig 1.9: Overview (a) and close up (b) of a wobble motor driving a gear rack [71, 72]. Note the anchoring of the gear rack in slots which were etched in the wafer prior to the structural polysilicon deposition.

1.4.8 Walking Motion

Walking motion was introduced to linear actuators by Burleigh [73] in a patent for a piezoelectric *inch-worm* motor. The motor consists of three basic elements: A front clamp, a back clamp and a body which can contract (fig.1.10). The walking cycle starts with only the front clamp activated (a). In the next stage the body contracts (b) and the back clamp shifts

forward. Next the back clamp is activated (c) and the front clamp is released (d). The body relaxes and extends (e), shifting the front clamp forward. Finally the front clamp is activated (f) and the back clamp released (a). Burleigh [74] has implemented the principle in several piezoelectrically driven motors. These have a resolution of 4 nm and up to 200 mm of travel. The actuators have a circular cross-section with a diameter in the order of 1 cm and a length of several cm, depending of the maximum travel distance. The max. load is 10 N and the max. speed is 1.5 mm/s. Koster [76] has implemented the walking concept in combination of a mechanical amplification mechanism to increase the walking velocity. The motor has a peak velocity of 30 mm/s, because of heating by dissipation in the PZT-actuators, the continuous max. velocity is 3 mm/s. The motor includes a special clamping design, which is less sensitive to variations of the diameter of the shaft, along which the mechanism walks.

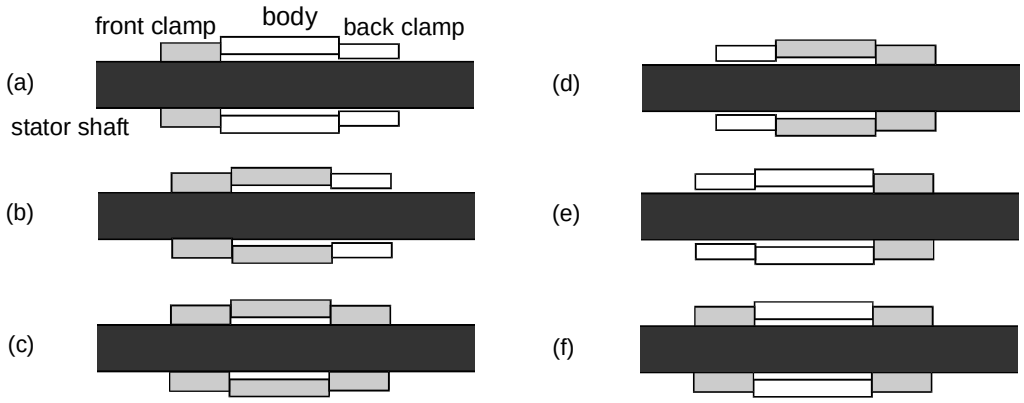

Fig. 1.10: Walking cycle of the Burleigh's inch-worm motor. The motor consists of three basic elements: A front clamp, a back clamp and a body which can contract. The walking cycle starts with only the front clamp activated (a). In the next stage the body contracts (b) and the back clamp shifts forward. Next the back clamp is activated (c) and the front clamp is released (d). The body relaxes and extends (e), shifting the front clamp forward. Finally the front clamp is activated (f) and the back clamp released (a).

In the presented motors so far, the moving part contains the clamp- and displacement actuators. Walking motion can also be implemented with a passive moving part, which is driven by a pair of drive-units ('legs'), each containing a clamp and a pull actuator. The drive-units are fixed to the substrate. This concept has been implemented by Yeh et al. [46, 47] for electrostatic actuation of microrobots. The implementation is realized using the commercially available MUMPs surface micromachining process [68]. Fig. 1.11 illustrates the walking cycle. The walking cycle starts with both pull actuators relaxed, and clamp c1 activated to hold the shuttle (a). The shuttle is displaced by pull actuator p1 (b) and clamp c2 is activated (c) to take over the clamping from c1. Next, c1 is released (d), p1 is relaxed (e) and p2 contracts to displace the shuttle (e). Then c1 is activated (f), c2 is released (g), and p2 is relaxed (a). Clamping is generated by electrostatic attachment of the clamp shoes to the shuttle. The step motion is generated by gap-closing actuator arrays, each consisting of 10 rotor-stator beam pairs with a 60 μm overlap, working in parallel. The actuator arrays are made of 3.5 μm thick polysilicon, which is obtained by stacking of two layers of the MUMPs

process in which the motor is realized. The produced force was estimated at 6 μN with 35 V driving voltage. The maximum deflection measured was 40 μm in 20 steps of 2 μm [47].

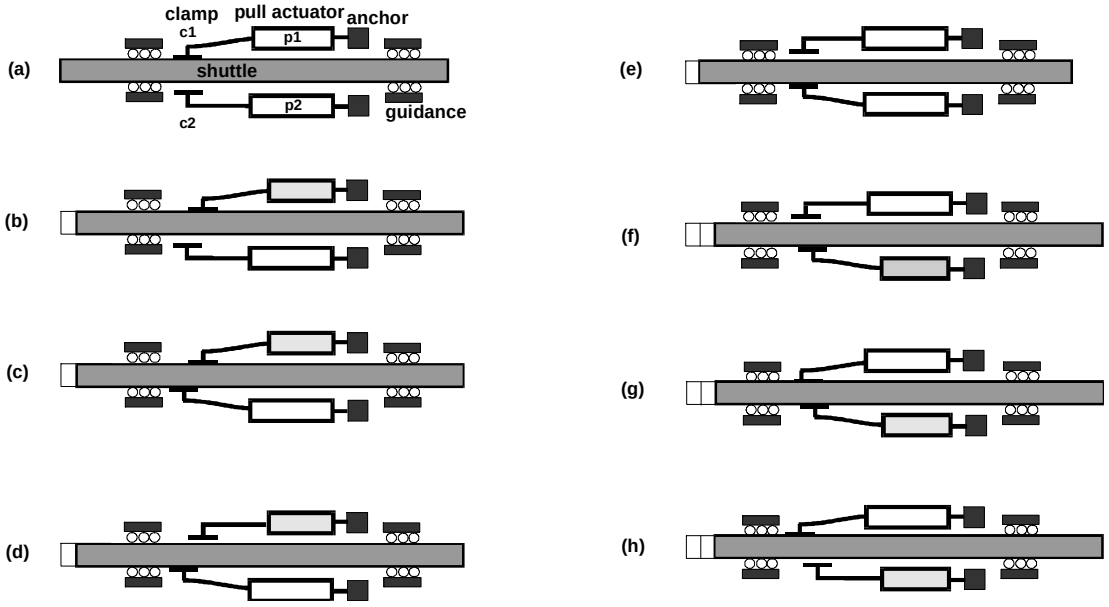

Figure 1.11: Cycle of the linear motor with passive moving part and drive units fixed to the surroundings. The motor consists of two drive units, each containing a clamp and a pull actuator. The walking cycle starts with both pull actuators relaxed, and clamp c1 activated to hold the shuttle (a). The shuttle is displaced by pull actuator p1 (b) and clamp c2 is activated (c) to take over the clamping from c1. Next, c1 is released (d), p1 is relaxed (e) and p2 contracts to displace the shuttle (e). Then c1 is activated (f), c2 is released (g), and p2 is relaxed (a).

1.4.8 Choice of Propulsion Principle

It was decided to concentrate on implementation of walking motion electrostatic surface micromachined actuators. This concept has a number of attractive features:

1. The walking motion intrinsically facilitates a large dynamic range (reach / resolution).
2. Clamp and propulsive actuation can be separated, which gives design freedom to optimize these functions.
3. There is only sliding contact in the inactive clamps, therefore wear is expected to be lower than in mechanisms where clamped parts have to slide, as in for example the scratch drive and the inertial drive.
4. If there is wear this is not directly fatal, as the shape of the contacting parts in the clamps is not critical.

We would like to stress that this choice does not imply that the other principles are less attractive. We think that a fair comparison of the propulsion principles, should be based on the performance of realized devices with a comparable degree of optimization. At the current stage of development of most of the micromotors this is not yet possible. Our implementations of walking motion are treated in chapter 5 and 6.

1.5 Microtribology

Due to the large surface to volume ratio in micromechanics, surface forces become relative large compared to body forces. To give an indication: The gravitation force acting on surface micromachined elements is typically in the range of 0.1 - 10 nN. The adhesion force between surface micromachined elements can easily become in the order of 1 μN and larger. This can cause friction much larger than the friction caused by the gravitational load. [24, 46, 47, 77, 78, 79**]**. For walking motion it is necessary to create controllable friction in the clamps. Friction in the clamps should be low (say < 1 μN) if the clamps are not activated (zero load), and should large (> 100 μN) if the clamps are activated (large load). In particular the first demand can be troublesome to achieve, because due to the adhesion between the two contacting surfaces in the clamp, significant friction can remain if the clamp is not activated. A model for the friction in adhesive microcontacts is therefore desirable. We will therefore briefly introduce existing friction theory.

Generally two friction mechanisms are distinguished: Ploughing and shearing friction. Ploughing friction exists if asperities of the harder contact material create scratches in the softer material [80]. Shearing friction (also called adhesive friction) exists if asperities slide across the counter surface, continiously creating and breaking bonds. In MEMS contacting surfaces often consists of rather hard materials ((poly)silicon, silicon-dioxide, silicon nitride) and are rather smooth. It is therefore expected that adhesive friction is the main friction mechanism.

From macro-tribology it is known that the friction force is almost proportional to the load force, and is almost independent of the apparent contact area (Amontons' Law). According to Bowden and Tabor [80] the shearing friction equals the product of the real contact area and a characteristic maximum shear stress in the interface. If the contacting asperities deform plastically, it follows from this model that the real contact area is proportional to the load and independent of the apparent contact area. Therefore the friction will be proportional to the load. In 1966 Greenwood and Williamson showed that Amontons' Law also applies to rough surfaces of which the contacting asperities deform elastically [81]. This result is important for MEMS contacts: In MEMS devices materials are often hard and smooth. This implies that elastic deformation will frequently be encountered in MEMS contacts. In section 4.3.4 the condition for pure elastic deformation is given.

In the 1970s Johnson, Kendall and Roberts [82] and Derjaguin, Muller and Toporov [83] derived expressions for the contact area and pull-off force for a single asperity elastic contact, including adhesive load. Fuller and Tabor [84] implemented the JKR single asperity model in the statistical model of Greenwood and Williamson, in order to calculated the separation force of rough, elastic, adhesive contacts. A similar approach has been followed by Maugis [85] to calculate the real contact area in an elastic adhesive contact, as a function of externally applied load, and elasticity, roughness, adhesion parameters. A combination of this latter model and the Bowden and Tabor model provides us with a friction model for rough, elastic, adhesive contacts. From Maugis [85] it follows that in adhesive elastic contacts the real contact area

and thus the friction force strongly depends on the surface topography. This is confirmed experimental results [86]. The influence of surface topography on friction will therefore be one of the main topics in our tribology study. In chapter 4 the mentioned contact models are treated in detail. It will be tested if the derived (static) friction model can be employed under the conditions that encountered in MEMS sliding contacts.

1.6 Lateral vs. Normal Actuation

We distinguish two different realization concepts to generate motion: Normal to the wafer surface (normally driven), and parallel to the wafer surface (laterally driven). The advantage of the first is that a large electrode area can be obtained simply by making a plate suspended over a lower electrode. The disadvantage is that there are at least two polysilicon layers necessary to form electrodes of two polarities. In a laterally driven mechanism like the comb-drive shown in fig. 1.12, a stator and a moving electrode can be created from a single polysilicon layer. However, in order to make a large electrode area, the design is more complicated.

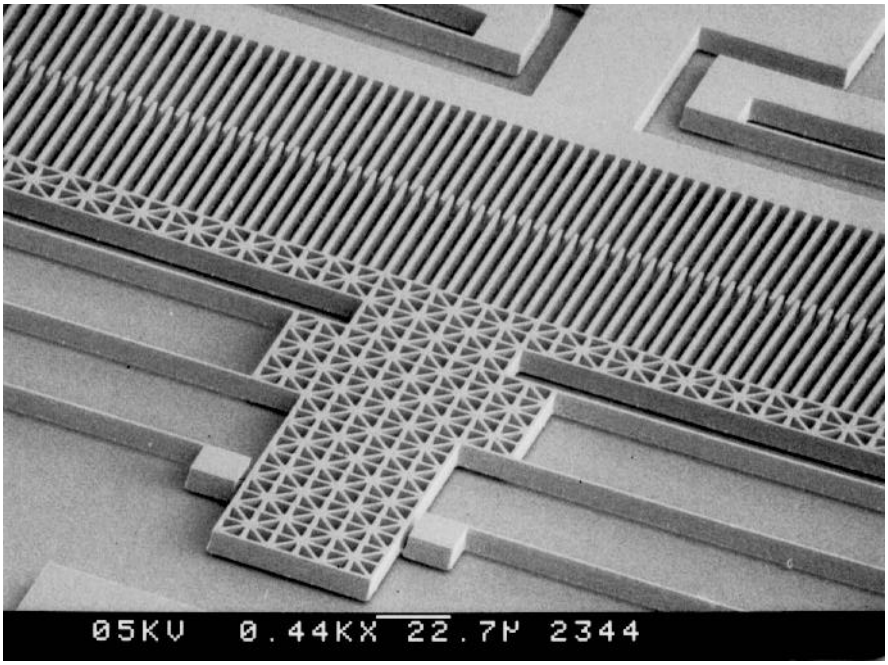

Figure 1.12: Close-up of a large comb-drive actuator with compliant guidance springs by R. Legtenberg [75].

For the normally driven actuator the effective electrode area equals the wafer area it occupies. For the laterally driven actuator this depends on the height of the electrodes, and the lateral resolution of the fabrication process. For 5 μm electrode height and 2 μm lateral gaps and electrode widths, the effective electrode area equals 1.2 times the occupied wafer area. In theory, if 100% of a 1 mm^2 area is occupied by electrodes with a 2 μm gap spacing between both polarities, a force of 1 mN can be generated with a 30V driving voltage. Practically the generated force is generally much lower, because a significant part of the wafer surface is

occupied by passive structures like the suspension and the construction connecting the electrodes and the output member. For example, the comb-drive actuator of fig. 1.12 only generates 1 μN at 20 V driving voltage. It occupies appr. 0.3 x 1 mm^2. This indicates that it is probably necessary to include a mechanical lever to obtain forces of at least 0.1 mN. This will be worked out in chapter 5 for laterally driven mechanisms, and in chapter 6 for normally driven motors.

1.7 Formulation of the Research Questions

The research topics which have been distinguished in the previous paragraphs have been worked out to obtain questions which we would like to answer in this thesis. The questions are listed below. In chapter 7 we will conclude by answering the listed questions explicitly.

1.7.1 Electrostatic Actuator Theory

Q1: What is the maximum voltage that is allowed before electrical break-down in air occurs?

Q2: How can the produced force and the output stiffness be calculated for electrostatic actuators

Q3: Can the produced force be expressed in a way which is convenient for conceptual design of electrostatic actuators?

Q4: Can we realize 0.1 mN force and more than 10 μm stroke in a 1x1x1 mm^3 electrostatic actuator driven by 30 V?

1.7.2 Fabrication

Q5: How can stiction of freed parts of the mechanism to the substrate, be reduced or avoided?

1.7.3 Micro Tribology

Q6: Is it possible to make electrostatic clamps with low enough adhesion, using surface micromachining?

Q7: Will there be elastic or plastic deformation in the micro contacts ?

Q8: What is the influence of surface roughness on the friction in an elastic adhesive contact?

Q9: Can the statistical Maugis [85] contact model be applied to MEMS contacts?

Q10: How can the adhesion forces be accounted for in a simple expression for the friction, similar to Amontons' Law ?

1.7.4 Laterally driven actuators

Q11: Is it possible to obtain controlled friction between etched polysilicon side-walls?

Q12: Is it possible to include a lever to increase the force?

Q13: How can the electrostatic pull-down of moving parts to the substrate be avoided?

1.7.5 Normally driven actuators

Q14: How can a normal movement be transformed into a lateral movement?

Q15: How can a lever be made in a normally driven mechanism?

Q16: In a normally driven walking motor there will be contact between the top surface of the lower electrodes, and the bottom surface of the moving electrodes. Can the friction between these thin films be controlled?

1.7.6 General

Q17: Can reliable walking motion be produced by electrostatic actuation of a surface micromachined structure?

Q18: What performance can be achieved, with respect to the specifications?

1.8 Literature

[1] Sander L., Baartman J-P.,"Specifications of Magnetic Lin. Rec., Harddisk , and CD storage systems", internal communication, Oct. 96.

[2] J.G.E. Gardeniers, A.G.B.J. Verholen, N.R.Tas and M. Elwenspoek," Direct Measurement of Piezoelectric Properties of Sol-Gel PZT Films", J. of the Korean Physical Society, Vol. 32, Febr. 1998, pp. S1573-S1577.

[3] M. Blom, "Integration of PZT thin films and surface-micromachining for a linear microactuator", M.Sc. Thesis, Faculty of Applied Physics, University of Twente, 1998.

[4] K.E.Peterson,"Silicon as a mechanical material", Proc. IEEE, 1982, pp. 420-457.

[5] www.sensonor.com

[6] www.intersema.ch

[7] www.microproducts.nl

[8] www.analog.com

[9] www.el.utwente.nl/mesa/aquamarijn/

[10] www.microflown.com

[11] Madou M.,"Fundamentals of Microfabrication", CRC-Press, New York, 1997.

[12] M. Elwenspoek, H. Jansen,"Silicon Micromachining", Cambridge University Press, 1998.

[13] R. Legtenberg,"Electrostatic Actuators Fabricated by Surface Micromachining Techniques", Ph.D. Thesis University of Twente, ISBN 90-3650796, 1996.

[14] H.V. Jansen,"Plasma Etching in Microtechnology", Ph.D. Thesis University of Twente, ISBN 903650810x, 1996.

[15] H.C. Nathanson, W.E. Newell, R.A. Wickstrom, and J.R. Davis Jr.,"The Resonant Gate Transistor", IEEE Trans. on Electron Devices, Vol. ED-14, no.3, March 1967, pp. 117-133.

[16] K. Dutta, P. Dev, P. Dewilde, B. Sharma, R. Newcomb,"Integrated micromotors concepts," Proc. of the Int. Conf. on Microelectronic Circuits and System Theory", Sydney, NSW, Australia, Aug. 1970, pp. 36-37.

[17] M. Mehregany, K.J. Gabriel, W.S.N. Trimmer,"Integrated Fabrication of Polysilicon Mechanisms", IEEE Trans. on Electron Devices, Vol. 35, no.6, June 1988, pp. 719-723.

[18] L-S. Fan, Y-C. Tai , and R.S. Muller,"Pin Joints. Gears, springs, cranks, and other novel micromechanical structures", Proc. 4th Int. Conf. on Solid-State Sensors and Actuators (Transducers 87), Tokyo, Japan, June 2-5 1987, pp. 849-852.

[19] L-S. Fan, Y-C. Tai, R.S. Muller,"Integrated Movable Micromechanical Structures for Sensors and Actuators", IEEE Trans. On Electron Devices, Vol. 35, no.6, June 1988, pp. 724-730.

[20] W.C. Tang, T-C H. Nguyen, and R.T. Howe,"Laterally Driven Polysilicon Resonant Microstructures", Proc. IEEE Micro Electro Mechanical Systems 1989, Salt Lake City, Utah, Febr. 20-22, 1989, pp. 53-59.

[21] W.C. Tang, T-C H. Nguyen, and R.T. Howe,"Laterally Driven Polysilicon Resonant Microstructures", Sensors and Actuators, Vol. 20, 1989, pp. 25-32.

[22] L-S. Fan, Y-C. Tai and R.S. Muller,"IC-processed Electrostatic Micro-motors", Int. Electron. Devices Meeting, Dec. 11-14 1988, pp. 666-669.

[23] L-S. Fan, Y-C. Tai, and R.S. Muller,"IC-processed Electrostatic Micromotors", Sensors and Actuators, Vol. 20, 1989, pp. 41-47.

[24] M. Mehregany, P. Nagarkar, S.D. Senturia, and Jeffrey H. Lang,"Operation of Microfabricated Harmonic and Ordinary Side-drive Motors", Proc. IEEE Workshop on Microelectromechanical Systems 1990, Napa Valley, CA, USA, 11-14 Febr. 1990, pp. 1-8.

[25] M. Mehregany, S.F. Bart, L.S. Tavrow, J.H. Lang, S.D. Senturia and M.F. Schlecht,"A study of Three Microfabricated Variable-capacitance Motors", Sensors and Actuators, A21-23, 1990, pp. 173-179.

[26] M. Sakata, Y. Hatazawa, A. Omodaka, T. Kudoh and H. Fujita,"An Electrostatic Top Motor and its Characteristic", Sensors and Actuators, A21-23, 1990, pp. 168-172.

[27] R.T. Howe,"Recent advances in Surface Micromachining", 13th Sensor Symposium IEE of Japan, June 8-9, 1995.

[28] Guckel H., Sniegowski J.J., Christenson T.R., Mohney S., Kelly T.F.,"Fabrication of micromechanical devices from polysilicon films with smooth surfaces", Sensors and Actuators, Vol. 20, 1989, pp. 117-122.

[29] Mastrangelo C.H., Hsu C.H.,"A simple experimental technique for the measurement of the work of adhesion of microstructures", Proc. IEEE Solid-State Sensors and Actuators Workshop, Hilton Head Island, SC, USA, June 22-25, 1992, pp. 208-212.

[30] Alley R.L., Cuan G.J., Howe R.T., Komvopoulus K.,"The effect of release-etch processing on surface microstructure stiction", Proc. IEEE Solid-State Sensors and Actuators Workshop, Hilton Head Island, SC, USA, June 22-25, 1992, pp. 202-207.

[31] Scheepers P.R., Voorthuyzen J.A., Olthuis W., Bergveld P.,"Investigation of attractive forces between PECVD silicon nitride microstructures and an oxidized silicon substrate", Sensors and Actuators A, Vol. 30, 1992, pp. 231-239.

[32] Legtenberg R., Tilmans H.A.C., Elders J., Elwenspoek M.,"Stiction of surface micromachined structures after rinsing and drying: model and investigation of adhesion mechanisms", Sensors and Actuators A, Vol. 43, 1994, pp. 230-238.

[33] M. Mehregany, S.M. Phillips, E.T. Hsu, and J.H. Lang,"Operation of Harmonic Side-Drive Micromotors Studied through Gear Ratio Measurement", Proc. 6th Int. Conf. on Solid-State Sensors and Actuators (Transducers 91), San Francisco, CA, USA, 1991.

[34] A.D. Moore (ed.),"Electrostatics and its applications", John-Wiley & Sons, New York, 1973.

[35] J.C. Poggendorff, Ann. Phys., Ser. 2, vol. 139, 1870, pp. 513-546.

[36] Zipernowski, "Zipernowski electrostatic motors", Elect. World, vol. 14, 1889, pp. 260-.

[37] Bollée B.,"Electrostatic Motors ", Philips technical review, vol. 30, no. 6/7, 1969, pp. 178-194.

[38] L.S. Tavrow, S.F. Bart, J.H. Lang, M.F. Schlecht,"A LOCOS Process for an Electrostatic Microfabricated Motor", Sensors and Actuators, A21-A23, 1990, pp. 893-898.

[39] S.C. Jacobson, R.H. Price, J.E. Wood, T.H. Rytting and M. Rafaelof,"A design Overview of an Eccentric-motion Electrostatic Microactuator (the Wobble Motor)", Sensors and Actuators, vol. 20, 1989, pp. 1-16.

[40] W.Trimmer and R.Jebens,"Harmonic Electrostatic Motors", Sensors and Actuators, vol. 20, 1989, pp. 17-24.

[41] T. Furuhata, T. Hirano, L.H. Lane, R.E. Fontana, L.S. Fan, H. Fujita,"Outer Rotor Surface-Micromachined Wobble Micromotor", Proc. IEEE Micro Electro Mechanical Systems Workshop 1993, Fort Lauderdale, Florida, USA, Febr. 7-10, 1993, pp. 161-166.

[42] R. Legtenberg, E. Berenschot, J. van Baar, Th. Lammerink and M. Elwenspoek,"An electrostatic lower stator axial gap wobble motor:design and fabrication", 8th Int. Conf. on Solid-State Sensors and Actuators (Transducers 95), and Eurosensors IX, Stockholm, Sweden, June 25-29, 1995, pp. 404-407.

[43] H. Fujita, A.Omodaka,"The Fabrication of an Electrostatic Linear Actuator by Silicon Micromachining", IEEE Trans. on Elec. Dev., vol. 35, no. 6, June 1988.

[44] T. Akiyama, K. Shono,"A New Step Motion of Polysilicon Microstructures", Proc. IEEE Micro Electro Mechanical Systems Workshop 1993, Fort Lauderdale, Florida, USA, Febr. 7-10, 1993, pp. 272-277.

[45] T. Akiyama, K. Shono,"Controlled Stepwise Motion in Polysilicon Microstructures", J. Microelectromechanical Systems, vol. 2, no. 3, 1993, pp. 106-110.

[46] R. Yeh, E.J.J. Kruglick, K.S.J. Pister,"Micro Electromechanical Components for Articulated Microrobots", The 8th Int. Conf. on Solid-State Sensors and Actuators, (Transducers 95) and Eurosensors IX, Stockholm Sweden, June 25-29, 1995, pp. 346-349.

[47] R. Yeh, E.J.J. Kruglick, and K.S.J. Pister,"Surface-Micromachined Components for Articulated Microrobots", J. Microelectromechanical Systems, vol. 5, no. 1, March 1996, pp. 10-17.

[48] S. Egawa, T. Higuchi,"Multi-Layered Electrostatic Film Actuator", Proc. IEEE Micro Electro Mechanical Systems Workshop 1990, Napa Valley, CA, USA, Febr. 11-14, 1990, pp. 166-171.

[49] T. Higuchi, Y. Yamagata, K. Furutani, K. Kudoh,"Precise Positioning Mechanism Utilizing Rapid Deformations of Piezoelectric Elements", Proc. IEEE Micro Electro Mechanical Systems Workshop 1990, Napa Valley, CA, USA, Febr. 11-14, 1990, pp. 222-226..

[50] K. Ikuta, A. Kawahara, S. Yamazumi,"Miniature Cybernetic Actuators Using Piezoelectric Device", Proc. IEEE Micro Electro Mechanical Systems Workshop, Nara, Japan, 1991, pp. 131-136.

[51] K. Ikuta, S. Aritomi, T. Kabashima,"Tiny Silent Linear Cybernetic Actuator Driven by Piezoelectric Device with Electromagnetic Clamp", Proc. IEEE Micro Electro Mechanical Sytems '92, Travemunde, Germany, Febr. 4-7, 1992, pp. 232-237.

[52] T. Uchiki, T. Nakazawa, K. Nakamura, M. Kurosawa, and S. Ueha,"Ultrasonic Motor Utilizing Elastic Fin Rotor", Jap. J. Appl. Phys., Vol. 30, no. 9b, Sept. 1991, pp. 2289-2291.

[53] G.-A. Racine, R. Luthier, and N.F. de Rooij,"Hybrid Ultrasonic Micromachined Motors", Proc. IEEE Micro Electro Mechanical Systems 1993, Fort Lauderdale, Florida, USA, Febr. 7-10, 1993, pp. 53-59.

[54] P. Muralt, M. Kohli, T. Maeder, A. Kholkin, K. Brooks, N. Setter, R. Luthier,"Fabrication and Characterization of PZT thin-film vibrators for micromotors", Sensors and Actuators A, vol. 48, 1995, pp. 157-165.

[55] A.P. Lee, D.J. Nikkel Jr., and A.P.Pisano,"Polysilicon linear microvibromotors", 7th Int. Conf. on Solid-State Sensors and Actuators (Transducers '93), Yokohama, Japan, June 7-10 1993, pp. 46-49.

[56] M.J. Daneman, N.C. Tien, O. Solgaard, A.P. Pisano, K.Y. Lau, R.S. Muller,"Linear Microvibromotor for Positioning Optical Components", Proc. IEEE Micro Electro Mechanical Systems Workshop 1995, Amsterdam, Jan. 29- Febr. 2, 1995, pp. 55-60.

[57] W.C. Tang, T.-C. H. Nguyen, M.W. Judy, R.T. Howe,"Electrostatic-comb drive of lateral polysilicon resonators", Sensors and Actuators, Vol. A21-23, 1990, pp. 328-331.

[59] Y-H Cho, A.P. Pisano, and R.T. Howe,"Viscous Damping Model for Laterally Oscillating Microstructures", J. Microelectromechanical Systems, Vol. 3, no.2, June 1994, pp. 81-87.

[60] M.J. Daneman, N.C. Tien, O. Solgaard, K.Y. Lau, R.S. Muller,"Linear Vibromotor-Actuated Micromachined Microreflector for Integrated Optical Systems", Solid-State Sensors and Actuators Workshop Hilton Head, South Carolina, June 2-6, 1996, pp. 109-112.

[61] K.M. Anderson, J.E. Colgate,"A Model of the Attachment/Detachment cycle of Electrostatic Micro Actuators", DSC-Vol. 32 (MEMS), ASME, 1991, pp. 255-268.

[62] A. Koga, K. Suzumori, T. Miyagawa, M. Sekimura,"Attachment/Detachment Electrostatic Micro Actuators for Pan-tilt Drive of a Micro CCD Camera", Proc. IEEE Micro Electro Mechanical Systems Workshop 1996, San Diego, California, USA, Febr. 11-15, 1996, pp. 509-514.

[63] S. Egawa, T. Niino, T. Higuchi,"Film Actuators: Planar, Electrostatic Surface-Drive Actuators", Proc. IEEE Micro Electro Mechanical Systems Workshop 1991, Nara, Japan, Jan. 30 - Febr. 2, 1991, pp. 9-14.

[64] T. Niino, S. Egawa, H. Kimura and T. Higuchi," Electrostatic Artificial muscle: Compact, High-Power Linear Actuators with Multiple-Layer Structures", Proc. IEEE Micro Electro Mechanical Systems Workshop 1994, Oiso, Japan, Jan. 25 - 28, 1994, pp. 130-135.

[65] A. Yamamoto, T. Niino, T. Higuchi," High Precision Electrostatic Actuator with Novel Electrode Design", Proc. IEEE Micro Electro Mechanical Systems Workshop 1998, Heidelberg, Germany, Jan 25-29, 1998, pp. 122-127.

[66] T. Niino, S. Egawa, N. Nishiguchi, T. Higuchi," Development of an Electrostatic Actuator Exceeding 10N Propulsive Force", Proc. IEEE Micro Electro Mechanical Systems Workshop 1992, Travemunde, Germany, Febr. 4 - Febr. 7, 1992, pp. 122-127.

[67] T. Akiyama, H. Fujita," A Quantitative Analysis of Scratch Drive Actuator Using Buckling Motion", Proc. IEEE Micro Electro Mechanical Systems 1995, Amsterdam, The Netherlands, Jan. 29 - Febr. 2, 1995, pp. 310-315.

[68] Koester et al.," MUMPs Design Handbook 4.0 (may 1999)", Cronos Integrated Microsystems, *see* mems.mcnc.org/mumps.html.

[69] L. Fan, R.T. Chen, A. Nespola, M.C. Wu," Universal MEMS Platforms for Passive RF Components: Suspended Inductors and Variable Capacitors", Proc. IEEE Micro Electro Mechanical Systems Workshop 98, Heidelberg, Germany, Jan. 25-29, 1998, pp. 29-33.

[70] L. Fan, M.C. Mu, K.D. Choquette, M.H. Crawford,"Self-Assembled Microactuated XYZ stages for Optical Scanning and Alignment", Proc. 1997 Int. Conf. on Solid-State Sensors and Actuators (Transducers 97), Chicago, USA, June 16-19, 1997, pp.319-322.

[71] R. Legtenberg, E. Berenschot, M. Elwenspoek, and J.H.J. Fluitman,"Electrostatic Microactuators with Integrated Gear Linkages for Mechanical Power Transmission", Proc. IEEE Micro Electro Mechanical Systems Workshop 1996, San Diego, CA, USA, Febr. 11-15, 1996, pp. 204-209.

[72] R. Legtenberg, E. Berenschot, M. Elwenpoek, J.H. Fluitman," A Fabrication Process for Electrostatic Microactuators with Integrated Gear Linkages", J. Microelectromechanical Systems, Vol. 6, no. 3, 1997, pp. 234-241.

[73] W.G. May, Jr.,"Piezoelectric electromechanical translation apparatus", United States Patent no. 3902084, Aug. 26, 1975.

[74] "Inchworm Motors", *see* www.burleigh.com.

[75] R. Legtenberg, A.W. Groeneveld and M. Elwenspoek," Comb-drive actuators for large displacements", J. Micromech. Microeng., Vol. 6, 1996, pp. 320-329.

[76] M.P. Koster," A walking piezo motor", Conf. Proc. Actuator 94", Bremen, Germany, June 15-17, 1994, pp. 144-148.

[77] M.G. Lim, J.C. Chang, D.P. Schultz, R.T. Howe, R.M. White,"Polysilicon microstructures to characterize static friction", Proc. IEEE Micro Electro Mechanical Systems Workshop, Napa Valley, CA, USA, 11-14 Febr. 1990, pp. 82-88.

[78] R. Kaneko," Microtribology related to MEMS", Proc. IEEE Micro Electro Mechanical Systems Workshop, Nara, Japan, 1991, pp. 1-8.

[79] Komvopoulos K.,"Surface engineering and microtribology for microelectromechanical systems", Wear, vol. 200, 1996, pp. 305-327.

[80] Bowden F.P., Tabor D.,"The friction and lubrication of solids", Oxford Clarendon Press, 1950.

[81] Greenwood J.A., Williamson J.B.P.," Contact of nominally flat surfaces", Proc. R. Soc. Lond. A, Vol. 295, 1966, pp. 300-319.

[82] Johnson K.L., Kendall K., Roberts A.D.,"Surface energy and the contact of elastic solids", Proc. R. Soc. Lond. A, Vol. 324, 1971, pp. 301-313.

[83] Derjaguin B.V., Muller V.M., Toporov Yu. P.,"Effect of contact deformations on the adhesion of particles", J. Colloid Interface Sci., Vol. 53, no.2, Nov. 1975, pp. 314-326.

[84] Fuller K.N.G., Tabor D.,"The effect of surface roughness on the adhesion of elastic solids", Proc. R. Soc. Lond. A., vol. 345, 1975, pp.327-342.

[85] Maugis D.,”On the contact and adhesion of rough surfaces”, J. Adhesion Sci. Technol., vol. 10, no.2, 1996, pp. 161-175.

[86] W.R.Chang, I.Etsion, D.B. Bogy,”Static friction coefficient model for metallic rough surfaces”, J. Tribology, Vol. 110, Jan. 1988, pp. 57-63.

2

Electrostatic Actuator Theory

Equilibrium and stability of conservative electrostatic transducers is studied by means of the energy stored in the mechanical and electrical buffers. States of stable equilibrium are found by minimization of a generalized potential with respect to the unconstraint state variables. Electrostatic actuators can become unstable if the effective actuator stiffness becomes negative. This can occur for both fixed charge and fixed voltage. The onset of instability of the gap-closing actuator loaded by a constant force F and driven with a fixed voltage is analyzed. The pull-in position is 2/3 ($x_0 + F / k$), with x_0 the initial position of the moving plate suspended by a spring with a stiffness k. The stable region of operation can be increased by suspending the moving electrode with a higher order spring. An actuator model has been made that expresses the electrostatic force as the product of the energy density and the active area, which is the derivative of the volume containing the electric field, with respect to the direction of movement. From literature a maximum allowable electric field 2×10^8 V/m in a 2 μm gap in air has been found, limited by breakdown. This corresponds with an energy density of 2×10^5 J/m^3. The energy density is in the same order as can be obtained in magnetic actuators, and which is allowed in commercial PZT piezoelectric actuators. The maximum attainable electrostatic force on a 1 x 1 mm^2 area and using surface micromachining design rules, is 0.1 mN with a driving voltage of 30V for both the gap-closing and the comb-drive actuator. This force is large enough to meet our demands, however the stroke of 2 μm is too small. Three options to increase the product of force and stroke are presented. Finally, the principle of inertial matching is introduced. It can be used to maximize the output acceleration.

2.1. Introduction

In this chapter a general theory for equilibrium and stability analysis of generator type transducers is presented. The theory is based on the thermodynamic equilibrium analysis (section 2.2).The theory is applied to analyze variable capacitance electrostatic actuators driven with either a fixed charge or a fixed voltage (section 2.3). The fixed charge control is mainly of theoretical value, as it is difficult to realize in MEMS systems, where the actuator capacitances is in the fF-pF range. Parallel parasitic capacitors which are large compared to the variable actuator capacitance, effectively act as voltage sources. Mathematically, the transduction is expressed in the position dependent capacity of the gap between the fixed and the moving electrode. In section 2.4 the generated force of the comb-drive and the gap-closing actuators is expressed as a function of the electrical energy density in and the geometry of the active gaps. The resulting expression is a powerful tool for actuator design. In section 2.5 electrical break-down is analyzed using the Paschen-theory, in order to estimate the maximum possible energy density in the actuator gaps. In section 2.6 the theory of the previous two sections is used to estimate the maximum obtainable forces and strokes with electrostatic

actuators. Finally, in section 2.7 we apply the principle of inertial matching to derive the maximum attainable output acceleration.

2.2 Equilibrium of an isothermal multi-port transducer

2.2.1 Definitions and conditions

Let the transducer be isothermal and conservative [1], i.e. the energy $W(q_1,q_2,..q_n)$ of the transducer is a function of the extensive parameters, the state variables q_1, q_2,..q_n only, independent of the path taken to reach the state. In thermodynamic languages, the energy of the transducer would be called the *free energy*, because of the isothermal condition. W is the sum of the potential and kinetic energies of the buffers in the transducer. In the mechanical domain, the kinetic energy plays an equivalent role as the potential energy. This equivalence can theoretically be founded: In the state space, the kinetic energy meets all the conditions for a potential: In the kinetic domain the intensive parameter, also called effort or generalized force, is the velocity $\boldsymbol{v}$. The conserved quantity of the kinetic domain is the momentum $\boldsymbol{p}$. If $\boldsymbol{v}$ is indeed a conservative force, than it should be possible to define a potential T such that $\boldsymbol{v} = \tilde{\mathrm{N}}T$, with $\tilde{\mathrm{N}} \equiv \mathbf{e}_x\cdot\partial/\partial(p_x) + \mathbf{e}_y\cdot\partial/\partial(p_y) + \mathbf{e}_z\cdot\partial/\partial(p_z)$. The potential which satisfies is $T = \tfrac{1}{2}m\boldsymbol{v}\cdot\boldsymbol{v} = \tfrac{1}{2}\, m(v_x^2+v_y^2+v_z^2)$, the kinetic energy.

Following physical systems theory [2], we define equilibrium as the state in which all state variables q_i are constant. This is not necessarily a state in which all effort differences with the surroundings are zero. The effort difference with the surroundings can remain due to a constraint. A constraint is a fixation of the state variable q of the concerning domain. Equilibrium can exist for a constant, non-zero momentum, if W is independent of the associated position.

2.2.2 Equations of equilibrium and stability

Consider system A in fig. 2.1, a transducer with n ports in n physical domains. The transducer consists of n interconnected buffers, which store an amount q_h of the extensive quantity, at a potential level e_h (h = 1..n). For domain i = 1 .. k the state variables q_i are constrained at a known level. For domain $j = k + 1$ .. n the state variables q_j are unconstrained. The transducer is connected to the constant effort sources, through dissipators R_j. A constant effort source is equivalent with a buffer with a infinite large capacity. A flow will be present until the effort differences $e_{s,j}$ - e_j across the dissipators R_j are relaxed. It is assumed that system A and B fulfill the isothermal condition. The produced heat immediately flows to the surroundings, which in the thermal domain form a buffer with infinite capacity. The power P_{diss} dissipated in the R_j's corresponds with an entropy production P_{diss} / T_0 [2], however this is of no importance under the isothermal condition: due to the uniform temperature heat can not be used to perform work. Therefore, the entropy production and flow have not been drawn in fig. 2.1.

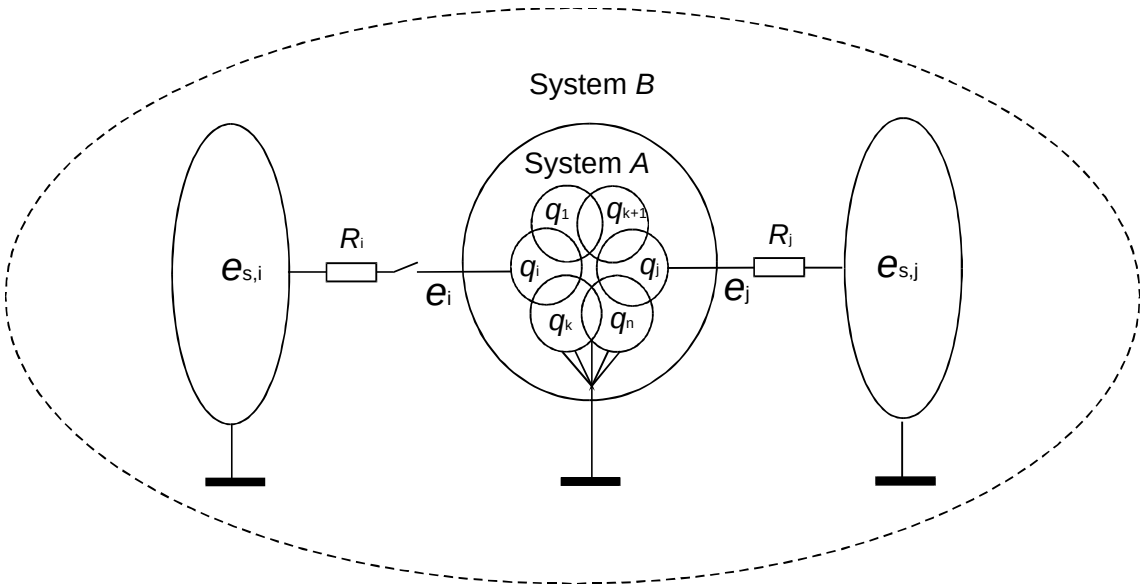

Figure 2.1: System *A* is a transducer which consists of *n* interconnected buffers. For domain $i = 1 .. k$ the state variables q_i are constrained at a known level. For domain $j = k + 1 .. n$ the state variables q_j are unconstrained. In equilibrium, the accompanied efforts e_j are equal to $e_{s,j}$, the efforts imposed by the connected effort sources. System *B* consists of the transducer and the *n* sources.

In our equilibrium analysis it is assumed that the energy *W* as a function of the state variables $q_{1..n}$ is known. For infinitesimal changes d*W* is given by:

$$\mathrm{d}W = \sum_{h=1}^{n} \left. \frac{\partial W(q_1, q_2, .. q_n)}{\partial q_h} \right|_{q_1, .. q_{h-1}, q_{h+1}, .. q_n} \cdot \mathrm{d}\, q_h \quad , h = 1..n \tag{2.1}$$

where the terms $(\partial W/\partial q_h)\cdot \mathrm{d}q_h$ should equal the work $e_h \cdot \mathrm{d}q_h$, done at the ports. Therefore, the efforts are given by:

$$e_h = \left. \frac{\partial W(q_1, q_2, .. q_n)}{\partial q_h} \right|_{q_1, .. q_{h-1}, q_{h+1}, .. q_n} , h = 1..n \tag{2.2}$$

The general procedure is to firstly derive the unknown state variables q_j, and secondly to calculate the unknown efforts e_i using eq. (2.2). The state variables q_j in equilibrium are found from (local) minimization of the generalized thermodynamic potential $Y(q_1, q_2, .. q_n, e_{s,k+1}, e_{s,k+2}, .. e_{s,n})$ with respect to the unconstrained state variables q_j [3, 4]. Following the definition of Thermodynamics, the generalized potential function Y of system *A* is defined by:

$$\Psi(q_1, q_2, .. q_n, e_{s,k+1}, e_{s,k+2}, .. e_{s,n}) = W(q_1, q_2, .. q_n) - \sum_{j=k+1.}^{n} q_j \cdot e_{s,j} \tag{2.3}$$

Where the q_i's and the $e_{s,j}$'s are independent and fixed. The equilibrium values of the q_j's are thus found by taking the partial derivatives of Y with respect to each q_j equal to zero, yielding (n-k) equations of the type:

$$\frac{\partial W(q_1, q_2, ..q_n)}{\partial q_j} - e_{s,j} = 0 \qquad j = k+1,\ k+2,\ ..n \tag{2.4}$$

From which the q_j's as a function of the q_i's and $e_{s,j}$'s can be solved. The calculated equilibrium is stable if the total variation $dY = d^1Y + d^2Y + ..$ is positive [4], which means that Y is in a minimum. This can be shown as follows. The work dA needed to displace the system away from the equilibrium point is given by:

$$dA\big|_{q_1,q_2,..q_k,e_{k+1},e_{k+2},..e_n} = d^1A + d^2A + ..\Big|_{...} = (dW - \sum_{j=k+1}^{n} e_j \cdot dq_j)\Big|_{...}^{*}$$

$$= d(W - \sum_{j=k+1}^{n} e_j \cdot q_j)\Big|_{...} = d\Psi\big|_{q_1,q_2,..q_k,e_{s,k+1},e_{s,k+2},..e_{s,n}}$$

* The sum $\sum_{j=k+1}^{n} e_j \cdot dq_j$ is exactly the work done at the ports of constant intensity e_j.

Here it is assumed that the displacement is done slow enough to maintain equilibrium, and therefore $e_j = e_{s,j}$. So, if dY is positive then dA is also positive, which means that the system resists the displacement from equilibrium and therefore the equilibrium point is stable. Because in equilibrium the first order variation of Y is equal to zero, the equilibrium is stable if the second order variation is positive for all combinations of infinitesimal variations of the q_j's:

$$d^2Y\big|_{q_1,q_2,..q_k,e_{s,k+1},e_{s,k+2},..e_{s,n}} = \frac{1}{2} \cdot \sum_{j=k+1}^{n} \sum_{m=k+1}^{n} \frac{\partial^2 Y}{\partial q_j \partial q_m} dq_j dq_m > 0 \tag{2.5a}$$

Because $d^2Y = d^2W$, it is possible to derive the condition for stable equilibrium from W:

$$d^2W\big|_{q_1,q_2,..q_k,e_{s,k+1},e_{s,k+2},..e_{s,n}} = \frac{1}{2} \cdot \sum_{j=k+1}^{n} \sum_{m=k+1}^{n} \frac{\partial^2 W}{\partial q_j \partial q_m} dq_j dq_m > 0 \tag{2.5b}$$

If also the second order variation is zero, than the analyses should continue with the third order variation etc. At this point it is important to realize that in equilibrium, $d^2Y = d^2W$, so for condition (2.5) both the energy W and the thermodynamic potential Y can be used. The terms $q_j \cdot e_{s,j}$ in eq. (2.3) represent the drop of the potential energy of the buffers. It can therefore be concluded that the minimization of Y, the generalized potential of system A, is equivalent with minimization of the free energy of system B, the transducer and the connected

buffers. Following the developed theory an interesting conclusion can be drawn for mechanical systems: Following the presented definition, the equilibrium condition for a mechanical system is that the sum of the potential (*in the traditional meaning*) and the kinetic energy should be stationary with respect to all possible infinitesimal changes $\mathrm{d}q_\mathrm{j}$ in position and momentum respectively. The theory presented here allows non-conservative external forces. This is an extension of the common equilibrium condition for conservative mechanical systems (both internal and external forces are conservative), which says that in equilibrium the potential energy is stationary with respect to all possible infinitesimal changes of the position [5].

2.2.3 Legendre Transformations

Using eq. (2.2) in principle it is possible to replace a q_p in the energy function, by the effort e_p of domain *p*. A new energy function W^* (q_1,.., $q_{\mathrm{p-1}}$, e_p, $q_{\mathrm{P+1}}$,.., q_n) results. For infinitesimal changes $\mathrm{d}W^*$ is given by:

$$\mathrm{d}W^* = \sum_{\substack{h=1..n \\ h\neq p}} \left.\frac{\partial W^*(q_1,..q_{h-1},e_h,q_{h+1}..q_n)}{\partial q_h}\right|_{q_1,..q_{h-1},q_{h+1}..q_n,e_p} \cdot \mathrm{d}q_h + \left.\frac{\partial W^*(q_1,..q_{p-1},e_p,q_{p+1}..q_n)}{\partial e_p}\right|_{q_1,..q_{p-1},q_{p+1},..q_n} \cdot \mathrm{d}e_p$$

In general, the efforts e_h are not equal to $\partial W^*/\partial q_\mathrm{h}$ as these derivatives include possible work done at port *p* due to a change of q_h. In order to be able to derive the e_h's directly from an energy function, a Legendre transformation for domain *p* is needed:

$$W'(q_1,..q_{p-1},e_p,q_{p+1},..q_n) = W^* - q_p(q_1,..q_{p-1},e_p,q_{p+1},..q_n)\cdot e_p$$

For infinitesimal changes $\mathrm{d}W'$ is given by:

$$\mathrm{d}W' = \sum_{\substack{h=1..n \\ h\neq p}} \left.\frac{\partial W'(q_1,..q_{h-1},e_h,q_{h+1}..q_n)}{\partial q_h}\right|_{q_1,..q_{h-1},q_{h+1}..q_n,e_p} \cdot \mathrm{d}q_h + \left.\frac{\partial W'(q_1,..q_{p-1},e_p,q_{p+1}..q_n)}{\partial e_p}\right|_{q_1,..q_{p-1},q_{p+1},..q_n} \cdot \mathrm{d}e_p$$

Because,

$$
\begin{aligned}
&\mathrm{d}(W^* - q_p e_p) \\
&= \mathrm{d}(W(q_1,..q_{p-1}, q_p(q_{1,}..q_{p-1}, e_p, q_{p+1},..q_n), q_{p+1},..q_n) - q_p(q_1,..q_{p-1}, e_p, q_{p+1},..q_n)\cdot e_p) \\
&= \sum_{\substack{h=1..n,\\ h\neq p}} \left[\frac{\partial W}{\partial q_h} dq_h + \frac{\partial W}{\partial q_p}\frac{\partial q_p}{\partial q_h}\mathrm{d}q_h \right] + \frac{\partial W}{\partial q_p}\frac{\partial q_p}{\partial e_p}\mathrm{d}e_p - \sum_{\substack{h=1..n,\\ h\neq p}} [e_p \frac{\partial q_p}{\partial q_h}\mathrm{d}q_h] - e_p \frac{\partial q_p}{\partial e_p}\mathrm{d}e_p - q_p \frac{\partial e_p}{\partial e_p}\mathrm{d}e_p \\
&= \sum_{\substack{h=1..n,\\ h\neq p}} [e_h \mathrm{d}q_h] - q_p \mathrm{d}e_p
\end{aligned}
$$

it can be concluded that:

$$e_h = \frac{\partial W'}{\partial q_h} \qquad \text{and} \qquad -q_p = \frac{\partial W'}{\partial e_p} \tag{2.6}$$

In a similar fashion, the Legendre transformation can be made for all of the *n* domains. This is not difficult, but one should be aware that many cross-terms are generated. The result is simply eq. (2.6) with *p* now indicating all the transformed domains. In practice it is convenient to transform all domains $j = k+1..n$ for which the efforts are independent. The result is an *W'* which is a function of the independent parameters q_i and e_j, from which all the dependent parameters can immediately be derived by differentation. The new energy representation *W'* can be used to find equilibrium states. Stability of the equilibrium states still has to be analyzed using eq. (2.5).

2.3 Equilibrium and stability of electrostatic actuators

2.3.1 General approach

The analysis which will be performed in this section focuses on variable capacitance actuators. Assume we have a capacitor with a fixed and a moving electrode. The moving electrode has a mass *m* and is supported by a linear spring. The spring is relaxed for $x = x_0$. The coordinate *x* represents the position of the moving electrode with respect to the fixed electrode. The moving electrode is allowed to move in the *x* direction only. The energy function for this configuration is given by:

$$W(x,q,p) = \frac{1}{2}\cdot k\cdot (x - x_0)^2 + \frac{1}{2}\cdot \frac{q^2}{C(x)} + \frac{p^2}{2m} \tag{2.7}$$

Where *q* is the charge stored in the capacitor, *C*(*x*) is the capacitance, *k* is the stiffness of the support spring and *p* is the momentum of the moving electrode. In the following analysis it is assumed that in the potential mechanical domain the transducer is driven by a constant force *F*. In the electrical domain it is driven by either a constant charge *q* or a constant voltage *U*. In the kinetic mechanical domain it is driven by a constant velocity $v = 0$. The latter condition implies that in equilibrium the momentum $p = m\cdot v$ of the moving electrode is zero. The analysis that follows describes equilibrium states only. The equilibrium condition $p = 0$ can

only be met if changes in F and in q or U are being made slowly, compared to the mechanical response time of the moving electrode. At the end of this section an example of a non-equilibrium path is presented, which shows that the kinetic domain can play an import role. Under the condition $p = 0$, eq. (2.7) reduces to:

$$W(x,q) = \frac{1}{2} \cdot k \cdot (x - x_0)^2 + \frac{1}{2} \cdot \frac{q^2}{C(x)} \tag{2.8}$$

The transducer now has two power ports. Equilibrium states can be derived from eq. (2.8), or from energy functions which are derived by Legendre transformation of eq. (2.8). For electrostatic actuators driven by fixed U and F, it would be convenient to use the double Legendre transformed of eq. (2.8). However, in order to make this transformation $x(F, U)$ should be known explicitly. We have not been able to derive this expression. Therefore, in this case only the Legendre transformation for the electrical domain is made. Unstable behavior can occur if the generated force changes with the actuator deflection x, inducing an effective negative stiffness. This can occur for fixed F and U and for fixed F and q. Condition (2.5b) implies that an equilibrium state of the two port transducer is stable if [6]:

$$b_{11} > 0,\ b_{22} = > 0, \qquad \{ b_{11} = \frac{\partial^2 W(x,q)}{\partial x^2},\ b_{22} = \frac{\partial^2 W(x,q)}{\partial x^2} \tag{2.9a}$$

$$\text{and } \frac{b_{11} b_{22}}{b_{12} b_{21}} < 1 \qquad b_{12} = \frac{\partial^2 W(x,q)}{\partial x \partial q},\ b_{21} = \frac{\partial^2 W(x,q)}{\partial q \partial x} \} \tag{2.9b}$$

For infinitesimal changes of x and q as a function of infinitesimal changes of F and U the following equation applies:

$$\begin{bmatrix} \mathrm{d}x \\ \mathrm{d}q \end{bmatrix} = \begin{bmatrix} a_{11} & a_{12} \\ a_{21} & a_{22} \end{bmatrix} \cdot \begin{bmatrix} \mathrm{d}F \\ \mathrm{d}U \end{bmatrix} = \begin{bmatrix} \dfrac{b_{22}}{b_{11}b_{22} - b_{12}b_{21}} & \dfrac{b_{12}}{b_{11}b_{22} - b_{12}b_{21}} \\ \dfrac{-b_{21}}{b_{11}b_{22} - b_{12}b_{21}} & \dfrac{b_{11}}{b_{11}b_{22} - b_{12}b_{21}} \end{bmatrix} \cdot \begin{bmatrix} \mathrm{d}F \\ \mathrm{d}U \end{bmatrix} \tag{2.10a}$$

And for infinitesimal changes of x and U as a function of infinitesimal changes of F and q:

$$\begin{bmatrix} \mathrm{d}x \\ \mathrm{d}U \end{bmatrix} = \begin{bmatrix} c_{11} & c_{12} \\ c_{21} & c_{22} \end{bmatrix} \cdot \begin{bmatrix} \mathrm{d}F \\ \mathrm{d}q \end{bmatrix} = \begin{bmatrix} \dfrac{1}{b_{11}} & \dfrac{-b_{12}}{b_{11}} \\ \dfrac{b_{21}}{b_{11}} & b_{22} - \dfrac{b_{12}b_{21}}{b_{11}} \end{bmatrix} \cdot \begin{bmatrix} \mathrm{d}F \\ \mathrm{d}q \end{bmatrix} \tag{2.10b}$$

The coefficients $1/a_{11}$ and $1/c_{11}$ represent the effective stiffness k_{eff} for fixed U and q respectively. Therefore, condition (2.9) for stable equilibrium, is equivalent with an effective actuator stiffness $k_{\text{eff}} > 0$ under the condition of fixed U or fixed q. In the following paragraphs, the equilibrium and stability of two commonly used configurations, the comb-

drive and the gap-closing actuator with a linear support spring, are analyzed, for both fixed charge and voltage. The criterion $k_{\text{eff}} > 0$ will be used in the stability analysis.

2.3.2 Equilibrium and stability of the comb-drive actuator.

Figure 2.2 shows the configuration of a comb-drive actuator. The moving electrode is supported by a linear spring. The equilibrium force can be derived from:

$$F_{ext} = \frac{\partial W(q,x)}{\partial x} = \frac{\partial}{\partial x}[\frac{1}{2}k(x-x_0)^2 + \frac{1}{2}\frac{q^2}{C(x)}] \qquad (2.11a)$$

For fixed charge q, and from:

$$F_{ext} = \frac{\partial W'(U,x)}{\partial x} = \frac{\partial}{\partial x}[\frac{1}{2}k(x-x_0)^2 - \frac{1}{2}C(x)U^2] \qquad (2.11b)$$

For fixed voltage U [6]. In both equations C(x) is the position dependent capacity of the air-gap across which the voltage U drops, and x_0 is the position of the moving electrode with the spring relaxed.

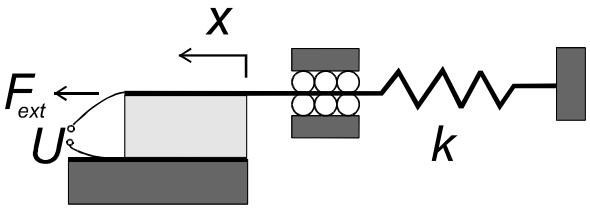

Figure 2.2: Comb-drive actuator. The light gray area represents the actuator volume where the uniform electric field is present. The moving plate is elastically suspended by a spring with stiffness *k*.

For the comb-drive (fig. 2.2) driven with control charge, the charge density on the fingers decreases due to a disturbance of the equilibrium by Δx. A force ΔF_{ext} larger than $k \times \Delta x$ is needed for the disturbance. This corresponds with positive electrical stiffness, which is added to the mechanical stiffness of the suspension. Therefore there will be no instability. The comb-drive actuator driven with controlled voltage has a contraction force which is independent of the overlap of the fingers. The electrical stiffness is zero and the actuator is stabilized by the mechanical stiffness of the suspension.

2.3.3 Equilibrium and stability of the gap-closing actuator

Fig. 2.4 shows the configuration of the gap-closing actuator. The moving electrode is suspended with a linear spring. The equilibrium force of this configuration is given by eq. (2.11a,b) for charge and voltage steering respectively. For the gap-closing actuator driven with controlled charge, the contraction force is independent of the distance *x*. The electrical stiffness is zero and the actuator is stabilized by the mechanical stiffness of the suspension.

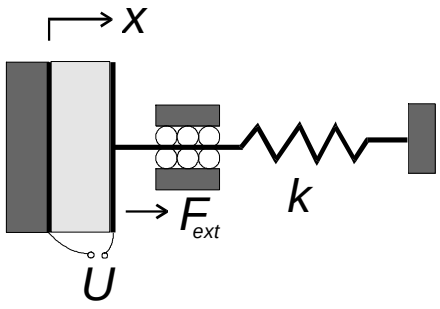

Figure 2.3: Gap-closing actuator. The light gray area represents the actuator volume where the uniform electric field is present. The moving plate is elastically suspended by a spring with stiffness *k*.

For the gap-closing actuator driven by a controlled voltage, the energy density increases with decreasing distance *x*. A force ΔF_{ext} smaller than $k \times \Delta x$ is needed for a disturbance of the equilibrium by Δx. This means that a negative electrical stiffness is added to the mechanical stiffness *k*. The transformed energy for the configuration of fig. 2.4 is given by:

$$W'(x,U) = W(x, q(x,U)) - q(x,U) \cdot U = \frac{1}{2} k (x - x_0)^2 - \frac{1}{2} \frac{eA}{x} U^2 \qquad (2.12)$$

Where x_0 is the distance between the plates with the spring relaxed, e is the permittivity of air, and A is the facing area of the plates. Pull-in occurs at a voltage where $k_{eff} = 0$ changing from positive to negative. Fig. 2.4 shows the energy as a function of *x*. The onset of instability for $F_{ext} = 0$ is indicated.

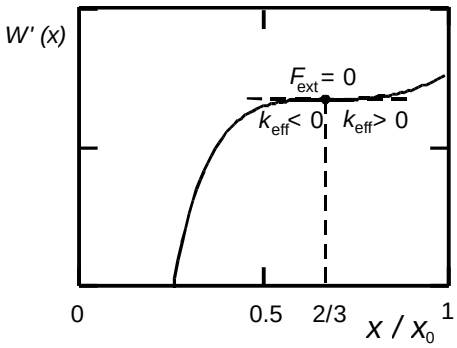

Figure 2.4: Transformed energy $W'(x,U)$ as a function of x for $U = U_{pi}$. The equilibrium $F_{ext} = 0$ at the onset of instability is indicated. For $x < 2/3\, x_0$ the stiffness $k_{eff} = \partial W'^2/\partial x^2 < 0$. This is the unstable region.

The pull-in voltage and gap can be calculated from $F_{ext} = \partial W'/\partial x = 0$ and $k_{eff} = \partial W'^2/\partial x^2 = 0$ yielding:

$$x_{pi} = 2/3\, x_0 \qquad (2.13)$$

$$U_{pi}^2 = \frac{8}{27} \frac{k \cdot x_0^3}{e \cdot A}$$

A similar calculation has been made for a gap-closing actuator loaded by a constant force F. The results is (App. C):

$$x_{\mathrm{pi}} = 2/3\ (x_0 + F / k)$$

$$U_{pi}^2 = \frac{8}{27}\frac{k\cdot(x_0+\frac{F}{k})^3}{e\cdot A}$$

Both the pull-in position and the pull-in voltage increase with increasing F. In Appendix C also the influence of a higher order spring on stability is analyzed. The result is that the stable region of operation increases with increasing order of the spring. For a spring with a constitutive relation $F_s = k\cdot(x - x_0)^n$, the pull-in gap is given by $x_{\mathrm{pi}} = 2x_0 / (n+2)$, where x_0 is the initial spacing between the plates (with the spring relaxed).

Non-equilibrium analysis (p > 0) of a gap-closing actuator.
Consider the configuration of fig. 2.3, now with a mass m of the moving electrode If in an equilibrium state the voltage across the capacitor is suddenly increased, a non-equilibrium state is caused. The electrostatic force will be larger than restoring elastic force, and the force difference will lead to acceleration of the movable electrode. As long as $p > 0$ there exists an effort difference between the transducer and the surroundings in the kinetic domain, so the transducer moves through non-equilibrium states. The kinetic energy gained can be a significant amount compared to the electrical energy supplied by the voltage source. To show this we have analyzed the response of the movable electrodes on a voltage step from 0 to U Volt, where $U = U_{\mathrm{pi}}$, the quasi-static pull-in voltage. The force F_a accelerating the mass can be found by differentation of eq. (2.12):

$$F_{ext} = k(x - x_0) + \frac{1}{2}\frac{e\cdot A}{x^2}U^2 \qquad (2.14)$$

Where F_{ext} is the force necessary to maintain equilibrium. In the non-equilibrium case $F_{\mathrm{ext}} = 0$, the moving electrode is accelerated in the $-x$ direction due to the force $F_a = -F_{\mathrm{ext}}$. The force can be integrated with respect to x to find the kinetic energy gained between x_0 and x, neglecting the air resistance:

$$\Delta W_{\mathrm{kin}}(x) = \int_{x_0}^{x} F_a \cdot \mathrm{d}x = -\frac{1}{2}k\cdot(x-x_0)^2 + \frac{1}{2}\frac{e\cdot A}{x}U^2 - \frac{1}{2}\frac{e\cdot A}{x_0}U^2 = -\Delta W_{\mathrm{spring}} + \Delta W_{\mathrm{elec}} \qquad (2.15)$$

The total change $\Delta W_{\mathrm{kin}}+\Delta W_{\mathrm{spring}}$ of the mechanical energy equals the change of electrical energy stored in the capacitor. This can also be concluded from an energy balance: At constant voltage U the source delivers $U\cdot\Delta q=\Delta C\cdot U^2$, and the electrical energy stored in the capacitor increases with $\frac{1}{2}\Delta C\cdot U^2$. The other half of the supplied energy is stored in the kinetic and the

potential mechanical domains. In order to give an indication of the importance of the kinetic energy term, we calculated $\Delta W_{kin}/\ \Delta W_{elec}$ for $U=U_{pi}$ at $x = x_{pi}= 2/3\ x_0$:

$$\frac{\Delta W_{kin}}{\Delta W_{elec}} = \left(\frac{1}{16}\cdot\frac{e\cdot A}{x_0}\cdot U^2\right) / \left(\frac{1}{4}\cdot\frac{e\cdot A}{x_0}\cdot U^2\right) = \frac{1}{4} \quad , \quad \left(U^2 = \frac{8}{27}\cdot\frac{k\cdot x_0^3}{e\cdot A},\ x = 2/3\ x_0\right)$$

This shows that the moving electrode still has significant kinetic energy when it reaches the critical position 2/3 x_0, which implies that the dynamic pull-in voltage will be significant lower than the quasi-static pull-in voltage.

2.4 Electrostatic force as a function of energy density and geometry

2.4.1 Expression for the energy in the actuator

The generated force of electrostatic actuators can be expressed as a function of the geometry and the energy density in the actuator. In this section this is explained for the two basic configurations: the gap-closing and the comb-drive actuator (fig. 2.5). The resulting expressions are useful tools for conceptual design of electrostatic actuators.

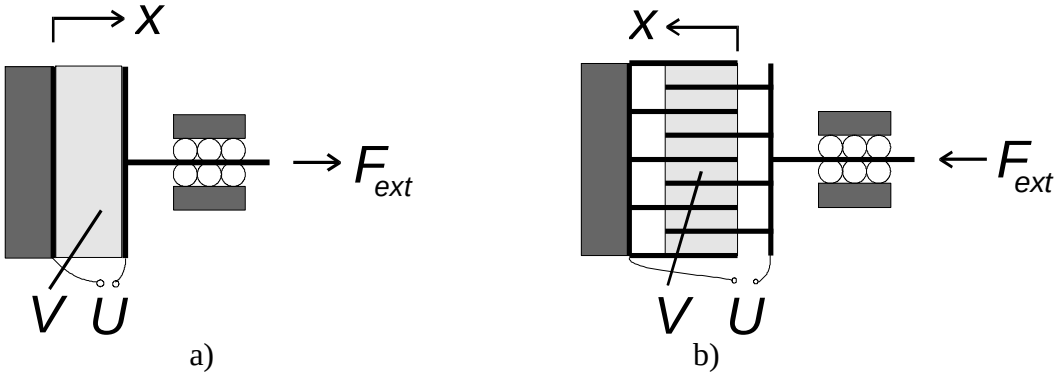

figure 2.5: a) Gap-closing actuator, b) Comb-drive actuator. The volume containing the electric field is drawn in light gray.

Define $V = A_a \times x$ the volume that contains the field energy (fig. 2.5). The active area A_a is defined by $A_a = dV/dx$, where x is the coordinate in the direction of movement. The field energy contained is given by:

$$W = A_a \cdot w \cdot x \qquad (2.16)$$

Where $w = 1/2 \cdot e \times E^2 = 1/2 \times D^2/e$ is the energy density for a homogeneous, isotropic medium. In this expression E is the electric field intensity, D the dielectric displacement.

2.4.2 Fixed Charge

The amount of charge on the plates is constant, therefore the produced force is given by:

$$F_{\text{ext}} = \frac{\partial W(x,q)}{\partial x} = A_{\text{a}} \cdot w(x,q) + A_{\text{a}} \cdot x \cdot \frac{\partial w(x,q)}{\partial x} \tag{2.17}$$

For the comb-drive the energy density is $w(x, q) = m / x^2$ (m independent of x) and therefore:

$$x \cdot \frac{\partial w(x,q)}{\partial x} = -2w(x,q)$$

So for the force we find:

$$F_{\text{ext}} = -A_{\text{a}} \cdot w(x,q) \tag{2.18}$$

Similar, for the gap-closing actuator w is independent of x which implies $\partial w / \partial x = 0$, therefore:

$$F_{\text{ext}} = A_{\text{a}} \cdot w(q) \tag{2.19}$$

2.4.3 Fixed Voltage

The electrical port is open and therefore $F_{\text{ext}} \neq \partial W(x, q(U, x)) / \partial x$. Using the Legendre transformation $W'(x,U) = W(x, q(U, x)) - U \times q(x, U)$ this problem is solved:

$$\begin{aligned} \frac{\partial W'(x,U)}{\partial x} &= \frac{\partial W}{\partial x} + \frac{\partial W}{\partial q}\frac{\partial q}{\partial x} - \frac{\partial}{\partial x}[U \cdot q(x,U)] \\ &= F_{\text{ext}}(x,U) + U^2 \frac{\partial C(x)}{\partial x} - U^2 \frac{\partial C(x)}{\partial x} = F_{\text{ext}}(x,U) \end{aligned} \tag{2.20}$$

Because , $W'(x, U) = W(x, q(U, x)) - U \times q(x, U) = ½\ U \times q(x, U) - U \times q(x, U) = -W(x, U)$ the following expression can be derived:

$$F_{\text{ext}} = \frac{\partial W'(x,U)}{\partial x} = -\frac{\partial W(x,U)}{\partial x} = -A_{\text{a}} \cdot w(x,U) - A_{\text{a}} \cdot x \cdot \frac{\partial w(x,U)}{\partial x} \tag{2.21}$$

For the comb-drive the energy density is independent of x, therefore $\partial w / \partial x = 0$ and:

$$F_{\text{ext}} = -A_{\text{a}} \cdot w(U) \tag{2.22}$$

The gap-closing actuator $w = m / x^2$ which implies:

$$x \cdot \frac{\partial w(x,U)}{\partial x} = -2w(x,U)$$

So for the force we find using eq (2.21):

$$F_{ext} = +A_a \cdot w(x,U) \tag{2.23}$$

2.4.4 Results

The results are summarized in table 2.1. In conclusion we can see that in all four cases the magnitude of the force is given by the active area dV / dx times the energy density. Also the direction of the force follows from the formalism.

	Charge control	Voltage control
Comb-drive	$F_{ext} = -A_a \times w(x,q)$	$F_{ext} = -A_a \times w(U)$
Gap-closing	$F_{ext} = +A_a \times w(q)$	$F_{ext} = +A_a \times w(x,U)$

Table 2.1: generated force under conditions of charge control and voltage control for the two configurations

The active area of the gap-closing actuator is straightforward the facing area of the electrodes, for the comb-drive it is indicated in figure 2.6 for one pair of fingers.

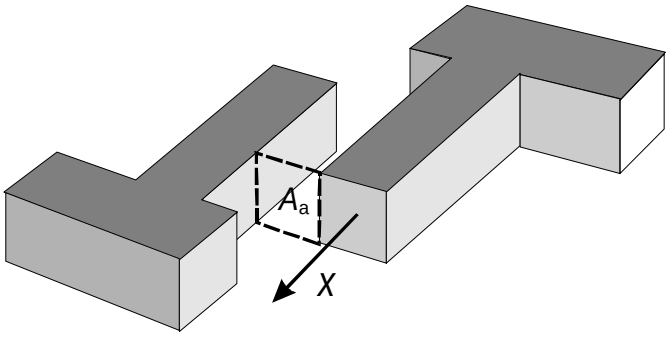

Figure 2.6: Active area for the comb-drive

2.5 Energy density limited by breakdown

In this section we analyze the maximum attainable electrical energy in air. The energy density is limited by electrical break-down. Break-down in caused by electrons freely moving in the gap. If the electric field is large enough, the electrons gain enough kinetic energy to ionize molecules they collide with in the gap. It was first recognized by Paschen [8] that the breakdown voltage is a function of the product $p \cdot d$ where p is the gas pressure, and d is the distance between the electrodes. His explanation of this principle is that the product $p \cdot d$ is a measure for the average number of molecules on the shortest path between the electrodes. The break-down voltage is a function of this number of molecules, because the electrodes traveling towards the anode should gain enough kinetic energy between successive collisions to be able to ionize the molecules they collide with. This ionization is needed to cause the break-down avalanche effect. According to Meek et. al. [9] and LLewellyn-Jones [10] the positive ions and the photons created in the electron-gas molecule collision cause secondary electron

emission at the cathode, which leads to increased ionization in the gap. Fig. 2.7 shows the shape of the Paschen curve. For large $p \cdot d$ the curve tends to the dashed line, indicating a constant electric field with changing $p \cdot d$. The explanation is that the voltage change between two collisions should be constant. For constant d the mean free path for the electrons in the gas decreases linearly with increasing p and therefore the electric field should increase linearly with increasing p. For constant p the mean free path is constant, and therefore the electric field should be constant in order to maintain the voltage change between successive collisions. For small values of $p \cdot d$ the number of molecules in the gap is low. In order to induce the avalanche effect, the average number of electrons produced in each collision should be high. Therefore, the voltage change between successive collisions should be high, which explains why the electric field should be larger than indicated by the slope of the dashed curve.

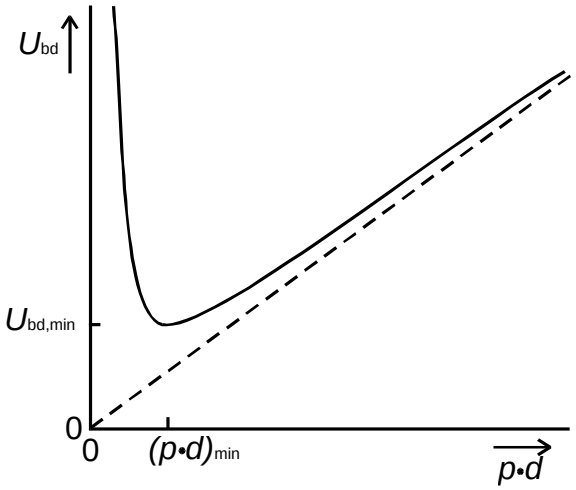

Figure 2.7: Paschen curve, showing the break-down voltage U_{bd} as a function of $p \cdot d$.

Dakin et al. [11] have plotted the Paschen curve of air, using breakdown data from many researchers. For air the minimum break-down voltage $U_{bd,\,min}$ is about 3.3 x 10^2 V for $p \cdot d_{min}$ = 7 Bar·µm [10]. So, for atmospheric pressure (1 Bar) the minimum is at $d \approx 7$ µm. This is ± 20 times the mean free path of electrons in air at this pressure: The mean free path for molecules-molecules in air at 1 Bar is appr. 66 nm [12]. The mean free path of electrons in air is about 0.4 µm, $4\sqrt{2}$ times larger than for molecule-molecule collisions. For large air-gaps (~10 cm) in atmospheric air, the breakdown electrical field equals 3 x 10^6 V/m. For a decreasing gap-size at constant pressure the break-down field increases gradually. For atmospheric pressure and gaps smaller than 10 µm, the break-down field increases rapidly for decreasing gap size and a value of 2 x 10^8 V/m is reached at 2.4 µm separation This electric field is still smaller than the field intensity 2 x 10^9 V/m, the field intensity at which field emission starts [10]. If the cathode is rough, field emission can start at significant lower global field intensity due to local field enhancement [10]. Most breakdown data in [11] has been retrieved at low pressures instead of small gaps. Breakdown measurements for µm-range gaps are scarce. Bollee [13] mentions a breakdown field of 1.7 x 10^8 V/m in a 2 µm gap, based on [14], [15]. Mehregany et al. [16] report an applied voltage of 26 V across a 1.5 µm gap in a micromotor,

corresponding with an electric field of 1.7 x 10^7 V/m. Dhariwal et al. [17] have measured the breakdown voltage for gaps down to 1 μm for copper, aluminium, iron and brass electrodes. They found a large deviation from the Paschen curve for gaps below 3 μm. For all four electrode materials the maximum field intensity was 1 x 10^8 V/m at 3 μm gap size, and drops rapidly with further decreasing gap size. The deviation may be caused by field enhancement due to microprotrusions on the electrode surface. Using the breakdown field as an upper limited, the electrostatic actuation can be compared with other actuation principles with respect to the energy density. For the comparison an electric field intensity of 2 x 10^8 V/m is taken for the electrostatic actuator. This corresponds with the breakdown electric field in a 2 μm gap in atmospheric air. The energy density of the electric field equals 2 x 10^5 J/m^3. In conventional magnetic actuators the maximum flux density equals 1 T , caused by the saturation of the magnetic core material [18]. This corresponds with an energy density $B^2 / 2\mu_0$ = 4.0 x 10^5 J/m^3, a factor two higher than the electric energy density. The maximum energy density of piezoelectric actuators is more arbitrary. In commercially available PZT an electric field intensity of 3 MV/m is allowed in the direction of poling [19, 20]. This corresponds with an energy density $\frac{1}{2} \cdot e \cdot E^2$ = 1.2 x 10^5 J/m^3 (ε_r = 3000). The forward field intensity of 3 MV/m is probably given with a safe margin to electric breakdown. In experimental sol-gel PZT thin films [21] breakdown occurs at E = 55 ± 5 MV/m, corresponding with an energy density of 1.2 x 10^7 J/m^3 (ε_r = 900). It can be concluded that the maximum energy density in electrostatic actuators is in the same order as those in magnetic and commercially available piezoelectric actuators. Experiments indicate that possibly the energy density in PZT actuators can be made more than an order higher.

2.6 Calculation of practical attainable force and stroke

In section 1.2 we wrote down the specifications for actuators to be designed within the project. In this section we will estimate if the desired force and stroke can be realized with a sufficient low driving voltage: F > 0.1 mN, Δx > 10 μm and V < 30 V. Using the expressions from table 2.1 the maximum attainable force can be estimated. This is done for our surface micromachining process, in which the resolution (minimum width of structures and minimum gap size) is 2 μm, and the maximum height of the polysilicon structures is 5 μm. Furthermore the actuator size is limited to 1 x 1 mm^2. The actuator force is calculated for an imaginary array of minimized unit cells, thereby neglecting the space consumed by suspension and connection beams. Figure 2.8 shows a minimized unit cell of both the comb-drive and the gap-size actuator. The gap-closing actuator has a initial forward gap of 4 μm, which allows a stroke Δx of 2 μm. The comb-drive actuator has a initial gap of 6 μm between the stator electrode and the front side of the fingers. After a stroke Δx of 2 μm the front side gap is reduced to 4 μm, and the force produced in the forward gap is still small compared to the force produced in the gap between the fingers. Both configurations have a backward gap of 8 μm in order to have a low backward electrostatic force.

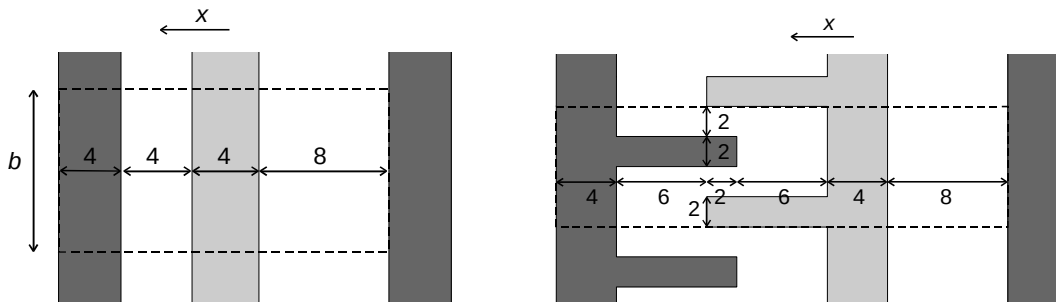

a) b)

Figure 2.8:a) Top view of a minimized unit cell of the gap-closing actuator, and b) Top view of a minimized unit cell of the comb-drive actuator. In both figures the moving electrode is drawn in light gray and the stator electrode in dark gray. The direction of motion is *x*.

Assuming the dimensions shown in figure 2.8a, the area of a unit cell of the gap-closing actuator is *b* x 20 μm. The corresponding active area is *b* x 5 μm. On a surface area of 1 mm^2 an active area of (1 mm^2 / (*b* x 20 μm)) x *b* x 5 μm = 0.25 mm^2 can be realized, where the area needed for the beams connecting the electrodes is neglected. Assuming the dimensions shown in figure 2.8b, the area of a unit cell of the comb-drive actuator is 8 x 30 μm^2. The corresponding active area is 4 x 5 μm^2. On a surface area of 1 mm^2 an active area of (1 mm^2 / (8 x 30 μm^2)) x 4 μm x 5 μm = 0.083 mm^2 can be realized, where again the area needed for the beams connecting the electrodes is neglected. The active area that can be obtained is three times larger for the gap-closing compared to the comb-drive actuator. However, the initial gap of the gap-closing actuator is twice the distance between the fingers. Therefore, the maximum energy density of the comb-drive actuator compared to the gap-closing actuator in the initial position is four times larger. The conclusion is that the maximum attainable force of both configurations is almost equal. Notice that although these are optimized designs, the active volume $\Delta x \cdot A_a$ of the comb-drive array is only 3%. With 30 V driving voltage across a 2 μm gap, an energy density *w* of 1.0 x 10^3 J/m^3 can be created. With this energy density the maximum attainable force, equals *w* x 0.083 mm^2 = 83 μN (calculated for the comb-drive). The calculated force is close to the desired minimum value. However, the stroke is 2 μm, which is too small. It is important to notice that it is the product of force and stroke which has to be increased. If the product is high enough, the desired stroke and force can be obtained by employing an appropriate lever. We distinguish three methods to increase the product of produced force and stroke: (1) Increasing the actuator volume by making higher structures, (2) employing a walking motion [22, 23], (3) employing field alternation (traveling field). It this project we choose option (2). Design and realization of electrostatic actuators employing walking motion will be presented in chapter 5 and 6.

2.7 Inertial Matching

The idea of the walking motion introduces extra freedom in actuator design, because initially one does not have to care about the total stroke which is needed. Therefore, one can now try to optimize the mechanical output by using a lever between the actuator and the load. The optimization criterion is a maximum acceleration of the load, which is a mass m_l. Fig. 2.9 shows the model. A mass m_l is driven through a lever, which at the other side is connected to the moving part of the actuator. This moving part is represented by its mass m_a. We define the mass ratio $r = m_l / m_a$

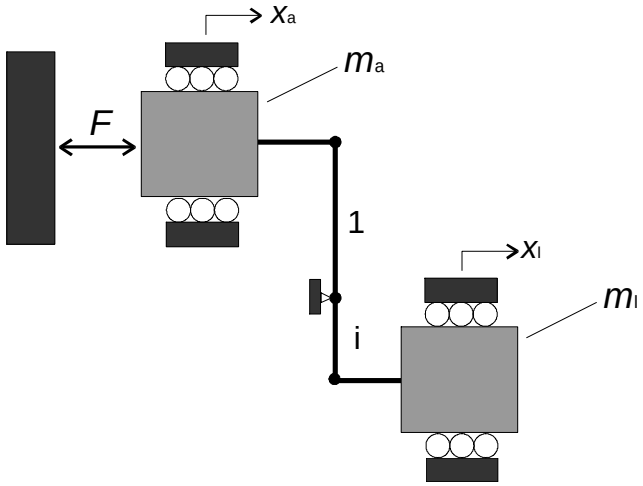

Figure 2.9: Actuator driving a mass m_l through a lever, with a transmission ratio $i = dx_l / dx_a$. The force produced in the actuator equals F. The moving part of the actuator is represented by its mass m_a.

The optimal value, with a_l maximal, is $i = \sqrt{1/r}$. This yields an effective mass $m_{eff} = m_a + i^2 m_l = 2m_a$ at the actuator side of the lever, and an maximum acceleration of the load equal to:

$$a_l = \frac{F}{2\sqrt{m_a m_l}}, \quad (i = \sqrt{1/r}) \tag{2.24}$$

This equation can be used to estimate the maximum acceleration of a given mass, produced by an actuator with a known mass, which drives the load through an optimized lever. If this principle is employed in a walking actuator, in theory very large accelerations can be obtained. Take for example the comb-drive array with unit cells as in fig. 2.8b. The moving mass of a 1mm^2 x 5 μm array is estimated to be 5 μg. Using a force F of 0.1 mN and a load of 1 mg, the optimized output acceleration equals 7×10^2 m/s^2. This calculation is based on an energy density of 1×10^3 J / m^3. The maximum possible energy density in air can be 100 times larger, which implies that accelerations as high as 7×10^4 m / s^2 can be generated with electrostatic actuators. In practical walking motors, the acceleration will decrease with increasing velocity, because the frequency at which the 'legs' can be moved is limited due to

their inertia. A second effect limiting the velocity is the air resistance. These effects make the acceleration velocity dependent. Therefore, the calculated large acceleration can only be reached in the initial phase of a displacement.

2.8 Conclusions

Equilibrium and stability of conservative electrostatic transducers can be studied using the expression for the energy stored in the buffers. States of stable equilibrium are found by minimization of a generalized potential with respect to the unconstraint state variables. Electrostatic actuators can become unstable if the effective actuator stiffness becomes negative. This can occur for both fixed charge and fixed voltage. The onset of instability of the gap-closing actuator loaded by a constant force F and driven with a fixed voltage has been analyzed. For a linear spring the pull-in position is 2/3 ($x_0 + F / k$), with x_0 the initial position of the moving plate suspended by a spring with a stiffness k. The stable region of operation can be increased by suspending the moving electrode with a higher order spring. For $F = 0$ the pull-in position becomes $x_{pi} = 2x_0 / (n+2)$ where n is the order of the spring. An actuator model has been made that expresses the electrostatic force as the product of the energy density and the active area, which is the derivative of the volume containing the electric field, with respect to the direction of movement. From literature a maximum allowable electric field 2×10^8 V/m in a 2 μm gap in air has been found, limited by breakdown. This corresponds with an energy density of 2×10^5 J/m^3. The energy density is in the same order as can be obtained in magnetic actuators, and which is allowed in commercial PZT piezoelectric actuators. The maximum attainable electrostatic force using surface micromachining design rules, is 0.1 mN with a driving voltage of 30V for both the gap-closing and the comb-drive actuator. This force has been calculated for a 1 x 1 mm^2 surface area, and 5 μm heigh actuator plates. It is large enough to meet our demands, however the stroke of 2 μm is too small. From the three presented options to increase the product of force and stroke, the walking motion has been selected to be employed in this project. Using a walking motion a virtually unlimited stroke can be made. It is the possible to optimize the actuator for a given mass to be moved, using a lever between the actuator and the load. Maximum output acceleration is reached if the effective mass of the moving electrode of the actuator equals the mass of the load. For an optimized comb-drive configuration, we estimate that a 1 mg mass can be given an acceleration of 7×10^4 m / s^2 when the actuator is driven at an energy density of 1×10^5 J / m^3, which is close to the maximum in air.

2.9Acknowledgment

The author wishes to thank Henri Jansen for his help with the development of the theory for equilibrium and stability of transducers.

2.10 Literature

1. Thomson Sir W., Tait P.G.,"Treatise on Narural Philosophy", Cambridge University Press, 1879.
2. Breedveld P.C.,"Physical Systems Theory in Terms of Bondgraphs", Ph.D. Thesis University of Twente, 1984.
3. Callen H.B.,"Thermodynamics and introduction to thermostatistics", 2nd edition, John Wiley & Sons, New York, 1985.
4. Bailyn M.," A survey of thermodynamics", AIP Press, New York, 1994.
5. Goldstein H.," Classical Mechanics", Addison-Wesley Publishing Company, Reading, 1985.
6. Elwenspoek M., Fluitman J., Krijnen G. "Transductietechniek" Lecture notes University of Twente.
7. Trimmer W., Gabriel K.," Design considerations for a practical electrostatic micro-motor", Sensors and Actuators, Vol. 11, 1987, pp. 189-206.
8. Paschen F.," Uber die zum Funkenubergang in Luft, Wasserstoff und Kohlensaure bei verscheidenden Drucken erforderliche Potentialdifferenz, Ann. Phys., Vol. 37, 1889, pp. 69-96.
9. Meek J.M., Craggs J.D., "Electrical breakdown of gases", Wiley & Sons, New York, 1978.
10. Llewellyn-Jones F., "Ionization and breakdown of gases", Science paperbacks and Methuen & Co LTD, 1966.
11. Dakin T.W., Luxa G., Oppermann G., Vigreux J., Wind G., Winkelkemper H., "Breakdown of gases in uniform fields. Paschen curves for nitrogen, air and sulfur hexafluoride", Electra, Vol. 32, 1974, pp. 61-82.
12. Atkins P.W.,"Physical Chemistry", 3rd ed., Oxford University Press, Oxford, 1987.
13. Bollee B., "Electrostatic motors", Philips technical review, Vol. 30, 1969, pp. 178-194.
14. Schumann W.O., "Elektrische Durchbruchfeldstärke von Gasen, Springer Verlag, Berlin, 1923.
15. Biermanns," Hochspannung und Hochleistung", Hanser, Munich, 1949.
16. Mehegany M., Tai, Y-C.," Surface micromachined mechanisms and micromotors", J. Micromech. Microeng., Vol. 1, 1991, pp. 73-85.
17. Dhariwal R.S., Milne N.G., Yang, S.J., Beerschwinger U., Rump G.F.A., King P.C., "Breakdown electric field strength between small electrode spacings in air", Micro Systems Technologies Conf., 1994, pp. 663-672.
18. Busch-Vishniac I.J.,"The case for magnetically driven microactuators", Sensors and Actuators A, vol. 33, 1992, pp. 207-220.
19. Randeraat J. van (ed.), "Piezoelectric ceramics", Philips data handbook 1968.
20. Philips electronics N.V.," CMA31 piezo-electric ceramic multilayer actuator", datasheet PA12, 1992.
21. Gardeniers J.G.E., Verholen A.G.B.J., Tas N.R., Elwenspoek M.," Direct measurement of piezoelectric properties of sol-gel PZT films", J. Korean Phys. Soc., Vol. 32, 1998, pp. s1573-s1577.
22. Akiyama T., Shono K.," Controlled stepwise motion in polysilicon microstructures", J. Microelectromechanical Syst., vol. 2-3, 1993, pp. 106-110.
23. Koster M.P.," A Walking Piezo Motor", Proc. Actuator 94 Conf., Bremen, June 1994, pp. 144-148.

3

Stiction in surface micromachining

Due to the flatness of the surfaces in surface micromachining, large adhesion forces between fabricated structures and the substrate are encountered. Four major adhesion mechanisms have been analysed: Capillary forces, Hydrogen-bridging, electrostatic forces and van der Waals forces. Once contact is made adhesion forces can be stronger than the restoring elastic forces and even short, thick beams will continue to stick to the substrate. Contact, resulting from drying liquid after release etching, has been successfully reduced. In order to make a fail-safe device stiction during its operational life-time should be anticipated. Electrostatic forces can cause pull-down of short, stiff structures already at moderate voltages. Also in particular applications, contact between moving parts is desired. In order to avoid in-use stiction, adhesion forces should therefore be minimised. This is possible by coating the device with low adhesive materials, by using bumps and side-wall spacers and by increasing the surface roughness at the interface. Capillary condensation should also be taken into account as this can lead to large increases in the contact area of roughened surfaces. The stiction reduction by means of robust side-wall spacers has been measured for the first time, yielding a stiction reduction which is slightly larger than the reduction of the geometrical contact area.

3.1 Introduction

Stiction is the permanent adherence of micromachined parts to the underlying substrate. It is a notorious cause of malfunctioning in microdevices. Surface micromachined structures which have been fabricated using the wet sacrificial layer etching technique can be pulled down to the substrate by capillary forces during drying [1, 2]. In recent years, a lot of attention has been paid to avoiding contact during drying. Section 3.4 gives an overview of the methods which have been developed. Analysis of the adhesion mechanisms [3, 4] shows that stiction may occur whenever flexible and smooth structures are brought in contact with the substrate (section 3.2 and 3.3). Therefore, for structures where there will or can be contact during operation, in-use stiction should be anticipated. It is clear that this is the case for the walking motors which we study. In case there is in-use contact, it is important to minimize adhesion forces between parts which move with respect to each other, either by reducing the contact area or by changing the surface properties. This is analysed in section 3.6. In this section, our experimental results of stiction reduction by using a new type of self-aligned side-wall spacers are presented.

This chapter is based on:
N.Tas, T.Sonnenberg, H. Jansen, R.Legtenberg, M. Elwenspoek, *Stiction in Surface Micromaching*, J. Micromech. Microeng., Vol.6, 1996, pp. 385-397
N.Tas, M.Elwenspoek, R.Legtenberg, *Side-wall spacers for stiction reduction in surface micromachined mechanisms*, Proc. Micromech. Workshop (MME'96), Barcelona, Spain, 21-22 Oct. 1996, pp. 92-95.

3.2 Origins of stiction

Adhesion of contacting surfaces has been studied extensively in tribology. Stiction phenomena are observed in harddisk systems where the roughness of the contacting surfaces approaches nanometer scale. Adhesion mechanisms have also been studied for wafer bonding purposes where stiction of contacted surfaces is desirable. Surface roughness plays an important role in adhesion. Surface micromachined structures are often very flat. Legtenberg [7] measured a RMS roughness between 1-3 nm at the bottom of released structures, depending on polysilicon and sacrificial (PECVD) silicon oxide thicknesses. The roughness of silicon wafer surfaces has been measured for bonding purposes. RMS roughness is typically below 1 nm [8, 9]. The Real Contact Area (RCA) can be a large fraction of the apparent contact area between these structures. In the first analysis of adhesion mechanisms, we assume that the contacting surfaces are perfectly flat. The influence of surface roughness will be analysed in section 3.6.3. Four adhesion mechanisms, which play an important role in stiction of surface micromachined structures, are discussed: Capillary forces, Hydrogen-bridging, electrostatic forces and van der Waals forces [7].

3.2.1 Capillary forces

A thin liquid layer between two solid plates can work as an adhesive. If the contact angle θ_C between liquid and solid is < 90° (fig. 3.1), the pressure inside the liquid bridge will be lower than outside and a net attractive force between the plates exists. The pressure difference Δp_{LA} at the liquid-air interface is given by the Laplace equation [10]:

$$\Delta p_{LA} = \frac{\gamma_{LA}}{r} \qquad (3.1)$$

Where γ_{LA} is the surface tension of the liquid-air interface, and r is the radius of curvature of the meniscus (negative if concave). In fig. 3.1, the liquid is trapped between the plates and the liquid contacts the solid at a fixed contact angle. Simply from geometry it follows that $r = -g/2\cos\theta_C$. In equilibrium, an external force F separating the plates must be applied to counterbalance the capillary pressure forces:

$$F = -\Delta p_{LA} \cdot A = \frac{2 \cdot A \cdot \gamma_{LA} \cdot \cos\theta_C}{g} \qquad (3.2)$$

Where A is the wetted area, and g is the thickness of the liquid layer. Note that a positive force F corresponds with a negative Laplace pressure.

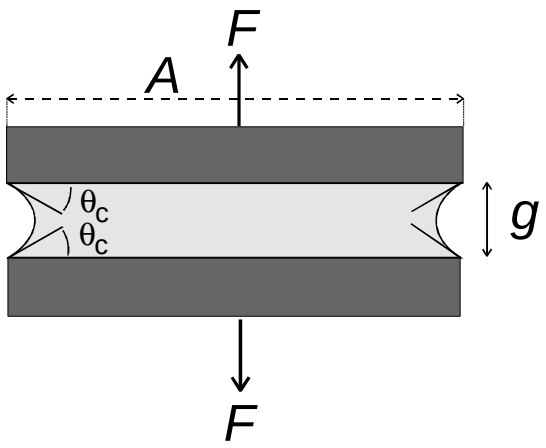

Figure 3.1: A thin layer of liquid working as an adhesive between two plates. q_C is the contact angle between liquid and solid in air, g is the liquid layer thickness, and A is the wetted area. A force F is applied to make balance with the Laplace pressure.

For stiction calculations it is convenient to calculate the surface energy stored at the interface that is bridged by a drop of liquid [2]. Consider a drop of liquid placed on a solid, surrounded by air. In equilibrium, the contact angle between liquid and solid (fig. 3.2) is determined by the balance between the surface tensions of the three interfaces. This balance is expressed by Young's equation [10] :

$$g_{SA} = g_{SL} + g_{LA}\cos q_C \,,\ 0<q_C<\pi \qquad (3.3)$$

Where g_{SA} is the surface tension of the solid-air interface, and g_{SL} is the surface tension of the solid-liquid interface. Young's equation is also valid for configurations other than shown in fig. 3.2. The contact angle is the same on a curved or irregular shaped surface, inside a capillary etc..

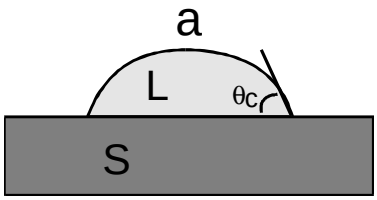

Figure 3.2: Liquid drop (L) on a solid (S) , in air (a). q_C is the contact angle between liquid and solid in air.

If the solid-air surface tension is smaller than the sum of the liquid-air and solid-liquid surface tensions, then the contact angle is larger than 0° and the liquid will be non-spreading. If the solid-air surface tension is larger than the sum of the liquid-air and solid liquid surface tensions, then it will be energetically favourable for the liquid to spread. The contact angle will equal 0°. A drop bridging two surfaces will form thin liquid films outside the bridged area (fig. 3.3).

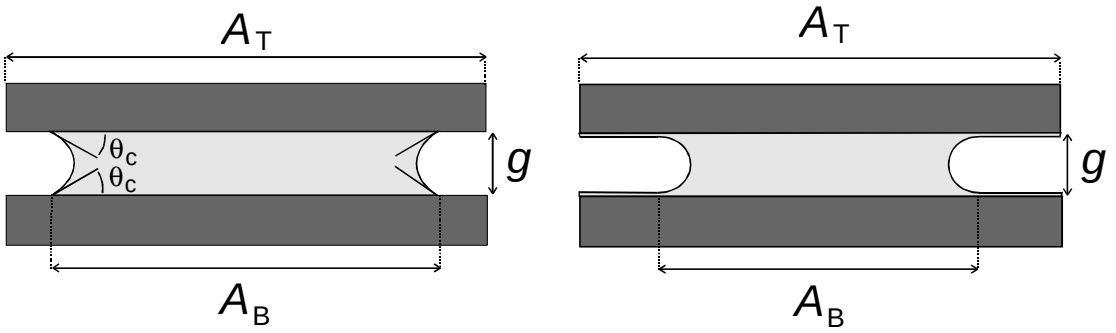

a) b)

Figure 3.3: Liquid bridging two solids. a) The liquid is non-spreading. The solid is only covered in the bridged area A_B. A_T is the total facing area. b) The liquid is spreading. Outside the bridged area A_B, a thin liquid film covers the solid.

The total surface energy of the area between the plates can be calculated by adding the surface tensions of the solid-air, solid-liquid and liquid-air interfaces [2]. It is assumed that the liquid is confined to a bridged area A_B, which is smaller than or equal to the total facing areas A_T. The total surface energy as a function of the bridged area can be written in a general form, which is valid for both the spreading and the non-spreading condition [2]:

$$W_s = C - 2 \cdot A_B \cdot \gamma_{LA} \cdot \cos\theta_C \qquad (3.4)$$

Where $\gamma_{LA}\cdot\cos\theta_C$ is the adhesion tension, and C is a constant depending on γ_{SA}, γ_{SL}, γ_{LA}, and A_T. The importance of liquid mediated adhesion is supported by both stiction and friction experiments. Stiction of released structures can show a large dependence on the relative humidity of air [11]. Friction measurements of silicon and silicon compounds [12], show a strong dependence of the static friction coefficient on relative humidity. In macro-tribology it is well known that adhesion of solids can strongly depend on relative humidity [13]. This is caused by capillary condensation. Liquids that wet or have a small contact angle on surfaces will spontaneously condense into cracks, pores, and into small gaps surrounding the points of contact between the contacting surfaces. At equilibrium the meniscus curvature equals the *Kelvin radius* [10]:

$$r_k = \frac{\gamma_{LA} V}{RT \log(p / p_s)} \qquad (3.5)$$

Where V is the molar volume, p is the vapour pressure, and p_s is the saturation vapour pressure. At room temperature, $\gamma_{LA}V/(RT)$ = 0.54 nm for water [10]. The meniscus curvature strongly depends on the relative vapour pressure p/p_s. For a relative humidity of 50% we find $\log(p/p_s)$ = -0.69 and r = -0.8 nm. At 100% relative humidity, $\log(p/p_s)$ = 0 and $r=\infty$ which means that a water film can grow all over the surface. The amount of condensed liquid in thermodynamic equilibrium is determined by both the Kelvin radius and the contact angle.

The meniscus curvatures are equal to the Kelvin radius and the contact angles satisfy Young's equation (fig. 3.4):

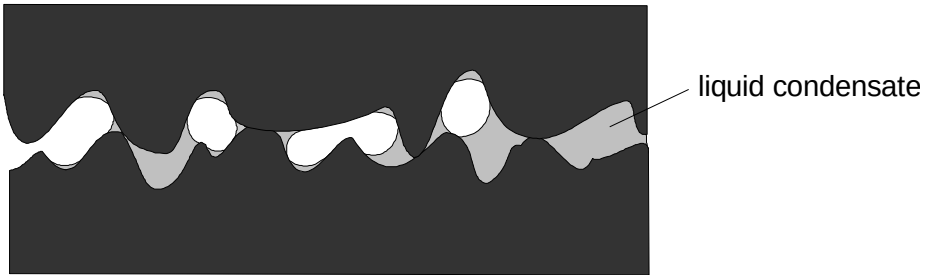

Figure 3.4: Capillary condensation between two contacting surfaces. In equilibrium the meniscus curvatures are equal to the Kelvin radius, the contact angles satisfy Young's equation.

Capillary condensation can lead to a large increase in the RCA (Real Contact Area) of solids by means of liquid bridging. It can, therefore, drastically increase the adhesion of those solids that due to their roughness show a low adhesion in a dry environment [13]. Models for the adhesion force due to capillary condensed liquid have been developed in harddisk tribology [14, 15, 16].

3.2.2 Hydrogen bridging

Hydrophilic silicon surfaces, under atmospheric conditions and temperatures well below 200ºC, contain adsorbed water layers. When two of these hydrated surfaces are brought into close contact, hydrogen bonds may form between molecules of the adsorbed water layers. Stengl et al. [17] have calculated a work of adhesion of about 100 mJ/m^2 based on this bonding model. From wafer bonding experiments [18, 19] and stiction experiments [4, 20], a work of adhesion Δg between 60 and 270 mJ/m^2 has been reported for hydrophilic surfaces (T < 200ºC).

3.2.3 Electrostatic forces

Electrostatic attractive forces across the interface can arise from a difference in work functions, or from electrostatic charging of opposed surfaces [21,18,22]. Difference in the work function leads to the formation of an electrical double layer by a net transfer of electrons from one surface to the other. Contact potentials are generally below 0.5 V, and the resulting surface charge densities are smaller than 10^{13} elementary charges per cm^2 [21]. At small separations the electrostatic pressure between flat surfaces is generally lower than the van der Waals pressure [21]. Temporary charging can occur during processing [22] or operation. Examples of this are tribocharging of rubbing surfaces [15] and charge accumulation in insulators of electrostatically operated micromotors [23]. Under fixed charge conditions, for example charges trapped in an insulator, the separation energy can become large, as initially the energy density in the gap does not decrease with increasing separation.

3.2.4 Van der Waals forces

The van der Waals dispersion forces between two bodies is caused by mutual electric interaction of the induced dipoles in the two bodies. Dispersion forces generally dominate over orientation and induction forces except for strongly polar molecules [24]. The interaction energy per unit area due to van der Waals interaction between two flat surfaces in the non-retarded regime (d < 20nm), is given by [10]:

$$W_{\mathrm{VDW}} = -\frac{A}{12p \cdot d^2} \tag{3.6}$$

Where A is the Hamaker constant, and d is the distance between the surfaces. For most solids and liquids, the Hamaker constant lies in the range 0.4-4 x 10^{-19} J [10]. For surfaces in contact a cut-off distance of $d = d_0$, slightly smaller than the interatomic distance, should be used to calculate the work of adhesion. Using a universal cut-off distance of d_0 = 0.165 nm and Hamaker constants calculated by the Lifshitz theory, a good agreement between experimental values and adhesion energies calculated with eq. (3.6) is found for non-H-bonding, non-metallic solids and liquids [10].

Eq. (3.6) with $d = d_0$ can be used to predict the adhesion energy of a clean hydrophobic silicon surface. However, the adhesion energy strongly depends on the surface termination. Often this is not exactly known. For pure silicon a Hamaker constant of 1.1 x 10^{-18} J is given [21], yielding a work of adhesion of 1.1 J/m^2 [10]. From wafer bonding literature [18] and stiction experiments [3, 20], a work of adhesion between 12 mJ/m^2 and 140 mJ/m^2 is reported. The reported values may be much lower than the theoretical value due to Hydrogen, Fluor or CH_x termination of the surface [18] and due to surface roughness. Compared to hydrophilic surfaces, the adhesion of hydrophobic surfaces might be more sensitive to surface roughness because smoothing by condensed water is absent.

3.3. Critical dimensions of beams and membranes

As soon as a structure touches the substrate, the total surface energy is lowered. The structure will stick to the substrate if the total (free) energy of the system reaches a minimum for a attachment length larger than zero. The total (free) energy of the system consists of the elastic deformation energy and the surface energy, which is a constant minus the work of adhesion. This energy balance is easily made for a cantilever beam [3]. Figure 3.5 shows a cantilever beam of length l, thickness t, width w, anchored at an initial gap spacing g. The beam attaches to the substrate at position x from the anchor. The elastic energy stored in the cantilever equals:

$$W_{\mathrm{m}} = \frac{E \cdot t^3 \cdot g^2 \cdot w}{2 \cdot x^3} \tag{3.7}$$

With E the Young's modulus.

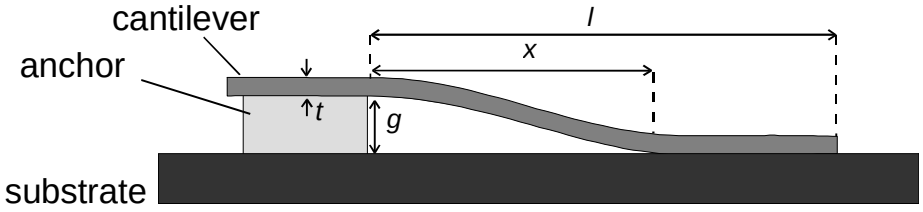

Figure 3.5: A cantilever beam of length l, thickness t, anchored at an initial gap spacing g. The beam attaches the substrate at position x from the anchor.

The surface energy as a function of the attachment length l-x equals:

$$W_{\mathrm{s}} = C - \Delta g \cdot (l - x) \cdot w \tag{3.8}$$

Where $\Delta g$is the work of adhesion per unit area. In equilibrium, the total energy W_{m}+W_{s} is minimal. An equilibrium detachment length x_{eq} can be found, where the decrease of the elastic energy equals the increase of the surface energy, by increasing the detachment length x:

$$\frac{W_{\mathrm{m}}}{x} + \frac{W_{\mathrm{s}}}{x} = 0 \tag{3.9}$$

Substitution of (3.7) and (3.8) in (3.9) yields:

$$\frac{3}{2} \frac{E \cdot t^3 \cdot g^2 \cdot w}{x_{eq}^{\ 4}} = \Delta g \cdot w \tag{3.10}$$

The critical length of cantilever beams is smaller than the detachment length x_{eq} because before complete detachment shear deformation at the tip will occur and the beam will touch the substrate under an angle [3]. The deformation energy at the point of snap back is about four times lower, and for the critical length can be written:

$$l_{\mathrm{crit}} = \sqrt[4]{\frac{3}{8} \cdot \frac{E \cdot t^3 \cdot g^2}{\Delta g}} \tag{3.11}$$

In case the residual stress and the stiffening due to stretching can be neglected, the critical length of doubly clamped beams show the same dependence on t, g, E and Δg Only the numerical constant in Eq. (3.11) should be changed, yielding a critical (total) length of doubly clamped beams that is 2.9 times larger than for cantilever beams [4]. To get an idea of the

strength of adhesion, we can evaluate the critical length of cantilever and doubly clamped beams, assuming a work of adhesion Δg= 100 mJ/m^2 and a Young's modulus of 150 GPa. Fig. 3.6 shows the length of the beams that are just kept down to the substrate, as a function of beam thicknesses, for three different gap spacings. The figure shows that even 10 μm thick cantilevers with a large gap spacing of 4 μm, have a critical length of only 310 μm (880 μm for doubly clamped beams). It is clear that stiction can easily cause malfunctioning in a lot of devices. Eq. (3.11) shows that the critical length depends on the work of adhesion by a fourth power root. A reduction factor of 16 of the work of adhesion only yields an increase in the critical length by a factor of 2.

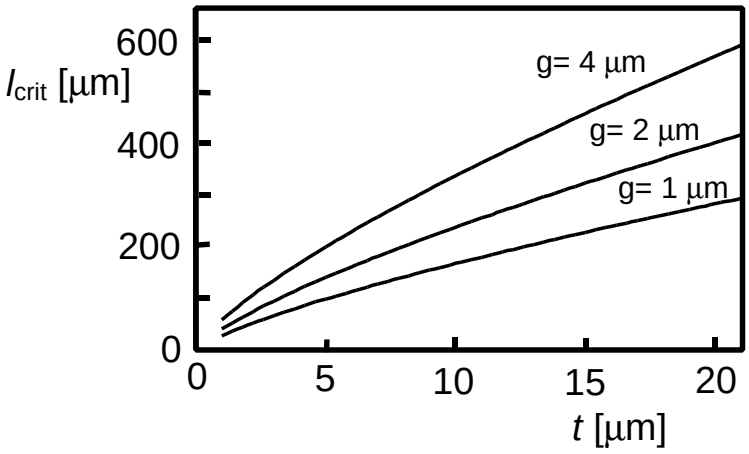

Figure 3.6: Critical lengths of cantilever beams as a function of beam thickness for different gap spacings, according to equation (3.11). A Young's modulus of 150 GPa and a work of adhesion of 100 mJ/m^2 is assumed. Beams shorter than the critical length will snap back after contacting the substrate.

3.4 Contact during fabrication

After wet sacrificial layer etching the released structure is immersed in liquid. During the subsequent drying, structures are pinned down to the substrate by capillary forces. Consider a beam with a thickness much smaller than its width. In the final state of the drying process the liquid volume approaches zero. If the tip of the beam touches the substrate, a very small amount of liquid can bridge a large area underneath the beam by forming an inside meniscus, and pulling a part of the beam flat against the surface (fig. 3.7). This is the state of lowest total energy as the liquid volume approaches zero.

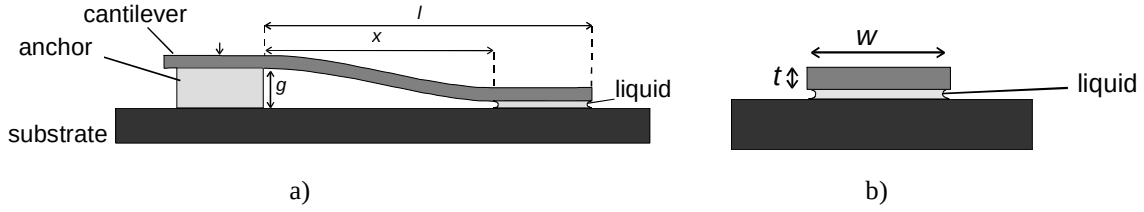

Figure 3.7: Final state of liquid drying underneath a cantilever beam a) Side view b) Front view. In the final state of drying a small amount of liquid can lower the surface energy by a large amount by bridging an area that is pulled flat against the substrate.

The work of adhesion by liquid bridging is found from equation (3.4). This final state is only reached if (a) the tip touches the substrate and (b) the surface energy plus the deformation energy has a minimum for a detachment length x smaller than the beam length l (See fig. 3.7a). This final state can be analysed by the substitution of the work of adhesion of the liquid bridge per unit area, $2\gamma_{la}\cdot\cos\theta_C$, into eq. (3.11). Although methods have been proposed to free sticking structures [25], most researchers prefer to use methods which reduce or avoid the capillary forces during drying, in order to avoid the structures to touch the substrate. The adhesion tension $\gamma_{LA}\times\cos\theta_c$ can be decreased choosing a low surface tension liquid for drying [11, 26], or by adjusting the contact angle. Scheepers [11] reports reduction of the stiction of silicon nitride beams after drying from n-hexane, which has a low surface tension (19 mJ/m^2) compared to DI water (73 mJ/m^2). By changing the combination of the surface materials and the liquid to be dried, one can try to obtain a contact angle near or over 90°. Only small negative, or even repulsive capillary pressures, result [27]. Abe et al. [28], have tried to increase yield by drying at elevated temperatures because surface tensions decrease by increasing temperature. An additional mechanism of stiction reduction when drying at high temperatures may be cavitation in the liquid bridge [13, 29]. If the pressure inside the liquid bridge (=pressure outside + Laplace pressure) drops below the vapour pressure (at the particular drying temperature) the liquid may start to boil locally [13]. This will limit the negative capillary pressure. Several methods have been proposed that apply *temporary support* to counteract the surface tensional forces during drying: Break-away polysilicon supports [30, 31], anchoring of freed structures using a photoresist grid [33] or polymer columns [32]. Other processes are based on avoiding the use of liquid completely by employing *dry sacrificial etching*: After full *polymerization* of a liquid in which the wafer was immersed [35, 36], the polymer can be ashed in an oxygen plasma. Sacrificial silicon oxide can be dry etched in vapour HF [27]. The *SCREAM*-process [37], as well as the *BSM-one run* [38] apply sacrificial layer etching of (poly)silicon. The *SIMPLE* process applies sacrificial layer etching of n+doped silicon [39]. Others use phase transition to avoid capillary forces: In the *supercritical drying* process, first reported by Mulhern et al. [34], liquid is transferred to vapour via the supercritical phase. Carbon dioxide is used because of its low critical temperature and pressure (T_c=31.1 °C, p_c = 72.8 atm). During evaporation of the supercritical carbon dioxide, no liquid/vapour interface exists, so there are no capillary forces working. Beams with a length of 850 μm (1.4 μm thick, 2.7 μm gap spacing) have been released [34]. *Freeze drying* as a liquid removing step was first applied to micromachining by Guckel et al. [1]. After HF etch, the wafer is rinsed in different liquids, until it is immersed in a liquid which can be removed by freeze drying. At MESA we use sublimation of cyclohexane at about -5 ºC [7]. The sublimation is done at atmosperic pressure on a plate cooled by a Peltier element under a continuous flow of nitrogen. The nitrogen flow aids the sublimation process by removing the cyclohexane vapour. It also prevents condensation of water on the substrate. For the same reason the wafer is heated to room temperature after completion of the

sublimation process. High yield fabrication of cantilevers up to 1 mm in length (2 μm thick, 2 μm gap spacing) has been achieved.

3.5. Contact during operation

Stiction originating from the fabrication process has been reduced quite successfully. Fail-safe devices should be designed to avoid stiction of released structures during their operational life-time. Sources of contact strongly depend on the application of the device. Here we analyze pull-down by electrostatic forces.

3.5.1 Electrostatic pull-down

To further our understanding of the effect of electrostatic forces, we will firstly examine cantilever beams which due to a voltage difference between the beams and the substrate, are pulled down to the substrate. The deflection of the beam is described by the following non-linear differential equation:

$$E \cdot I \cdot \frac{\partial^4 y(x)}{\partial x^4} = \frac{\varepsilon \cdot w \cdot U^2}{2 \cdot (g - y(x))^2} \qquad (3.12)$$

Where $y(x)$ is the deflection on position x along the cantilever, g is the initial gap to the substrate, EI is the flexural rigidity of the beam, ε is the permittivity, w is the width of the beam, and U is the voltage difference between the beam and the substrate (fig. 3.7). A full analytical solution has not yet been obtained. An approximate solution can be derived by looking at the total potential energy which consists of the electrical energy stored in the gap and the mechanical deformation energy stored in the beam. This can easily be done if a constant shape is assumed. The deflection function can only change in amplitude. The elastic deformation energy assuming the uniform load shape is a function of the tip deflection y of the cantilever beam:

$$W_m = \frac{48}{30} \frac{E \cdot I}{l^3} y^2 \qquad (3.13)$$

The capacitance between the beam and the substrate is calculated by assuming a linear shape between the tip and the anchor of the beam fig. 3.8b):

$$C(y) = \frac{e \cdot w \cdot l}{y} \ln \left| \frac{g}{g - y} \right| \qquad (y < g) \qquad (3.14)$$

Tip deflection as a function of the applied voltage U can be found from the Legendre transformation of the energy stored in the transducer:

$$W' = W_m(y) - \frac{1}{2}C(y)U^2 \tag{3.15}$$

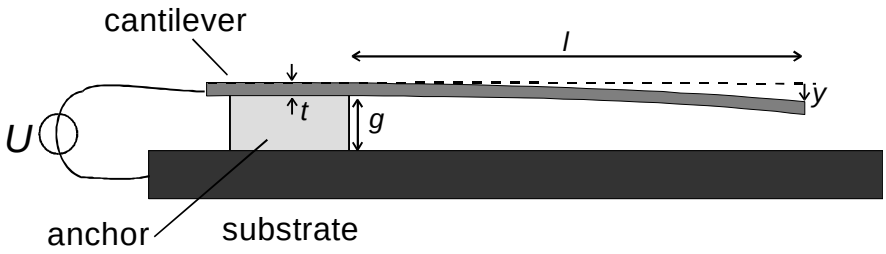

a)

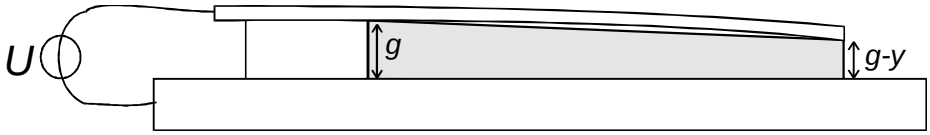

b)

Figure 3.8: a) Pull-down of a cantilever beam by electrostatic forces. *U* is the applied voltage difference between the beam and the substrate, *g* is the initial gap spacing, *l* is the length of the beam, *t* is the thickness, and *y* is the tip deflection. b) The shaded region is the gap for which the capacitance is calculated.

The condition of equilibrium is:

$$\partial W'(y) / \partial y = 0. \tag{3.16}$$

The system becomes unstable if the electrostatic pull-down force increases faster than the restoring elastic force with increasing *y*, which means that the negative electrical stiffness starts to dominate the positive mechanical stiffness. Therefore the equilibrium is stable if $\partial^2 W'/\partial y^2 > 0$, and unstable if $\partial^2 W'/\partial y^2 < 0$. At the edge of stability:

$$\partial^2 W' / \partial y^2 = 0 \tag{3.17}$$

Combination of equations (3.13 - 3.17) yields for the tip deflection at pull-in:

$$\ln\frac{g}{g-y} = \frac{y\cdot(g-\frac{4}{3}\cdot y)}{(g-y)^2} \tag{3.18}$$

Which gives $y_{pi} = 0.44g$. Substitution in eq. (3.16) gives for the pull-in voltage:

$$U_{pi} = \sqrt{0.22 \frac{E \cdot g^3 \cdot t^3}{e \cdot l^4}} \qquad (3.19)$$

Eq. (3.19) slightly underestimates the pull-in voltage, because the capacity is overestimated using the linear deflection profile. Accurate calculations have been done by Osterburg et al. [42]. They found a constant 0.28 in stead of 0.22. In [42] also the pull-in voltage of doubly clamped beams and circular membranes can be found. Fig. 3.9 shows pull-in voltages of cantilever beams as a function of l for different beam thicknesses and initial gaps according to eq. (3.19). A cantilever with a length of 100 μm, a thickness of 1 μm and a gap spacing of 1 μm is pulled to the substrate by a voltage difference of only 6.1 V. In electrostatic actuators voltages of up to a hundred volts are common. Vertical pull-in has to be anticipated in the design even if thick structures (10 μm) and large gap spacings (4 μm) are used (fig. 3.9). Pull-in to the substrate can be avoided by electrical shielding in order to give the substrate locally the same potential as the structures directly above. Another approach is to always keep rotor parts at the same voltage as the substrate and only to allow a voltage difference between the stator poles and the substrate.

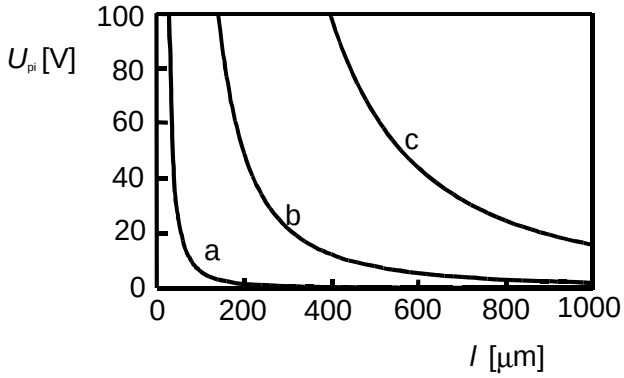

Figure 3.9: Pull-in voltage for a cantilever beam as a function of the length. a) Thickness t = 1μm, initial gap spacing g = 1 μm. b) t = 5 μm, g = 2 μm. c) g = 4 μm, t=10 μm.

3.6 Stiction reduction of contacting structures

In section 3.3 it was shown that an adhesion energy of 100 mJ/m^2 is high enough to make short , thick beams stick to the substrate. If large structures are supported by narrow beams the stiction forces will be even more dominant. The comb-drive shown in fig. 3.10 is an example of such a structure. Structures like this are also sensitive to applied mechanical shocks. It therefore requires special fabrication procedures and careful handling during its whole life-time. If stiction is to be eliminated in such a large structures, extreme reduction of the adhesion energy is necessary. Low adhesion energy is also desirable in devices where contact between moving parts is essential to the functioning of the device [5, 6]. Coating and reduction of the RCA is analysed here.

3.6.1 Reducing the work of adhesion

Coating can have a significant effect if capillary forces or hydrogen-bridging are the dominant adhesion mechanisms. By providing a hydrophobic surface, coating can eliminate water mediated adhesion [43, 44]. Adhesion by van der Waals forces will always remain. A typical low-adhesive material like PTFE, still has a surface tension in the order of 20 mJ/m^2. Other low-adhesive materials are the typical friction reducing coatings [45, 46, 47]. The work of adhesion of perfect flat surfaces, will hardly be lower than about 40 mJ/m^2. Coating alone will not be enough if large reductions of the work adhesion is desired. Reduction of the RCA should be applied.

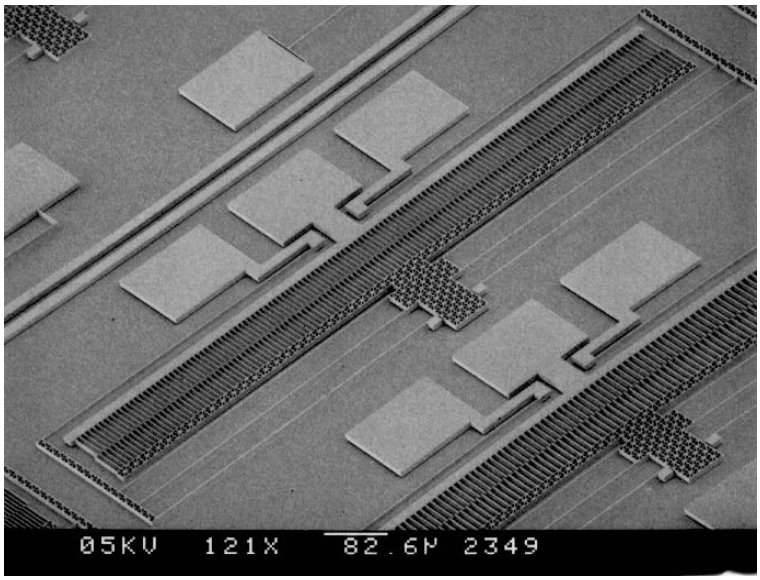

Figure 3.10: Photograph of a large combdrive actuator (Legtenberg [7]). Support springs are 1 mm long, and carry a large mass at the tip.

3.6.2 Reduction of the geometrical area contact

Bumps

Fan et al. [48,49] were the first to use stiction reducing bumps. They etched isotropically holes in the sacrificial oxide, before depositing polysilicon (fig. 3.11). These hemispherical bumps reduce the contact area to dimensions smaller than the resolution of the photolithography used. The bumps have found wide-spread application in surface micromachined devices, and have proven to be very effective in reducing the stiction. Despite their importance for MEMS devices, measurement of the amount of stiction reduction by the bumps have not been reported.

Figure 3.11: Fabrication of bumps according to [48, 49]. a) isotropic etch of hole b) deposit polysilicon structural layer c) release etch.

Side-wall spacers

The concept of side-wall spacers to reduce the geometrical area of contact, was introduced by Sandejas et. al. [50]. Due to the self-aligned nature of the process side-wall spacers can be fabricated without additional mask steps. The process can be applied to standard SOI-wafers, which is another advantage. Because there is no report on the effectiveness of these spacers, we have been done experiments to characterize the adhesion reduction. A new process has been developed to generate spacers that are grown partly underneath the structures, in order to make robust spacers. The process is illustrated in fig. 3.12.

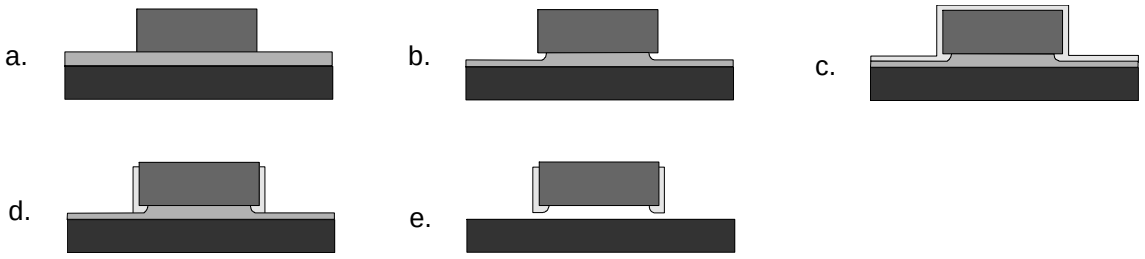

Figure 3.12: Processing scheme for robust side-wall spacers, starting from a) patterned silicon structural layer, b) isotropic thinning of sacrificial layer c) grow anti-stiction silicon nitride layer d) anisotropic silicon nitride etch e) sacrificial layer etch.

Fig. 3.13 shows a SEM-photograph of the bottom side of a structure with side-wall spacers. The characterization of these spacers is reported in appendix *B*. Stiction reduction for beams of three different widths, 12, 24 and 36 μm, has been measured. The result is a reduction of 2 x 10^1, 4 x 10^1 and 6 x 10^1 times of the work of adhesion per unit length of the beam. This is slightly larger than the reduction of the geometrical contact area due to the side wall spacers, which is 12, 24 and 36 times assuming a total spacer width of 2 x 0.5 μm. The spacers obtained are extremely robust. By using a probe pen, structures can be pushed down to the substrate. They could be moved easily across the surface. Even 2 μm small beams could be released by simple touching. Without spacers, the same structures stuck heavily and could not be released without damage. Spacers are especially useful for experimental devices: beams that stick, can be freed easily, and testing can continue.

Side-wall spacing, supports on substrate

Kozlowski et al. [36] have created side-wall spacing in an elegant way. After (dry) release of etched structures (fig.3.14a), fluorcarbon polymers are deposited, partly underneath the structures (figure 3.14b), thus giving robust, low surface energy spacers.

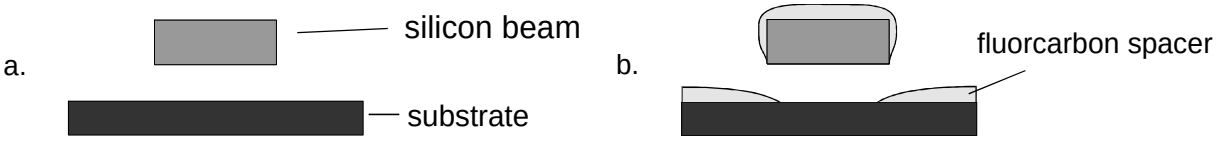

Figure 3.14: Creation of side-wall spacing [36]. a) Released structure b) deposition of fluorcarbon, partly underneath the structures.

As is the case with the temporary supports during drying (see paragraph 3.4.2), the maximum lateral spacing between the bumps is determined by the vertical stiffness of the structures.

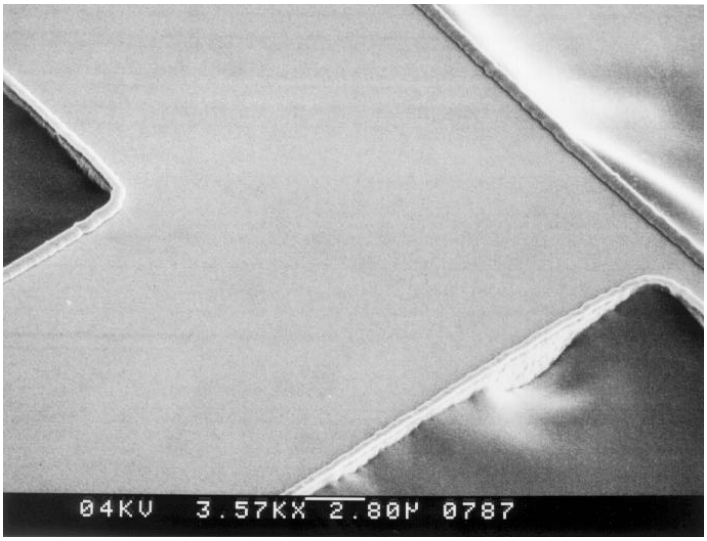

Figure 3.13: SEM-photograph of the bottom side of a structure with side-wall spacers. The structure is immersed in the glue of the tape which was used to tear it off.

3.6.3 Increase roughness

Adhesion of elastic solids is expected to be extremely sensitive to surface roughness [51, 52]. This can be illustrated using a simple contact model which is derived in appendix A. Figure 3.15 shows a rough elastic and a smooth rigid surface in contact The roughness is represented by spherical asperities with a radius R and a peak-valley distance z_0. The asperities undergo an elastic indentation z. The work of adhesion of the two solids is Δg

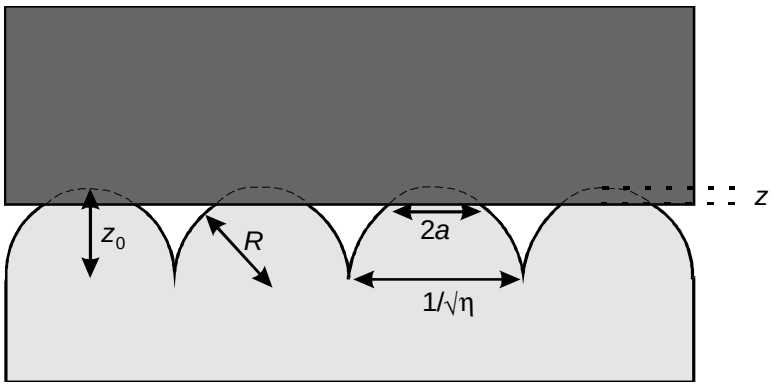

Figure 3.15: Contact of a smooth and a rough surface. The roughness is represented by spherical asperities with a radius R, a peak-valley distance z_0, and an asperity density h [m^{-2}]. The asperities undergo an elastic indentation z.

For $z_o < R$, the real contact area A_r normalized to the apparent contact area A_a is given by:

$$A_r^* = \frac{A_r}{A_a} = 1.34?^{-2/3}[\frac{p_{load}}{p_{adh}} + 1]^{2/3} \qquad (3.20)$$

Where p_{load} is the apparent load pressure, $p_{adh} = 2p \cdot ? \cdot \Delta ? \cdot R$ is the adhesive pressure and q^* is the dimensionless adhesion parameter:

$$q^* = \frac{z_0^{3/2}}{D \cdot \Delta g \cdot R^{1/2}} \tag{3.21}$$

D is the compliance as defined in appendix A. Fig. 3.16 shows the relative contact area as a function of q^* for zero applied load.

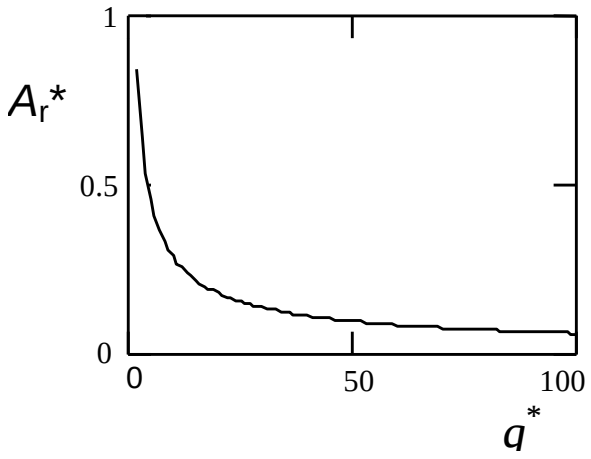

Figure 3.16: Relative real contact area as a function of q^* for zero applied load.

For polished prime quality wafers the roughness varies from batch to batch. A value of R=1-10 μm and z_0=0.2 nm was found by scanning with an AFM (Nanoscope III) across an area of 4 x 4 μm^2. Contacted by a smooth silicon surface this yields for R = 1 μm, an adhesion parameter q^* = 3.1, a relative real contact area of 0.6 and an adhesive pressure of 0.4 GPa (assuming a Young's modulus of 150 GPa, Poisson's ratio of 0.3, and Δg= 0.1 J/m^2). If for example the silicon wafer is roughened in such a way that R = 0.5 μm and z_0 = 1 μm then the adhesion parameter increases to q^* = 1.5 x 10^6, the relative real contact area drops to 1 x 10^{-4} and the adhesive pressure drops to 79 kPa. Such a rough surface can easily be created using reactive ion etching to grow 'micrograss'(fig. 3.17). Fuller and Tabor verified experimentally the decay of the pull-off force with increasing adhesion parameter for smooth rubber on roughended Perspex [51]. In magnetic recording, a strong dependence of stiction and friction on surface roughness has been measured [54]. Surface roughness modification to reduce stiction of (poly)silicon structures, has been shown to be effective [43, 55, 56, 57]. Reduction of the work of adhesion of at least 10 times are obtained. Houston et al. [43] report a work of adhesion as low as 0.3 mJ/m^2 (about 300 times smaller than untreated hydrophilic surfaces), after surface treatment with ammonium fluoride. Ammonium fluoride etches the silicon surface, leaving (111)-faceted protrusions. The resulting surfaces are hydrogen terminated hydrophobic. The low work of adhesion may be the result of the *combination* of rough and hydrophobic. Due to the hydrophobic properties of the surface, water mediated adhesion probably is avoided. This should be kept in mind if roughness is increased. In order to have

the full benefit of the reduced RCA by increased roughness, growth of the area of contact by capillary condensation around points of contact should be avoided. In atmospheric conditions where there is a chance of condensation of water this can be done by hydrophobic coating. In order to obtain a stable hydrophobic surface coating with fluorocarbon can be a good option [58].

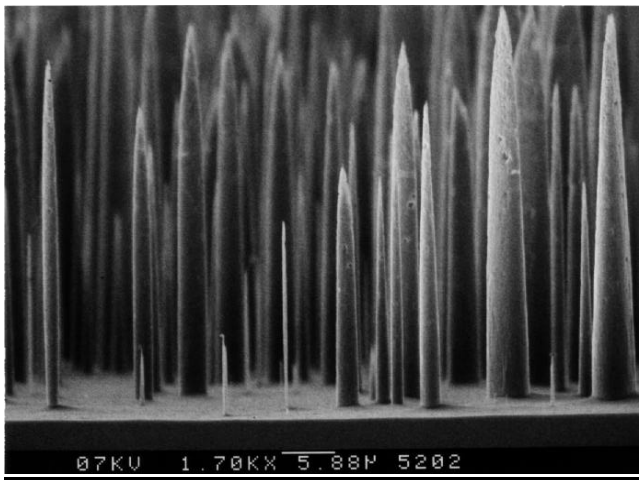

Figure 3.17: 'Micrograss' created by RIE (Jansen [53]).

3.7 Conclusions

Stiction research has firstly focused on diminishing the effect of pull-down forces of drying liquid during fabrication. Several methods have been developed that reduce the problems to an acceptable level. Stiction can also originate from contact during operation of the device. Electrostatic pull-down has been analyzed, and it can be concluded that even short beams can be pulled-down already at moderate voltages. In particular applications, one can design the device so that incidental touching of the substrate is impossible or that restoring elastic forces are high enough for snap back. In many applications this is not possible and low adhesion forces are desired to avoid stiction. Strongly reduced adhesion forces are also required in devices where contact between moving parts is essential to the functioning of the device. Reduction of additional forces can be obtained by choosing low surface energy contact materials and by reducing the real contact area. If one looks at practical material properties, lowering of the surface energy is not drastic enough to solve stiction problems in general. Reduction of the real contact area is therefore essential. This can be done by reducing the geometrical contact area (bumps, side-wall spacers), or by increasing the surface roughness.
Experiments have been done to characterize the effectiveness of side-wall spacers. For beams of 12, 24 and 36 μm the work of adhesion was reduced by a factor 2×10^1, 4×10^1 and 6×10^1 respectively, slightly larger than the reduction of the geometrical contact area.
In order to make fail-safe devices, large reductions of adhesion forces are needed. A combination of bumps or side-wall spacers and surface roughness may be needed. For devices that are operated in atmospheric conditions the increase of the surface roughness has to be

accompanied by measures that reduce the effect of liquid bridging due to capillary condensation of water.

3.8 Literature

1. Guckel H., Sniegowski J.J., Christenson T.R., Mohney S., Kelly T.F.,"Fabrication of micromechanical devices from polysilicon films with smooth surfaces", Sensors and Actuators, Vol. 20, 1989, pp. 117-122.
2. Mastrangelo C.H., Hsu C.H.," Mechanical stability and adhesion of microstructures under capillary forces-part I: basic theory", J. microelectromechanical systems, vol.2, no.1, March 1993, pp.33-43.
3. Mastrangelo C.H., Hsu C.H.," A simple experimental technique for the measurement of the work of adhesion of microstructures", Proc. IEEE Solid-State Sensors and Actuators Workshop, Hilton Head Island, SC, USA, June 22-25, 1992, pp. 208-212.
4. Mastrangelo C.H., Hsu C.H.," Mechanical stability and adhesion of microstructures under capillary forces-part II: Experiments", J. microelectromechanical systems, vol.2, no.1, March 1993, pp.44-55.
5. Legtenberg R., Berenschot E., Lammerink T., Elwenspoek M.,:An electrostatic axial gap wobble motor", The 8th International Conference on Solid-State Sensors and Actuators (Transducers '95), Stockholm, Sweden, June 25-29 1995, pp. 404-407.
6. Tas N.R., Legtenberg R., Berenschot J.W., Elwenspoek M.C., Fluitman J.H.J.,"The electrostatic shuffle motor", Proc. Micromechanics Europe Workshop, Copenhagen, Denmark, 1995, pp. 128-131.
7. Legtenberg R.," Electrostatic actuators fabricated by surface micromachining techniques", Ph.D. Thesis University of Twente, Enschede, The Netherlands, 1996, ISBN 90-3650796-0.
8. Roberds B., Farrens S.," An AM Study on the roughness of silicon wafers correlated with direct wafer bonding", Proc. Vol. 92-7 of The Electrochemical Soc, Proc. of the third int. symposium on semiconductor waferbonding: physics and applications, Reno, 1995, pp. 326-341.
9. Ljungberg K.,"Phenomenology of silicon wafer bonding", Ph.D. Thesis Uppsala University, 1995, ISBN 91-554-3633.
10. Israelachvili J.N.,"Intermolecular and surface forces", Academic Press, London, 1992.
11. Scheepers P.R., Voorthuyzen J.A., Olthuis W., Bergveld P.,"Investigation of attractive forces between PECVD silicon nitride microstructures and an oxidized silicon substrate", Sensors and Actuators A, Vol. 30, 1992, pp. 231-239.
12. Deng K., Ko W.H.," A study of static friction between silicon and silicon compounds", J. Micromech. Microeng., Vol. 2, 1992, pp. 14-20.
13. Rabinowicz E.,"Friction and Wear of Materials", John Wiley and Sons, New York, 1965.
14. Matthewson M.J., Mamin H.J.,"Liquid mediated adhesion of ultra-flat solid surfaces". Mat. Res. Soc. Symp. Proc. Vol. 119, 1988, pp. 87-92.
15. Bhushan B.,"Tribology and mechanics of magnetic storage devices",Springer-Verlag, New York, 1990.
16. Li Y., Trauner D., Talke F.E.,"Effect of humidity on stiction and friction of the head/disk interface", IEEE Trans. on magnetics, Vol. 26, no. 5, sept. 1990., pp. 2487-2489.
17. Stengl R., Tan T., Gosele U.," A model for the silicon wafer bonding process", Japanese Journal of Applied Physics, Vol. 28, no. 10, Oct. 1989, pp. 1735-1741.
18. Spierings G.A.C.M., Haisma J.," Diversity and interfacial phenomena in direct bonding", Proc. Vol. 92-7 of The Electrochemical Soc., Proc. of the first int. symposium on semiconductor wafer bonding, science, technology and applications, Phoenix AZ, Oct. 13-18, 1991, pp. 18-32.
19. Backlund Y., Hermansson K., Smith L.," Bond-strength measurements related to silicon surface hydrophilicity", J. Electrochem. Soc., Vol. 139, No. 8, August 1992., pp. 2299-2301.
20. Legtenberg R., Tilmans H.A.C., Elders J., Elwenspoek M.," Stiction of surface micromachined structures after rinsing and drying: model and investigation of adhesion mechanisms", Sensors and Actuators A, Vol. 43, 1994, pp. 230-238.

21. Krupp H.,"Particle adhesion", Adv. Coll. Interf. Sci., Vol. 1, 1967, pp. 111-239.
22. Alley R.L., Cuan G.J., Howe R.T., Komvopoulus K.,"The effect of release-etch processing on surface microstructure stiction", Proc. IEEE Solid-State Sensors and Actuators Workshop, Hilton Head Island, SC, USA, June 22-25, 1992, pp. 202-207.
23. Anderson K.M., Colgate J.E.," A model of the attachment/detachment cycle of electrostatic micro actuators", DCS-Vol. 32, Micromech. Sensors, Actuators, and Systems, ASME 1991, pp. 255-268.
24. Israelachvili J.N., Tabor D.,"The measurement of van der Waals dispersion forces in the range 1.5 to 130 nm", Proc. R. Soc. Lond. A, Vol. 331, 1972, pp. 19-38.
25. Gogoi B.P., Mastrangelo C.H.,"Post-processing release of microstructures by electromagnetic pulses", The 8th International Conference on Solid-State Sensors and Actuators (Transducers '95), Stockholm, Sweden, June 25-29 1995, pp. 214-217.
26. Ohtsu M., Minami K., Esashi M,"Fabrication of packaged thin beam structures by an improved drying method", Proc. IEEE Micro Electro Mechanical Systems Workshop '96, San Diego, CA, Feb. 11-15 1996, pp. 228-233.
27. Jansen H.V.,"Plasma etching in microtechnology", Ph.D. Thesis University of Twente, Enschede, The Netherlands, 1996, ISBN 90-3650810x.
28. Abe T., Messner W.C., Reed M.L.," Effects of elevated temperature treatments in microstructure release procedures", Journal of MEMS, vol. 4, no. 2, June 1995.
29. Abe T., Messner W.C., Reed M.l.," Effective methods to prevent stiction during post-release-etch processing", Proc. IEEE Micro Electro Mechanical Systems Workshop '95, Amsterdam, the Netherlands, Jan. 29 - Feb. 2 1995, pp. 94-99.
30. Kim C.-J., Pisano A.P., Muller R.S., Lim M.G.,"Polysilicon microgripper", Proc. IEEE Solid-State Sensor and Actuator Workshop, Hilton Head Island, South Caroline, U.S.A., June 1990, pp. 48-51.
31. Fedder G.K., Howe R.T.,"Thermal assembly of polysilicon microstructures", Proc. Micro Electro Mechanical Systems 1991, Nara, Japan, 30 Jan.- 2 Febr. 1991, pp. 63-68.
32. Mastrangelo C.H., Saloka G.S.," A dry-release method based on poymer columns for microstructure fabrication", Proc. IEEE Micro Electro Mechanical Systems Workshop '93, Fort Lauderdale, Florida, Feb. 7-10, 1993, pp. 77-81.
33. Kobayashi D., Kim C., Fujita H.,"Photoresist-assisted release of movable microstructures", Proc. 7th Inth. Conf. Solid-State Sensors and Actuators (Transducers '93), Yokohama, Japan, June 7-10 1993, Abstr. late news papers pp. 14-15.
34. Mulhern G.T., Soane D.S., Howe R.T.," Supercritical carbon dioxide drying of microstructures",Proc. 7th Inth. Conf. Solid-State Sensors and Actuators (Transducers '93), Yokohama, Japan, June 7-10 1993, pp. 296-299.
35. Orpana M., Korhonen A.O.," Control of residual stress of polysilicon thin films by heavy doping in surface micromachining", Proc. 6th Int. Conf. Solid-State Sensors and Actuators (Transducers 1991), pp. 957-960.
36. Kozlowski F., Lindmair N., Scheiter Th., Hierold C., Lang W.," A novel method to avoid sticking of surface micromachined structures", The 8th International Conference on Solid-State Sensors and Actuators (Transducers '95), Stockholm, Sweden, June 25-29 1995, pp. 220-223.
37. Shaw K.A., Zhang Z.L., MacDonald N.C.," Scream 1: A single mask, single-crystal silicon process for microelectromechanical structures", Proc. IEEE Micro Electro Mechanical Systems Workshop '93, Fort Lauderdale, Florida, Feb. 7-10, 19931993, pp. 155-160.
38. De Boer M., Jansen H.V., Elwenspoek M.,"The black silicon method V: A study of the fabricating of movable structures for micro electromechanical systems", The 8th International Conference on Solid-State Sensors and Actuators (Transducers '95), Stockholm, Sweden, June 25-29 1995, pp. 565-568.
39. Li Y.X., French P.J., Sarro P.M., Wolffenbuttel R.F.,"Fabrication of a single crystalline silicon capacitive lateral accelerometer using micromachining based on single step plasma etching", Proc. IEEE Micro Electro Mechanical Systems Workshop ' 95, Amsterdam, the Netherlands, Jan. 29 - Feb. 2 1995, pp. 368-373.

40. Hirano T., Furuhata T., Fujita H.,"Dry releasing of electroplated rotational and overhanging structures", Proc. IEEE Micro Electro Mechanical Systems Workshop '93, Fort Lauderdale, Florida, Feb. 7-10, 1993, pp. 278-279.
41. Tilmans H.A.C., "Micro-mechanical sensors using encapsulated built-in resonant strain gauges", Ph.D. Thesis University of Twente, Enschede, The Netherlands, 1993, ISBN 90-9005746-3.
42. Osterberg P.M., Gupta R.K., Gilbert J.R., Senturia S.D.,"A quantitative model for the measurement of residual stress using electrostatic pull-in of beams", Proc. Solid-State Sensor and Actuator Workshop, Hilton Head Island, South Caroline, U.S.A., June 13-16 1994, pp. 184-188.
43. Houston M.R., Maboudian R., Howe R.T.,"Ammonium fluoride anti-stiction treatments for polysilicon microstructures", The 8th International Conference on Solid-State Sensors and Actuators (Transducers '95), Stockholm, Sweden, June 25-29 1995, pp. 210-213.
44. Man P.F., Gogoi B.P., Mastrangelo C.H.,"Elimination of post-release adhesion in microstructures using thin conformal fluorcarbon films", Proc. IEEE Micro Electro Mechanical Systems Workshop '96, San Diego, CA, Feb. 11-15 1996, pp. 55-60.
45. Deng K., Collins R.J., Mehregany M., Sukenik C.N.,"Performance impact of monolayer coating of polysilicon micromotors", Proc. IEEE Micro Electro Mechanical Systems Workshop '95, Amsterdam, the Netherlands, Jan. 29 - Feb. 2 1995, pp. 368-373.
46. Zarrad H., Chovelon J.M., Clechet P., Jaffrezic-Renault N., Martelet C., Belin M., Perez H., Chevalier Y.,"Optimization of lubricants for silica micromotors", Sensors and Actuators A, Vol. 46-47, 1995, pp. 598-600
47. Bhushan B.,"Nanotribology and nanomechanics of MEMS devices", Proc. IEEE Micro Electro Mechanical Systems Workshop '96, San Diego, CA, Feb. 11-15 1996, pp. 91-98.
48. Fan L.-S., Tai Y.-C., Muller R.S.,"IC-processed electrostatic micromotors", Tech. Digest, IEEE INT. Electron Devices Meet. San Francisco, CA, Dec. 11-14, 1988, pp. 666-669.
49. Fan L.S., Tai Y., Muller R.S.,"IC-processed electrostatic micromotors", Sensors and Actuators, Vol. 20, 1989, pp. 41-47.
50. Sandejas F.S.A., Apte R.B., Banyai W.C., Bloom D.M.,"Surface microfabrication of deformable grating light valves for high resolution displays, Proc. 7th Inth. Conf. Solid-State Sensors and Actuators (Transducers '93), Yokohama, Japan, June 7-10 1993, Abstr. late news papers pp. 6-7.
51. Fuller K.N.G., Tabor D.,"The effect of surface roughness on the adhesion of elastic solids", Proc. R. Soc. Lond. A., Vol. 345, 1975, pp. 327-342.
52. Arai F., Andou D., Fukuda T.,"Adhesion Forces Reduction for Micro Manipulation Based on Micro Physics", Proc. IEEE Micro Electro Mechanical Systems Workshop '96, San Diego, CA, Feb. 11-15 1996, pp. 354-364.
53. Jansen H.V.,"Plasma etching in microtechnology", Ph.D. Thesis University of Twente, Enschede, The Netherlands, 1996, ISBN 90-3650810x.
54. Raman V., Tang W.T., Jen D., Reith T.R.,"The dependence of stiction and friction on roughness in thin film magnetic recording disks", J. Appl. Physics, 70 (1991), pp. 1826-1836.
55. Alley R.L., Mai P., Komvopoulos K., Howe R.T.,"Surface Roughness Modification of Interfacial Contacts in Polysilicon Microstructures", Proc. 7th Inth. Conf. Solid-State Sensors and Actuators (Transducers '93), Yokohama, Japan, June 7-10 1993, pp. 288-291.
56. Yee Y., Chun K., Lee J.D.,"Polysilicon surface modification technique to reduce sticking of microstructures",The 8th International Conference on Solid-State Sensors and Actuators (Transducers '95), Stockholm, Sweden, June 25-29 1995, pp. 206-209.
57. Ando Y., Ino J., Ozaki K., Ishikawa Y., Kitahara T.,"Friction and pull-off force on silicon surface modified by FIB", Proc. IEEE Micro Electro Mechanical Systems Workshop '96, San Diego, CA, Feb. 11-15 1996, pp. 349-353.
58. Jansen H.V., Gardeniers J.G.E., Elders J., Tilmans H.A.C., Elwenspoek M.C.,"Applications of fluorcarbon polymers in micromechanics and micromachining", Sensors and Actuators A, Vol. 41-41, 1994, pp. 136-140.

4

Elastic Adhesive Friction Models for Application in MEMS

Reduction and control of friction is an important issue in MEMS. Using the Greenwood and Williamson elastic contact model, the dependence of static friction on the surface topography is analyzed. Static friction in shearing mode is assumed to be proportional to the real contact area. The real contact area is almost proportional to the load. The mean elastic contact pressure is almost independent of the load. The effect of adhesion is included using Maugis' expansion of the Greenwood and Williamson model. Analysis of low loaded conditions reveals that the statistical models fail, as there can be a too small number of contact points. In particular the adhesive load is underestimated in this case. A discrete contact model is presented to calculate the friction under low loading conditions, when the number of contact points is too small to use the statistical models. The transition from elastic to plastic contact is analyzed. With increasing roughness the friction coefficient decreases to a lower limit, until the friction coefficient of the plastic contact is reached. Static friction in a polysilicon side-driven friction meter is characterized, and related to the surface topography. The measured friction vs. load fits well the relation found using the discrete contact model with three contact points.

4.1 Introduction

The application of friction reducing elements, like ball bearings, magnetic levitation and hydrostatic bearings is often too complicated in MEMS devices. Therefore, dry sliding friction is used in most bearings and joints. Tests of the first electrostatic micromotors showed a significant effect of friction on micromotor performance [1,2]. Therefore, in situ static friction measurements have been done, yielding friction coefficients up to 4.9 ± 1 [3]. Due to the large surface to volume ratio in MEMS devices, adhesion forces become relatively large, and can lead to friction force much larger than the applied normal force [2,4,5]. Measurement, reduction and control of friction have become a major concern in the development of micromechanisms [5-15]. One of the striking outcomes of these studies is the wide range of the measured static friction coefficients for the structural materials used in MEMS [16]. Differences in the surface topography can be one of the causes of the spread in the measured friction coefficient. Therefore, in this chapter the static friction dependence on surface topography is studied. In MEMS devices the typical contact materials are silicon, silicon

This chapter is based on:
N.R.Tas, C.Gui, M.Elwenspoek, *Elastic Adhesive Friction Models for Application in MEMS*, Proc. IEEE MEMS Conf., Miyazaki, Japan, Jan. 23-27 2000, pp. 193-198.
Gui C., Elwenspoek M., Tas N., Gardeniers J.G.E., *The effect of surface roughness on direct wafer bonding*, J. Appl. Phys., Vol. 85, issue 10, 1999, pp. 7448-7454.
N.R.Tas, B. Vogelzang, M.Elwenspoek, L. Legtenberg, *Adhesion and friction in MEMS*, ed. Bhushan B., NATO ASI series vol. 330, Kluwer, The Netherlands, 1997, pp. 621-629.

dioxide and silicon nitride, which are rather hard. Therefore, in most contacts elastic deformation occurs, and elastic contact models [17 ,18] can be used. Because the aim of this paper is to explain the basic physics of static friction, we prefer the use of these models with a simple surface topography representation. An overview of more refined representations is given by Majumdar et. al. [19]. In MEMS devices a wide range of surface roughness is found, varying from the almost atomically smooth surface of a chemical-mechanically polished silicon wafer, to the rough surface of deposited polysilicon. From stiction and wafer bonding experiments it is known that the adhesive attractive forces between contacting surfaces drop rapidly with increasing surface roughness [20, 21]. However, the forces in MEMS devices are often so small (μN's), that even in rough contacts the contribution of the adhesion forces to the total load compressing the surfaces can not be neglected [22] The influence of adhesion, and its dependence on the surface roughness is therefore included in the elastic contact model. In section 4.4 the friction theory is applied to analyze the static friction measured between two rather rough polysilicon side walls, as a function of the electrostatically generated clamp force. The results of the measurement illustrates the need for the presented model modifications for low loading conditions.

4.2 Basic Friction Theory

According to Tabor [23], two basic friction mechanisms can be distinguished in sliding contacts: ploughing of the asperities of the harder material through the softer material, and shearing of the junctions in the region of contact. In this paper we focus on the shearing friction, because the interfaces in MEMS are often between almost equally hard materials, and the asperities are mostly rather blunt. Following Tabor [23] the shearing friction force is given by:

$$F_f = s \times A_r \qquad (4.1)$$

Where s is the shear strength of the interface and A_r is the real area of contact. We will assume that s is pressure independent. One should be aware that this not true for all materials: For polymers it is known that the shear strength is pressure dependent [24]. In case the asperity tips are plastically deformed in the contact region, the real contact area is given by $A_r = L / H$ and the friction force is given by $F_f = (s / H) \cdot L$ where L is the (externally) applied load force, and H is the hardness of the contacting materials [25]. In case the asperities touching the counter surface are deformed elastically, the contact force for each asperity is given by Hertzian theory. If all asperities were located at the same height, the contact area would increase with $L^{2/3}$. For real surfaces and many contact points, the asperity summit level is distributed, and the area of contact becomes almost proportional to L [17]. The friction coefficient for the elastic contact can now be written as $m_e = s / p_e$, where p_e is the mean elastic contact pressure L / A_r (see paragraph 4.3). This representation of the friction coefficient explains the friction reduction by application of low adhesive monolayer coatings

[26-30]. Application of such a coating reduces the shear strength of the interface, while due to the small thickness of the coating, the elastic properties of the interface do not change.
Because the real contact area is proportional to the load in both plastic and elastic contacts, the friction force will be proportional to the load force, as is expressed by the famous Amontons' Law:

$$F_f = m \cdot L \tag{4.2}$$

In section 4.3.2 this relation is modified to include the adhesive load.

4.3 Multi Asperity Contact Models

4.3.1 The Greenwood & Williamson model

Greenwood and Williamson have modeled the elastic contact of nominally flat and parallel surfaces, of which one is smooth and the other is rough. Adhesion is neglected in the model. The rough surface is covered by asperities, which at least near there summits, are spherical with a radius R. For two rough surfaces the composite $R = (1/R_1 + 1/R_2)^{-1}$ is used. The other parameters describing the surfaces are the elasticity of the materials, the asperity density h [m^{-2}] , and the spread s in the asperity summit levels. For two rough surfaces $h = h_1 + h_2$. The asperities have a summit level distribution $f(x)$ where $f(x)dx$ is the probability to find an asperity with a summit level between x and $x+dx$ above a reference plane in the rough surface (see fig. 4.1). The level of the smooth plane is d above the reference plane at $x = 0$, and d is called the separation.

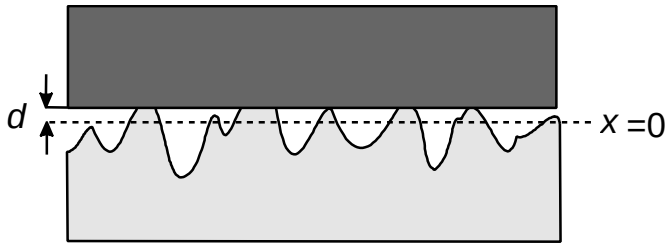

Figure 4.1: The separation d is defined as the level of the smooth plane with respect to the reference plane at $x = 0$.

For one asperity, the relation between the contact radius a, the indentation z and the compressive force P pressing the asperity to the flat surface is given by Hertz's equations [31, 32]:

$$a^2 = R \cdot z \tag{4.3a}$$

$$P = \frac{a^3}{R \cdot D} = \frac{R^{1/2} z^{3/2}}{D} \tag{4.3b}$$

Where D is the composite compliance of the two contacting materials, defined as:

$$D = \frac{3}{4} \cdot \left(\frac{1-n_1^2}{E_1} + \frac{1-n_2^2}{E_2}\right)$$

Where $E_{1,2}$ and $\nu_{1,2}$ are the Young's modulus and the Poisson ration of the two surfaces respectively.
The number of asperities in contact with the flat surface is given by the sum of the products of the asperity density, the apparent contact area A_a ,and the probability to find an asperity with a height x larger than the separation d:

$$N = hA_a \int_d^\infty f(x)dx \tag{4.4}$$

The total area of contact is given by the integral for x >d of the product of asperity density, apparent contact area, the asperity contact are $\pi R(x\text{-}d)$ and the probability to find an asperity with a height x :

$$A_r = hA_a Rp \int_d^\infty (x-d)\, f(x)dx \tag{4.5}$$

The total load L is given by the integral for $x > d$ of the product of asperity density, apparent contact area, the asperity contact force $R^{1/2}(x\text{-}d)^{3/2} / D$ and the probability to find an asperity with a height x :

$$L = \frac{hA_a R^{1/2}}{D} \int_d^\infty (x-d)^{3/2}\, f(x)dx \tag{4.6}$$

The asperity height distribution depends on the surface preparation prior to the contact. In engineering practice the summit level distribution is often close to Gaussian [17]. It is therefore assumed here that the distribution is Gaussian with a standard deviation s and centered around $x = 0$:

$$f(x) = \frac{1}{s\sqrt{2p}} \exp\left(-\frac{x^2}{2s^2}\right)$$

For two rough surfaces the composite standard deviation $s^2 = s_1^2 + s_2^2$ is applied. The asperity heights x and the separation d can be normalized according to $y = x / s$ and $h = d / s$. Furthermore eq. (4.4-4.6) can be made dimensionless, yielding:

$$N^* = \frac{N}{hA_a} = F_0(h) \tag{4.7a}$$

$$A^* = \frac{A_r}{hR\,sA_a} = pF_1(h) \tag{4.7b}$$

$$L^* = \frac{D \cdot L}{hA_a R^{1/2} s^{3/2}} = F_{3/2}(h) \tag{4.7c}$$

Where:

$$F_n(h) = \frac{1}{\sqrt{2p}} \int_h^\infty (y-h)^n e^{-\frac{y^2}{2}} ds \tag{4.8}$$

The dimensionless group $hR\,s$ in eq. (4.7b) has been shown to be in the range of 0.05 - 0.1 by Archard [33].The relation between N^*, L^* and A^* can not be made explicitly, because it is hard to solve for the separation h. However it is possible to plot for example A^* vs. L^* and N^* vs. L^* for a certain range of h. Similary, in fig. 4.2 we have plotted the normalized mean real contact contact pressure L^* / A^* vs. L^*.

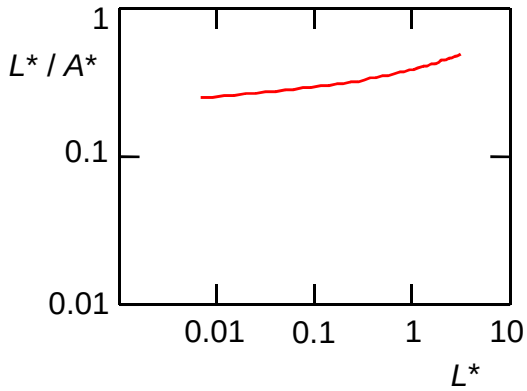

Figure 4.2: The normalized mean real contact pressure L^*/ A^* as a function of L^*, (h=-2 .. 2). The contact pressure varies less than a factor 2 over three decades of L^*.

Fig. 4.2 shows that the normalized contact pressure L^*/ A^* as a function of L^*, varies less than a factor 2 over three decades of L^*. The explanation for this is, that as the load is increased, the separation h decreases and new contacts are created. The number of contact points increases slightly less than linearly with the load. The average contact area per asperity

increases with a power slightly more than zero. The normalized contact pressure can be transformed into the mean elastic contact pressure L / A_r by using eq. (4.7b,c):

$$p_e = \sqrt{\frac{s}{R}} \cdot \frac{F_{3/2}(h)}{DpF_1(h)} \tag{4.9}$$

In section 4.3.4, p_e is used to analyze the effect of the surface topography on the friction coefficient.

4.3.2 Including the effect of adhesion

Johnson, Kendall and Roberts [34] modified the Hertz to include the effect of adhesion (JKR theory). The JKR theory assumes that the adhesion only acts in the region of direct contact. The contact stresses are different from the Hertzian stresses due to the adhesion forces: The stresses are tensile at the edge of the contact and compressive at the center. The deformation profile directly outside the contact region changes, so that the profile of the spheres meet the interface vertically in stead of horizontally. The adherence (pull-off) force equals $3/2\ \pi \cdot \Delta g R$ where Δg is the work of adhesion (per unit area) and R is composite radius of the spheres. Fuller and Tabor [35] implemented the single asperity JKR theory in the statistical contact model of Greenwood and Williamson [17], and showed that the adherence force of a multi asperity contact depends strongly on the surface roughness. Their theory was shown to be in accordance with measurements of the pull-off force of rubber spheres in contact with perspex. Deryaguin, Muller and Toporov [36] calculated the effect of adhesion in a contact of an elastic sphere to a rigid plane. They assumed that the adhesion forces act in the region around a Hertzian contact. The deformation profile remains Hertzian, as if the adhesion forces could not deform the surfaces. In the DMT model the adherence force decreases from $2\pi \cdot \Delta g R$ to $\pi \cdot \Delta g R$ as the approach increases. Maugis has shown that this is not correct: The adherence force equals $2\pi \cdot \Delta g R$ independent of the compression of the sphere to the plane [18]. This value is identical to the value calculated by Bradley for the contact of rigid spheres [37]. For both theories the influence of adhesion is accounted for in Δg and is not dependent on the exact form of the interaction potential [38]. The applicability of the DMT and JKR theory is determined by the value of a Tabor's elasticity parameter [39], which is a measure of the magnitude of the elastic deformation at the point of separation compared with the range of surface forces:

$$m = \left(\frac{R \cdot \Delta g^2}{E^{*2} z_0^3}\right)^{1/3}$$

Where z_0 is the equilibrium spacing in the Lenard-Jones interaction potential, and $E^* = E_1(1-\nu_1^2)\ //\ E_2(1-\nu_2^2)$ is the combined elasticity modulus. According to Johnson [40] the DMT model is valid for small values of m, $m < 0.1$, and the JKR model is valid for large values of m, $m > 5$. In between there is a continuous transition from the one model to the other, which has

been calculated by for example Maugis [41] using the Dugdale approximation. So the JKR is valid for soft materials with a large surface energy and a large asperity radius. The DMT theory is valid for hard solids with a low surface energy and a small asperity radius. Because the materials used in MEMS are often hard, we will concentrate on the DMT model from now on. The work of adhesion Δg takes into account the adhesion due to Van der Waals forces or due to hydrogen bonds. Other possible mechanisms for the adhesion are electrostatic forces and capillary forces. The effect of capillary forces will be discussed in section 4.3.3.
Following the DMT model the adhesion force of each contacting asperity is given by $2\pi \cdot \Delta g R$, independent of the indentation z. The distribution of stresses in the region of contact is Hertzian and their integral equals the sum of the adhesion force $2\pi \cdot \Delta g R$ and the applied load P. For each contacting asperity of which the tip is elastically displaced a distance z, the contact radius a and the load P are now given by:

$$a^2 = R \cdot z \tag{4.10a}$$

$$P + 2p \cdot \Delta g \cdot R = \frac{a^3}{R \cdot D} = \frac{R^{1/2} z^{3/2}}{D} \tag{4.10b}$$

Following the procedure of paragraph 4.3.1 the expression for the total load L compresssing the surfaces becomes [18]:

$$L = \frac{hA_a R^{1/2} s^{3/2}}{D} F_{3/2}(h) - hA_a 2p \cdot \Delta g \cdot R \cdot F_0(h) \tag{4.11}$$

The expressions (4.4, 4.5 and 4.7a,b) for the total area of real contact and the number of contacting asperities remain the same. Eq. (4.11) can be normalized according to:

$$L^* = \frac{D \cdot L}{hA_a R^{1/2} s^{3/2}} = F_{3/2}(h) - \frac{2p}{q} F_0(h) \tag{4.12}$$

The dimensionless group q is the adhesion parameter, as defined by Fuller and Tabor [35], it expresses the competition between the adhesion force between lower asperities trying to hold the surfaces together and the elastic force exerted by the higher asperities trying to separate the surfaces.

$$q = \frac{s^{3/2} R^{1/2}}{D \cdot \Delta g \cdot R} \tag{4.13}$$

The adhesive load is proportional to the number of contacting asperities. It is extremely sensitive to changes in the surface roughness. This can be shown by calculation of fraction of contacting asperities as a function of the adhesion parameter, using eq. (4.7a) and (4.12): For

$L^* = 0$ and q increasing from 1 to 30 the fraction of contacting asperities decreases from 1 to 0.001 (fig. 4.3). At the same time the relative real contact area A_r / A_a decreases from 1 to 0.0001, assuming $h \cdot R \cdot s = 0.1$ [21].

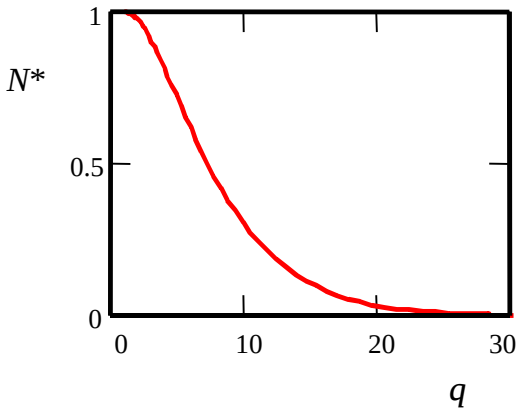

Figure 4.3: The fraction of asperities in contact as a function of the adhesion parameter, for $L^* = 0$.

Fig. 4.4 shows $A^*(h)$ vs. $L^*(h)$ for different values of q. This is the expected shape of the friction vs. load curves.

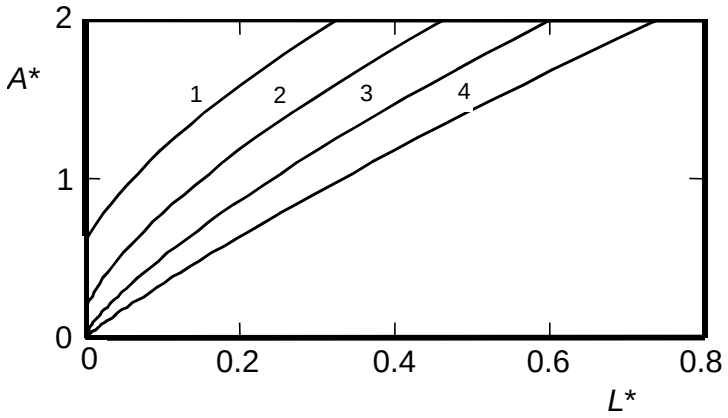

Figure 4.4: A^* vs. L^* for (1) $q = 10$, (2) $q = 15$, (3) $q = 30$ and (4) $q = \infty$.

Both the zero load contact area and the slope of the curves are a function of q. Fig. 4.4 shows that adhesion leads to a non-linear relation between A_r and L. Only in a limited range, the friction can be described with a first order relation:

$$F_f = m_{e,a}(F_a^0 + L) \qquad (4.14)$$

Where the adhesion is accounted for in both the zero load adhesion force F_a^0 and the friction coefficient $m_{e,a} = dF_f / dL$ for elastic adhesive contact. The friction coefficient accounts for the increase of the adhesive load with increasing L, which is caused by the fact that the number of contacting asperities increases with increasing L.

4.3.3 Effect of capillary forces

In chapter 3 it was already explained that capillary forces due to condensation of water around the points of contact of hydrophilic surfaces can be an important cause of adhesion of the two surfaces. The capillary force between a sphere and a plane is analyzed in this paragraph. Figure 4.5 shows the contact of a sphere with a radius of R with a flat surfaces. The contact angle a and the meniscus curvature determine the radius a and the thickness t of the water film.

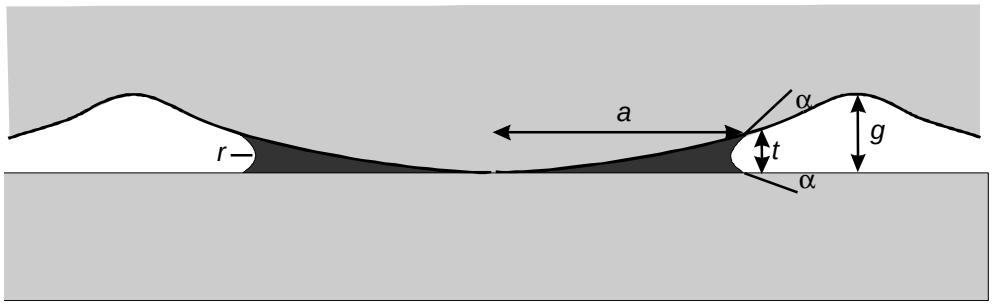

Figure 4.5: Condensed water in around a contact point of spherical asperity and a flat surface. The contact angle a and the meniscus curvature determine the radius a and the thickness t of the water film. g Is the peak valley height.

In equilibrium the curvature r of the meniscus equals the Kelvin radius (eq. 3.5). Figure 4.6 shows $-r_K$ as a function of the relative water vapour pressure p / p_s.

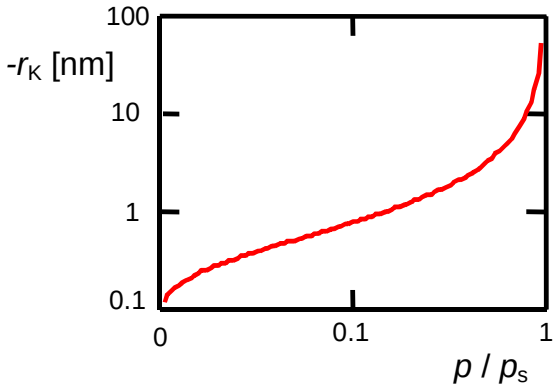

Figure 4.6: Minus the Kelvin radius as a function of the relative humidity at room temperature.

The pressure difference across the liquid-air interface is the Laplace pressure (eq. 3.1): $p_{la} = \gamma_a / r_K$. ,where γ_a is the surface tension of water. It acts on a surface $\pi a^2 = 2\pi R \cdot t$ ($t << R$). For $a << R$ the film tickness t equals $-2 \cdot r_K \cos a$ and therefore (in equilibrium) the capillary force pulling the surfaces together equals [42]:

$$F_{cap} = 4\pi R \gamma_a \cos a \qquad (4.15)$$

The capillary force in eq. (4.15) is independent of the relative humidity of the air. As long as $t < g$, liquid bridge of neighboring asperities do not touch and eq. (4.15) applies. This is the toe dipping regime [29].The total adhesion force is proportional to the number of contacting asperities, and the adhesion force per asperity $2\pi\cdot\Delta\, gR$ in eq. (4.11) can be replaced by F_{cap} (eq.(4.15)). If the thickness t increases to g , the water bridges of neighboring asperities merge and the interface can be flooded with water. Thus, for zero contact angle, the condition for the toe-dipping regime is $-2r_K < g$. In the flooded regime the total adhesion force in eq. (4.11) should be replaced $A_a \cdot p_{la}$.

4.3.4 Transition from Elastic to Plastic Contact

The model that is described so far is based on elastic deformation in the contact points. Plastic deformation becomes important when the maximum of the Hertzian pressure approaches H, with $H = H_1 \,//\, H_2$ the hardness of the contacting materials [17]. The maximum pressure q_0 in the Hertzian contact is given by:

$$z = \frac{4}{9} p^2 q_0^2 D^2 R \qquad (4.16)$$

Where z is the indentation. For the Gaussian distribution model, the conditions for plastic or elastic contact can be represented in a dimensionless group, the plasticity index [17]. Significant plastic deformation develops if the mean real elastic contact pressure as defined in eq. (4.9) is larger than a certain fraction of the hardness [17]: $p_e > 0.24\ H$. This condition applies for both adhesive and non-adhesive contacts. As p_e rises beyond $0.24\ H$, with increasing $\sqrt{s\,/\,R}$, the mean real contact pressure approaches H. For the friction coefficient this means that for $p_e < 0.24H$ the friction coefficient equals $s\,/\,p_e$, which is at least four times larger than the lower limit $m_p = s\,/\,H$. For $p_e > 0.24\ H$ the friction coefficient tends to this lower limit. For many materials s is of order $0.2\ H$ and the friction coefficient $m_p = 0.2$ [25].

4.3.5 Low Loading Conditions

For small loads the statistical model (eq. 4.7a) can predict a number of contact points smaller than one. This results in an underestimate of the adhesive load. The number of contact points has to be at least 1, 2, or 3 depending on the degrees of freedom of the contacting surfaces. Adapting eq. (4.10a,b) for N equally loaded contact points and application of eq. (4.1) yields:

$$F_f(L) = s \cdot A_r(L) = s \cdot N \cdot pR \cdot [\frac{1}{N}\frac{D}{R^{1/2}} \cdot (L + N \cdot 2p \cdot \Delta\, g \cdot R)]^{2/3} \quad (N = 1,2,3)$$

(4.17)

4.4 MEMS Friction Experiment

In order to test the clamps of a polysilicon stepper motor [22], a friction meter, similar to [38], has been fabricated. The friction as a function of the applied load has been measured. We have analyzed this experiment using the presented friction theory.

Friction is measured by pushing the shoe against the wall with a defined electrostatic force, and measuring the electrostatic pull force at the onset of slip (fig. 4.7). The contact material was polysilicon, covered with a thin layer of native oxide. Gap-closing actuator arrays have been used, because the moment of slip can easily be determined, as these actuators show pull-in. The measurements have been done using a clamp actuator with 30 plates, and a pull actuator with 15 plates, each plate having an active area of 100 x 5 μm^2. The total load consists of the clamp force L plus the interfacial adhesive load. The measurements have been carried out under the condition $L > 0$, as the clamp voltage is chosen above the level that is necessary to make initial contact. Fig. 4.8 shows the measured pull-voltage squared as a function of the applied clamp voltages squared. Pull and clamp voltages have been chosen large enough to obtain pull-in of the pull actuator, directly from the initial position. The measurements indicate that there is a close to linear relation between the load L and the F_f, and therefore eq. (4.14) can be used. The clamp force L consists of the generated electrostatic clamp force minus the elastic deformation force of the clamp actuator suspension and the drive beam connected to the pull actuator:

$L = F_{elec} - F_{spring}$. The elastic force F_{spring} equals 7 ± 2 μN, calculated from the stiffness of the suspension and the pull connection beam, times the initial gap between the shoe and the rigid wall.

a) 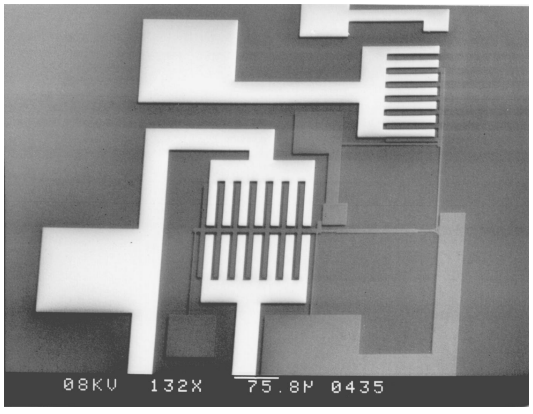

b) 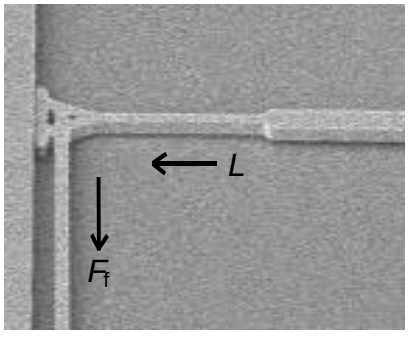

Figure 4.7a) The friction meter. It consists of an actuator array that lamps a shoe against a rigid wall, and an actuator array pulling the shoe along the wall. Friction is determined by measuring the pull force at the onset of slip of the shoe along the wall. The stator poles of the pull and clamp actuator are white due to charging in the SEM. b) Close-up of the clamp shoe pushed against the rigid side-wall. The height of the shoe is 5 μm, the width is 20 μm.

The friction force and the applied load can be obtained by $F_{pull} = a_{pull} \cdot V^2_{pull}$ and $F_{elec} = a_{clamp} \cdot V^2_{clamp}$, where a_{pull} and a_{clamp} are the conversion factors from actuator voltage to force [N/V^2] depending on the actuator geometry. Due to uncertainties in the gap sizes of the actuator there is a significant uncertainty in the conversion factors: $a_{clamp} = (1.4 \pm 0.5) \times 10^{-8}$ N/V^2 and $a_{pull} = (3.8 \pm 0.8) \times 10^{-9}$ N/V^2. Using the conversion factors and subtraction of F_{spring}, the voltages have been converted into forces. Represented in the form of eq. (4.14) it follows for the measured relation that $m_{e,a} = 0.7 \pm 0.3$ and $F_a^0 = F_f\,(L=0) / m_{e,a} = 2.0 \pm 1.3$ μN. The exact calculation can be found in appendix G. The expression for the measured friction is:

$$F_f = (0.7 \pm 0.3) \cdot (2.0 \pm 1.3\mu N + L) \qquad (L > 0) \qquad (4.18)$$

Next, have tried to calculate the friction vs. load using the elastic adhesive contact model. Surface topography parameters have been derived from a top view of a side-wall in the friction tester (fig.4.9). One should realize that the side-walls are not nominally flat, and that top view SEM photo from which the roughness has been measured may not be completely representative for the whole side-wall. Also possible small asperities (lateral size < 0.1 μm) on top of the larger asperities have been cancelled due to the limited resolution of the roughness measurement. Therefore, the model calculations for this experiment should be considered as an estimate.

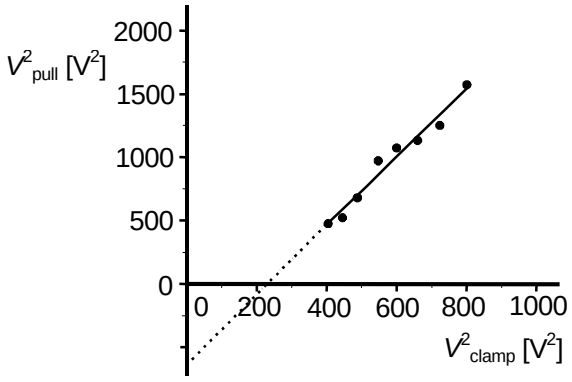

Figure 4.8: The measured pull voltages squared at the onset of slip, as a function of the applied clamp voltage squared. The measurements have been carried out at a relative humidity of the air of 35±5%.

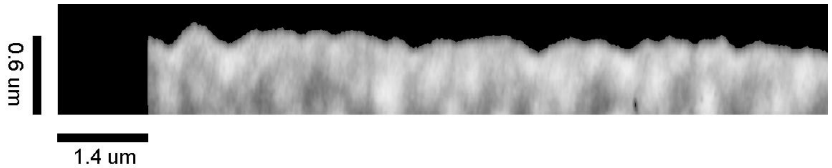

Figure 4.9: SEM photograph (top view) of the roughness of a side-wall in the friction meter.

The measured parameters (table 4.1) yield an adhesion parameter $q = 1 \times 10^4$. Using eq. (4.7a, 4.8, 4.12) the zero load number of contact points can be calculated. It is negligible small,

which indicates that the statistical model is not valid, and the discrete contact model has to be used. In order to fix the rotational degrees of freedom, three contact points are needed. Assuming $N = 3$ in eq. (4.17), a good correspondence between measured friction ($L > 0$) and calculated friction vs. load is found.

Asperity Density	h	4×10^{12} m^{-2}
Asperity Radius	R	0.5 ± 0.3 µm
Work of Adhesion	Δg	0.1 J·m^{-2}
SD Summit Level	s	0.04 µm
Compliance	D	9.1×10^{-12} Pa^{-1}
Apparent contact area	A_a	100 µm^2

Table 4.1: Parameters of the contacting surfaces. The radius R, the summit level standard deviation σ and the compliance D account for both surfaces. The value of Δγ is known from wafer bonding with hydrophilic surfaces [38].

The shear strength was used as (the only) fit parameter, in order to fit the calculated slope in $L = 3$ µN with the measured $m_{e,a} = 0.7$. This leads to a value $s = 1.4$ GPa. With this value an apparent zero load adhesion force $F_a^0 = s \cdot A_r(L = 0) / m_{e,a} = 2.3$ µN is found (fig. 4.10). The calculated F_a^0 is in good correspondence with the measured value. The strong non-linearity of the curve for $L < 0$ explains why the apparent zero load adhesion force F_a^0 is larger than the real calculated adhesion force $F_a = 6\pi \cdot \Delta g R = 0.9$ µN: For spherical asperities and small total loads ($L + F_a$), dA_r / dL is large and the friction force rises rapidly with increasing L, with a slope larger than $m_{e,a}$. With the help of eq. (4.16) and assuming a hardness of 9 GPa for polysilicon, it was confirmed that the deformations in the contact are indeed elastic.

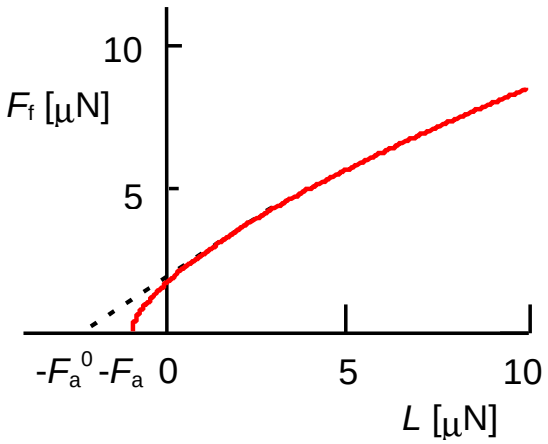

Figure 4.10: F_f as a function of L in the discrete model with 3 contact points, for $R = 0.5$ µm and $s = 1.4$ GPa. The shear strength has been fit to obtain $m_{e,a} = 0.7$ for $L > 0$. The relation between F_f and L yields a good fit with the measured $F_a^0 = 2.0 \pm 1.3$ µN.

4.5 Conclusions

According to the presented friction models the following conclusions can de drawn for shearing mode static friction: For zero adhesive load, the friction force as a function of the load is given by Amontons' Law. For plastic contact the friction coefficient is given by s / H and for elastic contact by s / p_e. For elastic contact, the mean real contact pressure depends on the surface topography: It increases proportional to s / R until the p_e is so large that plastic deformation starts. The friction coefficient decreases with increasing s / R. The lower limit is given by the friction coefficient for plastic contact s / H. The adhesive load increases with the number of contacting asperities, and therefore it depends on the applied (external) load. In the statistical model the influence of adhesion can be accounted for by a single dimensionless number, the adhesion parameter. For low loading conditions the statistical models can predict an unrealistic low number of contact points and underestimate the adhesive load. In these cases 1, 2 or 3 should be taken for the number of contact points, depending on the degrees of freedom of the contacting members. A MEMS friction experiment has been analyzed in order to relate the measured friction with surface topography, adhesion energy and elastic properties. The experiment illustrates the need for special attention to low loading conditions, which can be encountered in MEMS. Future work should concentrate on experimental verification of the presented models. How to relate the idealized roughness representation to the real roughness will be a primary issue. Furthermore, the conditions in which eq. (4.1) is valid should be determined.

4.6 Acknowledgment

The authors would like to thank Bart Vogelzang (formerly with the Tribology Group UT) for his help with the development of the friction models, and Tonny Sonnenberg for his help with the friction measurements. We thank Henri Jansen (formerly with Micromechanical Transducers Group, UT) and Hans Moes, Wytze ten Napel (Tribology Group, UT) for valuable discussions.

4.7 Literature

1. Tai Y-C, Muller R.S.,"Frictional study of IC-processed motors", Sensors and Actuators, A21-23, 1990,.180-183.
2. Mehregany M., Nagarkar P., Senturia S.D., Lang J.H.,"Operation of microfabricated harmonic and ordinary side-drive motors", Proc. IEEE Workshop on MEMS, Napa Valley, CA, Feb. 1990, pp. 1-8.
3. Lim M.G., Chang J.C., Schultz D.P., Howe R.T., White R.M.,"Polysilicon microstructures to characterize static friction", Proc. IEEE Workshop on MEMS, Napa Valley, CA, Feb. 1990, pp. 82-88.
4. Gabriel K.J., Behi F., Mahadevan R.,"In situ friction and wear measurenemts in integrated polysilicon mechanisms",Sensors and Actuators, A21-23, 1990, pp. 184-188.

5. Mehregany M.,"Friction and wear in microfabricated harmonic side-drive motors", Techn. Digest of the IEEE Solid-state Sensors and Actuators Workshop, Hilton Head Island, South Carolina, June 1990, pp. 17-22.
6. Suzuki S., Matsuura, Uchizawa M., Yura S., Shibata H.,"Friction and wear studies on lubricants and materials applicable to MEMS", Proc. IEEE Workshop on MEMS, Nara, Japan, Jan. 30 Feb. 2 1991, pp. 143-147.
7. Kaneko R.,"Microtribology related to MEMS", Proc. IEEE Workshop on MEMS, Nara, Japan, Jan. 30 - Feb.2 1991, pp. 1-8.
8. Noguchi K., Fujita H., Suzuki M.,"The measurement of friction on micromechatronic elements", Proc. IEEE Workshop on MEMS, Nara, Japan, Jan. 30 - Feb.2 1991, pp. 148-153.
9. Mehregany M., Tai Y-C,"Surface micromachined mechanisms and micromotors", J. Micromech. Microeng., vol. 1, 1991, pp. 73-85.
10. Deng K., Ko W.H.,"A study of static friction between silicon and silicon compounds", J. Micromech. Microeng., vol.2, 1992, pp.14-20.
11. Mehregany M., Senturia S.D., Lang J.L., Nagarkar P.,"Micromotor fabrication", IEEE Trans. on Electron Dev., vol. 39, no. 9, Sept. 1992, pp. 2060-2069.
12. Huang J.-B., Mao P.-S, Tong Q.-Y. and R.-Q. Zhang,"Study on Si electrostatic electroquasistatic micromotors", Sensors and Actuators *A*, vol. 35, 1993, pp. 171-174.
13. Garcia E.J., Sniegowski J.J.,"Surface micromachined microengine", Sensors and Actuators *A*,Vol. 48, 1995, pp. 203-214.
14. Yeh R., Kruglick E.J.J., Pister K.S.J.,"Microelectromechanical components for articulated microrobots", The 8th Int. Conf. on Solid-State Sensors and Actuators, and Eurosensors IX, Stockholm, Sweden, June 25-29, 1995, pp. 346-349.
15. Beerschwinger U., Reuben R.L., Yang S.J.,"Frictional study of micromotor bearings", Sensors and Actuators *A*, vol. 63, 1997, pp. 229-241.
16. Komvopoulos K.,"Surface engineering and microtribology for microelectromechanical systems", Wear, Vol. 200, 1996, pp. 305-327.
17. Greenwood J.A., Williamson J.B.P.,"Contact of nominally flat surfaces", Proc. R. Soc. Lond. A, Vol. 295, 1966, pp. 300-319.
18. Maugis D.,"On the contact and adhesion of rough surfaces", J. Adhesion Sci. Technol., vol. 10, no.2, 1996, pp. 161-175.
19. Majumdar A., Bhushan B., in:"Handbook of micro-and nano tribology" ed. Bhushan B., CRC Press, New York, 1995.
20. Alley R.L., Mai P., Komvopoulos, Howe R.T.,"Surface roughness modifications of interfacial contacts in polysilicon microstructures", Proc. 7th Int. Conf. on Solid-State Sensors and Actuators, Yokohama,Japan, June 7-10, 1993, 288-291.
21. Gui C., Elwenspoek M., Tas N., Gardeniers J.G.E.,"The effect of surface roughness on direct wafer bonding", J. Appl. Phys., Vol. 85, issue 10, 1999, pp. 7448-7454.
22. Tas N.R., Sonnenberg A.H., Sander A.F.M. and Elwenspoek M.,"Surface micromachined linear electrostatic stepper motor", Proc. IEEE Workshop on MEMS, Nagoya, Japan, Januari 26-30, 1997, 215-220.
23. Bowden F.P., Tabor D.,"The friction and lubrication of solids", Oxford Clarendon Press, 1950.
24. Amuzu J.K.A., Briscoe B.J., Chaudhri M.M.,"Frictional properties of explosives", J. Phys. D: Appl. Phys., Vol. 9, 1976, pp. 133-143.
25. Tabor D.,"Friction-The present state of our understanding", J. Lubrication Techn., vol. 103, 1981, pp.169-179.
26. Clechet P., Martelet C., Belin M., Zarrad H., Jaffrezic-Renault N., Fayeulle S.,"Lubrication of silicon micromechanisms by chemical grafting of long-chain molecules", Sensors and Actuators *A*, vol. 44, 1994, pp. 77-81.
27. Zarrad H., Chovelon J.M., Clechet P., Jaffrezic-Renault N., Martelet C., Belin M., Perez H., Chevalier Y.,"Optimization of lubricants for silica micromotors", Senors and Actuators *A*, vol. 46-47, 1995, pp. 598-600.

28. Deng, K., Collins R.J., Mehregany M., Sukenik C.N.,"Performance impact of monolayer coating of polysilicon micromotors", J. Electrochem. Soc., vol. 142, no.4, April 1995, pp. 1278-1285.
29. Bhushan B.," Nanotribology and nanomechanics of mems devices",Proc. IEEE Workshop on MEMS, SanDiego, CA, Feb. 14-15, pp. 349-353.
30. Srinivasan U., Foster J.D., Habib U., Howe R.T., Maboudian R., Cowell Senft D., Dugger M.T.,"Lubrication of polysilicon micromechanisms with self-assembled monolayers", Techn. Digest of the Solid-State Sensors and Actuator Workshop, Hilton Head Island, South Carolina, Jun. 8-11, 1998, pp. 165-161.
31. Landau L.D., Lifschitz E.M.," Elastizitaetstheorie", Akademie Verlag, Berlin, 1975.
32. Timoshenko S.P., Goodier J.N.,"Theorie of Elasticity", McGraw-Hill, New York 1970.
33. Archard," Surface topography and tribology", Tribology Int., Oct. 1974, pp. 213-220.
34. Johnson K.L., Kendall K., Roberts A.D.," Surface energy and the contact of elastic solids", Proc. R. Soc. Lond. A, Vol. 324, 1971, pp. 301-313.
35. Fuller K.N.G., Tabor D.,"The effect of surface roughness on the adhesion of elastic solids", Proc. R. Soc. Lond. A., vol. 345, 1975, pp.327-342.
36. Derjaguin B.V., Muller V.M., Toporov Yu. P.," Effect of contact deformations on the adhesion of particles", J. Colloid Interface Sci., Vol. 53, no.2, Nov. 1975, pp. 314-326.
37. BradleyR.S.,"The cohesive force between solid surfaces and the surface energy of solids", London, Edinburgh and Dublin Phil. Mag. J., vol. 13, 1932, pp. 853-862.
38. Muller V.M., Yuschenko V.S., Derjaguin B.V.," General theoretical consideration of the influence of surface forces on the contact deformations and the reciprocal adhesion of elastic spherical particles", J. Colloid Interface Sci., Vol. 92, no.1, 1983, pp.92-101.
39. Tabor D.," Surface forces and surface interactions", J. Colloid Interface Sci., Vol. 58, no.1, 1977, pp.2-13.
40. Johnson K.L.," A continuum mechanics model of adhesion and friction in a single asperity contact", ed. Bhushan B., NATO ASI series vol. 330, Kluwer, The Netherlands, 1997, pp. 151-168.
41. Maugis D.," Adhesion of spheres: The JKR-DMT transition using a Dugdale model", J. Colloid Interface Sci., Vol. 150, no.1, 1992, pp. 243-269.
42. Israelachvili J.N.,"Intermolecular and surface forces", 2nd edition, Academic Press London, 1991.
43. Prasad R., MacDonald, N., Taylor D.," Micro-instrumentation for tribological measurement", 8th Int. Conf. Solid-State Sensors and Actuators, Transducers'95 and Eurosensors IX, Stockholm Sweden, June 25-29, 1995.
44. Stengl R., Tan T., Gosele U.," A model for the silicon wafer bonding process", Jap. J. of App. Phys., Vol. 28, no. 10, 1989, pp. 1735-1741.

5

Laterally driven walking motors

Three different laterally driven motors have been developed and tested. The first design (concept *A*) uses drive beams which attach to the shuttle, and generate motion by contraction of the drive beams due to bending. Electrostatic forces are generated by applying a voltage difference between the drive beams and the shuttle. The experiments show that it is hard to generate a high enough clamping force. The second design therefore uses separated clamp and propulsion actuators, which yields more freedom in the generation of clamp and propulsion forces. Using this design static friction in the clamps as a function of the clamp force has been measured. The experiment shows that there is friction with zero applied clamp force. This is caused by adhesion, which has to be added to the externally applied load. The adhesion in is the order of 1 μN, small enough to be overcome by the switchable electrostatic forces in the clamp actuators. Walking motion has been successfully generated with this design. The third design (concept *C*) is based on the second. The difference is that it has been tried to include levers to increase the propulsion force. The most difficult issue in this concept is how to increase the clamp force, and still be able to close the initial 1-2 μm gap between the clamp shoe and the shuttle. Three different solutions have been proposed for the clamping. The one which has been implemented uses a voltage difference between the clamp shoe and the shuttle (across the side-wall insulator layers) to generate the clamp force. It turned out that this force becomes smaller than required, due to an effective air gap caused by side-wall roughness which remains during clamping. Walking experiments with this concept have failed, due to the fact that the impact of the incoming second clamp disturbs the clamping of the first, and the first step made is lost. A strategy is developed to improve concept *C*.

5.1. Introduction

We define mechanisms which only have parts moving parallel to the wafer surface as *laterally driven*. The advantage of such mechanisms can be the simple fabrication process. The most simple laterally driven devices can be made using only one mask step. In this section three designs of laterally driven linear electrostatic micromotors are treated. The first design (*A*) is based on integration of the clamp force and the step generating actuation in one actuator. In the second (*B*) and third design (*C*) the clamp force and step motion are generated in separate actuators, in order to obtain a better control on the motions. These designs employ the walking cycle of fig. 1.11. Design *B* is meant to test if walking motion is feasible in our most simple single mask surface micromachining fabrication process. The focus is at possible stiction in the clamps (section 5.3). Design *C* is an effort to enlarge the generated forces by employing mechanical levers. Different concepts for clamp force and step motion generation are discussed (section 5.4).

Section 5.3 is based on: N.R.Tas, A.H. Sonnenberg, A.F.M. Sander, and M. Elwenspoek,"Surface Micromachined Linear Electrostatic Stepper Motor", Proc. IEEE Workshop on Micro Electro Mechanical Systems 1997, Nagoya, Japan, Jan. 26-30 1997, pp. 216-220.

As far as we know only two other groups have presented experiments with a laterally driven surface micromachined electrostatic walking motor [1,2]. Both designs are similar to concept *B*, and will therefore be compared with our design.

5.2 Concept *A*: Walking motor with combined clamp and pull actuator

5.2.1 Principle of Operation

Walking motion in this concept is generated by drive units (see fig. 5.2), each consisting of two drive beams. Figure 5.1 shows the step generation by one drive unit. As the attachment length of the beams to the shuttle increases, the tips of the beams move to the left. With sufficient friction the shuttle will follow to the left.

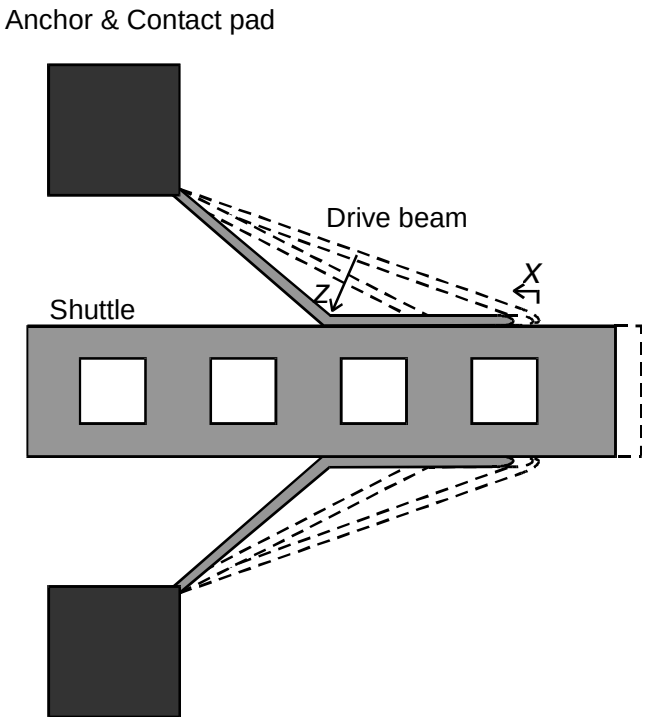

Figure 5.1: A drive-unit consists of two anchored drive beams. Part of the shuttle is shown as well. The lighter gray parts are moveable, the darker gray parts are anchored. Generation of a step is indicated. As the clamp voltage is increased the attached length increases and, assuming a fixed length of the drive beam, the tip displaces to the left.

Figure 5.2 shows the walking cycle of motor concept *A*. (fig. 5.2a) Initially both drive-units are inactive. (fig. 5.2b) First drive-unit 1 is activated. Its drive beams are clamped onto the shuttle and the shuttle is pulled to the left due to the contraction of the beams, induced by the bending of the beams. (Fig. 5.2c) Drive unit 2 is activated. Initially its beams will slip along the shuttle, until the clamp area is large enough to have enough static friction in the attached region to stop the slip of the tips of the beams. Here it is assumed that the position of the shuttle is fixed by drive-unit 1. This will be true for drive beams with high enough bending

stiffness. The apparent *x*-stiffness due the attached beams will much larger than this *z*-bending stiffness (see fig. 5.2), provided that there is a large transformation ratio d*z* / d*x*. After releasing drive unit 1 the attachment length of the beams of drive-unit 2 can increase, and the shuttle is moved to the left (fig. 5.2d). Now the cycle continues in (fig. 5.2b), however with the role of drive-units 1 and 2 interchanged.

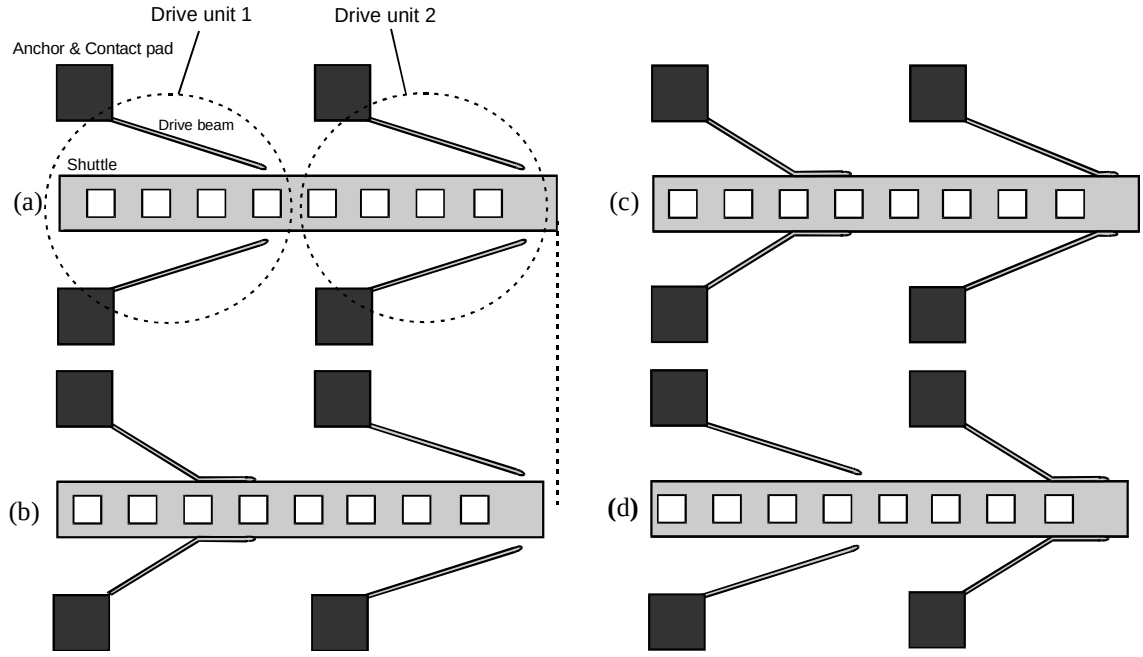

Figure 5.2: Walking cycle of motor concept *A*. The shuttle is driven by two drive units, in total containing four drive beams. The shuttle is guided linearly by an elastic suspension (not shown in the figure). (a) Initially both drive-units are inactive. (b) First drive-unit 1 is activated. Its drive beams are clamped onto the shuttle and the shuttle is pulled to the left due to the contraction of the beams, induced by the bending of the beams. (c) Drive unit 2 is activated. Initially its beams will slip along the shuttle, until the clamp area is large enough to have enough static friction in the attached region to stop the slip of the tips of the beams. Here it is assumed that the position of the shuttle is fixed by drive-unit 1. (d) After releasing drive unit 1 the attachment length of the beams of drive-unit 2 can increase, and the shuttle is moved to the left. Now the cycle continues in (b), however with the role of drive-units 1 and 2 interchanged.

5.2.2 Model of the electromechanical energy conversion

A simple expression for the generated force can be found from an energy model of the transducer. This model only contains the electrical energy stored in the gap, the mechanical deformation energy is neglected. Fig. 5.3 shows the definitions of variables.

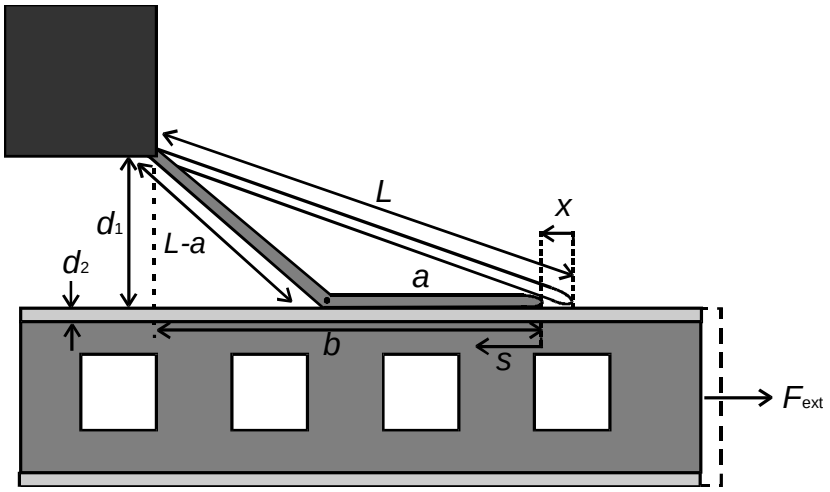

Figure 5.3: Definitions of model variables. L is the length of the drive beam, a is the attached length, L - a is the unattached length, d_1 is the size of the air gap between the fixed end of the drive beam and the side-wall of the slider, d_2 is the thickness of the silicon nitride insulator (for the electrical model the silicon nitride on the drive beam is virtually transferred to the shuttle), b is the projected length of the beam onto the side-wall of the slider, s is the position along the shuttle edge starting at the tip of the beam, x is the displacement of the beam tip by contraction, and F_{ext} is the external force exerted on the shuttle to maintain balance

Figure 5.3 shows the definitions of the variables in the energy model. L is the length of the drive beam, a is the attached length, L - a is the unattached length, d_1 is the size of the air gap between the fixed end of the drive beam and the side-wall of the slider, d_2 is the thickness of the silicon nitride insulator, b projected length of the beam onto the side-wall of the slider, s is the position along the shuttle edge starting at the tip of the beam, x is the displacement of the beam tip by contraction, and F_{ext} is the external balance force exerted on the shuttle. For reasons of simplicity the insulator of both the beam and the side-wall have been added into one layer. The force F_{ext} under voltage control can be calculated from the derivative of the Legendre transformed energy function $W'(x, U)$. In the model only the electrical energy is accounted for, and the expression for the force becomes:

$$F_{ext} = -\frac{\partial W'(x,U)}{\partial x} = \frac{\partial}{\partial x}[\frac{1}{2}C(a(x))\cdot U^2] = \frac{\partial}{\partial a}[\frac{1}{2}C(a(x))\cdot U^2]\frac{\mathrm{d}a}{\mathrm{d}x} \qquad (5.1)$$

Where the minus sign applies because the force is pointing towards $-x$. The justification of neglecting the mechanical deformation energy will be discussed later.The capacity $C(a)$ of the gap between the beam and the shuttle is calculated by assuming a small ratio d_1 / (b - a). This implies that the capacitance between the oblique part of the beam and the shuttle can be calculated by integration with respect to s of infinitesimal parallel plate elements with an area t·ds, with t the thickness of the polysilicon (in the direction perpendicular to the paper). In appendix H the calculations for the energy model can be found. It results in an expression for the drive beam contraction (eq. H.3) and for the generated force (eq. H.5). Fig. 5.4b shows the produced force of a drive unit $F_{drive}= 2F_{ext}$, and fig. 5.4a the produced drive beam contraction

x as a function of the attachment length a, for a driving voltage U = 10 V, L = 400 µm, d_1 = 10 µm, d_2 = 0.3 µm, t = 5 µm, e_1 = 8.85 x 10^{-12} F/m and $e_2 = 7.5e_1$ (silicon nitride).

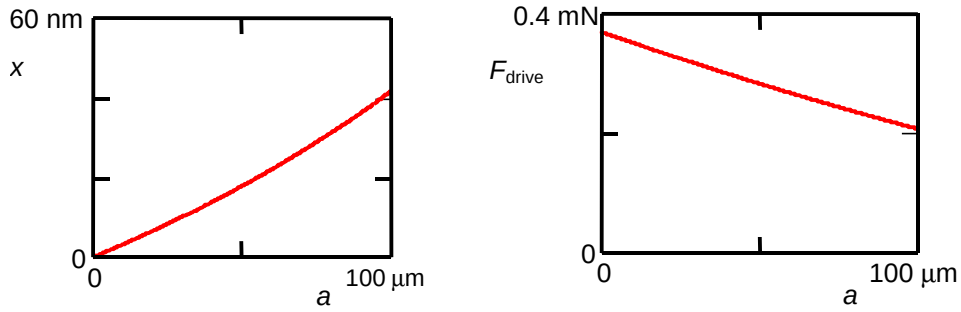

(a) (b)

Figure 5.4: (a) Contraction of the drive beams as a function of the attachment length. (b) Force F_{drive} produced by a drive unit as a function of the attachment length. The parameters used are: U = 10 V, L = 400 µm, d_1 = 10 µm, d_2 = 0.3 µm, t = 5 µm, e_1 = 8.85 x 10^{-12} F/m and $e_2 = 7.5e_1$.

For a = 100 µm the generated force is large enough (> 0.1 mN). Also the contraction (± 40 nm) is in the right range. The displacement of the shuttle will be smaller than the contraction x of the drive beam , because of initial slip due to insufficient clamping near a = 0. The clamp force can easily be estimated by assuming that electrostatic forces only act in the attached region. Under this assumption the clamp force increases linearly with the attachment length. The clamp force of two drive beams is given by:

$$F_c = \frac{U^2 \cdot a \cdot t}{e_3 \cdot (\frac{d_3}{e_3} + \frac{d_2}{e_2})^2} \qquad (5.2)$$

Where d_3 is the effective air gap thickness in the attachment region, for example due to roughness, and e_3 is the permittivity in the gap. Here we have neglected the bending stiffness of the beams. The maximum clamp force is found for d_3 = 0 and is given by:

$$F_{c\text{-}max} = \frac{e_2^2 \cdot U^2 \cdot a \cdot t}{e_3 \cdot d_2^2} \qquad (5.3)$$

For d_3 = 0, d_2 = 0.3 µm, t = 5 µm, e_3 = 8.85 x 10^{-12} F/m and $e_2 = 7.5e_3$ (silicon nitride), and at a = 100 µm, the clamp force of two drive beams equals 1.3 mN at U = 20 V applied. The clamp force is extremely sensitive for a possible small air gap in the attached region. This is illustrated in fig. 5.5 where the normalized clamp force $F_r = F_c / F_{c\text{-}max}$ is plotted as a function of the relative air gap thickness $d_r = d_3 \cdot e_2 / d_2 \cdot e_3$. The graph shows that at $d_3 = d_2 \cdot e_3 / e_2$ the clamp force is lowered 4 times compared to the maximum. For 0.3 µm silicon nitride as the dielectric material, d_r = 1 corresponds with d_3 = 0.04 µm. This calculation indicates that

roughness will also lower the produced contraction force, as $\partial C(a) / \partial a$ in eq. (5.1) drops with increasing air gap thickness in the clamp region.

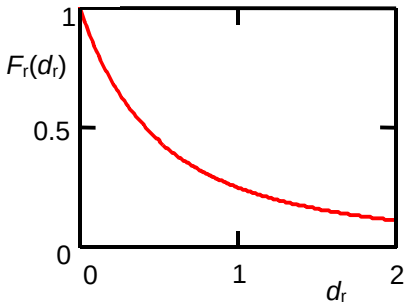

Figure 5.5: Normalized clamp force $F_r = F_c / F_{c\text{-}max}$ as a function of the normalized air gap thickness $d_r = d_3 \cdot e_2 / d_2 \cdot e_3$.

5.2.3 Lateral pull-in vs. pull-down

For proper operation of the motor, the drive beams should be pulled towards the shuttle and not downwards to the substrate. We have therefore calculated the lateral pull-in voltage as well as the pull-down voltage. The calculations follow the procedure of section 3.5.1, and are presented in appendix I. In section 5.2.5 the values for the realized motors are presented and compared with the measured values.

5.2.4 Fabrication

Fabrication starts with growing a 2.3 μm thick thermal oxide, which serves as the sacrificial layer. Next, 5.3 μm thick polysilicon layer is deposited by LPCVD. The polysilicon is made conductive by dotation with Boron, deposited from a solid source, and indiffused by a 1 hour heat cycle at 1100 °C. After stripping the B_2O_5 from the surface, the 1.2 μm thick silicon oxide etch mask for the RIE of the polysilicon is deposited by PECVD. Next a 3 hours post-anneal is done to obtain a uniform distribution of the Boron. After patterning the oxide mask by photolithography and RIE, the polysilicon is anisotropically etched in RIE using a SF6/CHF3/O2 plasma. In the next step the silicon oxide etch mask is removed by RIE, and the sacrificial oxide is etched in 50% HF for 4½ minutes to obtain a small gulley underneath the polysilicon structures for the robust side-wall spacers to be formed. A 160 nm thick silicon nitride layer is deposited by a LPCVD process which is optimized for low stress. The silicon nitride is removed from the top of the polysilicon structures and the exposed surface of the sacrificial oxide. Only at the side-walls and underneath the structures silicon nitride remains. Finally, the structures are released by sacrificial layer etching in 50% HF. After rinsing with IPA and cyclohexane the structure is dried by means of freeze drying of the cyclohexane [3]. The detailed processing sequence is listed in appendix D. The fabrication process has been based on a process developed by Legtenberg et al. [4]. Compared to [4], steps have been added to create the silicon nitride layer at the side-walls, to serve as insulator and/or side-wall spacer (steps 25,26, and 27 in appendix D). Also the post-anneal (step 17 in appendix D) has

been added in order to obtain uniform distribution of the Boron in the polysilicon, which is necessary to avoid stress gradients.

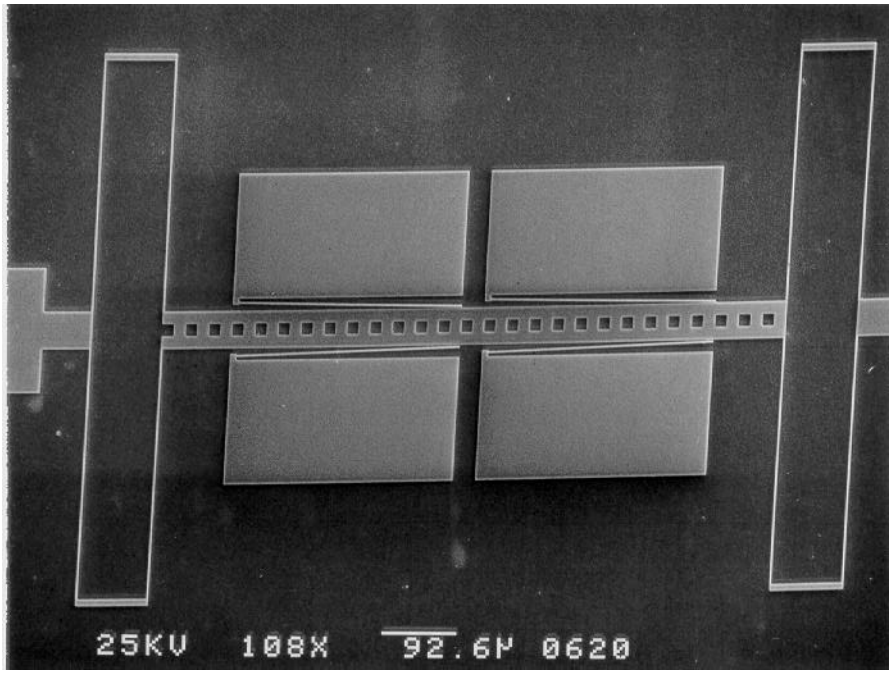

Figure 5.6: SEM picture of the fabricated motor. The length of the drive beams is 400 µm.

5.2.5 Experiments

Tests have been done on the motor shown in fig. 5.6. For this motor the length L of the drive beams is 400 µm, on the mask d_1 = 10 µm, g = 2 µm. Due to the photolithographic process the width of the drive beams has become 2.2 µm, so w_1 = 1.1 µm. Due to the deposition of $2w_2$ = 0.3 µm silicon nitride, the resulting g = 1.5 µm and d_1 = 9.5 µm.

Lateral pull-in

From the lateral pull-in analysis (appendix I) it follows that with the mentioned parameters c = 4.44 and $v_{pi}(L)$ = 8.57 µm. In the inactive state $v(L)$ = 8 µm therefore it can be concluded that the pull-in deflection $y_{PI}(L)$ = 0.57 µm = 0.48 g. Using eq. (I.5) the predicted pull-in voltage is 4.8 V (E_1 = 150 Gpa, E_2 = 330 GPa). The measured lateral pull-in voltage equals 6.8 ± 0.1 V (inaccuracy based on 5 subsequent measurements). It is not clear what causes the discrepancy. An explanation can be that the beam has slightly bent towards the substrate, due to the tensile stress of the silicon nitride spacers underneath the beam. This can cause a lower than expected active area for the electrostatic pressure to act on.

Pull-down

For t = 5 µm, the normal gap g_n = 2 µm, E_2 = 330 Gpa, and the dimensions mentioned above, eq. (I.1) predicts a pull-down voltage of 12.1 V. It can be concluded that there is a voltage window, between 7 V and 12 V, for which the beams can be laterally driven without pull-down to the substrate.

Walking Experiments

A voltage pattern with an amplitude of 10V was applied to generate the walking cycle described in fig. 5.2. There was no movement of the shuttle visible. This means that either there were no steps at all generated, or a small number (<5), therefore movement of the shuttle could not be seen using an optical microscope. Two important observations could be done:

1. Drive beams were often sticking to the shuttle. As the initial gap between the beam tips and the shuttle was 1.2 μm and the stiffness at the tip is 0.05 μN/μm, this means that there is a stiction force of at least 0.1 μN. The calculations in section 4 show this can already be caused by a single asperity contact, if the stiction is caused by adsorbed water layers (capillary forces or hydrogen bonds). Another cause can be electrostatic stiction due to the charging of the side-wall silicon nitride.
2. The attachment length is small: a < 50 μm with U = 10 V, and a < 80 μm for U = 40 V. This means that the clamp force will be much lower than the value calculated in section 5.2.3 for a = 100 μm. Possible causes are the bending stiffness of the drive beams, and the reduced electrostatic contact pressure due a roughness induced air gap. Using eq. (5.6) it follows that with an effective air gap thickness of 0.3 μm due to roughness and a small attachment length a = 10 μm, the clamp force of a pair of drive beams reduces to only 0.8 μN (with 10 V).

For the same voltage, the attachment length can be increased by increasing the length of the drive beams, or by making the drive beams more narrow. However, both lead to increased risk of stiction to the side-wall and are therefore rejected. This dilemma might be solved by employing electrical shields underneath activated released parts, in order to reduce the normal pull-in. This than may enable the use of higher driving voltages.

5.2.6 Discussion & Conclusions

A concept for walking motion generated by drive units with integrated clamp and pull actuators has been analyzed and tested. Walking motion could not be produced. Probably the clamping of drive beams is too weak compared to the pull force. The clamp force can be increased with the help of longer or more narrow drive beams, and by decreasing the side-wall roughness. However, all these measures lead to an increased risk of stiction of the drive beams to the side-wall. It can be concluded that a different design of the drive units is desirable. A suggested change is the use of electrical shields underneath active parts, to reduce the pull-down force and to allow an increase of the driving voltage.

In the next section we present a different concept, which offers more freedom to design the clamp and the propulsion functionality separately.

5.3 Concept *B*: Walking motor with separated clamp and pull actuators

5.3.1 Introduction

In the following design separation of the clamp and the propulsive actuation has been realized. The electrostatic stepper motor presented here is fabricated in a very simple single mask surface micromachining process. The motor is made in a single level of 5.3 μm polysilicon and is operated laterally. The motor consists of two drive units that alternately generate a step to move a shuttle, following the scheme of fig. 1.11. The main goal of the work presented here is to investigate the stepwise motion on microscale. The experiments with this design have focused on the friction and adhesion in the clamps.

5.3.2 Design

Single mask design

The clamp force can be generated by applying a voltage difference between the clamp shoe and the shuttle [1]. A problem with this approach can be that there is a voltage difference between either the shuttle and the substrate or the clamp shoe and the substrate. To avoid electrostatic pull-down of one of these moving parts to the substrate, electrical shields are needed, unless the charged structures are made very stiff [5]. We have investigated the application of separate clamp actuators, in which all moving parts are kept at the same potential as the substrate in order to avoid electrostatic pull-down of released structures. Drive voltages are applied to the stator poles of the electrostatic actuators. Therefore electrical shields underneath moving parts are not required, which saves one mask step. By means of a timed sacrificial layer etch, the distinction between anchored and released parts can be made. This saves an additional mask step. All released parts are made narrower than 10 μm, and all anchored parts wider than 10 μm.

Actuators

The clamp and pull actuators are formed by arrays of gap-closing parallel plate capacitors (fig. 5.7). The gap-closing array actuators combine a high energy density by means of multiple small gaps, with a large change of the actuator volume per unit deflection. This combination explains the relative high force output of this type of actuators.

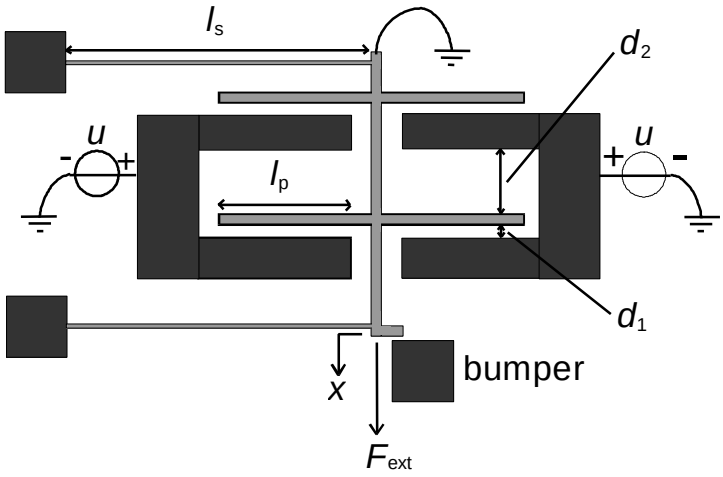

Fig. 5.7: An array of two parallel plate gap-closing actuators. The moving part is drawn black, the anchored part is dark grey. F_{ext} is the external force that makes equilibrium. The forward initial gap-size is d_1, the backward initial gap-size is d_2. The bumper protects the actuator against short-circuit. The drive voltage u is applied between the stator plates (grey) and the moveable plates (black). The moveable part is kept on the same potential as the substrate. The length of the suspension equals l_s, the length of the electrode plates l_p.

The two parallel suspension springs serve as a linear guidance for the actuator array. Residual tensile stress in the polysilicon will be released in this configuration. The actuators are voltage controlled. Therefore, F_{ext} is found from the Legendre transform of the energy function W according to $W' = W - U \cdot Q$, with Q the charge stored in the capacitor:

$$W'(u,x) = -\frac{1}{2} \cdot \frac{e \cdot A_f \cdot U^2}{d_1 - x} - \frac{1}{2} \cdot \frac{e \cdot A_b \cdot U^2}{d_2 + x} + \frac{1}{2} \cdot k \cdot x^2 \qquad (5.4)$$

Where A is the total overlapping area of the actuator plates, d_1 is the initial forward gap, d_2 is the applied backward gap, A_f is the forward active area, A_b is the backward active area, u is the applied voltage between the plates, e is the permittivity of air, x is the actuator deflection and k is the suspension stiffness. The external force making equilibrium, F_{ext}, equals the derivative of the W' with respect to x:

$$F_{ext} = -\frac{1}{2} \cdot \frac{e \cdot A_f \cdot U^2}{(d_1 - x)^2} + \frac{1}{2} \cdot \frac{e \cdot A_b \cdot U^2}{(d_2 + x)^2} + k \cdot x \qquad (5.5)$$

If the electrostatic attraction force increases faster with x than the restoring spring force, then the actuator becomes unstable and will make a full stroke. Neglecting the backward force, the pull-in voltage can easily be estimated using eq. (2.13). The suspension stiffness (two parallel springs) equals [6]:

$$k = 2 \cdot \frac{E \cdot h \cdot w^3}{l_s^3} \qquad (5.6)$$

Where l_s = 200 μm is the length of the springs, h = 5 μm is the height of the springs, w = 2 μm is the width of the springs and E = 150 GPa is the Young's modulus. This yields a suspension stiffness k = 1.5 N/m. The actuator area A is given by $n \cdot h \cdot l_p$ where l_p = 100 μm is the overlapping plate length and n is the number of plates involved. For the pull actuator, which creates the step, we have chosen n = 7 plates, and d_1 = 3 μm, which gives using eq. (2.13) u_{pi}= 19.7 V. The clamp actuator has got n = 14 plates, and d_1 = 4 μm, which corresponds with U_{pi} = 21.4 V. The net actuator force at 40 V actuation voltage as a function of the actuator deflection is shown in fig. 5.8. Both the forward and backward electrostatic forces, as well as the suspension stiffness are included in the evaluation. For the pull actuator d_1 = 3 μm and d_2 = 7 μm, and the minimum produced force equals 1.9 μN for x = 0. For the clamp actuator d_1 = 4 μm and d_2 = 6 μm, and the minimum produced force is 2.3 μN for x = 0. Note that the number of backward active electrodes is 6 and 12 for the pull and the clamp actuator respectively.

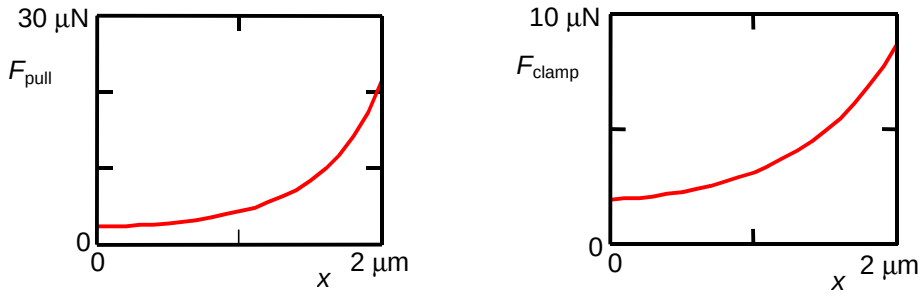

a) *b)*

Figure 5.8: Actuator force as a function of actuator deflection x. a) Pull actuator, n=7, d_1 = 3 μm and d_2 = 7 μm. b) Clamp actuator, n = 14, d_1 = 4 μm and d_2 = 6 μm. Note that these forces represent $-F_{ext}$, which was defined in fig 5.7.

The maximum stroke of each actuator is limited by a bumper that protects it against short-circuit by collision of the plates. The bumper in the pull actuator allows a maximum stroke of 2 μm. The clamp actuator has a maximum stroke of 3 μm.

Drive Units

A drive unit consists of a clamp actuator, a pull actuator a clamp shoe, and elastic beams that connect the actuators to the shoe (fig. 5.9). The beam that connects the clamp actuator to the shoe is stiffened in the middle to increase the buckling load. A stiffened beam of length $7/6 \cdot L$ as drawn in fig. 5.10 has a buckling load $F_{y,max}$ that is 9 times larger than a simple beam of length L and width w, while the stiffness F_x / x is almost the same: 108/109 times the stiffness of the simple beam [7].

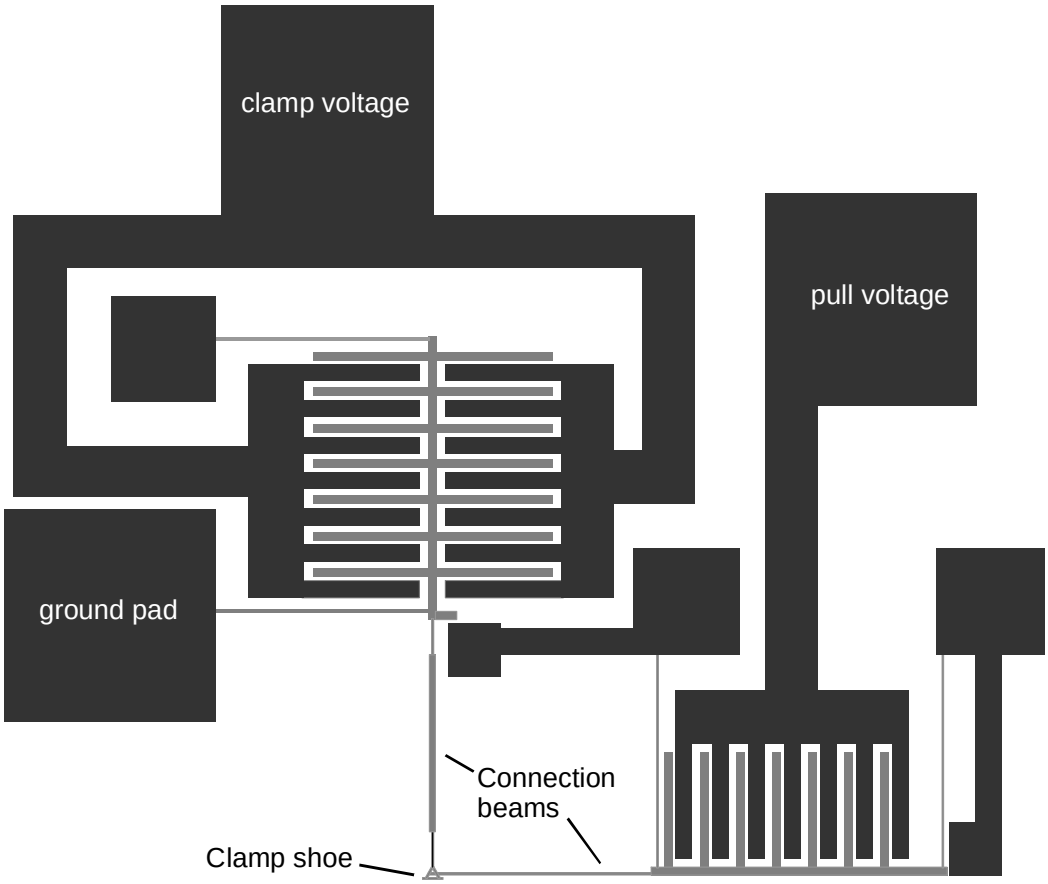

Figure 5.9: Layout of a drive unit, consisting of a clamp actuator, a pull actuator both connected to a clamp shoe by means of elastic beams. All moveable parts have been drawn light gray, all fixed parts dark gray.

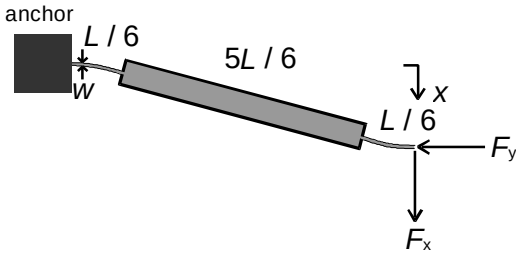

Figure 5.10: A stiffened beam of length 7/6·L as drawn has a buckling load $F_{y,max}$ that is 9 times larger than a simple beam of length L and width w, while the stiffness F_x / x is almost the same: 108/109 times the stiffness of the simple beam [7].

Complete motor

The complete motor consists of two drive units, one on each side of the shuttle. The suspension of the shuttle is loaded in the y-direction (fig. 5.11) by the drive units from both sides. Therefore, it has been designed to be both stiff and stable in this direction. Fig. 5.11 shows the layout of the shuttle plus suspension. Holes have been made in the shuttle to minimize the under etch distance for the timed release etch. The suspension springs have been stiffened in the middle to avoid buckling. The total length of the suspension beams is 7/6 x 400 μm, yielding a stiffness k_x = 0.20 N/m (E = 150 GPa, w = 2 μm, h = 5.3 μm). A deflection Δx in x-introduces a small displacement $\Delta y \cong \Delta x^2/2l_s$. This leads to a reduction of

the clamp force at one side, because the closed-gap size in the clamp actuator becomes larger. For example, a shuttle displacement $\Delta x = 18$ μm gives a displacement $\Delta y = 0.4$ μm.

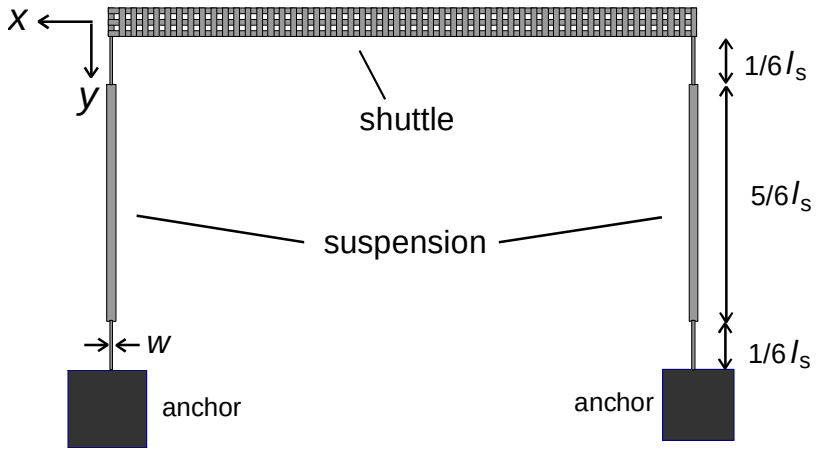

Figure 5.11: Layout of the shuttle and its suspension springs. The moving part has been drawn light gray, the anchors dark gray. The suspension springs are stiffened in the middle to increase the buckling load. Holes are etched in the shuttle in order to keep the under etch distance small.

5.3.3 Fabrication

The fabrication is similar to the fabrication of the device in paragraph 5.2, with a difference that the deposition and etching of silicon nitride for the side-walls is omitted (steps 25,26 and 27) in appendix D. By a timed etch of the sacrificial layer it is possible to under etch only narrow structures (fig. 5.12), which makes it possible to omit a mask to define anchors. Fig. 5.13 shows a microscope picture of the complete motor. Figure 5.14 shows a SEM-picture of a clamp shoe and two elastic drive beams.

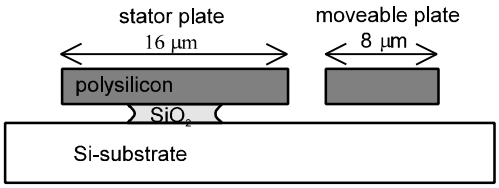

Figure 5.12: Narrow structures are released selectively, by a timed oxide etch in HF.

5.3.4 Experiments

Before trying to generate walking motion, we have measured friction between a clamp shoe driven by a single drive-unit and a rigid wall. This experiment has been described in section 4.4. The result was a linear relation between the applied clamp force L and the measured friction force: $F_f = m_{e,a}(F_a^0 + L)$ with the friction coefficient $m_{e,a} = 0.7 \pm 0.3$ and the (apparent) zero load adhesion force $F_a^0 = 2.0 \pm 1.3$ μN. This measurement shows that there is significant adhesion in the clamps, however that it is considerably smaller than 10 μN, which we use as the limit for which the clamp can be actuated by a simple electrostatic actuator. Also it can be concluded that the friction in the clamp is in the same order as the applied clamp force. Next we have tried to generate walking motion. Fig. 5.15 shows the voltage pattern applied to the

actuators. The voltages have been applied to the stator poles of the actuators. All moving structures as well as the substrate have been grounded.

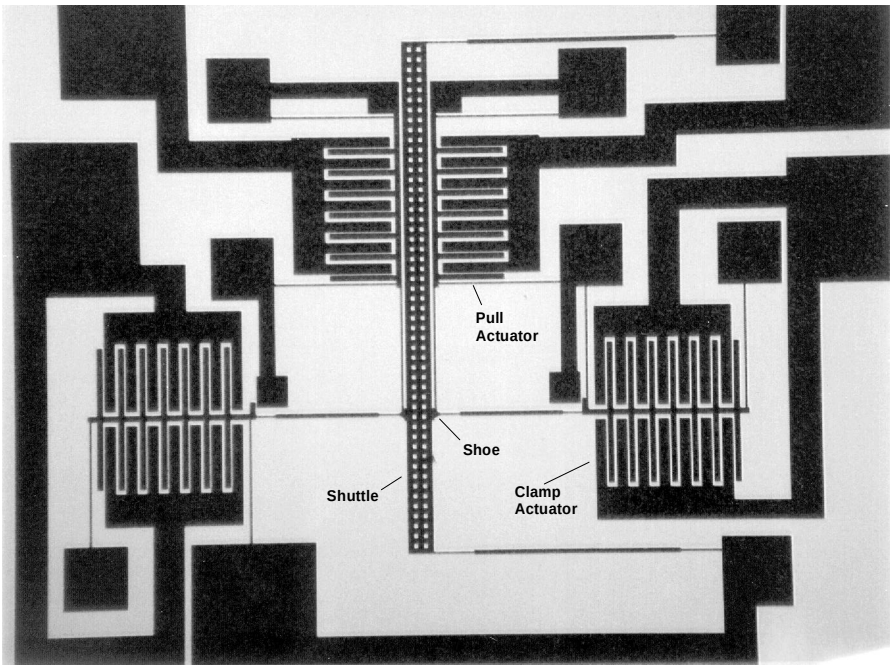

Figure 5.13: Microscope picture of a fabricated motor (1x1 mm^2). The motor consists of a shuttle and two drive units at both sides of the shuttle. Each drive unit consists of a clamp actuator, a pull actuator, a clamp shoe and elastic beams that connect the actuators and the shoe.

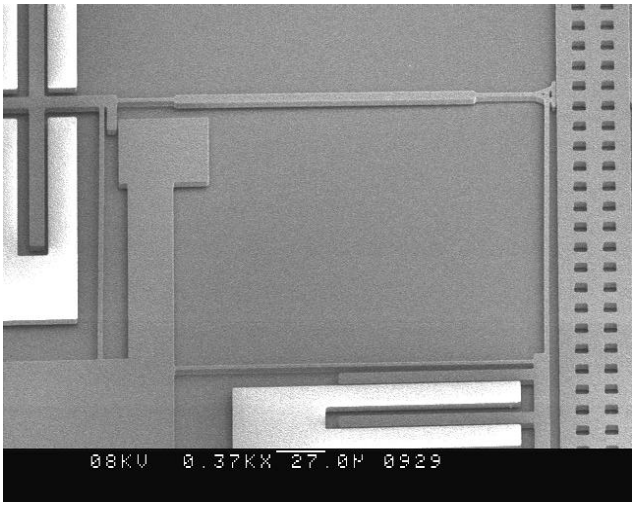

Figure 5.14: SEM photograph of a clamp shoe and two elastic drive beams. The beam connecting the shoe and the clamp actuator is stiffened in the middle to increase the buckling load. Due to charging of the actuators in the SEM, the shoe is clamped against the shuttle.

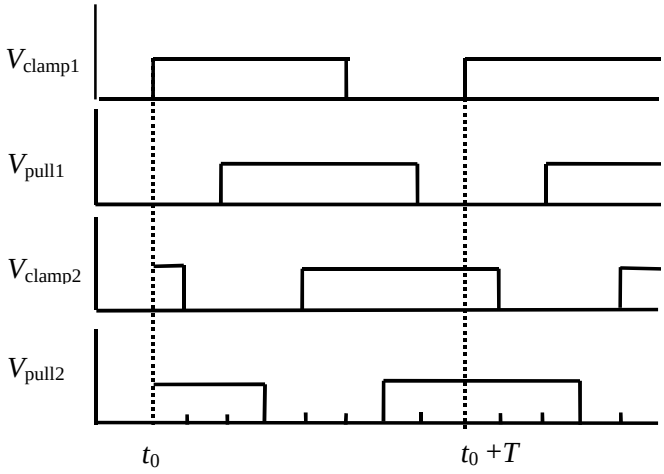

Figure 5.15: Voltage pattern applied to the actuators.

A complete stepping cycle has been performed successfully at a potential of 40V and a cycle frequency of 1 Hz. Steps have been added to obtain a total displacement of 15 μm, limited by the suspension. Based on the geometry of the suspension of the shuttle, this corresponds with a generated force of 3 μN. The effective step size decreases from 2 μm to zero with increasing shuttle displacement due to slip, mainly in one of the clamps. The reason for this is that the clamp force reduces due to the sideward displacement of the shuttle as a consequence of the linear guidance used (see section 5.3.2). Figure 5.16 shows a picture taken from the video of the motor in operation. Note the deflection of the shuttle suspension.

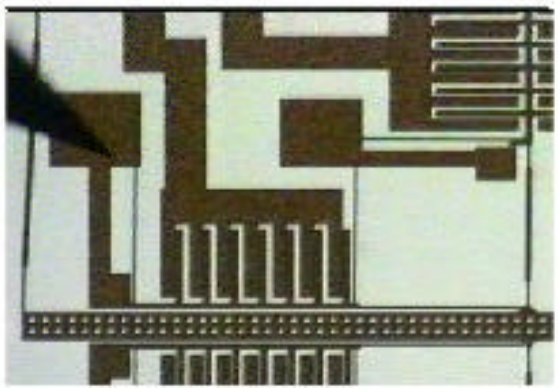

Figure 5.16: picture taken from the video of the motor in operation. Note the deflection of the shuttle suspension.

5.3.5 Comparison with reported experiments from other groups

In literature we have found two other reports on MEMS laterally driven walking motors [1,2]. Baltzer et al. [2] use external clamp and propulsion actuators. They report a generated force larger than 1 μN driven at 30 V, and a maximum produced displacement of 110 μm. The displacement is significantly larger than we could generate. The explanation for this is that Baltzer et al. used two polysilicon layers, and were therefore able to realize an unsuspended shuttle. Yeh et al. [1] used a slightly different configuration. The clamp force was generated by applying a voltage difference between the clamp shoe and the shuttle. To enable this concept, also two polysilicon layers are needed: polysilicon shields have to be made

underneath the clamp feet and their suspension, in order to avoid electrostatic pull-down towards the substrate. Their motor generated 6.5 μN at 35 V applied, and generated displacements up to 40 μm. Both the force and the displacement are comparable to our results.

5.3.6 Conlusions

A linear electrostatic stepper motor has been realized in a single mask surface micromachining process. A friction coefficient of 0.7 ± 0.3 has been measured in the clamp of a drive unit. The friction measurements indicate that there is significant adhesion in the clamp. Walking motion has been generated successfully, yielding a total stroke of 15 μm with a step size of about 2 μm, decreasing to zero. The generated force is 3 μN at 40 V driving voltage.

5.3.7 Acknowledgment

The authors would like to thank D. Blank (Low Temperature Group, UT) and H. Visscher (Tribology Group, UT) for valuable discussions on design and friction measurements.

5.4 Concept *C*: Walking motor with levers to increase the force

5.4.1 Introduction

In section 5.3 we generated walking motion using separate clamp and propulsion actuators. It was concluded that (1) it is possible to generate controlled friction in a microcontact, (2) that this friction is increases linearly with increasing clamp force, with a friction coefficient of 0.7 ± 0.3, and (3) that the adhesion is low enough to enable the release of the clamp shoe by the elastic forces of the suspension, when the clamp actuator is switched off. In the design of section 5.3 the generated force was low, < 10 μN with a 40 V driving voltage. The aim for the laterally driven motors is at least 0.1 mN at 30 V. In this section we describe our efforts to increase the generated force up to the desired value using mechanical levers. For the design presented here, we allowed the use of slightly larger driving voltages: ≤ 50V.

5.4.2 Design of the propulsion actuator

For the propulsion actuator the intended generated force is 0.1 mN. The intended step size is 50 nm. Several concepts for implementation of a lever have been investigated [8]. Here we will treat the most simple design, which is a translating gap-closing actuator in combination with a simple lever with a constant transformation ratio (fig. 5.17). Assuming a generated step of 2 μm at the actuator side of the lever, and a step size of 50 nm at the output side of the lever, a transmission ratio $r = \Delta x_{out} : \Delta x_{in} = 1{:}40$ is required (fig. 5.18). For the net generated force (electrostatic force – elastic deformation force) this means that 0.1 mN / 40 = 2.5 μN is required at the lever input. Extra force is needed because of the stiffness of the actuator suspension and the elastic joints in the lever. This effective stiffness at the input will be

calculated next, in order to show the feasibility of the implementation of a lever in MEMS electrostatic actuation.

Input stiffness of the lever with elastic joints

Fig. 5.17 shows the lay-out of an actuator with lever. The definition is of variables used is given in fig. 5.18. By choosing the joint lengths l_1 and l_3 large enough, the stiffness in the *y*-direction of joint 2 is largest, and it can be assumed that the center of rotation is located halfway of joint 2. This implies that the transformation ratio $\Delta x_{out} : \Delta x_{in} = l_{out} / L$. In our design we choose L = 400 μm and l_{out} = 10 μm. The displacement of the lever beam in the *y*-direction is determined by the displacement y_2 of the tip of joint 2, induced by the moment exerted by the lever beam. The effective stiffness measured at the input side of the lever due to the bending stiffness of the joints is calculated in appendix J. The input stiffness is given by:

$$k_{in} = \frac{\partial F_{in}}{\partial x_{in}} = \frac{(4l_1 - 3 \cdot l_2) \cdot E \cdot I_1}{L^2 \cdot l_1^2} + \frac{E \cdot I_2}{L^2 l_2} + \frac{(4l_3 + 3l_2 + 6w_{lever}) \cdot E \cdot I_3}{L^2 \cdot l_3^2} + k_s \quad (5.7)$$

Here we have neglected the q^2 term in the expression for $y_1(y_2,q)$. With l_1 = 50 μm, l_2 = 10 μm, l_3 = 50 μm, $w_1 = w_2 = w_3$ = 2 μm, t = 5 μm, E = 150 GPa the total rotational stiffness of the lever, measured at the input, equals 1.0 μN / μm. The stiffness k_s of the actuator suspension equals 1.5 μN / μm calculated for two parallel polysilicon springs with l_s = 200 μm, w_s = 2 μm, t_s = 5 μm. The total stiffness k_{in} which has to be overcome by the actuator therefore is 2.5 μN / μm.

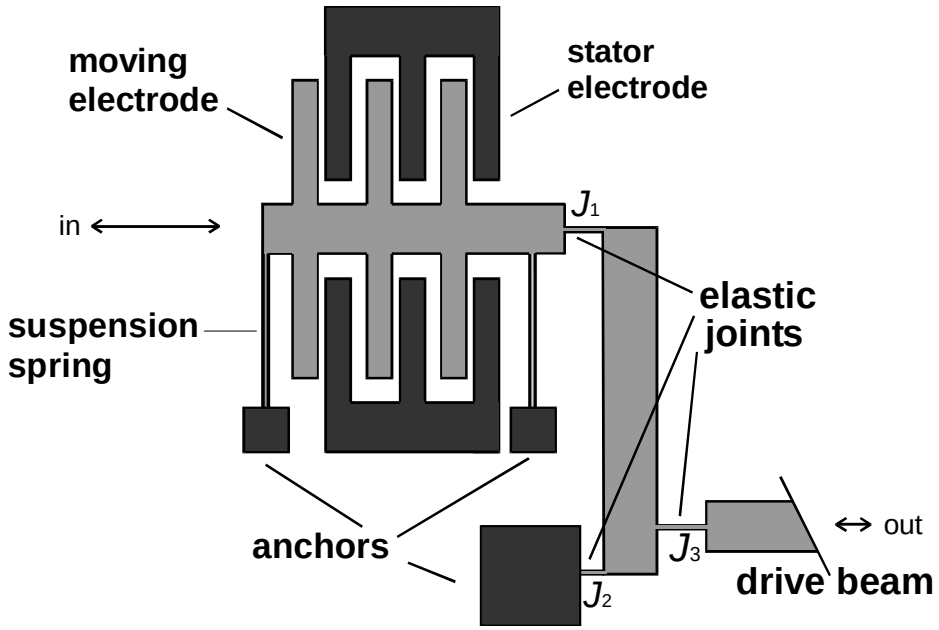

Figure 5.17: Lay-out of the propulsion actuator with a lever. The light gray parts are released, and are on the same potential as the substrate. The dark gray parts are fixed to the substrate by insulating silicon oxide. The three elastic joints are indicated by J_1, J_2, J_3.

Delivered Force

The force F_{out} delivered at the output of the lever is given by:

$$F_{out}(x_{in}) = \frac{1}{r} \cdot \left(\frac{1}{2} \cdot \frac{n \cdot e \cdot t \cdot l_a \cdot U^2}{(g - x_{in})^2} - k_{in} \cdot x_{in} \right) \tag{5.8}$$

Where r is the transformation ratio $\Delta x_{out} : \Delta x_{in}$, n is the number of plates, l_a is the overlap length of the actuator plates, g is the initial gap, e is the permittivity, and U is the driving voltage. It is assumed that the backward gap is large enough to neglect the backward electrostatic force.

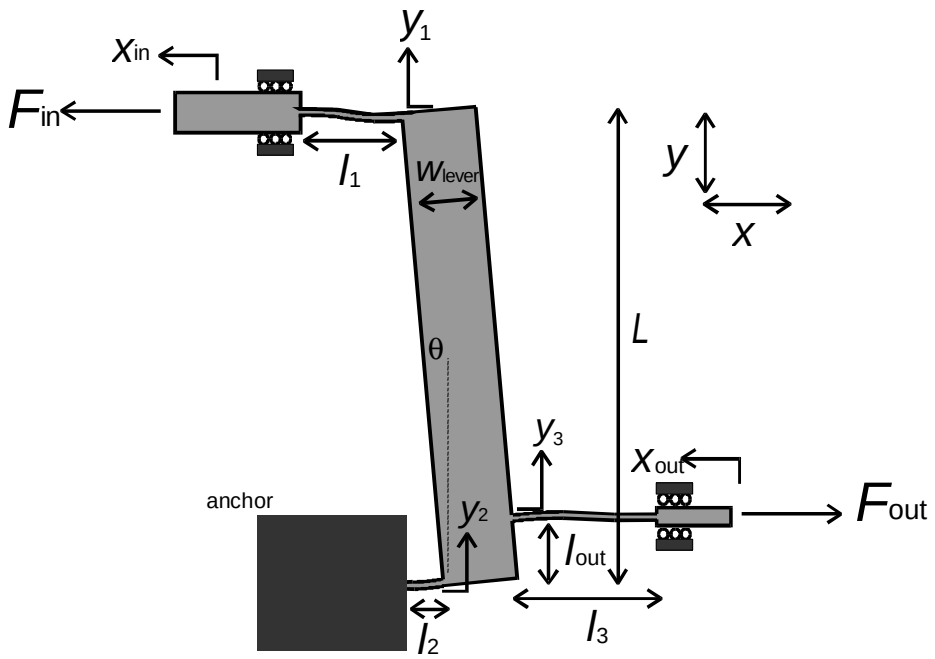

Figure 5.18: Definitions of variables for the stiffness analysis of the lever.

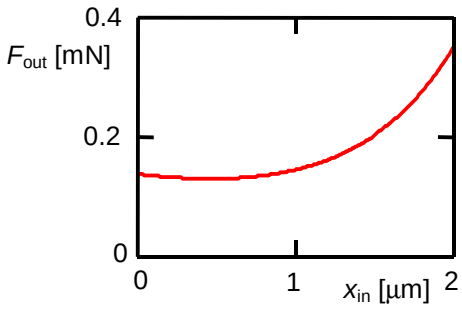

Figure 5.19: Static equilibrium force at the output, with a 1 : 40 lever and 50 V driving voltage. For the actuator 10 plates with a length of 100 µm, a height of 5 µm, and an initial electrode gap of 4 µm were taken. An input stiffness k_{in} = 2.5 µN / µm has been used.

Fig. 5.19 shows the force $F_{out}(x_{in})$ delivered through a r = 1 : 40 lever by an electrostatic actuator consisting of 10 plates, each with a length of 100 µm and a height of 5 µm, an initial

electrode gap of 4 μm and a driving voltage of 50 V. As can be seen in fig. 5.19 the output force is larger than the required 0.1 mN over the whole 2 μm input stroke x_{in}.

Output stiffness

The generated deflection can be lost by bending of the lever beam, and by elastic elongation of the elastic joints. This can be analyzed by fixation of the input, and measuring the stiffness at the output. Both are calculated in appendix J. The criterion we use is that the stiffness should be large enough to loose less than 5% of the 2 μm actuator stroke, with the actuator force being equal to 100 μN. The bending stiffness, measured at the output, is given by:

$$k_b = \frac{3E \cdot I_b}{L^3} \cdot \frac{(L - l_{out})^2}{l_{out}^2} \tag{5.9}$$

Where $I_b = w^3 \cdot t / 12$ is the moment of inertia of the lever beam. For a polysilicon beam with L = 400 μm, a width w of 40 μm and a height t of 5 μm this yields $k_b = 3 \times 10^5$ μN / μm. The effective tensile stiffness of the three joints measured at the output is given by:

$$k_t = \frac{1}{\frac{l_{out}^2}{L^2 \cdot k_{t1}} + \frac{(L - l_{out})^2}{L^2 \cdot k_{t2}} + 1/k_{t3}} = \frac{E \cdot t}{\frac{l_{out}^2 \cdot l_1}{L^2 \cdot w_1} + \frac{(L - l_{out}) \cdot l_2}{L^2 \cdot w_2} + \frac{l_3}{w_3}} \tag{5.10}$$

Where k_{ti} is the tensile stiffness of joint i. With L = 400 μm, l_{out} = 10 μm, l_1 = 50 μm, l_2 = 10 μm, l_3 = 50 μm, $w_1 = w_2 = w_3$ = 2 μm, t = 5 μm, E = 150 GPa the output stiffness equals 25 x 10^3 μN / μm. The effective output stiffness is given by:

$$k_{out} = \left(\frac{1}{k_b} + \frac{1}{k_t}\right)^{-1} \tag{5.11}$$

With the dimensions mentioned it follows that $k_{out} = 23 \times 10^3$ μN / μm. This corresponds with 4 nm output deflection with F_{out} = 0.1 mN, which is sufficiently small compared to the 50 nm full stroke. In order make it possible to release the rather wide lever (40 μm) by sacrificial layer etching, holes have to be introduced in the beam to reduce the diffusion length in the etching process.

Implementation

In the final design, the design of the lever has been changed, in order to obtain an area efficient configuration. Figure 5.20 shows the lever design. The transformation ratio is now given by $l_{out} : L$.

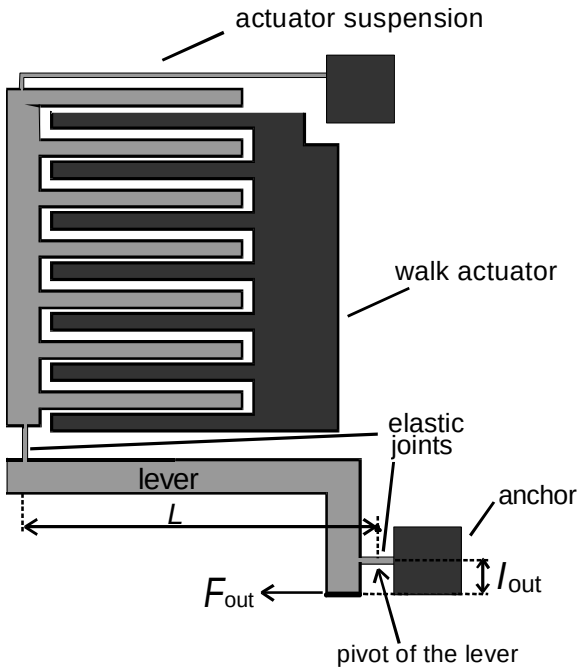

Figure 5.20: Lay-out of the area efficient design for the propulsion actuator with folded lever. In this configuration the transformation ratio is given by $l_{out} : L$.

5.4.3 Design of Clamp

For the previously described motor we have characterized friction in the clamps. The measured friction coefficient was 0.7 ± 0.3. For the design of the clamp actuator we assume a low value out of this range: $\mu = 0.5$. Because the aim is a propulsive force of 0.1 mN, this implies for the clamp force that it should be at least 0.2 mN. Within our surface micromachining design rules this force can not be generated directly by an external electrostatic clamp actuator: Based on the calculations in section 2.6, a force of 0.2 mN could just be generated by a 1 mm^2 comb-drive array driven by 50V. The required area of 1 mm^2 is too much as this is the area available for the whole motor. With an external clamp actuator, the use of a lever is therefore required. If a lever with a constant transformation ratio is employed, it is hard to generate both the required force and the minimum stroke of 2 µm needed to close the initial gap between the clamp shoe and the shuttle. We could find a number of possible solutions to generate a 2 µm displacement in combination with a 0.2 mN clamp force:

1. Lever with changing transformation ratio
2. Lever and pre-clamp spring
3. Clamp force generated in the clamp interface

1. *Changing transformation ratio*

Figure 5.21 shows an possible configuration to implement a changing transformation ratio, using a toggle joint lever. The transformation ratio dx / dy is given by:

$$i = \frac{\mathrm{d}x}{\mathrm{d}y} = \frac{2y}{l}$$

It reduces to zero when the mechanism is fully stretched (fig. 5.21b). The critical point for implementation in our motor is that with decreasing dx / dy the output force F_{ext} becomes large. In the motor this means that the clamp shoe should just touch the shuttle when the transformation ratio has just become small enough. This demands a high absolute accuracy of the fabrication process, in order to obtain the desired initial clamp gap exactly. To illustrate this we assume that sufficiently clamp force is generated if i < 0.1. This means that the electrostatic actuator force should be at least 20 μN. The full step size $x(y = y_0)$ equals y_0^2 / l. With extra fabrication steps the initial gap can be reduced to 1 μm. This is taken as the desired stroke at the output. Realistic values for l and y_0 can be l = 400 μm and y_0 = 30 μm. To make a 2 μm stroke at the output, the input deflection y has to increase from zero to 7.6 μm. If there is an uncertainty of 0.4 μm in the initial gap size, an extra input stroke is necessary to create x = 1.4 μm. The input deflection has then to be increased to 11.6 μm. The combination of the desired large input stroke (> 10 μm) and a rather high input force (> 20 μN), implies that this concept for the clamping still needs large clamp actuators, and is in our opinion not very attractive.

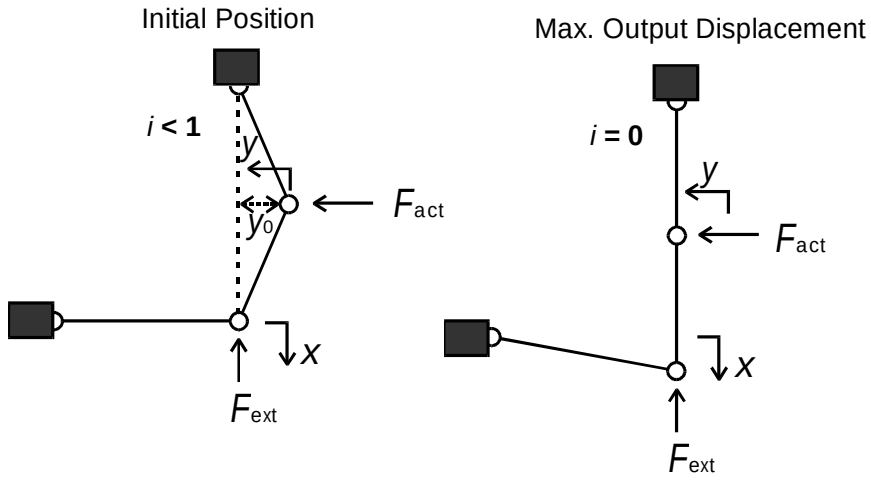

(a) (b)

Figure 5.21: Toggle joint lever with changing transformation ratio. The ratio i = dx /dy decreases with increasing input displacement y. Here x is the output displacement with respect to the initial position with y = 0. The local i is also a measure for dF_{act} / dF_{ext}, with F_{act} the input force applied by the actuator, and F_{ext} the external force reacting at the output.

2. Pre-clamp spring

This concept is based on the principle that it is tried always to keep contact between either one of the clamp shoes, and the shuttle. This is accomplished by applying a constant pre-tense force, which for example is generated by a pre-tensed spring. Changing the on/off-state between the two clamps is done by extension of the connection between one of the clamps and

a common pre-clamp body at which the pre-tense force is applied. In fig. 5.22 this is illustrated for a toggle joint lever, which is used to lift one of the clamp shoes.

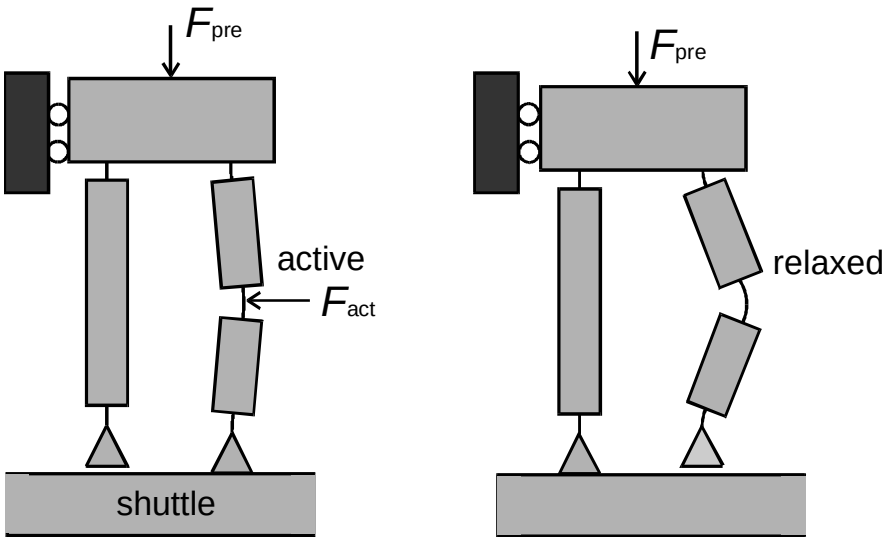

(a) (b)

Figure 5.22: Pre-tense principle. a) The lever is stretched actively by the actuator (force F_{act}) and the clamp shoe is clamped to the shuttle. The other clamp shoe is lifted from the shuttle. b) The lever is relaxed and the connected clamp shoe is lifted. The other clamp carries the pre-tense force.

The displacement required to lift one clamp shoe with respect to the other, should be able to overcome the pre-clamp force. However, this can be realized by means of a large lever ratio, as the required displacement of the clamp shoe can be very small. In principle this concept is very attractive, however it requires a pre-clamp force, which is not readily available. This has been the reason why this principle has not been employed.

3. Electrostatic force generated in the clamping region

The third clamp principle is based on generation of the clamp force by applying a voltage difference (U_c in fig. 5.23) across the insulators covering the shuttle and clamp shoe side-walls. This way an electrode distance smaller than 1 μm can be created, resulting in a high field intensity at moderate voltages applied.

The clamp force F_c generated by the electrostatic forces between charges at both sides of the insulator layers is, similar to eq. (5.2), given by:

$$F_c = \frac{U_c^{\,2} \cdot A}{e_a \cdot \left(\frac{d_a}{e_a} + \frac{d_i}{e_i}\right)^2} - F_{spring} \qquad (5.12)$$

Where U_c is the applied clamp voltage, e_a is the permittivity of air, e_i is the permittivity of the insulator, d_i is the total thickness (two layers) of the insulator, d_a is the thickness of the air gap between the two electrodes, and F_{spring} is the restoring force of the clamp-shoe suspension. For an 2 μm initial gap, and an assumed suspension spring constant of 6 μN / μm, F_{spring} = 12 μN.

For a 5 x 50 μm^2 active area of the clamp shoe and in total a 0.3 μm silicon nitride layer eq. (5.12) yields an electrostatic clamp force F_{elec}= 0.35 mN. The effective clamp force will be 0.33 mN. Here we have assumed that the air gap thickness d_a with the closed air gap is zero. The pull-in voltage for the same active area, suspension stiffness and initial gap, is 80 V. To lower this, a pre-clamp actuator is included (fig. 5.23), which has the function to bring the clamp shoe close enough to the shuttle for the charges at both outer-sides of the insulators to take over the clamping. Adding a pre-clamp actuator with an active area of 15 x 5 μm x 100 μm = 7.5 x 10^3 μm^2 and an initial gap of 4 μm, reduces the pull-in voltage to 41 V. The electrostatic clamp force increases to F_{elec} = 3.6 mN at 50 V. The effective clamp force will then be 3.5 mN, provided that the effective air-gap thickness is zero. This principle seams to make it possible to generate the required stroke and clamp force. Also it uses only processing steps which are already available. Therefore, it has been selected for implementation. The design of a clamp based on this principle is discussed next.

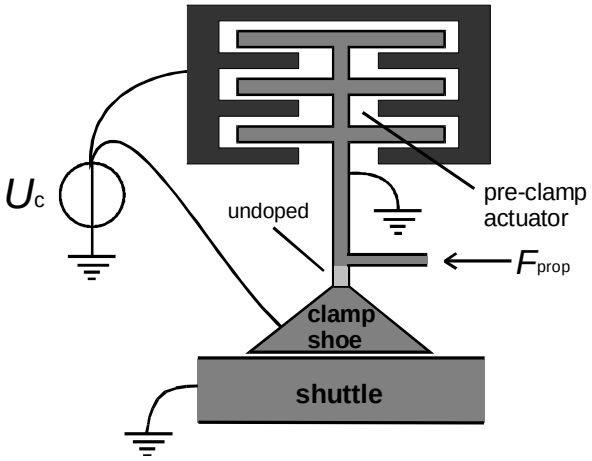

Figure 5.23: The clamp force is generated by applying a voltage difference U_c across the insulators covering the side-walls of the clamp shoe and the shuttle. The undoped region in the poly silicon is included to separate (electrically) the clamp shoe and the rest of the moving structure. This enables the grounding of the largest part of the moving structure, which is required to avoid electrostatic pull-down. The F_{prop} is the propulsion force acting on the clamp, for step generation.

The insulation of mechanically connected part by undoped polysilicon has been tested experimentally in 5 μm thick structures. The width of the masked region has been varied between 10 and 30 μm, in order to determine the diffusion length *d* of the Boron dopant underneath the mask (fig. 5.24). Resistance measurements show that the anneal step at 1100°C for 3 hours (see app. *D*) results in a lateral diffusion length d < 15 μm, as the resistance increases from < 300 Ω to > 20 MΩ for the mask width *m* increasing from 20 μm to 30 μm (fig. 5.24b).

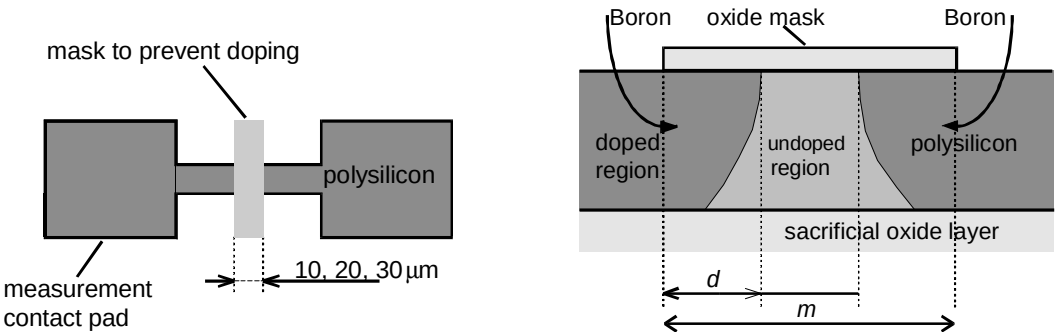

Figure 5.24: a) Top view of the polysilicon test structure. Between the two contact pads a mask is applied to prevent doping of the polysilicon locally, in order to create mechanically parts which are electrically separate. The width *m* of the mask has been varied between 10, 20 and 30 µm. b) Impression of the dopant profile after annealing. The dopant source layer has been deposited on top of the structure. At the start of the anneal the dopant diffuses top-down and laterally, underneath the mask. The maximum diffusion length under the mask is *d*.

The clamp shoe and its suspension are on a different voltage than the substrate. Fig. 5.25 shows these parts. The gray parts are the freestanding conductive parts of the clamp, which are at a different voltage than the substrate. Part 1,2 and 4 (indicated with their lengths l_1, l_2, l_4) are 2 µm wide springs. Spring 4 gives the clamp shoe the freedom to move in *y*-direction, springs 1 and 2 to move in x-direction. Spring 1 and the rigid connecting beam 3 have been added to reduce torsion of spring 2, due to the downward electrostatic forces acting on the clamp shoe and spring 4.

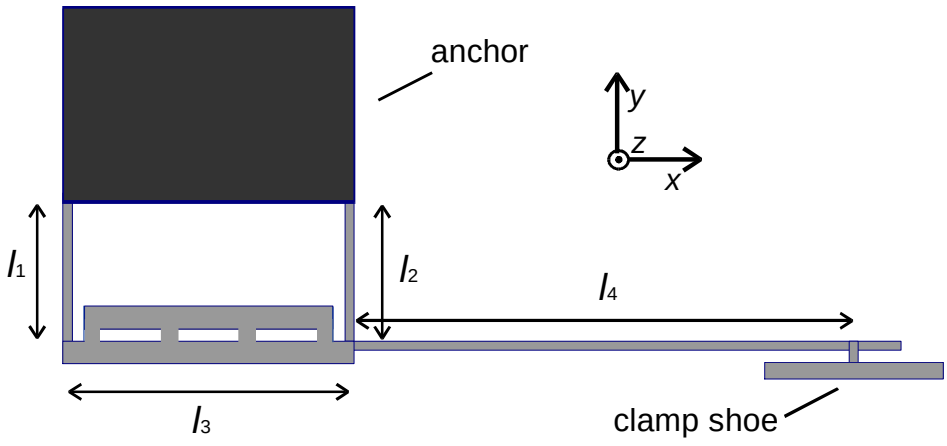

Figure 5.25: Top view of the clamp suspension and its anchor. The gray parts are the freestanding conductive parts, which are on a voltage different from the substrate. Part 1,2 and 4 (indicated with their lengths l_1, l_2, l_4) are 2 µm wide springs. Spring 4 gives the clamp shoe the freedom to move in *y*-direction, springs 1 and 2 to move in x-direction.

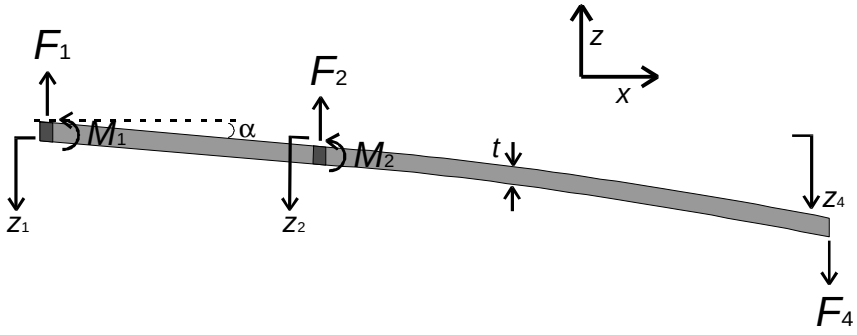

Figure 5.26: front view (y-direction) of the clamp suspension. The amount of torsion of spring 1 and 2 is given by the angle a. The clamp shoe moves downward due to (a) torsion of spring 1 and 2, (b) downward bending of these springs (tip deflection z_1 and z_2), and (c) bending of spring 4. The total tip deflection at the end of the suspension is represented bij z_4. The forces F_1, F_2 exerted by springs 1 and 2 , F_4 exerted by the electrostatic forces, and the moments M_1, M_2 exerted by springs 1 and 2, are inicated.

We have checked if at 50 V applied pull-in to the substrate will not occur. in appendix *F* this calculation is presented. The *z*-stiffness k_{z4} of the suspension is given by:

$$k_{z4} = \frac{1}{c_z + c_a + c_{b4}} \tag{5.13}$$

Where c_α is the compliance due to torsion, c_z is the compliance due to translation of the center of rotation by bending of springs 1 and 2, and c_{b4} is the compliance due to bending of spring 4. With $l_1 = l_2 = 40$ μm , $l_3 = 80$ μm, $l_4 = 133$ μm, beam widths $w_1 = w_2 = w_4 = 2$ μm and heights $t = 5$ μm, the compliance of spring 4 mainly determines the *z*-stiffness: The effect of torsion, and the downward deflection (z_2 in fig. 5.25) of the tip of spring 2 are very small. We estimate the downward pull-in voltage by taking the total area of the clamp shoe and spring 4 as the electrode area (374 μm^2), the gap at the tip of spring 4 as the electrode spacing, and the calculated z-stiffness as the stiffness supporting the moving electrode. Initially the gap at the tip $g = 2.3$ μm. With the help of eq. (3.19) a pull-in voltage of 67 V results. This is an underestimate, as we have overestimated the effective electrode area. Also the *z*-stiffness added by the drive beams is neglected. As it is planned to operate the motor at a maximum of 50 V, the chosen dimensions are appropriate.

5.4.4 Lay-out of the complete motor

Figure 5.27 shows the lay-out of the assembled motor.

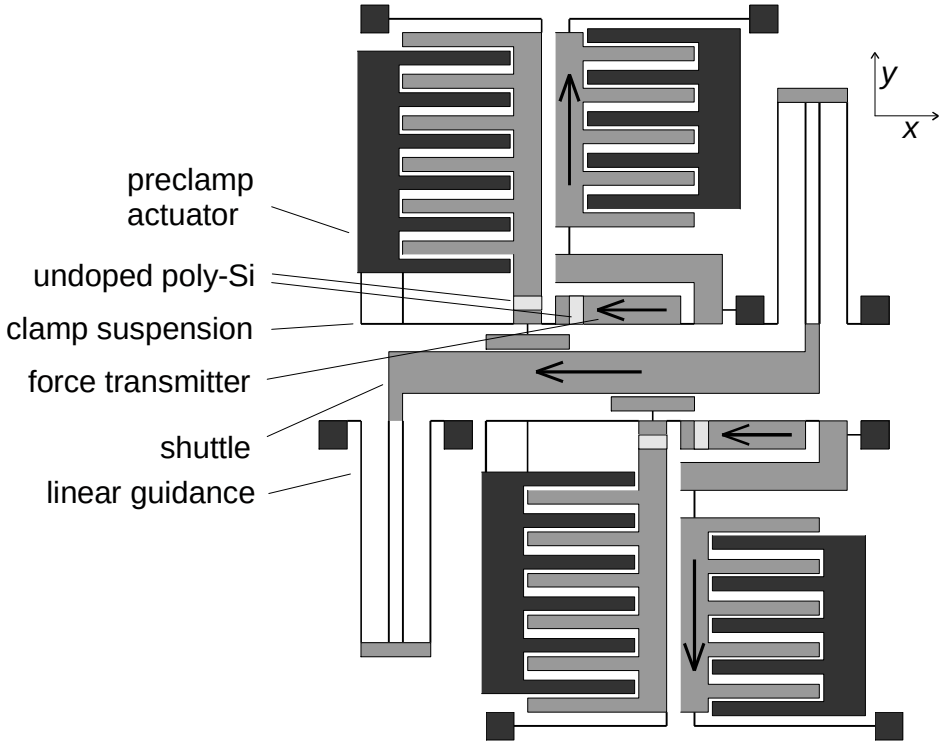

Figure 5.27: The lay-out of the assembled motor. The number of plates shown here is smaller than in reality: In the fabricated motor the pre-clamp actuator consists of 15 plates with a length of 100 μm and 5 μm height. The propulsion actuator consists of 11 similar plates.

Force Transmitter

The force transmitter (see fig. 5.27) couples the output of the propulsion actuator and lever to the clamp shoe. The requirements for this element are (measured at the clamp side) a high stiffness in *x*-direction, and a low stiffness in *y*-direction. In order to increase the tensile stiffness (*x*-direction) while keeping the *y*-stiffness lowest as possible, it consists of short flexible parts at both ends and a stiff center part. The flexible parts have a length of 10 μm and a width of 2 μm. The length of the stiff part is 200 μm.

Shuttle

The shuttle length has been chosen as short as possible, because for structures with a large length, some out-of plane bending can occur. The bending is caused by stress gradients in the polysilicon, which for example can be caused by gradients in the Boron dopant concentration throughout the height of the structure. Based on experience with our surface micromachining process, we use the design rule that the maximum length of structures should be smaller than 1 mm, in order to limit the out of plane bending to 1 μm. The shuttle length in the basic (uni-directional) motor is 0.6 mm.

The *y*-stiffness of the shuttle should be high enough to withstand the force exerted on the shuttle by the preclamp actuator of the an activated clamp. Assume that both ends of the shuttle are fixed in *y*-direction, but are free to rotate. The *y*-deflection Δy_{sh} of the middle of the shuttle due to a force $F_{y,sh}$ of exerted on the middle of the shuttle is given by [6]:

$$\Delta y_{sh} = \frac{F_{y,sh} \cdot L_{y,sh}^3}{48 \cdot EI_{sh}} \qquad (5.14)$$

Where L_{sh} is the length of the shuttle, and EI_{sh} is its bending stiffness. With $F_{y,sh}$ equal to 2 μN for a clamp actuator with 15 plates and an forward gap of 2 μm at 50V, the deflection is limited to 0.04 μm for a shuttle width of 16 μm and L_{sh} = 0.6 mm. This value is acceptable.

Linear Guidance

The linear guidance used in concept *B* (fig. 5.12) has the disadvantage that there is significant (undesirable) *y*-deflection, increasing with Δx^2. Furthermore it does not have the largest possible ration between *x*- and *z*-stiffness. Different concepts have been analyzed [8] to overcome these shortcomings. The selected guidance is optimized for a largest as possible stiffness ratio $R_{guide} = k_{z,guide} : k_{x,guide}$. To judge this, the stiffness ratio will be compared to the reference ratio $R_{single} = k_{z,single} : k_{x,single}$ of a single flexure deflected similarly in *x*- and *z*-direction as shown in figure 5.28. The stiffness $k_{z,single}$ and $k_{x,single}$ are defined by:

$$k_{z,single} = \frac{12 \cdot EI_x}{L^3} = \frac{E \cdot t^3 \cdot w}{L^3}, \quad k_{x,single} = \frac{12 \cdot EI_z}{L^3} = \frac{E \cdot t \cdot w^3}{L^3} \qquad (5.15)$$

Width *E* the Young's modulus *w* the width, *L* the length and *t* the height of the flexure, I_x is the moment inertia with respect to the x-axis, and I_z the moment of inertia with respect to the z-axis of The stiffness ratio is given by:

$$R = \frac{t^2}{w^2}$$

For the typical values t = 5μm and w = 2 μm, R has the value 6.25. The selected elastic linear guidance consists of two crab-flexures, each connected to one end of the shuttle (fig. 5.29). From the top view (a) and the front view (b) it becomes clear that all flexible beams have the same bending profile as the single beam in fig. 5.28, both for the *x*- and *z*-deflection, and the ratio in the *z*- and *x*-deflection amplitude is equal to that of the single beam. Therefore the stiffness ratio $R = R_{guide} : R_{single} = 1$. It is important that the moment exerted by the flexures on the shuttle do not induce torsion of the shuttle, as this would lower the *z*-stiffness.

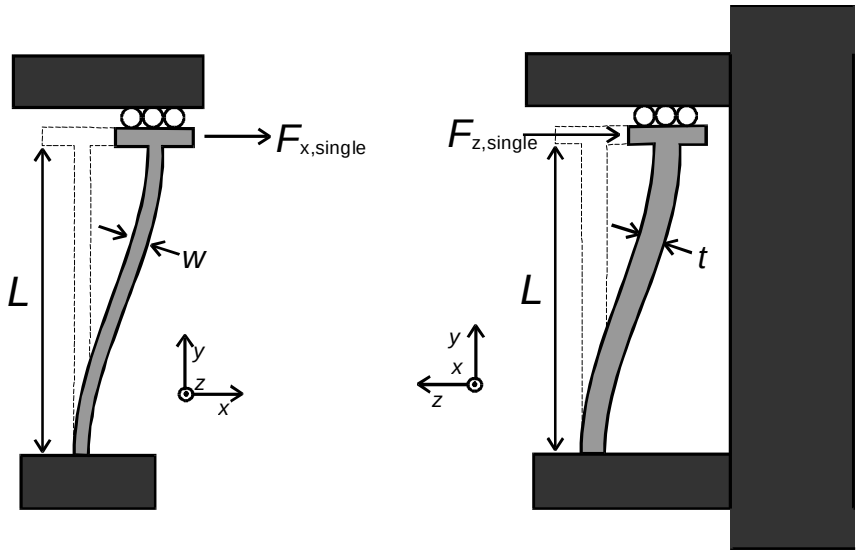

a) b)

Figure 5.28: Definition of the reference flexure. The flexure has a length *L*, a width *w* and a height *t*. Stiffness in a) *x*-direction b) *z*-direction are measured at the tip of the flexure.

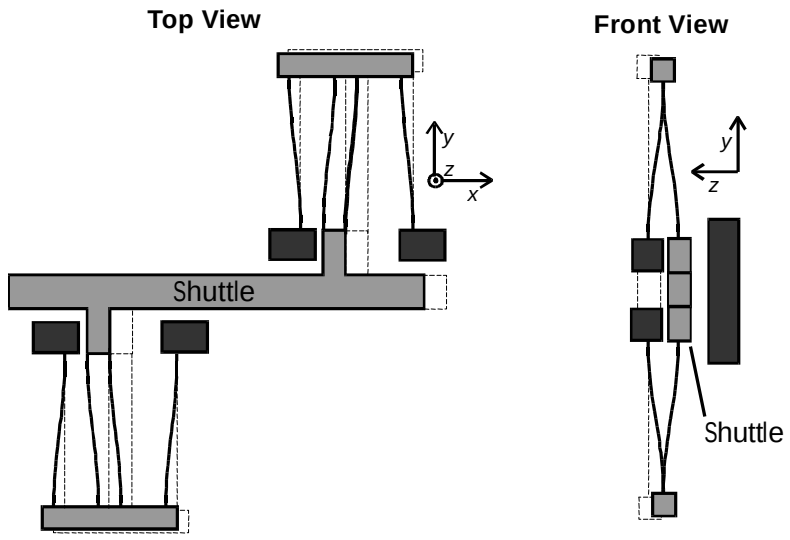

a) b)

Figure 5.29: The selected elastic linear guidance. It consists of two crab-flexures each connected at one end of the shuttle. From the top view (a) and the front view (b) it becomes clear that all flexible beams have the same bending shape as the single beam in fig. 5.28. both for the *x*- and *z*-deflection. Therefore the stiffness ratio $R = R_{guide} : R_{single} = 1$.

One could possibly ask why a larger R_{guide} can not be obtained, for example by giving the end of the flexures freedom to rotate around the *z*-axis. In order to realize this joints are needed. These can not be realized because in practice the flexures will already have the minimum width of 2 μm, as defined by the photolithography. Well regarded the construction in fig. 5.29 is over-determined twice. This could be solved by introducing two extra degrees of freedom in the shuttle. Also it can be solved by replacing the twin beams between the slider and the intermediate bodies by a single beam with double *x*-stiffness. This means that the width of this

beam has to be $2^{1/3}$ times the width of the initial flexures. Therefore, the *z*-stiffness of the new beam will increase only by this factor $2^{1/3}$ and the ratio *R* will decrease. If the spacing between the twin beams is kept small, we expect that concerning the degrees of freedom they will nearly act as one beam. The positive features of this linear guidance design are: The optimal stiffness ratio $R = 1$ between z-direction and x-direction is reached. The structure is (approximately) not over-determined. The motion is a straight line. It is possible to move in the positive and negative x-direction. The *y*-stiffness is large, because the intermediate bodies cannot rotate round the z-axis. The negative features are: The slider is loaded with a torque during loading in the z-direction, due to the asymmetrical placing of the suspension beams. The beams must be quite long in order not to be too stiff. The stiffness in the y-direction is highest in the starting position. When the suspension deflects, a force acting in the *y*-direction can induce a force in *x*-direction.

The equations for the *x*-stiffness and *z*-stiffness of the linear guidance (two crab-flexures) are: $k_{x,guide} = 2k_{x,single}$ and $k_{z,guide} = 2k_{z,single}$, with $k_{x,single}$ and $k_{z,single}$ as defined in eq. (5.15). The *x*-stiffness of the linear guidance is designed at 1 μN / μm, which leads to $L = 229$ μm with $E = 150$ GPa, t = 5 μm and $w = 2$ μm.

Other Motor Configurations

The motor explained above is the most basic configuration. Other configurations which have been made are: Uni-directional with double number of drive units at each side of the shuttle, bi-directional with in total four drive units (fig. 5.30), and the basic configuration connected to a displacement meter with 50x displacement amplification (see appendix D for lay-out).

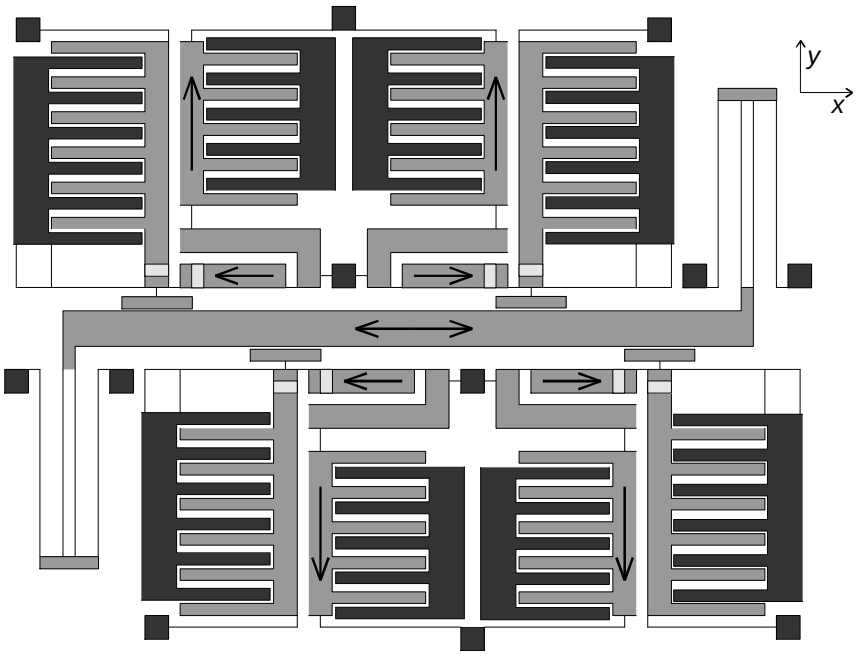

Fig. 5.30: Lay-out of motor the bi-directional motor. The dark gray parts are fixed to the substrate by silicon dioxide, the medium gray structures are suspended free parts. The light gray areas are undoped and serve as insulator.

5.4.5 Fabrication

Motors are fabricated by a three mask surface micromachining process. In the first mask step alignment marks are etched in the bare wafer surface by RIE. The etching process applied is tuned to roughen the wafer surface, which may help to reduce stiction. Next the 2.3 μm thick sacrificial silicon dioxide layer is grown by wet oxidation. Next, a 5.3 μm polysilicon structural layer is deposited by LPCVD. On top a 0.5 μm silicon dioxide mask layer is deposited by PECVD. Then the dope mask is applied and patterned, to mask the regions which should not be doped with Boron. After Boron doping using a solid source, the mask is removed and a new silicon dioxide layer (1.2 μm) is deposited by PECVD. This mask is used to enclose the doped polysilicon during the 3 hours post-anneal, which is needed to obtain a uniform distribution of the Boron in the polysilicon layer. In the third mask step, the oxide mask is patterned and the polysilicon is structured by RIE. Next, silicon nitride side-wall spacers are created, partly underneath the polysilicon structures. In the final step the sacrificial oxide is etched in 50% HF using timed etching to keep wide structures anchored. Freeze drying is employed to remove the liquid from the wafer, avoiding capillary forces pulling down the structures. A detailed process sequence is given in appendix D. The appendix includes a print of the mask lay-outs. Fig. 5.31 shows a close up of one of the undoped regions (indicated by the dotted line). Fig. 5.32 a-d show SEM-photographs of a fabricated motor. The roughness of the substrate wafer, as well as the nitride side-wall spacers are clearly visible in fig. 5.32d.

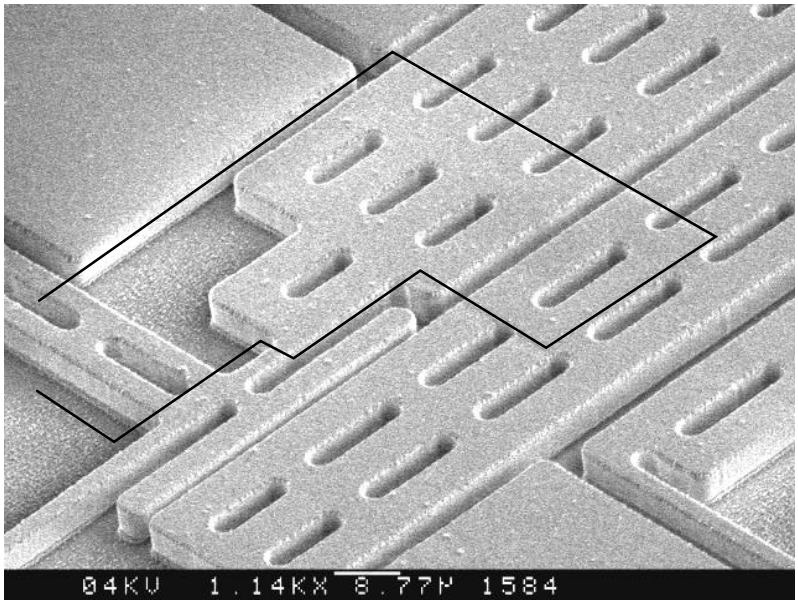

Figure 5.31: Close-up of a clamp and part of the shuttle with the SiO_2 sacrificial layer still present). The dotted line marks the position of the former doping mask

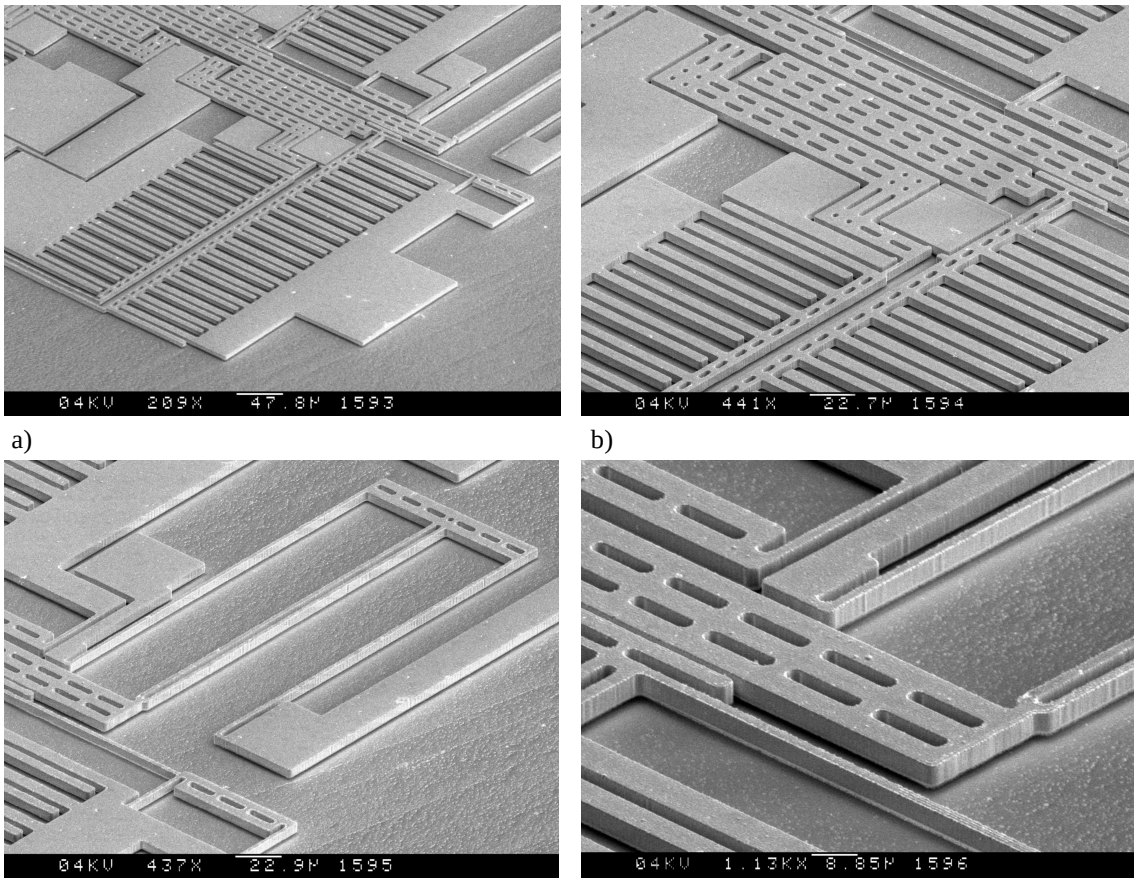

Figure 5.32: SEM-photographs of a fabricated motor. a) Overview of a drive unit. b) Close-up of the drive unit. c) One of the two elastic structures composing the linear guidance. d) Close-up of the shuttle with a clamp shoe, clamp suspension and part of the linear guidance. The roughness of the substrate wafer and the silicon nitride side-wall spacers are clearly visible.

5.4.6 Experiments

Test of the clamps, max. clamp voltage

First we have tested if the maximum voltage, 50 V, can be applied across the insulating silicon nitride in the clamp. Fig. 5.33 shows a cross section of an activated clamp. The most probable path for break down is through air, at the top of the clamp. We could apply 65 V across the silicon nitride layers, without the occurrence of break down. Assuming a straight path with a length of 0.32 μm, this corresponds with a field strength of 2×10^8 V/m. This is equal to the expected highest possible field strength as given in section 2.5. In this section the break down field was given for a 2 μm gap. The gap is much smaller in the realized clamps. Possibly, this allows even higher field strengths.

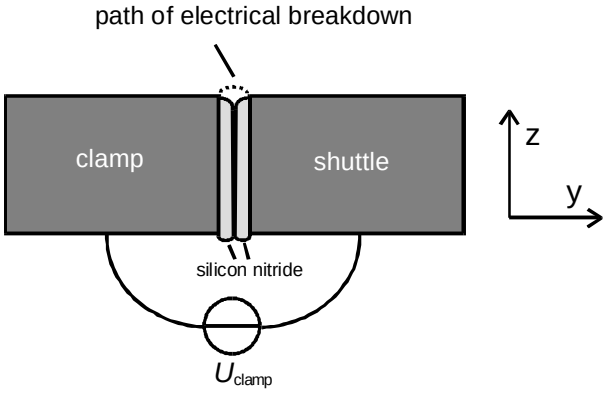

Figure 5.33: Cross section of an activated clamp. The most probable path for break down is through the air, just above the insulator.

Test of the clamps, friction

Static friction has been measured in a clamp, by displacing the shuttle by hand (using a probe needle). The procedure is as follows: Displace the shuttle, clamp with a high voltage, reduce the voltage until the slider starts to slide back driven by the elastic deformation force of the suspension. This voltage we call the critical voltage. The initial shuttle displacement times the stiffness of the suspension gives the measured friction force. The accompanying clamp force F_{clamp} is calculated similarly to the calculation in section 4.4: $F_{clamp} = F_{elec}$-F_{spring}. With F_{elec} the generated electrostatic clamp force (including pre-clamp actuation) and F_{spring} the restoring force of the clamp-shoe suspension. The relevant dimensions of the characterized clamp are listed in table 5.1. Fig. 5.34 shows the measured shuttle displacement vs. critical clamp voltages squared. Because of spread in the measurement results, the experiment was repeated three times. In the active state the restoring spring force F_{spring} = 15 μN. The (calculated) electrostatic clamp force F_{elec} = 3.6 mN at 50 V applied, assuming that the silicon nitride side-walls of the clamp shoe and the shuttle perfectly. Assuming a friction coefficient m = 0.5 the calculated friction force at 50 V applied equals 1.7 mN. This is much larger than the measured friction force at 50 V applied: For U_{crit}^2 = 2500 V^2 the measured friction force value equals (shuttle displacement x suspension stiffness) = (14 ± 2 μm) x 2.7 μN / μm = 4 ± 1 x 10^1 μN. The most plausible explanation for the discrepancy is the effective air gap between the insulator layers of the clamp shoe and the shuttle, due to surface roughness and non- parallel contact surfaces. The discrepancy between measured and calculated friction force can be explained by a 0.3 μN effective air gap thickness, which seems to be a reasonable value for the side-walls of RIE etched polysilicon structures. Using this value for the air gap thickness, the friction coefficient can be estimated to be: m = 0.3 ± 0.1. In the previous calculation we have neglected possible adhesion forces in the clamp. Including adhesion will lead to a larger estimated effective air gap. The measured friction force at 50V applied equals 40 μN. This is smaller than the needed 0.1 mN, however it is large enough to test the concept.

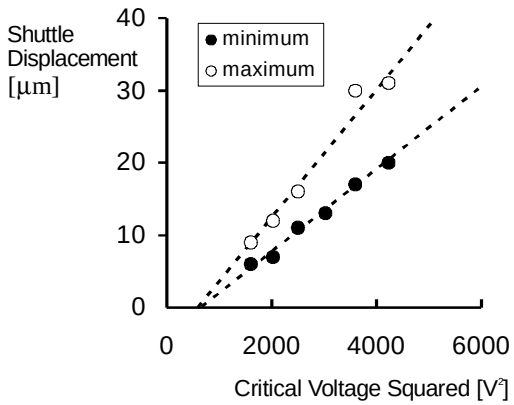

Figure 5.34: The measured shuttle displacement vs. critical clamp voltages squared ($U^2_{critical}$).

Stiffness of clamp suspension	8.8 μN / μm (based on 2.2 μm wide springs)
Stiffness of shuttle suspension	2.7 μN / μm
Initial gap between clamp shoe and shuttle	1.8 μm
Gap in pre-clamp actuator with clamp on	2.2 μm.
Active area of the clamp shoe	5 x 50 μm^2
Active area of pre-clamp actuator	15 x 5 μm x 100 μm = 7.5 x 10^3 μm^2
Thickness of twice the silicon nitride layer	0.32 μm

Table 5.1: Dimensions and stiffness in friction experiment

Walking Experiments

The walking motion has been tested by applying a drive voltage similar to the one shown in fig. 5.15. Using the strain meter (see appendix D) it could be made visible that generation of the first step was successful. The exact step size could not been measured using our optical microscope set up. We estimated that the strain pointer deflection is in the 1-3 μm range. This is in correspondence with the 50x amplification of the strain meter, and the designed 50 nm step size. In the experiments it became clear that the voltage required to drive the propulsion actuator was at least 55 V. This is caused by slightly wider structures than designed, and by insufficient decoupling of the clamp and the propulsion actuator. During the stroke of the pre-clamp actuator, a movement in the propulsion actuator is visible. This coupling results in enlargement of the initial gap in the propulsion actuator. Therefore, the pull-in voltage shifts to a higher level. To continue the experiments we used voltages up to 65 V to drive the propulsion actuator. No pull-down and no break down phenomena have been observed. We have analyzed the coupling of the two actuators via the force transmitter and the lever, and found that the movement of the propulsion actuator induced by the clamp actuator is caused by the shear force exerted by the force-transmitter on the lever (acting at the same point but perpendicular to F_{out} in fig. 5.20).

It turned out not to be possible to add a new step to the first step. When the second clamp hits the shuttle, apparently the first one releases the shuttle for a short while, and the shuttle returns to its initial position. This process could be confirmed by introducing a large displacement to the shuttle by means of manipulation with a probe needle (several micrometers), then activate first clamp and check if the friction is large enough to keep the shuttle in place. This is the case, however the shuttle snaps back at the moment that the second clamp hits the shuttle. The explanation is that apparently the second clamp transfers part of its momentum to the shuttle and the first clamp. Using the theory of section 2.3.3, it can confirmed that the kinetic energy gained by the second clamp after pull-in until the moment of impact, is large enough to separate the (activated) first clamp and the shuttle.

5.4.7 Conclusions Concept *C*

The use of mechanical leverage to increase the generated force of electrostatic linear motors has been investigated. It was shown both by stiffness calculations that it is possible to drive a lever with a micromechanical electrostatic actuator. Using the 50x amplifying strain meter, it was confirmed experimentally that 2 μm generated steps are transformed down into sub-micron displacements, and that the elastic joints in the lever can be deflected using an electrostatic actuator driven at moderate voltage (< 60 V).

The most difficult design issue is how to build a clamp which is able to: (1) close the initial gap of 2 μm, (2) once the clamp gap has been closed generate more than 0.2 mN clamp force. Two possible solutions have been presented: Pre-tension to maintain contact between the clamps and the shuttle continuously, and generation of the clamp force by applying a voltage across the insulators at both sides of the clamp interface. This latter method can be implemented using available microfabrication processes, and has been chosen. It was shown that it is possible to make the clamp suspension sufficiently stiff in the *z*-direction to allow a voltage difference between the clamp shoe and the substrate, without pull-down. The clamp has been tested by measuring the friction in between the clamp shoe and the shuttle as a function of the clamp voltage. This experiment showed that the friction force is much too low (a factor 7). This is probably caused by surface roughness and/or non-parallel clamp surfaces. In section 5.2.2 it was shown that the clamp force is very sensitive to the existence of a small air gap in the clamp.

Walking motion could not be generated: After the first step has been made, the impact of the second clamp making contact with the shuttle causes the first clamp to release the shuttle. Due to this event the first step is lost. The impact can be avoided when the clamp feet stay in contact with the shuttle continuously. In order to realize this, we recommend to develop clamps with a pre-tension spring.

5.5 Conclusions

In this chapter we have shown the feasibility of the implementation of walking motion in a laterally driven MEMS mechanisms, fabricated using the MESA surface micromachining

process. The maximum produced displacement was 15 μm, limited by the elastic linear guidance. The maximum produced force was 3 μN, with a 40V driving voltage. We attempted to increase the generated force by implementation of a lever. The most difficult issue in this attempt was the increase of the clamp force. Our choice to generate the clamp force by applying a voltage difference between the clamp shoe and the shuttle did not result in walking motion. Apparently, the closure of the initial gap in the clamps by the pre-clamp actuators genereated an impact strong enough to release the already active clamp. An alternative clamp principle which does not have this problem, is the use of a pre-clamp spring to keep the clamp shoe in permanent contact with the shuttle.

5.6 Acknowledgement

The author wishes to thank Tonny Sonnenberg and Robert Molenaar for their important contribution to the design, fabrication and testing of concept *B* and *C* respectively.

5.7 Literature

[1] Yeh, E.J.J. Kruglick, K.S.J. Pister, Microelectromechanical components for articulated microrobots, Proc. Int. Conf. On Solid-State Sensors and Actuators, and Eurosensors IX, Stockholm Sweden, June 25-29, 1995, pp. 346-349.

[2] Baltzer, Th. Kraus, E.Obermeier, A linear stepping actuator in surface micromachining technology for low volatges and large displacements. Proc. Int. Conf. On Solid-State Sensors and Actuators, Chicago, Ill. USA, June 16-19 1997, pp. 781-784.

[3] R. Legtenberg,"Electrostatic Actuators Fabricated by Surface Micromachining Techniques", Ph.D. Thesis University of Twente, 1996, ISBN 90-3650796-0.

[4] R. Legtenberg, E. Berenschot, M. Elwenspoek, J. Fluitman,"Electrostatic curved electrode actuators", Proc. IEEE Workshop on MEMS '95, Amsterdam, The Netherlands, Jan. 29 - Febr. 2, 1995, pp. 37-42.

[5] N.R.Tas, A.H. Sonnenberg, H.V. Jansen, R. Legtenberg, M.C. Elwenspoek,"Stiction in surface micromachining", Journal of Micromechanics and Microengineering, Vol. 6, 1996, pp. 385-397.

[6] J.M. Gere, and S.P. Timoshenko,"Mechanics of Materials", 3rd ed., Chapman & Hall, London, 1991.

[7] M.P. Koster,"Constructieprincipes", ISBN 9036508320, University of Twente Press, Enschede, The Netherlands, 1996.

[8] R. Molenaar,"Design of a Powerful two-dimensional precision micro motor in a silicon layer", M.Sc. thesis, Faculty of Mechanical Engineering, University of Twente, Report no. WA519.

6

The Shuffle Motor: A Normally Driven Linear Electrostatic Motor

The shuffle motor is a linear electrostatic walking motor, employing a mechanical transformation to obtain an amplification of forces and reduction of the step size. The motor is normally driven in order to maximize the electrode area. The motor consists of three polysilicon and two silicon nitride layers and has been fabricated using surface micromachining. An energy model has been made to calculate the step size and the driving voltage as a function of the load force and the motor geometry. In theory the actuator is able to deliver up to 1 mN at 30V driving voltage. Tests show an effective step size of about 85 nm and a produced force of 43 μN at 40V driving voltage. The smaller than expected force is caused by weak clamping, which is the consequence of the modulated AC-voltage drive. The AC-voltage drive was introduced to reduce electrostatic stiction by charging of the silicon nitride insulating layer covering the bottom electrodes.

6.1 Introduction

This chapter deals with design, modeling and realization of normally (perpendicular to the wafer surface) driven electrostatic motor, which employs walking motion. In the shuffle motor we have maximized the generated force firstly by using electrodes parallel to the wafer surface in order to obtain a large active area, and secondly by employing a lever. This way a force of more than 1 mN can be produced in an actuator volume of 100x200x2 μm^3, using a driving voltage of only 30 V [1]. The produced steps are small, typically between 10 and 100 nm, and therefore sub-micrometer positioning accuracy can be achieved. In the shuffle motor a cyclic motion is used to produce a large stroke of the actuator, by adding the small single steps. The concept of the shuffle motor was already presented in [1], however the successful realization was difficult due to the lack of an accurate transducer model and due to stiction problems in the clamp feet of the motor. These problems have been overcome now.

6.2. Principle of Operation

Fig. 6.1 shows the principle of the shuffle cycle. First the front clamp is activated and the actuator plate is deflected downward. This causes contraction of the actuator and the back

This Chapter is based on:
N. Tas, J. Wissink, L. Sander, Th. Lammerink, M. Elwenspoek,"The shuffle motor: a high force, high precision linear electrostatic stepper motor", Proc. 8th Int. Conf. on Solid-State Sensors and Actuators (Transducers '97), Chicago, Il., USA, June 16-19 , 1997, Vol. 2, pp. 777-780.
N. Tas, J. Wissink, L. Sander, Th. Lammerink, M. Elwenspoek," Modeling, design and testing of the electrostatic shuffle motor", Sensors and Actuators A, Vol. 70, 1998, pp. 171-178.

clamp is pulled forward. Next the back clamp is activated, the front clamp and the actuator plate are released. The plate stretches and the front clamp is pushed forward.

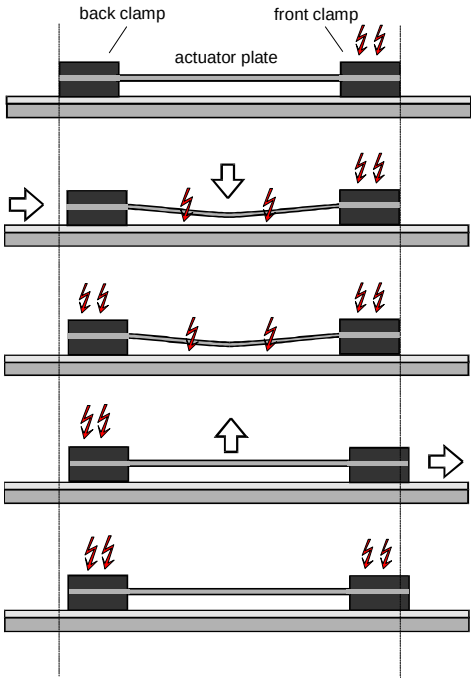

Figure 6.1: Principle of operation. First the front clamp is activated and the actuator plate is deflected downward. This causes contraction of the actuator and the back clamp is pulled forward. Next the back clamp is activated, the front clamp and the actuator plate are released. The plate stretches and the front clamp is pushed forward.

The electrostatic normal force acting on the actuator plate induces a friction force in the feet of about the same magnitude. Due to the built-in mechanical transformation, the developed lateral force can be larger than the friction force and can be high enough to make the feet sliding. The deformation of the plate by the electrostatic forces leads to a small but forceful contraction of the plate. A plate length of 200 µm and a center deflection between 0 and 2 µm, gives a changing transformation ratio i from 0 to 1/25 [2], where i is defined as the change of the lateral contraction Δd divided by the change of the center deflection y (see fig. 6.2). Preliminary calculations using a simplified, triangular deflection profile of the plate, show that with the dimensions mentioned, a contraction force of 1 mN can be generated with a driving voltage below 50V [1, 2]. More detailed calculations, presented in section 6.4.2, show that a 1 mN contraction force can even be reached at 30 V driving voltage.

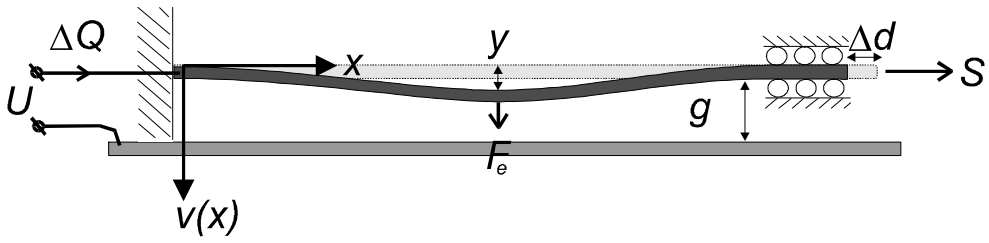

Figure 6.2: Ideal Physical Model of the transducer, where x is the position along the plate, $v(x)$ is the deflection of the plate, y is the center deflection, F_e is the electrostatic force concentrated in the center, g is the initial gap size, S is the tensile load force and Δd is the contraction which produces the step. The transducer converts electrical work $U \cdot \Delta Q$ into mechanical work $S \cdot \Delta d$.

6.3. Model of the Transducer

The actuator plate can be considered as an energy buffer with two power ports. It converts the electrical work $U \cdot \Delta Q$ into mechanical work $S \cdot \Delta d$ (fig. 6.2). An energy model has been made that expresses developed stroke Δd as a function of the tensile load force S and voltage U applied between the deflecting plate and the stator electrode.

6.3.1 Plate stiffness

The deflection of the actuator plate is described by a fourth order non-linear differential equation [3]. It is hard to solve this equation analytically. A solution could be obtained for the case where the electrostatic force is concentrated in the center of the plate, and the case where the electrostatic force is taken uniform along the plate length. The two shape functions can be used to enclose the solution to the original non-linear problem, where the electrostatic force distribution depends on the plate deflection. We introduce the model for the central force case here. For the uniformly distributed force case only the results are given (section 6.3.4).
The deflection $v(x)$ of the plate which is under a tensile force S, due to the central force F_e (see fig.6.2) is described by the following differential equation:

$$EI \frac{d^4 v(x)}{dx^4} - S \frac{d^2 v(x)}{dx^2} = 0 \qquad (6.1)$$

with boundary conditions $v(0) = 0$, $v'(0) = v'(l) = 0$ and $EI \cdot v'''(l) = \frac{1}{2} F_e$ and EI is the bending stiffness. The factor ½ results from the fact that we solve $v(x)$ for half of the plate. The solution to eq. (6.1) is given by:

$$v(F_e, K, z) = \frac{F_e l^3}{EI} \frac{1 - \cosh(K) - \cosh(K z) + z K \sinh(K) + \cosh(K(z-1))}{2 K^3 \sinh(K)} \qquad (6.2)$$

Where z is the normalized distance using half the plate length l, $z = x / l$ ($0 < z < 1$). The load S is present in parameter K which is defined as:

$$K \equiv l \cdot \sqrt{\frac{S}{EI}} \qquad (6.3)$$

The parameter K determines if the transducer is bending dominated or tensile force dominated. The deflection function can be split in an amplitude function $y(F_e, K)$ equal to the center deflection, and a shape function $V(K, z)$. Both amplitude and shape function depend on K:

$$v(K, z) = y(F_e, K) \cdot V(K, z) \qquad (6.4)$$

This way eq. (6.2) can be rewritten:

$$y(F_e, K) = \frac{F_e l^3}{24EI} \cdot \left\{ 3 \frac{\left(\frac{1}{2}K\right) - \tanh(\frac{1}{2}K)}{(\frac{1}{2}K)^3} \right\} \tag{6.5a}$$

$$V(K,z) = \frac{1 - \cosh(K) - \cosh(Kz) + zK\sinh(K) + \cosh(K(z-1))}{2 - 2\cosh(K) + K\sinh(K)} \tag{6.5b}$$

The center deflection y expressed in eq. (6.5a) depends linearly on F_e. We can therefore derive a stiffness function $k(K) = F_e / y$:

$$k(K) = \frac{24EI}{l^3} \cdot \left\{ \frac{1}{3} \frac{\left(\frac{1}{2}K\right)^3}{\left(\frac{1}{2}K\right) - \tanh(\frac{1}{2}K)} \right\} \equiv \frac{24EI}{l^3} G(K) \tag{6.6}$$

In eq. (6.6) $G(K)$ is the stiffness factor, which is a measure for the stiffening due to the tensile force S.

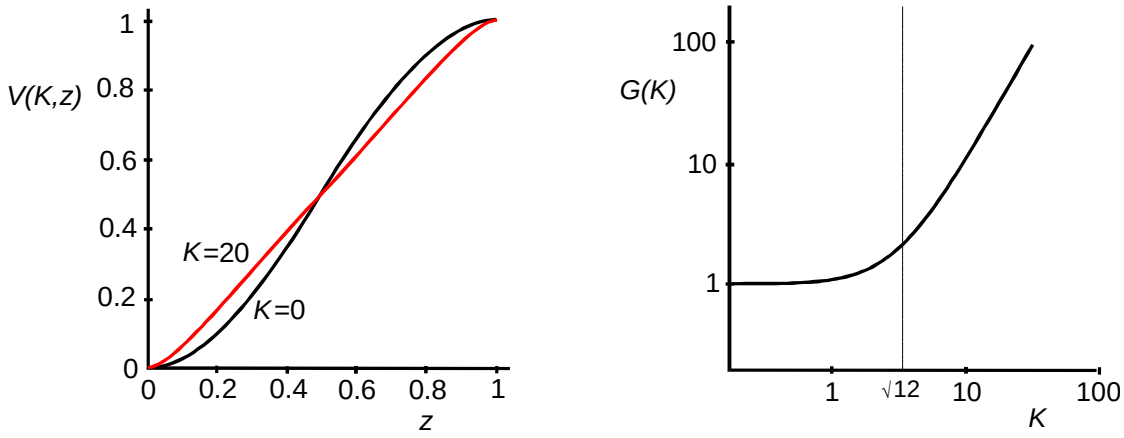

a) b)

Figure 6.3a) The shape function $V(K, z)$ versus z for two values of K. For K=0 the bending stiffness dominates, for K=20 the stiffness due to the tensile force dominates and the plate is pulled straight. b) The stiffness factor $G(K)$, as expressed by eq. (6.6). The turn-over point K=√12 where stiffening due to the tensile force becomes dominant is indicated.

In fig. 6.3a the shape function $V(K, z)$ is plotted for two values of K. At K = 20 the plate is pulled straight by the tensile load force. Fig. 6.3b shows the stiffness factor $G(K)$. For small K the effective stiffness is bending dominated and is consistent with the formulas for pure bending [4]:

$$\lim_{K\downarrow 0} k(K) = k_b = \frac{F_e}{y} = 24\frac{EI}{l^3} \tag{6.7}$$

For large K the tensile force acts as an effective stiffness F_e / y and the normal force F_e increases linearly with the center deflection y:

$$\lim_{K\to\infty} k(K) = k_s = \frac{F_e}{y} = \frac{2\cdot EI\cdot K^2}{l^3} = \frac{2S}{l} \tag{6.8}$$

At the turnover point the stiffness ratio is $k_s / k_b = 1$. From eq. (6.7) and (6.8) it follows that this is at $K^2 = 12$.

6.3.2 Relation between plate deflection and driving voltage

The plate driven by a constant voltage U shows pull-in behavior when a certain fraction of the initial gap is closed. The motor will be operated beyond this point of pull-in, therefore it gives a first indication for the driving voltage needed. The full-step size is estimated from the situation where the center of the plate contacts the bottom electrode ($y = g$). Using eq. (6.4) and by defining the normalized center deflection $a = y / g$ we can write for the capacitance:

$$C(K,a) = 2\int_0^l \frac{ew}{g - v(K,x)}\,\mathrm{d}x = 2\frac{e\cdot w\cdot l}{g}\int_0^1 \frac{1}{1 - a\cdot V(K,z)}\,\mathrm{d}z \equiv 2\frac{e\cdot w\cdot l}{g} C_n(K,a) \equiv C_0 C_n(K,a) \tag{6.9}$$

Where $C_n(K,a)$ is the normalized capacitance function, C_0 equals the zero deflection capacitance, w is the width of the plate and e is the permittivity in the gap. Pull-in behaviour of the voltage controlled actuator is studied from the Legendre transformed energy function:

$$W'(a,U) = W(a,U) - Q\cdot U = -\frac{1}{2}C_0 C_n(K,a)U^2 + \frac{1}{2}k(K)(ag)^2 \tag{6.10}$$

At voltages below the pull-in voltage, a relation between the equilibrium deflection a and applied voltage U can be found from $\partial W'(a,K,U) / \partial a = 0$:

$$U^2 = \frac{2a}{\frac{\mathrm{d}C_n}{\mathrm{d}a}(K,a)}\frac{k(K)\cdot g^2}{C_0} \tag{6.11}$$

The equilibrium becomes unstable once the second derivative of $W'(a, K, U)$ equals zero (turning from positive to negative). Combination with eq. (6.11) gives a dimensionless equation for the pull-in deflection. This equation has been solved numerically, yielding a pull-in center deflection increasing from $a_{pi} = 0.40$ for $K = 0$ to $a_{pi} = 0.44$ for $K = \infty$. Eq. (6.11) can

be rewritten using eq. (6.6), the definition of C_0 from eq. (6.9), and substitution of $I = wt^3 / 12$:

$$U_{\mathrm{pi}} = \pm\sqrt{G(K)}\sqrt{\frac{2a_{\mathrm{pi}}}{\frac{\mathrm{d}C_{\mathrm{n}}}{\mathrm{d}a}(K,a_{\mathrm{pi}})}\frac{E\cdot t^3\cdot g^3}{e\cdot l^4}} \qquad (6.12)$$

Where t is the thickness of the plate. Eq. (6.12) described the pull-in voltage as a function of the geometry and the tensile load force S which is present in the stiffness factor $G(K)$. The dimensionless factor $2a_{\mathrm{pi}} / (\mathrm{d}C_{\mathrm{n}}(K,a_{\mathrm{pi}}) / \mathrm{d}a)$ increases from 0.75 for K=0 to 0.83 for K=∞. For small K the stiffness factor $G(K)$ equals 1 and the the pull-in voltage is independent of the load force S:

$$U_{\mathrm{pi}} = \pm\sqrt{0.75\frac{E\cdot t^3\cdot g^3}{e\cdot l^4}} \qquad (K<<\sqrt{12}) \qquad (6.13)$$

For K>>√12 the pull-in voltage is determined by the load force S and does not depend on the bending stiffness:

$$U_{\mathrm{pi}} = \pm\sqrt{0.83\frac{S\cdot g^3}{e\cdot l^2\cdot w}} \qquad (K>>\sqrt{12}) \qquad (6.14)$$

In fig. 6.7 the pull-in voltage as a function of the load force S is plotted for the geometry that is chosen for the realized shuffle motor.

6.3.3 Contraction and transformation ratio

The lateral contraction can be found by calculating the path length along the plate using the deflection function $v(x)$. For small slopes $\mathrm{d}v/\mathrm{d}x$ the contraction is given by:

$$\Delta d = 2\int_0^l\sqrt{\left(1+\left(\frac{\mathrm{d}v}{\mathrm{d}x}\right)^2\right)}\mathrm{d}x - 2l \cong \int_0^l\left(\frac{\mathrm{d}v}{\mathrm{d}x}\right)^2\mathrm{d}x = \frac{y^2}{l}\cdot\int_0^1\left(\frac{\mathrm{d}V}{\mathrm{d}z}\right)^2\mathrm{d}z \qquad (6.15)$$

Where y is the plate center deflection of the plate and $z = x / l$ is the normalized position along the plate. The central force shape function v approximates the triangle shape for large K. For small K the plate is in the pure bending state, and curves of the deformed plate are smoother and the path length is slightly larger. Calculating the extremes of the integral in Eq. (6.15) yields:

$$\lim_{K\downarrow 0}\Delta d = \tfrac{6}{5}\frac{y^2}{l} \qquad (6.16a)$$

$$\lim_{K\to\infty} \Delta d = \frac{y^2}{l} \tag{6.16b}$$

From eq. (6.16) the transformation ratio $i = \partial(Dd) / \partial y$ can be derived:

$$\lim_{K\downarrow 0} i(y) = \frac{6}{5}\frac{2y}{l} \tag{6.17a}$$

$$\lim_{K\to\infty} i(y) = \frac{2y}{l} \tag{6.17b}$$

6.3.4 Uniformly spread electrostatic force model

A similar analysis has been performed for the case where the electrostatic force is spread uniformly along the plate. This results in an expression for the pull-in voltage similar to eq. (6.12). The pull-in voltages differ less than 1% for $K = 0$. For large K the uniform force shape yields a pull-in voltage that is 5% smaller than for the central force shape. The pull-in deflection is $y / g = 0.40$ for all K. The contraction for the uniform force case has been calculated using eq. (6.15) where the integral yields 128/105 for small K and 4/3 for large K. These slightly larger factors compared to the central force shape are a result of the smoother curves in the plate for the uniform force shape.

The shape functions for the central force model and for the uniformly spread force model enclose the solution to the original non-linear problem, where the force distribution depends on the deflection. Therefore, we can conclude that eq. (6.12) predicts the pull-in voltage for the non-linear problem with less than 5% error.

6.3.5 Design rules for the transducer plate

Equation (6.12) can be used to choose the dimensions of the actuator plate, for a given tensile load force S, maximum driving voltage, and elastic properties of the plate material. The second design rule is given by eq. (6.16), which can be used to choose the dimensions of the plate for a given desired step size. The third design rule is for the dimensions of the plate for a given step size. Basically the step size as predicted by eq. (6.16) should be larger than the loss of step due to the limited tensile stiffness of the plate. The step loss Δe is given by:

$$\Delta e = S \cdot \frac{2l}{E \cdot t \cdot w} \tag{6.18}$$

6.4. Design of the Shuffle Motor

6.4.1 Lay-out of the motor

The moving part of the motor consists of two polysilicon layers. A thin layer for the actuator plate, and a thick layer for the frame in which the plate is suspended. The frame consists of a

front part and a back part, connected by the connection springs and by the plate. Both the front and the back part contain two clamp feet (fig. 6.4). Polysilicon electrodes have been made underneath the feet and the plate, so that the front feet, the back feet and the plate can be activated independently. The electrodes are covered by a insulating silicon nitride layer. The moving part is grounded during operation.

1. Elevated front part
2. Elevated back part
3. Actuator plate
4. Connection springs
5. Support springs
6. Back clamp feet
7. Front clamp feet
8. Base electrodes
9. Anchors

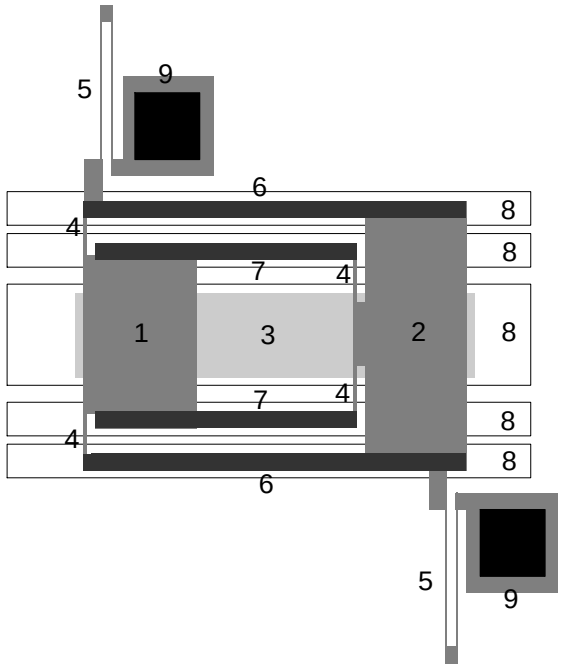

Fig. 6.4: The frame consists of an elevated part (medium gray) and a lower part (dark gray). The lower part composes the four clamp feet, resting on the electrodes. The elevated part consists of the folded support springs and the large stiff parts that connect the clamp feet and the actuator plate (light gray). The support springs are anchored at the black squares.

The frame is contracted by deflecting the plate downward (fig. 6.5), and stretches due to the bending stiffness of the plate, and due to the stiffness of the connection springs. The stiffness of the four connection springs together is about 1200 μN / μm.

Figure 6.5: Deformation of the connection springs due to contraction of the plate (the step size has been exaggerated). Both the bending stiffness and the connection springs push the two frame parts apart when the plate is released.

The whole moving part is supported by two folded springs which serve as a linear guidance with a stiffness of 1 μN / μm. The folded springs are also used to ground the moving part. The total size of the moving part excluding the guidance springs is 500 x 400 μm^2.

6.4.2 Design of the clamp feet

In the shuffle motor electrically controllable clamp feet are needed, which are continuously in contact with the base. In the first design [1] adhesion forces induced large friction forces, also when the clamps were inactive. In the current design we have been able to reduce the adhesion forces to an acceptable low level by means of anti-sticking bumps that have been made all along the clamp feet. The bumps have a height of 150 nm and therefore the size g of the air gap equals 150 nm. The bumps are placed with a 10 μm spacing to minimize the bending of the feet due to the high electrostatic pressure. The total area A_{clamp} of the two inner clamp feet (the smallest) is 600 x 20 μm^2. The capacity C between the feet and the bottom electrodes is determined by g, A_{clamp}, the thickness t_{SiN} of the silicon nitride, and its permittivity $e_0 e_r = 8e_0$. A thickness of 0.5 μm has been chosen for the silicon nitride. This may seem to be quite thick, however this is necessary because the silicon nitride is slowly etched during the 50 % HF sacrificial layer etch. In the expression for the capacity, we neglect the contribution of the (larger) electrostatic pressure underneath the bumps. From the derivative of co-energy - $\frac{1}{2}C(g)U^2_{clamp}$ with respect to g the expression for the clamp force results:

$$F_{clamp} = \frac{1}{2}\frac{e_0 \cdot U^2 \cdot A_{clamp}}{(g + \frac{t_{SiN}}{e_r})^2} \qquad (6.19)$$

For a clamp voltage of 30 V and the parameter values as mentioned above, an electrostatic clamp force F_{clamp} = 1.1 mN results. This is enough, as its in the same order as the generated lateral force at 30V.

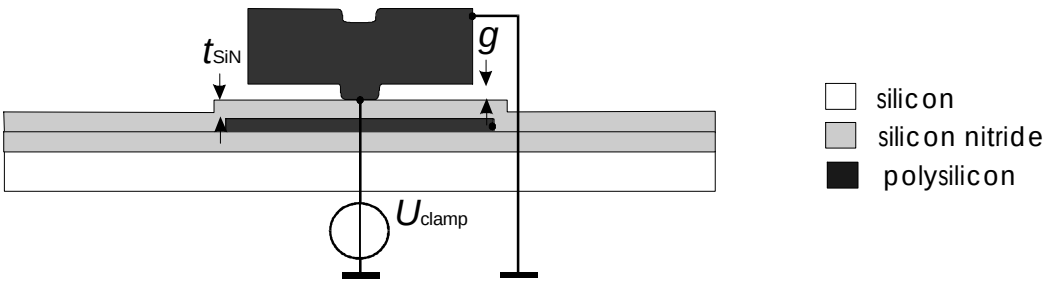

Figure 6.6: Cross section of the implemented electrostatic clamp. The electrostatic force is determined by the applied voltage U_{clamp}, the size of the air gap g, and the thickness t_{SiN} of the silicon nitride. The stand-off bumps touch the silicon nitride insulating layer and in the contact region free charge be transported from the charged clamp foot on to the silicon nitride.

The life-time of the shuffle motor is probably determined by the wear rate in the clamp feet, particularly in the bumps. The shape and the size of the bumps is not critical, therefore it is expected that the motor will be rather wear resistant.

6.4.3 Dimensions of the actuator plate

The plate pull-in voltage given by eq. (6.12) is used to choose the actuator dimensions. Figure 6.7 shows the pull-in voltage as a function of the tensile load force S for the chosen dimensions of the actuator: A thickness t of the plate of 0.5 μm, a width w = 100 μm, a length $2l$ = 200 μm and an initial gap size g = 2 μm.

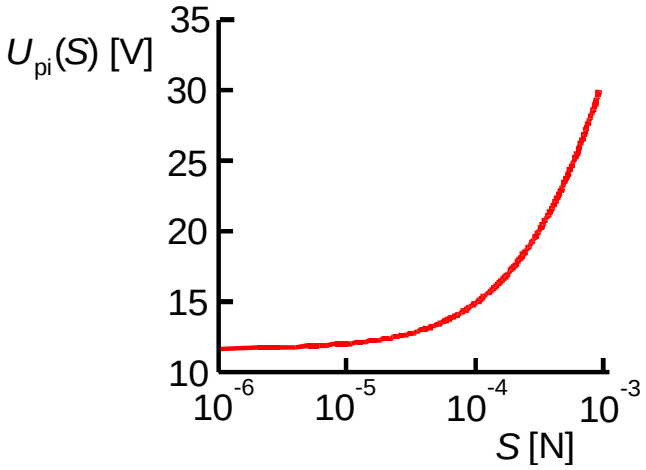

Figure 6.7: The pull-in voltage as a function of the tensile load force S, calculated using equation 12. The thickness t of the plate is 0.5 μm, the width w = 100 μm and the length $2l$ = 200 μm. A Young's modulus E = 150 GPa and the permittivity of air are used.

Eq. (6.16) gives a step size of 40 nm if the center of the plate just contacts the base ($y = g$). This is only an indication for the step size, because the deflection profile after pull-in is not taken into account in the model. Fig. 6.7 shows that a voltage of only 30V is enough to overcome a load force of 1 mN. The maximum load the actuator can pull is limited by the tensile stiffness of the actuator plate. In the current design, the tensile strain of the plate under a load of 1 mN is 27 nm, which is significant compared to the single step size. The nature of the load (e.g. friction, dynamic or constant) determines to what extent the limited tensile stiffness will cause loss of step size.

6.5 Fabrication process

The shuffle motor is fabricated using standard surface micromachining techniques. The final structure consists of three polysilicon layers, for the rails and the shields, the frame, and the actuator plate respectively. There are two silicon nitride layers, underneath and on top of the polysilicon actuation rails. The process sequence is treated briefly here, a detailed process scheme can be found in appendix E.

On a 3'' substrate wafer a 1.0 μm low stress LPCVD silicon nitride layer is grown to insulate the base electrodes from the substrate wafer. Next a 0.5 μm LPVCD polysilicon layer is deposited, doped with Boron by solid source indiffusion and patterned using RIE to form the electrodes. A second low stress LPCVD silicon nitride layer of 0.5 μm is grown to cover the electrodes. In this nitride layer the contact pads and anchor holes are etched using RIE. On

top of the nitride insulation layer the first sacrificial oxide layer (2.4 μm) is deposited using PECVD to create the gap between the actuator plate and ground electrode. The next layer is 0.5 μm of LPVCD polysilicon doped with boron, to form the actuator plate. After the patterning of the actuator plate (RIE) the first sacrificial layer is patterned (RIE). Only where the elevated parts in the frame are made **(**fig. 6.4), the oxide is kept. Next a 0.5 μm second sacrificial oxide layer is grown, using TEOS instead of PECVD to obtain better step coverage. This layer is used to release the clamp feet. The holes to form the anti sticking bumps (150 nm deep) and the plate-frame contact holes are etched in HF. Next, a 4.0 μm third LPCVD polysilicon frame layer is deposited and doped. Before patterning this layer, it is covered by a PECVD oxide layer and annealed at 1100 °C for three hours, in order to obtain a uniform distribution of the Boron dopant. This is important to avoid a stress gradient in the polysilicon. The thick polysilicon is patterned in RIE using a $SF_6/O_2/CHF_3$ plasma to form the frame. Last step is removing both sacrificial layers using 50% HF and freeze drying to avoid sticking of the free hanging structures. Holes have been etched in both the plate and the frame at intervals of 30 μm in order to shorten the sacrificial oxide etch time. In fig. 6.9 three cross sections are shown just before and after the sacrificial layer etch. Fig. 6.8 shows a close up around one of the two inner connection springs, and an overview of the shuffle motor with the actuator plate deflected downward.

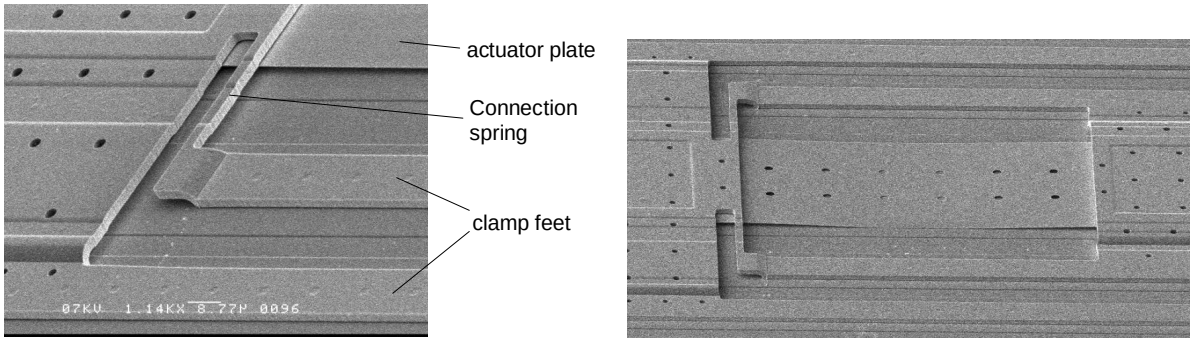

a) b)

Figure 6.8a) Close up around one of the two inner connection springs, showing the different levels in the motor. b) SEM picture of a motor with the actuator plate deflected downward.

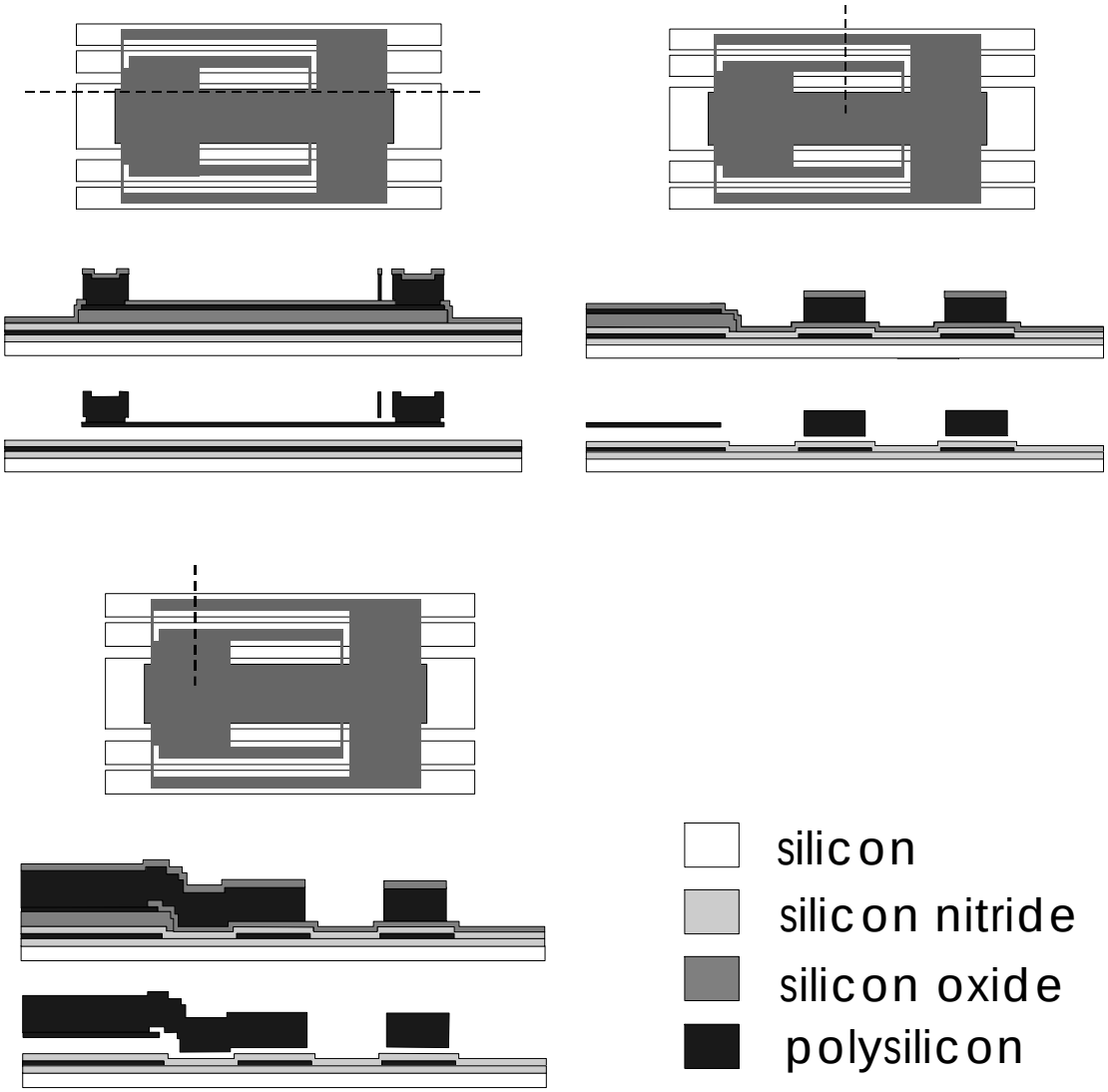

Figure 6.9: Cross sections just before and after the sacrificial oxide etching.

6.6 Experiments

6.6.1 Tests of the plate deflection

The measured zero load pull-in voltage varied between 12 and 13 V. This is reasonably close to the 11V predicted by the model. Voltages higher than the pull-in voltage resulted in the deflection as shown in fig. 6.12. The center part of the actuator plate is pulled flat to the bottom electrode. By increasing the voltage, the flat part increases and the effective step size increases. At 25 V the zero load step size is estimated by 140 nm. Repeated pull-in showed stiction of the actuator plate to the bottom electrode. The stiction is probably induced by charging of the insulating nitride covering the under electrode. Charge can be transferred from the charged plate to the surface of the silicon nitride when they contact. When the physical contact is broken, some charge may be left on the silicon nitride. The following observations support this explanation of the stiction:

- Actuator plate stiction disappeared after a few minutes.
- The cleaner the surface of the sample, the longer the stiction lasted.
- At low humidity the stiction was worst. Adsorbed water probably helps the discharging of the silicon nitride.
- Sometimes stiction disappeared after breathing on the sample.
- The voltage needed to activate the plate shifts up time if activation is repeated.

The stiction has been strongly reduced by applying a modulated AC voltage (fig. 6.10). The plate and the clamps have been activated with a 25 kHz square wave that changes polarity quickly compared to the mechanical response time of the plate. Therefore, the AC voltage results in the same deflection of the plate as a DC voltage with the same amplitude.

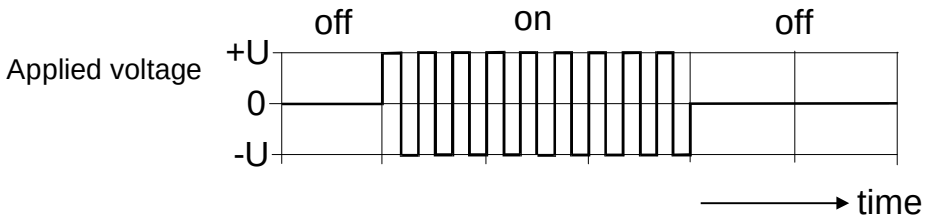

Figure 6.10: The modulated AC-voltage applied between the plate and the base electrode.

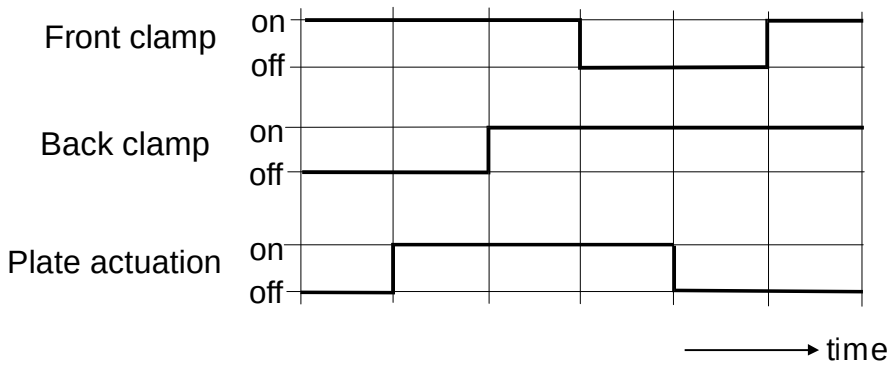

Figure 6.11: The control signals for a complete walking cycle. First the front clamp is activated. Next the plate is deflected, and the back clamp is activated. Then the plate is released and the front clamp is activated again. Finally, the back clamp is released and the cycle starts again.

6.6.2 Force and reach measurement

Motor tests have been done using the control signals shown in fig. 6.11. The modulated AC-voltage control has been used for both plate actuation and clamping. The maximum obtained reach was 43 μm (fig. 6.12) at a plate actuation voltage (amplitude) of 25 V and a clamp voltage (amplitude) of 40V and a stepping frequency of 1160 Hz. Based on the stiffness of the support springs, this corresponds with an effective generated force of 43 ± 13 μN. At 25 V the actuator should be able to produce a force up to 0.6 mN (See fig. 6.7). Slip in the clamps is the most probable explanation for the lower measured force. Considerable slip occurs when the AC-driving voltage is used. The clamps are shortly released when the voltage switches from positive to negative. This results in a dynamic equilibrium between walking forward and slipping backward.

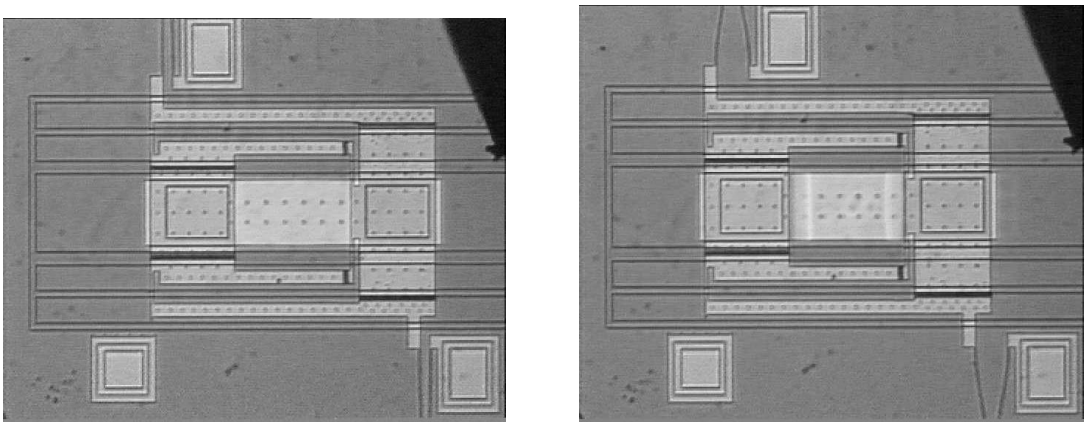

a) b)

Figure 6.12a) Microscope picture of the unactivated motor, and b) at maximum measured reach. The maximum measured reach is 43 μm, which corresponds with about 500 steps made. Note that the activated plate is pulled flat against the base electrode.

In order to increase the produced force, we have tried to apply a DC-voltage to the clamps in combination with a modulated AC-voltage on the actuator plate. This resulted in stiction in the clamps, probably again due to charging of the insulating nitride. A new design of the clamps where the charge induced stiction is diminished is recommended. We propose the design shown in fig. 6.14, which has only mechanical contact between equally biased conducting surfaces. In principle, this design can also be applied for creating electrical contact needed for biasing the moving structures, when the support springs are omitted. In practice, it will be a challenge to create good electrical contact, as in air a thin native oxide layer grows on the polysilicon surfaces.

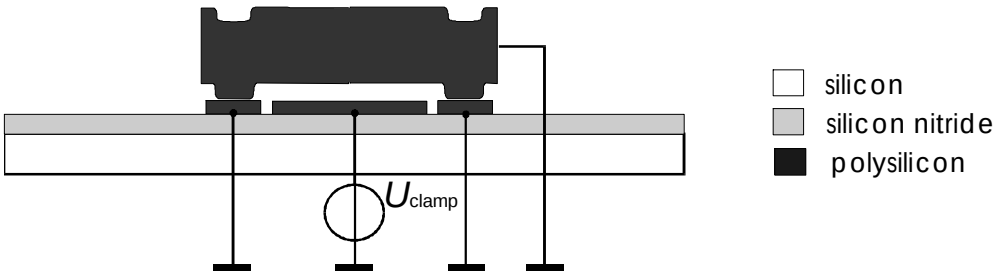

Figure 6.14: Proposed new clamp design. The bumps contact the grounded outer electrodes. Because both are of conducting polysilicon, it is expected that there will be no charge stored at the interface. The clamp force is generated by the voltage difference between the (grounded) clamp foot and the middle base electrode.

6.6.3 Speed measurements

The speed of the motor has been measured as a function of the cycle frequency (fig. 6.15). The highest measured speed of the motor is 100 ± 10 μm/s, at a cycle frequency of 1160 Hz. This frequency was limited by the driving electronics. Higher cycle frequencies should be possible, because the (zero load) resonance frequency of the actuator plate is about 60 kHz. It is expected that the maximum attainable speed is more than 1 mm/s. The measured speeds could be reproduced with a maximum deviation of 25% between three different

motors. The slope of the graph is a measure for the effective average step size, which is 85 ± 9 nm. The smaller than expected effective step size can be explained by the considerable slip in the clamps due to the used AC-driving voltage.

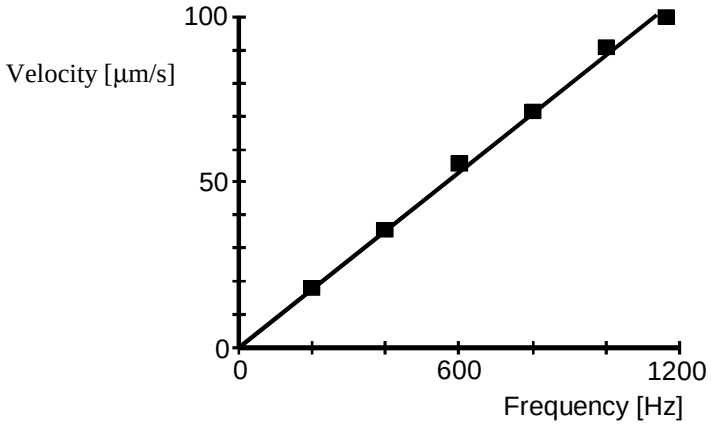

Figure 6.15: Measured velocity as a function of the cycle frequency. The inaccuracy in the velocity measurement is smaller than 10%. A voltage amplitude of 25 V is used to drive the plate, and an amplitude of 40 V is used to drive the clamps.

6.7 Discussion and Conclusions

This chapter shows the feasibility of the use of a mechanical transformation in order to increase both the force and the resolution of an electrostatic linear stepper motor. The key part in the motor is the contracting plate actuator, which is an effective implementation of the mechanical transformation. A detailed energy model of the bending plate transducer has been made, giving the output stroke as a function of the applied voltage and the load force. The model shows that forces as high as 1 mN can be produced with a realistic polysilicon actuator driven at only 30 V. Simple design rules have been extracted that facilitated the design of a walking motor based on the transducer. Testing of the walking motor showed stiction due to electrostatic charging of the silicon nitride insulator. The charging could be diminished by a modulated AC-voltage actuation. Walking motion has been produced at different cycle frequencies. In the measured frequency range (200-1160 Hz), the speed of the motor is proportional to the walking frequency. An effective average step size of 85 ± 9 nm has been determined from these measurements. A maximum force of 43 ± 13 μN has been measured at an applied actuator voltage of 25 V and a clamp voltage of 40 V. The generated force is comparable to the force produced by the scratch-drive actuator [5, 6], which is produced using similar fabrication process as the shuffle motor and has comparable dimensions. However, the shuffle motor is operated at slightly lower voltages. The force produced by the shuffle motor is now limited by the effective friction in the clamp feet, which is low due to the AC-driving voltage. Future work should concentrate on the improvement of the clamps in order to have the full benefit of the large force that can be generated by the plate actuator. A

new linear guidance, replacing the support springs, has to be developed in order to enlarge the reach of the motor. Electrical biasing of the moving part will be an important issue when the support springs are omitted.

6.8 Acknowledgment

This research is carried out in corporation with Philips Research. The author would like to thank Meint de Boer and Erwin Berenschot for their help with and advises on the processing, and Henri Jansen for helpful discussions about the model and the electrostatic charging. We are thankful to Arie Kooij, Huib van Vossen for making the masks, and Bert Otter for making the SEM-photographs

6.9 Literature

[1] N.R. Tas, R. Legtenberg, J.W. Berenschot M.C. Elwenspoek, J.H.J. Fluitman, "The Electrostatic Shuffle Motor", Proc. Micromechanics Europe '95 Workshop, Copenhagen, Denmark, Sept. 3-5 1995, pp. 128-131.

[2] N. Tas, J. Wissink, L. Sander, Th. Lammerink, M. Elwenspoek,"The shuffle motor: a high force, high precision linear electrostatic stepper motor ",Proc. 1997 Int. Conf. on Solid-State Sensors and Actuators (Transducers '97), Chicago, Illinois USA, June 16-19 1997, Vol. 2, pp. 777-780.

[3] H.A.C. Tilmans, "Micro-mechanical sensors using encapsulated built-in resonant strain gauges", Ph.D. Thesis University of Twente, 1993, ISBN 90-9005746-3.

[4] J.M. Gere, S.P. Timoshenko, "Mechanics of Materials", Chapman & Hall, London, 1991.

[5] T. Akiyama, K. Shono,"Controlled stepwise motion in polysilicon microstructures", J. of Microelectromechanical Systems, vol. 2, no. 3, Sept. 1993, pp. 106-110.

[6] T. Akiyama, H. Fujita,"A quantitative analysis of scratch drive actuator using buckling motion", Proc. IEEE Micro Electro Mechanical Systems '95 Workshop, Amsterdam, The Netherlands, Jan.29- Febr. 2, 1995, pp. 310-315.

7

Discussion and Conclusions

7.1 General Conclusions

7.1.1 Overview

It has been shown that it is possible to make linear micromotors employing walking motion, based on electrostatic actuation and surface micromachining fabrication technology. The realized motors use walking motion in order to obtain a large dynamic range (reach : resolution). Three laterally driven and one normally driven motors have been realized and tested (section 5 and 6 respectively). Only in the laterally driven motor design *B*, walking motion has been successfully generated. This design generates rather large steps (1-2 μm) and small force (appr. 3 μN), actuated at 40 V. The maximum generated stroke has been 15 μm, limited by the elastic linear guidance. We have designed a normally driven motor, the *shuffle motor*. The main advantage compared to the laterally motors is that active area for the electrostatic actuation of the clamps can be made larger. In the shuffle motor the displacement is generated by a deflecting plate, which transforms its normal deflection into lateral contraction. Due to the built in lever the produced force can be as high as 1 mN with 30V driving voltage. In the realized device this value could not be obtained, because of electrostatic stiction problems. In order to reduce electrostatic charging of insulators in the motor, a modulated driving AC-voltage had to be used. This greatly reduced the effective clamp force. The motor could reach a 43 μm displacement by adding approximately 500 steps of (on average) 85 nm. The displacement was limited by the guidance springs. Using an estimate of the stiffness of the elastic guidance it can be concluded that the produced force is 43 ± 13 μN. The driving voltages were 25 V for the step generation and 40 V for the clamping. For the shuffle motor it is recommended to investigate possibilities to reduce the electrostatic charging of the insulators, in order to allow a modulated DC-driving voltage. This is very important, because a large (up to 20 times!) increase of the clamp force can then be expected.

7.1.2 Performance

Performance with respect to the specifications

Q18a: First we compare the performance of the shuffle motor with the desired specifications (table 1.1), as this motor has reached the largest stroke and generated force, and the smallest step size. The specification which have successfully been fulfilled are a linear size < 1mm, and a maximum measured stroke much larger than 10 μm. It can be driven at voltages as small as 13 V (pull-in voltage), although the measured force of 43 μN has been obtained with a 40

V clamp force. In order to obtain a force larger than 0.1 mN it is necessary to improve the clamps in such way that the clamps can be driven by a modulated DC-voltage, in stead of the modulated AC-voltage necessarily used in the experiments to avoid charging of the silicon nitride insulating layer.

Q18b: For the laterally motors we were not (yet) able to implement walking motion in combination with levers to increase the force. In comparison with the specifications the demands for reach, resolution and produced force are therefore not fulfilled.

Performance with respect to other reported linear micromotors

In section one we presented a number of different concepts of linear micromotors. The different concepts are fabricated in many different ways, and show large differences in the size of the motors. Therefore, it mainly makes sense to compare our realized micromotors with reported surface micromachined micromotors, as these have comparable dimensions. All motors discussed next have sizes smaller than 1 mm x 1 mm x 5 μm. Our laterally driven motor concept *B*, has a maximum stroke of 15 μm and a generated force of 3μN with 40 V driving voltage. The vibromotor [1, 2] has a reported reach of over 100 μm. The difference is that in our design the shuttle is elastically suspended, while in the vibromotor the shuttle is guided by a slider bearing. This is why the vibromotor accomplished a significant larger reach. Due to the same difference the generated force of the vibromotor can not be estimated by measuring the maximum stroke. The walking motor made by Baltzer et al. [3] also uses a slider bearing. It has a reach of over 100 μm, while again the generated force is not known. Yeh et al. [4, 5] have made a laterally driven walking motor with the elastic suspension. They have measured a maximum deflection of 40 μm and a generated force of 6.5 μN, driven at 35 V. Both are approximately double compared to our motor.

The normally driven shuffle motor can best be compared with the scratch drive actuator (SDA) [6-8], which is also a normally driven motor. The shuffle motor accomplished a reach of 43 μm and a force of 43 ± 13 μN, driven at 25 V for the propulsion and 40 V for the clamp actuation. The force generated by the SDA increases from 10 μN to 63 μN, with the driving voltage increasing from 68 – 112V. Therefore we can conclude that for the same driving voltage the shuffle motor produces a considerable larger force. However, the surface area of the SDA is about 10 times smaller than of the shuffle motor. Therefore, the force produced per unit area with equal driving voltage is comparable. It is important to remember that the shuffle motor is expected to generate a much larger force (up to 1mN with 30 V driving voltage) if the clamps are improved. For the SDA it is not clear how much it can be improved, because there exists no quantitative model for the generated force. Looking at the reach, the SDA can produce more than 100 μm strokes. The explanation for the larger stroke of the SDA is that the tested SDAs did not have an elastic suspension.

7.1.3. Reliability

Q17: Systematic reliability tests have not been done. For the laterally driven motors it is necessary first to increase the performance (in particular the generated force) by adjusting the

designs, before reliability becomes relevant. For the shuffle motor it has become clear that the main reliability issue is stiction. In particular the electrostatic stiction due to charging of the silicon nitride insulator during operation, has to be reduced. To do so, a new design of the clamps has been proposed (section 6.6).

7.2 Electrostatic Actuator Theory

7.2.1 Answers to research questions

Q1 (*Maximum force, Section 2.5*): The maximum voltage that can be applied across a 2 μm gap before break-down occurs, is around 500V. This corresponds with an electric field of 2 x 10^8 V/m, and an energy density of 1.8 x 10^5 J/m^3 (section 2.5). In vacuum the field strength can be up to a factor 10 larger, as the onset of field emission is at approximately 2 x 10^9 V/m. For small gaps and rough electrodes this value will probably be smaller.

Q2 (*Generated force and output stiffness, section 2.2*): The (equilibrium) output force and output stiffness of electrostatic (variable capacitance), isothermal actuators can be calculated from the derivative of the total (free) energy with respect to the displacement coordinate. The stiffness from the second order derivative. If the actuator is controlled by a constant voltage source, than the energy of the source (a reservoir with a large capacitance) should be included in the equilibrium and stiffness analysis. This energy is taken into account in the generalized potential (section 2.2).

Q3 (*Actuator model convenient for actuator design, section 2.4*): A model for the force generation in electrostatic actuators as a function of the actuator geometry has been derived. It has been shown that the force produced in an electrostatic actuator can be expressed by the product of the energy density and a characteristic active area, which is defined as dV / dx with V the volume containing the (uniform) electric field and x the actuator deflection. The model enables quick evaluation of different actuator designs.

Q4 (*Generated force in 1 mm^2 substrate area, section 2.6*): Based on characteristic unit cells for both the comb-drive and the gap-closing actuator it is possible to generate 0.1 mN on a chip surface area of 1 x 1 mm^2 in combination with a 2 μm stroke, for structures with a 5 μm height and using a 30 V driving voltage. The generated force can be made much larger by taking a higher driving voltage (up to 400 - 500 V should be possible), and by creating higher structures.

7.2.2 Recommendations for future research

The maximum possible electric field intensity before break-down takes place is based on measurements on large gaps, and on only few measurements on small gaps (1-10 μm). Also, local field concentration due to roughness of the electrodes play an important role in the break-down process. It is therefore recommended to do measurements using electrodes and gaps which resemble those used in the motors to be made (section 2.5).

7.3 Fabrication

7.3.1 Answer to research question

Q5 (*Stiction reduction, section 3*): The main topic concerning fabrication, has been the reduction of pre-use and in-use adhesion of released parts (often called *stiction*), fabricated by surface micromachining. It can be concluded that stiction can be reduced by reducing the real contact area. Reduction of the real contact area can be done by reduction of the apparent contact area by means of stand-off bumps (section 3.6.2), by means of side-wall spacers (section 3.6.2, appendix B), and by increased surface roughness of the contacting surfaces (section 3.6.3). We have successfully introduced and characterized self-aligned side-wall spacers, which are extremely robust due to the fact that they are partly folded underneath the beams. The reduction of the adhesion energy has been shown to be in correspondence with the reduction of the apparent contact area. Extremely strong adhesion can occur between released structures and the substrate if the structures have been fabricated on top of a smooth, polished substrate wafer. Reports in literature show that increasing the surface roughness can drastically reduce stiction (more than ten times has been reported). We have presented a simple contact model which supports this theoretically (Appendix *A*).

7.3.2 Recommendations for future research

We recommend experimental verification of the theoretically derived relation between surface roughness, adhesion and real contact area. An important issue will be how to relate the real roughness with the simplified roughness representation in the elastic contact model.

7.4 Micro Tribology

7.4.1 Answers to research questions

Q6: (*Electrostatic clamps with low adhesion, Section 4.4*) For the laterally driven motors it has been shown both experimentally and theoretically that the adhesion between rough side-walls can be kept low, in the order of 1 μN. This value is low enough to make it possible to release the clamp contacts in the walking motors, because electrostatic forces of an order larger can easily be generated. It is important to mention that the rather low adhesion force can become drastically larger if the side-walls become smoother.

Q7 *(elastic or plastic deformation)***:** It is hard to make a general statement if the contacts in MEMS devices will be mainly elastic or plastic, because the surface topography varies between extremely smooth (polished wafer surface) to quite rough (side-walls of RIE etched polysilicon parts). Also a large range of contact forces is encountered, typically in the range of 1μN - 1 mN. Nevertheless, it has been possible to find a criterion, the plasticity index, for the transition form elastic to plastic contact (section 4.3.4). In this index, surface topography, elasticity, and hardness parameters are taken into account.

Q8: *(Relation between surface roughness and friction, section 4.3)* We have assumed that static friction in shearing mode can be expressed as the product of real contact area and a

characteristic shear strength s of the interface. In an elastic contact, the surface roughness together with the elastic properties of the contacting materials determine the mean real pressure p_e (= load / real contact area) in the contact (equation 4.9). The friction coefficient can be written as s / p_e. Because p_e increases proportionally with the topography parameter R / s it is clear that (in elastic contacts) the friction coefficient decreases with increasing R / s, with a lower limit s / H, the friction coefficient for plastic contact (section 4.3.4). Furthermore, the surface roughness has strong influence on the effective adhesion of contacting surfaces (fig. 4.3). Increasing the surface roughness will therefore lead to reduction of the adhesive load and therefore of the friction force (fig. 4.4).

Q9 *(applicability of the Maugis model in MEMS)***:** The statistical model of Maugis can be applied to elastic adhesive MEMS contacts, however because of the low loading conditions that can be encountered in MEMS devices it is necessary to check if there are enough contact points to allow the use of the statistical model (sections 4.3.5, 4.4). Discrete contact model for 1,2, or 3 contacting asperities have been developed (section 4.3.5).

Q10 *(simple expression for friction in adhesive contacts)***:** For non-adhesive contacts the static friction force can be expressed by the product of the friction coefficient and the applied load (Amontons' Law): $F_f = m \cdot L$, where $m = s / p_e$ in elastic, and $m = s / H$ in plastic contacts (section 4.3.4). If adhesive load is included, a non-linear relation between F_f and L results (section 4.3.2). Only in a limited range the friction can be expressed by a linear relation (eq. (4.14)). In this relation the effect of adhesion is accounted for in both the friction coefficient and the (apparent) zero load adhesion force.

7.4.2 Recommendations for future research

We recommend experimental verification of the elastic contact model, in particular the relation between RCA, surface roughness and applied load. It has been assumed that the friction force in shearing mode is given by the product of the real contact area and the (contact pressure independent) shear strength of the interface. The conditions for which this is valid should be determined.

Furthermore, we recommend experimental verification of the influence of the adhesive load, which is accounted for by the adhesion parameter, and theoretically leads to friction vs. load curves as shown in fig. 4.4.

In the presented models, the surface topography is characterized by the (average) asperity tip radius, the spread in the summit levels, and the asperity density. These parameters are extracted from the measured surface topography by hand. In order to make this extraction more objective it is recommended to automate it. For example, the asperity density can be calculated from the dominant wavelength which can be determined from a FFT of the topography data.

7.5 Laterally Driven Motors

7.5.1 Overview

In laterally motor design *A* clamping and propulsion are generated by the same beam. It turned out that with the current design rules it is hard to obtain sufficient clamping. Clamping can be increased by increasing the length of the drive beams, by reducing the roughness of the side-walls in the clamping region, and by reducing the minimum width of the drive beams. All three possible improvements have the risk of increasing the amount of stiction between the shuttle and the drive beams. In the laterally driven motor design *B*, walking motion has been successfully generated. This design generates rather large steps (1-2 μm) and small force (appr. 3 μN), actuated at 40 V. The maximum generated stroke has been μm, limited by the elastic linear guidance. Test of a configuration (design *C*) which uses mechanical levers to increase the force and reduce the step size, have shown that it is difficult to create sufficient clamping to side-walls (section 5.4). Also it has appeared that the generation of several subsequent steps was difficult, as the impact of the next clamp to become active can cause the already active clamp to release the shuttle and the first step is lost.

7.5.2 Answers to the research questions

Q11 *(controlled friction in laterally driven actuators)***:** The adhesion between side-walls of RIE-etched structures is low enough compared to the electrostatic clamp forces, to make it possible to control the friction in the clamps by means of the controllable electrostatic forces.

Q12 *(employing a lever to increase the generated force)***:** In order to enlarge the produced forces we have tried to include a lever in a surface micromachined mechanism. In the laterally driven motor concept *C* (section 5.4) the propulsion actuator is composed of a separate electrostatic actuator array and a lever. We could observe that sub-micron displacements were generated, which indicates that the lever functions. However, due to the problems with multiple-step generation we have not been able to confirm the increase of the force by the lever.

Q13 *(electrostatic pull-down towards the substrate)***:** Different methods have been proposed to reduce pull-down by electrostatic forces:

1) Try to keep all free elements at the same potential as the substrate .

2) Give structures which have a potential different from the substrate a sufficiently stiff suspension in the normal direction. This has been done in concept *C* (section 5.4).

3) Use electrical shields underneath free moving structures, and keep the shield at the same potential as the structures above. This has been done in the shuffle motor (chapter 6)

7.5.3 Recommendations for future research

We propose elastic pre-clamping presented in section 5.4.3 to solve both the problems of insufficient clamp force and impact of an incoming clamp. In this concept there is a need for a spring which after the release etch pushes the clamp feet continuously to the shuttle. We think that by selective dotation of polysilicon beams such a spring can be made.

7.6 Normally Driven Motor

7.6.1 Answers to the research question

Q14,15 (*how to realize a lever, and how to realize a transformation from normal movement into lateral movement*): In the shuffle motor (chapter 6) both the lever and the transformation from normal to lateral force has been implemented by the downward deflection of the center of a plate which is supported at both ends. Due to the center deflection a small but forceful contraction, in lateral direction, is generated.

Q16: The adhesion and friction between the clamp feet and the bottom electrodes has not been measured. Qualitatively we sometimes observed adhesion of the feet to the bottom electrodes in the initial position of the motor. Once it has moved, significant adhesion is not observed any more. The adhesion in the initial position is probably caused by the fact that in this position the roughness on the bottom side of the feet fits the roughness on top of the bottom electrodes.

7.6.2 Recommendations for future research

Its recommended to redesign the clamps in such a way that the charging of the insulating layer between the electrodes of the clamps is avoided. The clamps can then be driven by DC-voltage and it is expected that significant larger friction forces can be generated in the clamps. In section 6.6.2 a new configuration for the clamps has been proposed.

7.7 More Topics for Future Research

Besides the recommendations done in relation with the separate chapters, there are a few general recommendations for future research.

7.7.1 Walking motors

To find out more about the performance of walking motors is it recommended to find out more about the dynamics of walking motion. What is the maximum speed? Is it possible to move in different modes (e.g. walking and running)?

7.7.2 Electrostatic Actuators General

In principle it is possible to generate extreme large accelerations using electrostatic actuators. To employ this to move objects with substantial mass, it is required to increase the actuator volume by making higher structures. For example, with an 1 x 1 x 0.04 mm^3 volume it is possible to generate 6 mN and a 10 μm stroke, based on a 1 x 10^5 J/m^3 energy density. After transformation to fulfill the inertial matching condition (section 2.7), this is enough to generate a 2 μm stroke, in combination with maximal 1.3 x 10^5 m / s^2 acceleration of a 1 mg load.

7.7.3 Fabrication

Higher structures: As mentioned in 7.7.2, creating higher structures to increase the actuator volume is very much desirable. We refer to Keller et al. [9] and Hirano et al. [10] for examples of new fabrication processes which have been developed to create higher structures.

Stress problems: In particular with the multi-layer surface micromachining process for the shuffle motor, the stress in the layers induce significant bending of the substrate, which makes it more difficult to handle the wafers, for example because clamping with a vacuum chuck does not work properly. The stresses of all different layers should be characterized, and strategies have to be developed to reduce the bending during fabrication.

Adherence silicon nitride to polysilicon: During fabrication it became clear that the interface of polysilicon and silicon nitride layers is easily attacked by HF. To reduce this problem we added a HF dip of the polysilicon surface prior to deposition of the silicon nitride, in order to remove possibly present native oxide. This reduced but did not eliminate this problem. It should be found out what is the cause. A possible cause could still be the formation of native oxide, rapidly due to the high temperature encountered while loading the LPCVD tube before deposition of the silicon nitride.

7.8 Literature

[1] M.J. Daneman, N.C. Tien, O. Solgaard, K.Y. Lau, R.S. Muller,"Linear Vibromotor-Actuated Micromachined Microreflector for Integrated Optical Systems", Solid-State Sensors and Actuators Workshop Hilton Head, South Carolina, June 2-6, 1996, pp. 109-112.

[2] M.J. Daneman, N.C. Tien, O. Solgaard, A.P. Pisano, K.Y. Lau, R.S. Muller,"Linear Microvibromotor for Positioning Optical Components", Proc. IEEE Micro Electro Mechanical Systems Workshop 1995, Amsterdam, Jan. 29- Febr. 2, 1995, pp. 55-60.

[3] M. Baltzer, Th. Kraus, E. Obermeier," A linear stepping actuator in surface micromachining technology for low voltages and large displacements", Proc. Int. Conf. On Solid-State Sensors and Actuators, Chicago, June 16-19, 1997, pp. 781-784.

[4] R. Yeh, E.J.J. Kruglick, K.S.J. Pister," Micro Electromechanical Components for Articulated Microrobots", The 8th Int. Conf. on Solid-State Sensors and Actuators, (Transducers 95) and Eurosensors IX, Stockholm Sweden, June 25-29, 1995, pp. 346-349.

[5] R. Yeh, E.J.J. Kruglick, and K.S.J. Pister," Surface-Micromachined Components for Articulated Microrobots", J. Microelectromechanical Systems, vol. 5, no. 1, March 1996, pp. 10-17.

[6] T. Akiyama, K. Shono," A New Step Motion of Polysilicon Microstructures", Proc. IEEE Micro Electro Mechanical Systems Workshop 1993, Fort Lauderdale, Florida, USA, Febr. 7-10, 1993, pp. 272-277.

[7] T. Akiyama, K. Shono," Controlled Stepwise Motion in Polysilicon Microstructures", J. Microelectromechanical Systems, vol. 2, no. 3, 1993, pp. 106-110.

[8] T. Akiyama, D. Collard, H. Fujita," Scratch Drive Actuator with Mechanical Links for Self-Assembly of Three-Dimensional MEMS", J. Microelectromechanical Systems, vol. 6, no. 1, March 1997, pp. 10-17.

[9] C. Keller, M. Ferrari," Milli-Scale Polysilicon Structures", Proc. Solid-State Sensor and Actuator Workshop, Hilton Head, South Carolina USA, June 13-16, 1994, pp. 132-137

[10] T. Hirano, L-S Fan," MEMS Milliactuator for Hard-Disk-Drive Tracking Servo", J. MEMS, Vol. 7, no. 2, June 1998, pp. 149-155.

A

Elastic adhesive contact of rough surfaces, uniform height.

A.1 Model

In this appendix the influence of the surface roughness on the adhesion of elastic solids is modelled.The interface which has been modelled consists of one flat and one rough surface. The rough surface is described by identical spherical asperities with a radius R which all have the same summit level. The other parameters describing the surfaces are the elasticity of the material, the asperity density h, and the work of adhesion Δg needed to separate the two materials.

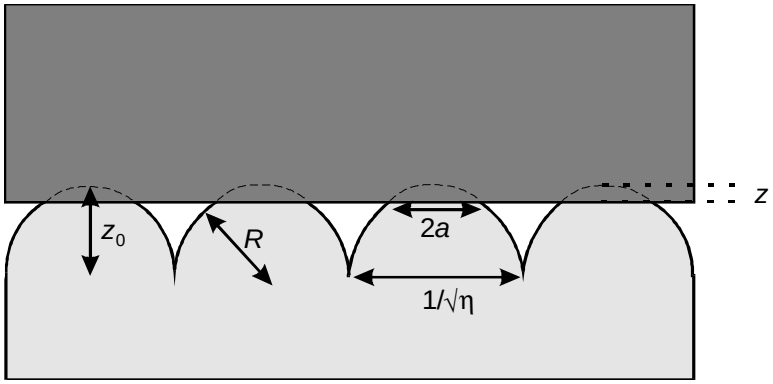

Figure A.1: Rough surface in contact with a flat plane, with z the indentation of the asperities, z_0 the peak-valley distance, a the contact radius, R the radius of the spherical asperities and $\ddot{0}h$ the linear asperity density.

For two rough surfaces the roughness is transfered to the one rough surface by calculating a combined radius of the asperities $R=R_1//R_2$. Where R_1 and R_2 are the radii of the asperities of surface one and surface two respectively. For the interaction of a single asperity with a flat rigid plane the DMT (Derjaguin, Muller and Toporov) model is used [1]. The DMT theory is valid for hard solids with a low surface energy and a small asperity radius [2].This is discussed in chapter 4 in more detail. Following the DMT model the adhesion force of each contacting asperity is given by $2\pi\cdot\Delta gR$, independent of the indentation z. The distribution of stresses in the region of contact is Hertzian [3, 4] and their integral equals the sum of the adhesion force $2\pi\cdot\Delta gR$ and the applied load P. Therefore, for each contacting asperity of which the tip is elastically displaced a distance z, the contact radius a and the load P are now given by:

$$a^2 = R \cdot z \tag{A.1}$$

$$P + 2p \cdot \Delta g \cdot R = \frac{a^3}{R \cdot D} = \frac{R^{1/2} z^{3/2}}{D} \tag{A.2}$$

For these equations to be used, z_0 should be large compared to the range of the adhesion forces. The elastic properties of the two contacting surfaces are combined in the compliance D according to

$$D = \frac{3}{4} \cdot \left(\frac{1-n_1^2}{E_1} + \frac{1-n_2^2}{E_2}\right)$$

In which E_1, E_2 and n_1, n_2 are the Young's modulus and the Poisson's ratio of surface one and two respectively. Eq. A.2 can be changed into a pressures balance by multiplication with the asperity density h:

$$p_{\text{load}} + 2p \cdot h \cdot \Delta g \cdot R = \frac{h \cdot R^{1/2} z^{3/2}}{D} \tag{A.3}$$

Where the load pressure p_{load} is defined the load force P per asperity times the asperity density, which is equal to the load force L divided by the apparent contact area A_a. Equation (A.3) can be solved for z to find the balance indentation:

$$z = \left[\frac{D}{h \cdot R^{1/2}} \left(p_{\text{load}} + 2p \cdot h \cdot \Delta g \cdot R\right)\right]^{2/3} \tag{A.4}$$

The real contact area formed is given by the contact area per asperity times the asperity density times the apparent contact area:

$$A_r = h \cdot A_a \cdot p a^2 \tag{A.5}$$

Using Eq. A.1, A.4 and A.5 the following dimensionless expression for the relative real contact area A_r^* can be derived:

$$A_r^* = \frac{A_r}{A_a} = 2^{2/3} p^{5/3} h \cdot R^{4/3} D^{2/3} \Delta g^{2/3} \left[\frac{p_{\text{load}}}{2p \cdot h \cdot \Delta g \cdot R} + 1\right]^{2/3} \tag{A.6}$$

The asperity density, radius of curvature and peak-valley height are related. From simple geometry calculation (figure A.1) it follows for $z_0 < R$:

$$R = \frac{1}{8 z_0 h} \tag{A.7}$$

Substitution in (A.6) to eliminate h yields:

$$A_r^* = \frac{A_r}{A_a} = 2^{-7/3} p^{5/3} q^{*-2/3} [\frac{p_{load}}{p_{adh}} + 1]^{2/3} = 1.34 q^{*-2/3} [\frac{p_{load}}{p_{adh}} + 1]^{2/3} \tag{A.8}$$

Where q^* is the dimensionless group which is analogue to the adhesion parameter as defined by Fuller et al. [6] for surfaces which have a distributed summit level.

$$q^* = \frac{z_0^{3/2}}{D \cdot \Delta g \cdot R^{1/2}} \tag{A.9}$$

And the adhesive pressure is equal to:

$$p_{adh} = 2p \cdot h \cdot \Delta g \cdot R = \frac{p \cdot \Delta g}{4 z_0} \tag{A.10}$$

In figure A.2 the relative real contact area is plotted as a function of q^* for the case that the adhesive pressure dominates the load pressure (p_{load} / p_{adh}= 0).

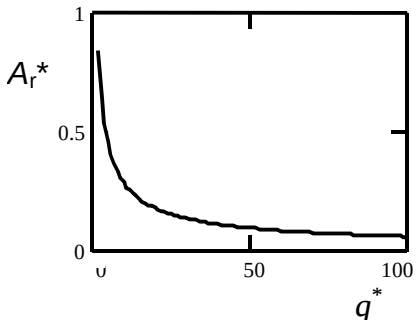

Figure A.2: Relative real contact area as a function of q^* for zero load.

Figure A.3 shows A_r^* as a function of $p^* = p_{load}/ p_{adh}$ for three values of q^*.

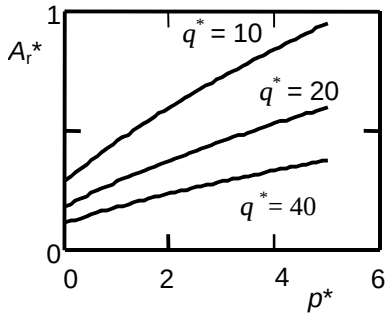

Figure A.3: A_r* as a function of $p^* = p_{load}/p_{adh}$ for three values of q*.

The area of contact increases as $p^{*2/3}$ (shifted due to the adhesion). Because the adhesive pressure is independent of z this means that the area of contact increases as $p_{load}^{2/3}$. This is caused by the Hertzian elastic deformation of the asperities which have identical summit level. An almost linear relation between the area of contact and p_{load} is found if the summit level is Gaussian distributed [7]. The model presented here is only valid for spherical asperities for which the standard deviation s of their summit level distribution is smaller than the indentation z.

A.2 Literature

1. Derjaguin B.V., Muller V.M., and Toporov Y.P., Effect of contact deformation on the adhesion of particles, J. of Colloid and Interface Science, Vol. 53, no. 2, 1975, pp. 314-326.
2. Johnson K.L.,"A continuum mechanics model of adhesion and friction in a single asperity contact", ed. Bhushan B., NATO ASI series vol. 330, Kluwer, The Netherlands, 1997, pp. 151-168.
3. Landau L.D., Lifschitz E.M., Elastizitaetstheorie, Akademie Verlag, Berlin, 1975.
4. Timoshenko S.P., Theory of Elasticity, McGraw-Hill Book company, New York, 1970.
5. Maugis D., Adhesion of spheres: The JKR-DMT transition using a Dugdale model, J. of Colloid and Interface Science., Vol. 150, no.1, 1992, pp. 243-269.
6. Fuller K.N.G., Tabor D., The effect of surface roughness on the adhesion of elastic solids, Proc. R. Soc. Lond., A.345, 1975, pp. 327-342.
7. Greenwood J.A., Williamsson J.B.P,"Contact of nominally flat surfaces", Proc. R. Soc. Lond. A, Vol. 295, 1965, pp. 300-319.

B

Robust side-wall spacers for stiction reduction

A new process has been developed to generate spacers that are grown partly underneath the structures, in order to make robust spacers. The process is illustrated in fig. B.1. After the structural layer has been etched by RIE (fig. B.1a), isotropic etching of the oxide is done in 5% BHF, for 3 minutes (fig. B.1b). The lateral etch rate of the used SOI-oxide is 2-3 nm/s, which is higher than the expected 1 nm/s for thermal oxide. LPCVD silicon nitride (150 nm) is grown all around (fig. B.1c). Next, the silicon nitride is etched anistropically in RIE, leaving it on the side-walls and underneath the structure (fig. B.1d). Finally the structure is released in 50% HF (fig. B.1e).

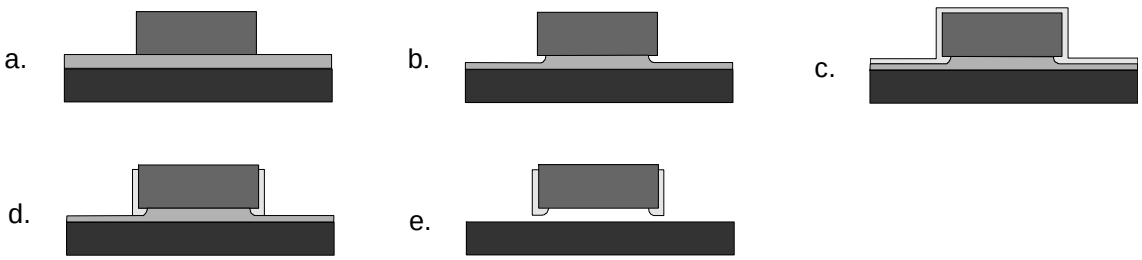

Figure B.1: Processing scheme for robust side-wall spacers, starting from a) patterned silicon structural layer, b) isotropic thinning of sacrificial layer c) grow anti-stiction silicon nitride layer d) anisotropic silicon nitride etch e) sacrificial layer etch.

The spacers obtained are extremely robust. By using a probe pen, structures can be pushed down to the substrate. They could be moved easily across the surface. Even 2 μm small beams could be released by simple touching. Without spacers, the same structures stuck heavily and could not be released without damage. Spacers are especially useful for experimental devices: beams that stick, can be freed easily, and testing can continue. From the initial experiments we learned that side-wall spacers do not entirely eliminate stiction. Therefore, the detachment length of cantilever beams with and without side-wall spacers has been measured. The stiction of beams of three different widths, 12, 24 and 36 μm, has been measured. The cantilever beams have been fabricated on a SOI wafer having a structural layer thickness of 4.5 μm and an oxide layer thickness of 1.0 μm. Side wall spacers have been fabricated according to the processing scheme shown in fig. B.1. Fig. B.2 shows close ups of the bottom side of a fabricated beam.

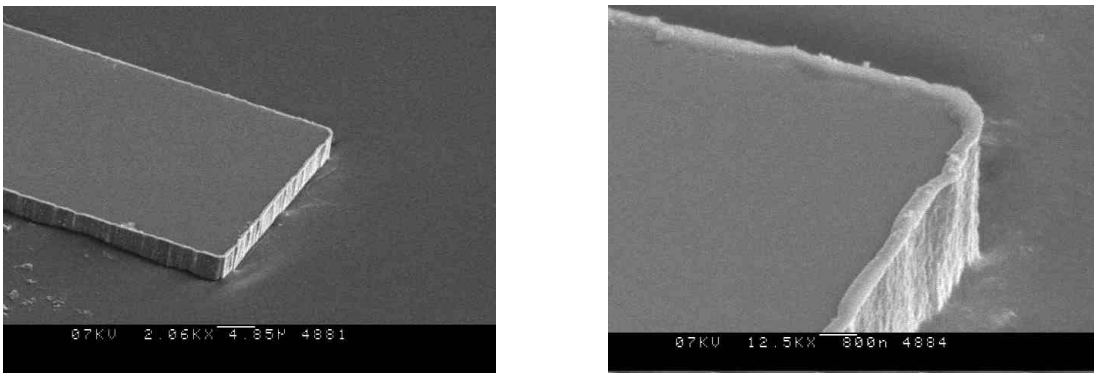

a) b)

Figure B.2: a) SEM-photograph of the bottom-side of a cantilever beam b) Close-up, the width of the spacers is about 500 nm.

The spacers have a width of about 500 nm, due to the higher than expected lateral etch-rate of the oxide. In order to obtain stiction, samples have been dried from IPA after the sacrificial layer etching. Detachment lengths have been measured using an optical microscope with the interference contrast method. Ten cantilevers of each type have been measured upon. Table B.1 shows the average detachment length:

	Cantilever width [μm]	Detachment length (average, n=10) [100 μm]
Without spacers	12	1.2 ± 0.2
	24	1.2 ± 0.2
	36	1.2 ± 0.2
With spacers	12	2.6 ± 0.4
	24	3.0 ± 0.4
	36	3.4 ± 0.4

Table B.1: Measured detachment length for three different beam widths. Beams with and without side wall spacers are compared.

A work of adhesion of 0.10 ± 0.07 J/m^2 can be calculated for the cantilevers without spacers. From the average detachment lengths, a reduction of 2×10^1, 4×10^1 and 6×10^1 times for the adhesion energy per unit length of the beam can be calculated using eq. (3.10). This is slightly larger than the reduction of the geometrical contact area due to the side wall spacers, which is 12, 24 and 36 times assuming a total spacer width of 2 x 0.5 μm. The roughness of the spacers as well as the adhesion energy of the silicon nitride to silicon might explain for the difference. It can be concluded that the side-wall spacers help to reduce the contact area as expected. They are an important aid in the reduction of stiction problems in test devices. Although the contact area is reduced as much as 6×10^1 times for the widest beams, the critical length is only increased by a factor 2.8. An additional increase by a factor of about 1.5 in the detachment length should be feasible by making smaller spacers.

C

Equilibrium and Stability of Peculiar Electrostatic Configurations and Control Conditions

C.1 Stability of the gap-closing actuator loaded by a constant force

Figure C.1 shows the gap-closing actuator. Pull-in voltage and gap is calculated as a function of a constant applied external force $F_{ext} = F$.

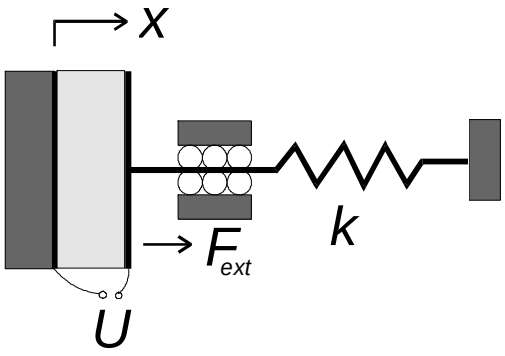

Figure C.1: Gap-closing actuator. The light gray area represents the actuator volume where the uniform electric field is present. The moving plate is elastically suspended by a spring with stiffness *k*.

The energy function (2.12) applies:

$$W'(x,U) = \frac{1}{2}k(x - x_0)^2 - \frac{1}{2}\frac{eA}{x}U^2$$

Where e is the permittivity, A is the active electrode area, k is the suspension stiffness, x is the position of the moving electrode, and $x_0 = x$ when the spring is relaxed. The equilibrium point at the onset of instability follows from $F_{ext} = \partial W'/\partial x = F$ and $k_{eff} = \partial W'^2/\partial x^2 = 0$, yielding:

$$x_{pi} = 2/3\ (x_0 + F/k)$$

$$U_{pi}^2 = \frac{8}{27}\frac{k \cdot (x_0 + \frac{F}{k})^3}{e \cdot A}$$

Figure C.2 shows the co-energy as a function of x with $U = U_{pi}$ for a positive F.

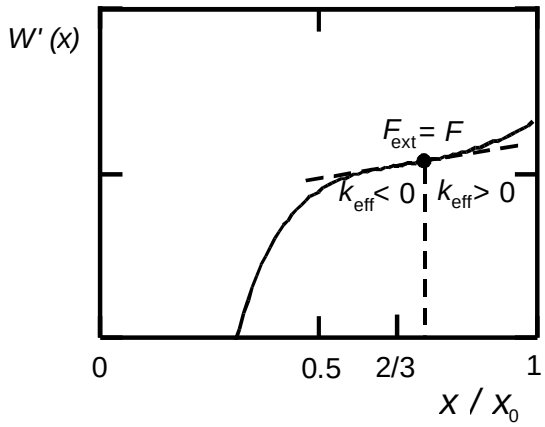

Figure C.2: Co-energy as a function of x with $U = U_{pi}$ for a positive F. The equilibrium $F_{ext} = \partial W'/\partial x = F$ at the onset of instability is shown. The unstable region is $x < 2/3(x_0 + F/k)$ where the stiffness

$$k_{eff} = \partial W'^2/\partial x^2 < 0.$$

C.2 Stability of a gap-closing actuator loaded by a higher order spring

Suspension of the moving electrode with a higher order support spring leads to a different stable operation region and voltage. Assume that for n odd (1,3,5,..) the spring force is given by $F_s = k(x-x_0)^n$. The co-energy is given by:

$$W'(U,x) = \frac{1}{n+1}k(x-x_0)^{n+1} - \frac{1}{2}\frac{eA}{x}U^2$$

For n is even (2,4,6,..) the spring force is given by $F_s = k(x-x_0)|x-x_0|^{n-1}$ and the co-energy is given by:

$$W' = \frac{1}{n+1}k|x-x_0|^{n+1} - \frac{1}{2}\frac{eA}{x}U^2$$

Note that the unit of the spring constant k is N/m^n. The pull-in voltage and gap can be calculated from $F_{ext} = \partial W'/\partial x = 0$ and $k_{eff} = \partial W'^2/\partial x^2 = 0$ yielding:

$$x_{pi} = 2\,x_0 / (n+2) \qquad \text{(C.1a)}$$

$$U_{pi}^2 = \frac{8x_0^{n+2}k \cdot n^n}{eA(n+2)^2} \qquad \text{(C.1b)}$$

Eq. (C.1a) shows that the pull-in position x_{pi} changes from $2/3\,x_0$ at $n = 1$ to $2/4\,x_0$ at $n = 2$ and to $2/5\,x_0$ at $n = 3$. The stable region of operation (between x_{pi} and x_0) increases with increasing order of the spring.

C.3 Stability of a cantilever beam driven with fixed charge

Fig. C.3a shows the configuration of a cantilever beam facing a lower electrode. The variable capacitance of this configuration can lead to instability for fixed charge. With fixed charge it is meant that the transducer is charge controlled, with the charge changing slowly compared to the mechanical response time. The free energy of the transducer consists of a mechanical deformation energy and a electric energy stored in the capacitor. This can easily be calculated if a constant shape is assumed. The deflection function can only change in amplitude. The elastic deformation energy assuming the uniform load shape is a function of the tip deflection *y*:

$$E_m = \frac{48}{30}\frac{E \cdot I}{l^3} y^2 \qquad \text{(C.2)}$$

Where $E \cdot I$ is the flexural rigidity of the beam, e is the permittivity, w is the width of the beam and l is the length of the bending part of the cantilever. The capacitance between the beam and the substrate is calculated by assuming a linear shape between the tip and the anchor of the beam (fig. C.3b):

$$C(y) = \frac{e \cdot A}{y} \ln\left(\frac{g}{g - y}\right) \qquad 0 < y < g \qquad \text{(C.3)}$$

Where g is the initial gap size, e is the permittivity, and A is the active area of the capacitor plates.

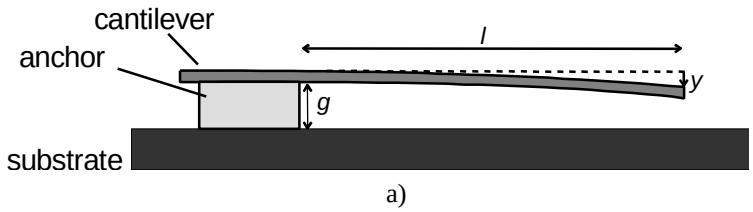

a)

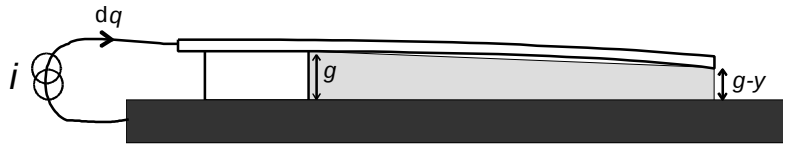

b)

Figure C.3: a) Pull-down of a cantilever beam by electrostatic forces. *U* is the applied voltage difference between the beam and the substrate, *g* is the initial gap spacing, *l* is the length of the beam, *t* is the thickness, and *y* is the tip deflection. b) The shaded region is the gap for which the capacitance is calculated.

Tip deflection as a function of the fixed charge *q* can be found from the free energy:

$$W(q,y) = E_m(y) + \frac{q^2}{2C(y)} \tag{C.4}$$

In equilibrium the energy has an extremum:

$$\partial W(y) / \partial y = 0. \tag{C.5}$$

The system becomes unstable (pull-in) if the electrostatic pull-down force increases faster than the restoring elastic force with increasing y, therefore at the edge of stability:

$$\partial^2 W / \partial y^2 = 0. \tag{C.6}$$

Combination of equation (C.2-6) yields for the tip deflection at pull-in:

$$\frac{\frac{1}{y\cdot\ln(\frac{g}{g-y})} - \frac{1}{\left[\ln(\frac{g}{g-y})\right]^2\cdot(g-y)}}{\frac{-2}{\left[\ln(\frac{g}{g-y})\right]^2\cdot(g-y)} + \frac{2y}{\left[\ln(\frac{g}{g-y})\right]^3\cdot(g-y)^2} - \frac{-y}{\left[\ln(\frac{g}{g-y})\right]^2\cdot(g-y)^2}} = 1$$

Which gives $y_{pi} = 0.711 \cdot g$. Fig. C.4 shows the energy of the transducer as a function of the tip deflection, for $q = 0.9q_{pi}$ and for $q = q_{pi}$. The transition from stable to unstable equilibrium with increasing q can clearly be seen. At $q = q_{pi}$ the minimum in the energy function disappears an the transducer is marginal stable.

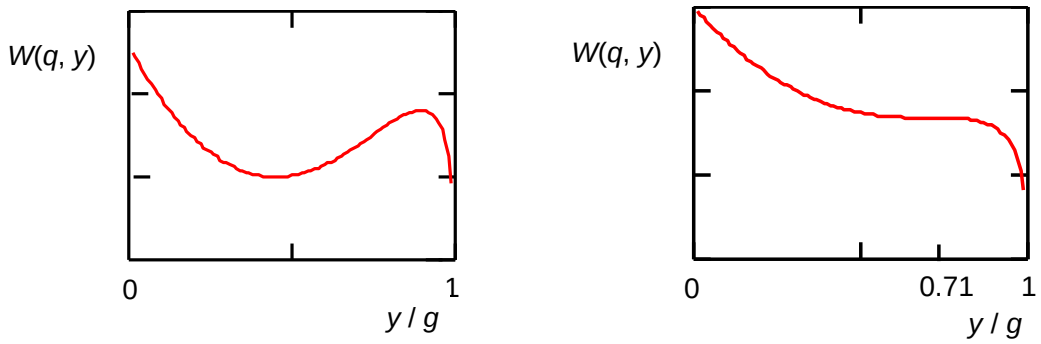

a) b)

Figure C.4: The transducer energy as a function of the tip-deflection for a) $q = 0.9q_{pi}$ and b) $q = q_{pi}$. The equilibrium state is where $\partial W(q,y) / \partial y = 0$. The curves clearly show the transition from stable equilibrium (a) to the marginal stable equilibrium (b).

The instability is caused by the displacement of the charge towards the tip of the beam which is closest to the lower electrode. This effect increases the electrostatic force, which on its turn increases the deflection.

D

Processing Scheme of Laterally Driven Walking Motors

Concept A (section 5.2): Steps 2 - 5 and 9-13 are omitted.
Concept B (section 5.3): Steps 2 - 5, 9 - 13 and 23 - 27 are omitted.
Concept C (section 5.4): Full sequence.

O 1. Start with <100> p-type wafer, 5-10 Ωcm thickness 380 µm.
- Check flatness: Dektak 50 mm scan, amplitude < 15 µm.

O 2. Standard wafer cleaning (SWC):
- Fuming nitric acid, beaker 1, *t* = 5'.
- Fuming nitric acid, beaker 2, *t* = 5'.
- DI quick dump rinse (QDR).
- Boiling nitric acid 70%, *t* = 15'.
- QDR.
- Spin drying.

O 3. Photolithography mask 0, *URKS*:
- Dry bake , *T* = 120°C, *t* = 5'.
- Spray HMDS, wait 10", spin 4000 RPM, *t* = 30".
- Immediately apply S1813, spin 4000 RPM, *t* = 30".
- Prebake *t* = 20', *T* = 90 °C.
- Expose *t* = 6", Contact mode, $p_{N2} \approx 1.0 - 1.5$ bar.
- Develop Shipley 351, *t* = 1' (fresh developer, 1:5), QDR, spin dry.
- Check using fluorescence microscope.
- Postbake *t* = 30', *T* = 120 °C.

O 4. Etch *URKS* and roughen wafer, RIE:
- *p* ≈ 0, *P* = 75 W, *T* = 10°C, APC = off, no shower head, styros electrode, 50 sccm SF6 , 15 sccm O_2, (etch rate ≈ 0,5 ... 1 µm/min), *t* = 1'.

O 5. Strip photoresist (check for remains):
- O_2 plasma 120W, *T* = 150 ºC, *t* = 15'.

O 6. SWC.

O 7. Grow SiO2, 2.3 µm, by wet oxidation oven 3:
- H_20, N_2 1 l/min, *T* = 1150 °C, *t* = 900'.

O 8. LPCVD polySi, 5.3 µm:
- *p* = 250 mT, *T* = 590 °C, SiH_4 50 sccm, *t* = 16 hr.

O 9. Deposit PECVD oxide 0.5 µm:
- *p* = 650 mT, *P* = 60W LF, *T* = 300 °C, 200 sccm SiH_4/N_2 , 710 sccm N_2O, *t* = 18'.

O 10. Photolithography mask 1, *DOPE*:
- Dry bake , *T* = 120 °C, 5'.
- Spray HMDS, wait *t* = 10", spin 4000 RPM, *t* = 30".
- Immediately apply S1813, spin 4000 RPM, *t* = 30".
- Prebake *t* = 20', *T* = 90 °C.

- Expose 6”, mask 1, contact mode, $p_{N2} \approx 1.0$ - 1.5 bar.
- Develop Shipley 351, t = 1’(fresh developer, 1:5), QDR, spin dry.
- Check using fluorescence microscope.
- Postbake t = 30’, T = 120 °C.

O 11. Pattern oxide:
- BHF (1:7 “standard SiO_2 etch”) t = 5’.
- QDR.

O 12. Strip photoresist (check for remains):
- O_2 plasma 120W, T = 150 ºC, t = 15’.

O 13. SWC

O 14. Boron doping, solid source, 4.5 Ω/square.*
- Activate Boron source.
- SWC
- Remove native oxide: 1% HF, t = 60”.
- Boron deposition + drive-in diffusion, 1 hours, T = 1100 ºC. NB: load wafers quickly.

O 15. Etch B_2O_5:
- BHF, t = 60’.
- QDR, spin drying.
- Check sheet resistance (± 4 Ω/).

O 16. PECVD SiO_2 , 1.2 µm.
- p = 650 mT, 60 W LF, 200 sccm SiH_4, 710 sccm N_2O, T = 300 °C, t = 40’.

O 17. Post-anneal:
- 3 hours, T = 1100 ºC, 1 l/min N_2, ramp via t = 30’ T = 800ºC.

O 18. Standard wafer cleaning (SWC):
- Fuming nitric acid, beaker 1, t = 5’.
- Fuming nitric acid, beaker 2, t = 5’.
- DI quick dump rinse (QDR).
- Boiling nitric acid 70%, t = 15’.
- QDR.
- Spin drying.

O 19. Photolithography mask 2, *STRUC*:
- Dry bake , T = 120°C, t = 5’.
- Spray HMDS, wait 10”, spin 4000 RPM, t = 30”.
- Immediately apply S1813, spin 4000 RPM, t = 30”.
- Prebake t = 20’, T = 90 °C.
- Expose t = 6”.
- Develop Shipley 351, t = 1’, QDR, spin dry.
- Check using fluorescence microscope.
- Postbake t = 30’, T = 90 °C.

O 20. RIE SiO_2 mask.
- 20 mT, 50 W, styros electrode,10 sccm CHF_3, T = 10 ºC, t = 40’.

O 21. Strip photoresist:
- O_2 plasma 120W, 150 ºC, t = 20’.

O 22. Etch polysilicon:
p = 100 mT, P = 100 W, silicon electrode, 30 sccm SF_6, 10 sccm O_2, 7 sccm CHF_3, T = 10 °C, t = 2’ steps, t = 1’ steps once the polysilicon is removed from the wafer edge. Remove and expose to air the sample, for t = 10’ between steps. Total etch time appr. t = 10’.

O 23. Strip FC on sidewalls:

- O_2 plasma P = 120W, T = 150 ºC, t = 20'.

O 24. Strip SiO2 mask in RIE
- p = 20 mT, P = 50 W, T = 10 °C, styros electrode, 10 sccm CHF3, t = 30'.

O 25. HF dip and underetch for anti-stiction structures:
- 1 % HF, t = 60''.

O 26. LPCVD silicon nitride, low stress, 160 nm.
- p = 200 mT, T = 850 °C, 70 sccm DCS, 18 sccm NH_3, t = 20'.

O 27. RIE Si_3N_4.
- p = 10 mT, P = 75W, T = 24° C, 5 sccm O_2, 25 sccm CHF_3, styros electrode, t = 4' (almost double time because of narrow gaps).

O 28. Sacrificial layer etching:
- 50% HF, t = 4'30" (underetch 10 μm around holes, with 2.3 μm thermal oxide).
- Dilute with IPA, t = 2'.
- Dilute with IPA, t = 2'.
- Transfer to IPA1, wait t = 10'.
- Transfer to IPA2, wait t = 10'.
- Transfer to cyclohexane, wait t = 15'.
- Freeze-drying (-6°C) under dry nitrogen flow, warm up to room temperature before removing.

a) b)

Figure D.1: a) Mask for etching of the polysilicon in concept *C*. b) The gray fields indicate the undoped regions.

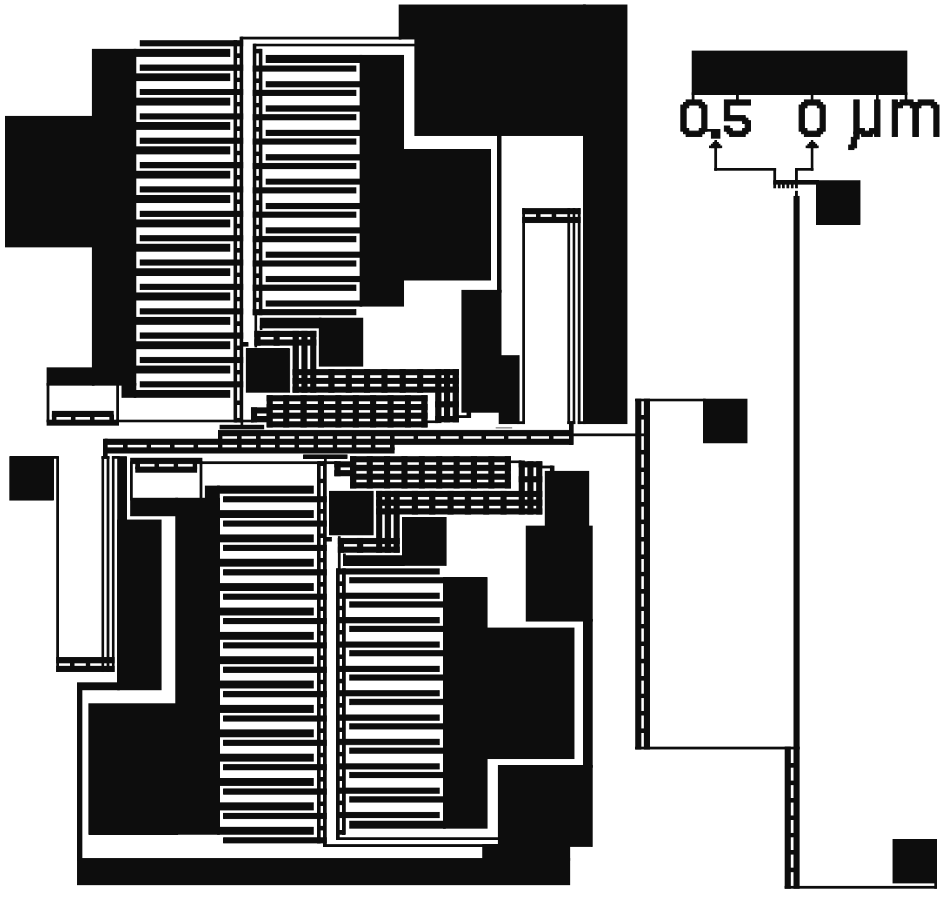

Figure D.2: Concept *C*, uni-directional motor with two-stage 50x displacement meter.

E

Processing Sequence of the Shuffle Motor

O 1. Use p- or n-type, <100>, 5-10 Ωcm wafers:
- Check flatness: Dektak: 10 μm/5 cm, amplitude < 10 μm.

O 2. Activate Boron Source.(12 hours before usage).

O 3. SWC (Standard Wafer Cleaning):
- Fuming nitric acid, beaker 1, *t* = 5'.
- Fuming nitric acid, beaker 2, *t* = 5'.
- DI quick dump rinse (QDR).
- Boiling nitric acid 70%, *t* = 15'.
- QDR.
- Spin drying.

O 4. LPCVD Silicon Nitride, low stress, 1.0 μm:
- *p* = 200 mT, *T* = 850 °C, 70 sccm DCS, 18 sccm NH_3, *t* = 120'.

O 5. LPCVD PolySilicon, 0.5 μm:
- *p* = 250 mT, *T* = 590 °C, 50 sccm SiH_4, *t* = 90'.

O 6 Boron doping, solid source, 40 Ω/square.*
- SWC
- Remove native oxide: 1% HF, *t* = 60".
- Boron deposition + drive-in diffusion, *t* = 1 hours, *T* = 1100 ºC. NB: load wafers quickly to avoid oxidation.

O 7. Strip B_2O_5:
BHF (1:7), *t* = 60'.

O 8. Check sheet resistance (prometrix at ICE) 40 Ω/square.

O 9. Photolithography *Polysilicon Rails* (mask 1).
Dry bake , *T* = 120 °C, *t* = 5'.
- Spray HMDS, wait 10", spin 4000 RPM, *t* = 30".
- Immediately apply S1818, spin 4000 RPM *t* = 30".
- Prebake *t* = 20', *T* = 90 °C.
- Expose *t* = 8", Contact mode, $p_{N2} \approx 1.0 - 1.5$ bar.
- Develop Shipley 351, *t* = 1'(fresh developer, 1:5), QDR, spin dry.
- Check using fluorescence microscope.
- Postbake *t* = 30', *T* = 120 °C.

O 10. RIE Polysilicon rails:
- *p* = 100 mT, *P* = 100 W, Styros electrode with 6'' silicon wafer, 30 sccm SF_6, 7 sccm CHF_3, 10 sccm O_2, *T* = 10 °C, *t* = 1'30''.

O 11. O_2-plasma strip:
O_2-plasma, P = 120 W, *T* = 150°C, *t* = 15'.

O 12. SWC

O 13. Remove native oxide:
5% HF, *t* = 2'. (Make new solution with 50% HF)

O 14. LPCVD silicon nitride, low stress, 0.5 μm:

P = 200 mT, T = 850 °C, 70 sccm DCS, 18 sccm NH_3, t = 60'.

O 15. Photolithography *Rail contact holes* (mask 2):
S1818, spin t = 30'', expose t = 8'', Develop t = 1'.

O 16. RIE Si_3N_4 Rail contact holes:
- p = 10 mT, P = 75 W, 5 sccm O_2, 25 sccm CHF_3, styros electrode, t = 7'30''.

O 17. Plasma strip photoresist:
- O_2 plasma, P = 120 W, T = 150°C, t = 15'.

O 18. Activate Boron Source (12 hours before usage)

O 19. SWC

O 20. PECVD SiO_2 Sacrificial layer 1, 2.4 µm.
P = 650 mT, P = 60W LF, 200 sccm SiH_4, 710 sccm N_2O, T = 300 °C, t = 84'.

O 21. De-gas TEOS before PolySi layer is deposited:
Anneal t = 30', T = 800°C, N_2 environment.

O 22. LPCVD Polysilicon Actuator plate, 0.5 µm:
p = 250 mT, T = 590 °C, 50 sccm SiH_4, t = 100'.

O 23. Solid Source Boron Doping (SSDROB):
- SWC
- Remove native oxide: 1% HF, 60".
- Boron deposition + drive-in diffusion, t = 1 hours, T = 1100 ºC. NB: load wafers quickly to avoid oxidation.

O 24. Strip B_2O_5:
BHF (1:7), t = 60'.

O 25. Check sheet resistance (prometrix) 40 Ω/square.

O 26. Photolithography *Actuator plate* (mask 3):
S1818, spin t = 30'', expose t = 8'', develop t = 1'.

O 27. RIE Polysilicon Actuator plate, 0.5 µm:
p = 100 mT, P = 100 W, Styros electrode with 6 inch silicon load wafer, 30 sccm SF_6, 7 sccm CHF_3, 10 sccm O_2, T = 10 °C, t = 1'30''.

O 28. Plasma strip photoresist:
O_2-plasma, P = 120 W, t = 15', T = 150°C

O 29. SWC

O 30. Photolithography *Sacrificial Oxide Layer 1* (mask 4):
S1828, Spin t = 30'', Expose t = 12'', Develop t = 1'10''.

O 31. RIE SiO_2 Sacrificial layer 1, 1.9 µm:
p = 20 mT, P = 50 W, styros electrode, 10 sccm CHF_3, T = 10 °C, t = 60'.

O 32. Etch sacrificial SiO_2 layer 1, 0.5 µm:
BHF (1:7), t = 14'.

O 33. Strip photoresist:
O_2-plasma, P = 120 W, t = 15', T = 150°C.

O 34. SWC

O 35. TEOS Sacrificial layer 2, 0.5 µm:
p = 400 mT, 50 sccm TEOS, tube T = 700 °C, bubbler T = 60 °C, t = 65' (130 minutes / µm).

O 36. Photolithography *Anti Sticking bumps* (mask 5):
S1818, Spin t = 30'', Expose t = 8'', Develop t = 1'.

O 37. 1% HF Anti sticking Bumps 150 nm, t = 4'15'' (35 nm / minute)

O 38. SWC (resist strip)

O 39. Photolithography *Frame/Actuator-plate contact holes* (mask 6):
S1828, Spin t = 30'', Expose t = 12'', Develop t = 1'10''.

O 40. Etch contact holes in SiO_2, 0.5 μm:
BHF (1:7), *t* = 4'.
O 41. SWC (resist strip)
O 42. De-gas TEOS before thick PolySi layer:
Anneal at *T* = 800°C, N_2 environment, *t* = 30''.
O 43. Activate Boron Source.(12 hours before usage)
O 44. Remove native oxide:
1% HF, *t* = 45'' (very critical step)
O 35. LPCVD Polysilicon, 4.0 μm:
p = 250 mT, *T* = 590 °C, 50 sccm SiH_4, *t* = 800'.
O 36. Solid Source Boron Doping (SSDROB) NB: Load wafers quickly to avoid native oxide formation:
Boron deposition + Drive in diffusion + Annealing *T* = 1100 °C, 1 hour.
O 37. Strip B_2O_5:
BHF (1:7), *t* = 60'.
O 38. Check sheet resistance; 0.5 μm: (prometrix at ICE, 5 Ω/square)
O 39. SWC
O 40. PECVD SiO_2, 1.2 μm:
p = 650 mT, *P* = 60W LF, 200 sccm SiH_4, 710 sccm N_2O, *T* = 300 °C, *t* = 41'.
O 41. Post anneal to spread Boron:
T = 1100 °C, 3 hours (N_2), heat up via *t* = 30' at *T* = 800 °C.
O 42. Photolithography *Frame* (mask 7):
Critical in removing resist at large height step, eventually use *repair mask* (mask 8) to expose critical regions twice , S1818, Spin *t* = 30'', Expose *t* = 8'', Develop *t* = 1'.
O 43. RIE SiO_2, 1.2 μm:
p = 20 mT, *P* = 50 W, styros electrode, 10 sccm CHF_3, *T* = 10 °C, *t* = 40'.
O 44. Strip photoresist:
O_2-plasma, *T* = 150°C, *P* = 120 W.
O 45. Check if all resist is removed (focus at steps).
O 46. Break wafers in 4 quarters
O 47. RIE Polysilicon Actuator Frame:
Process in steps of *t* = 2' untill silicon disappears, then in step of *t* = 30''.
p = 100 mT, *P* = 100 W, Styros electrode with 6 inch silicon load wafer, 30 sccm SF_6, 7 sccm CHF_3, 10 sccm O_2, *T* = 10 °C.
O 48. SWC
O 49. Remove sacrificial layer 1 and 2 and freeze drying samples:
50 % HF, *t* = 25'.
Freeze drying:
- *t* = 20' IsoPropanol 1
- *t* = 20' IsoPropanol 2
- *t* = 20' Cyclohexane
- Freeze drying -5 [°C] under dry N_2 flow.
- Postbake *t* = 30', *T* = 120 °C.

F

Pull-in calculation of clamp suspension, section 5.4

The clamp-shoe as well as its suspension are electrically connected to the clamp actuator stator electrode. Therefore they are at a different voltage than the substrate, and pull-in to the substrate can occur. Figure F.1 shows a top view of the clamp suspension. The gray parts are free-standing. The suspension consists of four beams, indicated by their lengths l_1, l_2, l_3, l_4. For calculation of the pull-in voltage to the substrate, all electrostatic forces acting on beam 4, as well as the clamp shoe are added, and concentrated at the tip of beam 4 (force F_4 in fig. F.2). The resulting pull-in voltage will therefore be an underestimate. we first calculate the *z*-stiffness.

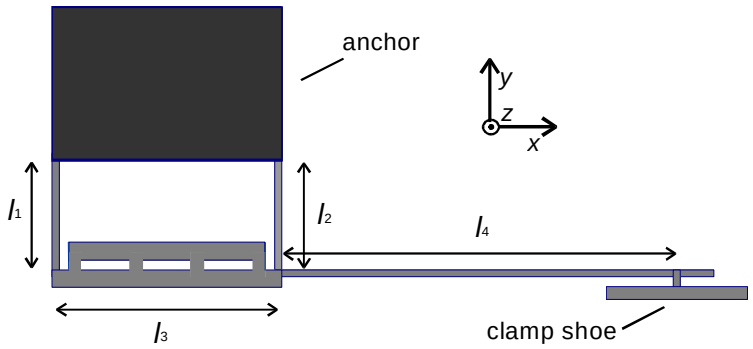

Figure F.1: Top view of the clamp suspension. The gray parts are the freestanding conductive parts of the clamp, which are at a different voltage than the substrate. Part 1,2 and 4 (indicated with their lengths l_1, l_2, l_4) are 2 µm wide springs. Spring 4 gives the clamp shoe the freedom to move in *y*-direction, springs 1 and 2 to move in x-direction. The wide beam 3 is assumed to be rigid.

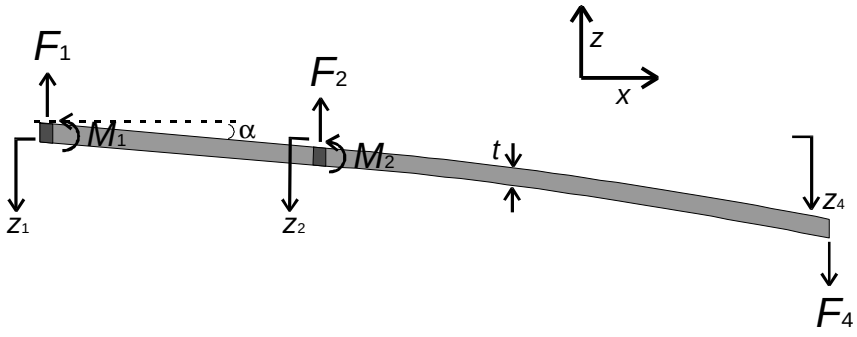

Figure F.2: front view (y-direction) of the clamp suspension. The amount of torsion of spring 1 and 2 is given by the angle a. The clamp shoe moves downward due to (a) torsion of spring 1 and 2, (b) common downward bending of these springs, and (c) bending of spring 4. The total tip deflection at the end of the suspension is represented bij z_4. The forces F_1, F_2 exerted by springs 1 and 2 , F_4 exerted by the electrostatic forces, and the moments M_1, M_2 exerted by springs 1 and 2, are indicated. The tip deflections of spring 1 and 2 are represented by z_1 and z_2. The height of the structure is represented by *t*.

Fig. F.2 shows a front view (*y*-direction) of the clamp suspension. The clamp shoe (connected to the tip of spring 4) can move downward due to *a)* torsion of spring 1 and 2 with angle *a*, *(b)* common downward bending of these springs, and *(c)* bending of spring 4. In static equilibrium the following equations apply. Torque balance with respect to tip of spring 1:

$$M_1 + M_2 - (l_3 + l_4) \cdot F_4 + F_2 \cdot l_3 = 0 \qquad \text{(F.1)}$$

In which M_1 and M_2 are the moments exerted by springs 1and 2 on beam 3, and F_2 is the force exerted by spring 2 on beam 3. Force balance:

$$F_4 = F_1 + F_2 \qquad \text{(F.2)}$$

Geometry:

$$z_2 = z_1 + a \cdot l_3 \qquad \text{(F.3)}$$

With z_1 and z_2 the tip deflections of spring 1 and 2 respectively. Bending stiffness:

$$\frac{F_1}{z_1} = \frac{3E \cdot I_{x1}}{l_1^3} \qquad \text{(Spring1)} \qquad \text{(F.4a)}$$

$$\frac{F_2}{z_2} = \frac{3E \cdot I_{x2}}{l_2^3} \qquad \text{(Spring2)} \qquad \text{(F.4b)}$$

$$\frac{F_4}{z_4} = \frac{3E \cdot I_{y4}}{l_4^3} \qquad \text{(Spring 4)} \qquad \text{(F.4c)}$$

Where E is the Young's modulus and I_{x1}, I_{x2} are the moments of inertia of spring 1 and 2 with respect to the *x*-axis:

$$I_{x1} = \frac{w \cdot t^3}{12} \quad \text{and} \quad I_{x2} = \frac{w_2 \cdot t^3}{12}$$

Where $w_{1,2}$ are the widths of spring 1 and 2, and t is the height of the springs. I_{y4} is the moment of inertia of spring 4 with respect to the *y*-axis:

$$I_{y4} = \frac{w_4 \cdot t^3}{12}$$

With w_4 the width of spring 4. Torsional stiffness:

$$M_1 = \frac{a \cdot G \cdot I_{xz1}}{l_1} \qquad \text{(Spring 1)} \qquad \text{(F.5a)}$$

$$M_2 = \frac{a \cdot G \cdot I_{xz2}}{l_2} \qquad \text{(Spring 2)} \qquad \text{(F.5b)}$$

With $I_{xz1,2}$ the polar moments of inertia of spring 1,2 for torsion around the *y*-axis:

$$I_{xz1} = \frac{w_1 \cdot t}{12} \cdot (w_1^2 + t^2) \quad \text{and} \quad I_{xz2} = \frac{w_2 \cdot t}{12} \cdot (w_2^2 + t^2)$$

And G is the shear modulus of elasticity:

$$G = \frac{E}{2(1+n)}$$

With ν the Poisson's ratio. Combination of (F.2), (F.3) and (F.4a,b) yields:

$$z_2 = \frac{1}{(1 + \frac{I_{x2} \cdot l_1^3}{I_{x1} \cdot l_2^3})} \cdot (\frac{F_4 \cdot l_1^3}{3E \cdot I_{x1}} + a \cdot l_3) \qquad \text{(F.6a)}$$

Define the constants *H*, *K* and *D*:

$$z_2 = H \cdot (F_4 \cdot K + a \cdot D) \qquad \text{(F.6b)}$$

The torque balance can be rewritten as:

$$a[\frac{G \cdot I_{xz1}}{l_1} + \frac{G \cdot I_{xz2}}{l_2}] = F_4 \cdot (l_3 + l_4) - z_2 \cdot \frac{3E \cdot I_{x1}}{l_2^3} \cdot l_3 \qquad \text{(F.7a)}$$

Define the constants *A*, *B* and *C*:

$$a \cdot C = F_4 \cdot A + z_2 \cdot B \qquad \text{(F.7b)}$$

Eq. (F.6, F.7) can be used to express a as a function of F_4:

$$a = F_4 \frac{A + B \cdot K \cdot H}{C - B \cdot D \cdot H} \qquad \text{(F.8)}$$

The suspension deflection at the clamp shoe attachment point is given by:

$$z_4 = z_2 + a \cdot l_4 + F_4 \cdot \frac{l_4^3}{3E \cdot I_{y4}} \tag{F.9}$$

Combination of eq. (F.6b),(F.8) and (F.9) yields z_4 as a function of F_4 only. The stiffness k_{z4} can now be expressed by:

$$k_{z4} = \frac{F_4}{z_4} = \frac{1}{(\frac{H \cdot (C \cdot K + D \cdot A)}{C - B \cdot D \cdot H}) + (l_4 \cdot \frac{A + B \cdot K \cdot H}{C - B \cdot D \cdot H}) + \frac{l_4^3}{3E \cdot I_{y4}}} = \tag{F.10}$$

$$= \frac{1}{c_z + c_a + c_{b4}}$$

Where c_z is the compliance due to z-translation of spring 2, c_α the compliance due to torsion of spring 1and 2, and c_{b4} the compliance due to bending of spring 4. The pull-in voltage is derived in the same way as in section 3.5 and 5.2:

$$U_{pi} = \sqrt{\frac{8}{27} \cdot \frac{k \cdot g^3}{e \cdot A}}$$

Where k is the stiffness of the spring supporting the moving electrode, with active area A. The initial gap between the electrodes (with the spring relaxed) is represented by g. For k we take k_{z4}, the z-stiffness of the suspension. The electrode area used equals 374 μm^2, which is the sum of the bottom area of the clamp shoe, and the bottom area of spring 4. The initial gap is determined by the thickness of the sacrificial silicon oxide, which is 2.3 μm. With these values the pull-in voltage U_{pi} = 67 V.

G

Calculation of the measured friction vs. load from the measured voltages (section 4.4)

The total load consists of the clamp force L plus the interfacial adhesive load. The measurements have been carried out under the condition $L > 0$, as the clamp voltage is chosen above the level that is necessary to make initial contact. Fig. G.2a shows the measured pull-voltage squared as a function of the applied clamp voltages squared. The measurements indicate that there is a close to linear relation between the load L and the F_f. Eq. (4.14) can therefore be used, and the adhesive load is accounted for in a term F_a^0, the apparent adhesion force at $L = 0$, and a term proportional to L, which is accounted for in the friction coefficient $m_{e,a}$. The clamp force L consists of the generated electrostatic clamp force minus the elastic deformation force of the clamp actuator suspension and the drive beam connected to the pull actuator:

$$L = F_{elec} - F_{spring} \qquad \text{(G.1)}$$

F_{spring} equals 7 ± 2 μN, calculated from the stiffness of the suspension and the pull connection beam, times the initial gap between the shoe and the rigid wall. To calculate the clamp force, we need to know the electrostatic clamp force F_{elec}. This force can be calculated from the voltage applied on the clamp actuator, V_{clamp}, according to $F_{elec} = a_{clamp} \cdot V_{clamp}^2$, where a_{clamp} is the conversion factor from actuator voltage to force [N/V^2] which depends on the actuator geometry as follows:

$$a_{clamp} = \frac{e \cdot A_{c1}}{2 \cdot (d_{c1} - g)^2} - \frac{e \cdot A_{c2}}{2 \cdot (d_{c2} + g)^2} \qquad \text{(G.2)}$$

Where $A_{c1} = 1.5 \times 10^4$ (μm)^2 is the forward clamp actuator area, $A_{c2} = 1.4 \times 10^4$ (μm)^2 is the backward clamp actuator area, $d_{c1} = 3.6 \pm 0.2$ μm is the forward initial gap of the clamp actuator, $d_{c2} = 5.2 \pm 0.2$ μm is the backward initial gap of the clamp actuator and $g = 1.4 \pm 0.2$ μm is the initial gap between the shoe and the shuttle (fig. G.1). The gaps have been measured from SEM photographs. Due to the uncertainty in the gap sizes, the conversion factor has a significant uncertainty: $\alpha_{clamp} = (1.4 \pm 0.5) \times 10^{-8}$ N/V^2.

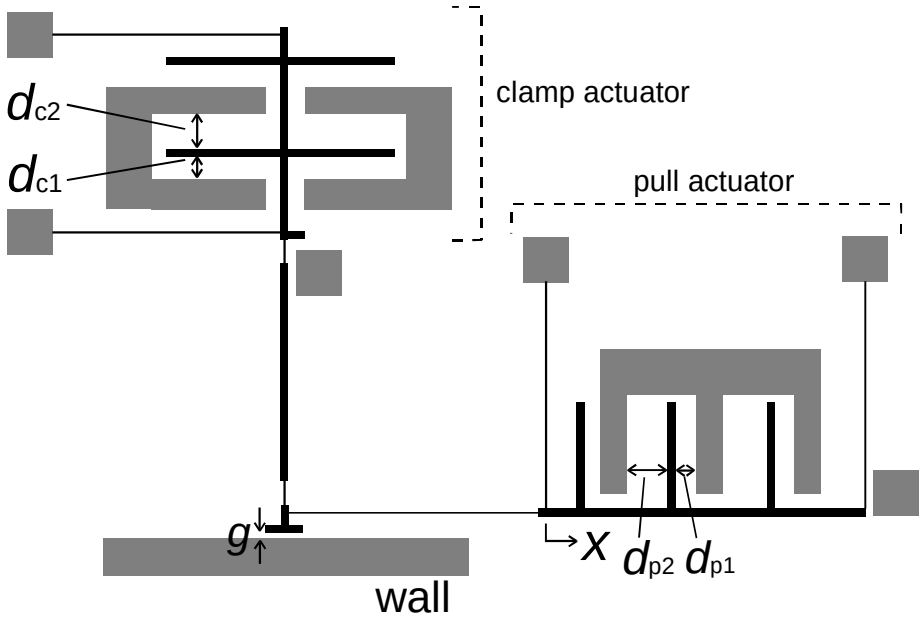

Figure G.1: Layout of the friction meter. The grey elements are fixed to the substrate, the black elements have been released. d_{c1} is the forward initial gap of the clamp actuator, d_{c2} is the backward initial gap of the clamp actuator, d_{p1} is the forward initial gap of the pull actuator, d_{p2} is the backward initial gap of the pull actuator and g is the initial gap between the shoe and the shuttle.

The friction measurement is started with the shoe is clamped to the shuttle while the pull actuator is in rest. Therefore the spring force of the suspension of the pull actuator is zero, and for the pull force as a function of the applied pull voltage we can write $F_{\text{pull}} = a_{\text{pull}} \cdot V_{\text{pull}}^2$, where α_{pull} is the conversion factor from actuator voltage to force [N/V^2] which depends on the actuator geometry as follows:

$$a_{\text{pull}} = \frac{e \cdot A_{\text{p1}}}{2 \cdot d_{\text{p1}}^2} - \frac{e \cdot A_{\text{p2}}}{2 \cdot d_{\text{p2}}^2} \qquad \text{(G.3)}$$

A_{p1} = 7.5 x 10^3 μm^2 is the active forward pull actuator area, A_{p2} = 7.0 x 10^3 μm^2 is the active backward pull actuator area, d_{p1} = 2.7 ± 0.2 μm is the forward initial gap of the pull actuator and d_{p2} = 6.2 ± 0.2 μm is the backward initial gap of the pull actuator. Due to the uncertainty in the gap sizes, the conversion factor has a significant uncertainty: α_{pull} = (3.8 ± 0.8) x 10^{-9} N/V^2. Pull-voltages larger than 22V have been used, in order to obtain the clearly visible pull-in of the pull actuator. Using the conversions factors and eq. (G.1), the voltages have been converted to forces. Four curves have been derived for combinations of smallest and largest F_{spring} and smallest and largest $m_{\text{e,a.}}$ all under the condition $L > 0$ (fig. G.2b). The values of the apparent zero load adhesion force, and the friction coefficient are listed in table G.1.

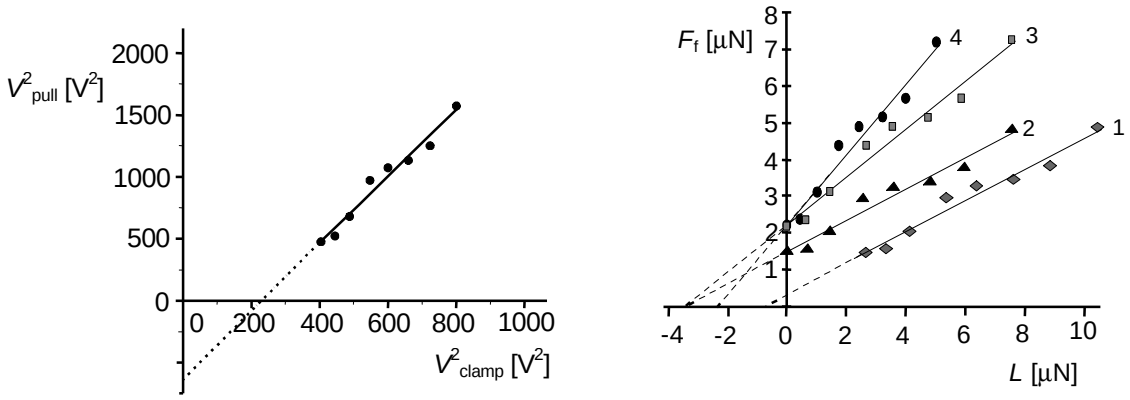

a) b)

Figure G.2a) The measured pull voltages squared at the onset of slip, as a function of the applied clamp voltage squared. The measurements have been carried out at a relative humidity of the air of 35±5%. b) The measured static friction force as a function of the clamp force, for four extremes: Smallest and largest F_{spring} in combination with smallest and largest friction coefficients, all under the condition $L > 0$.

1. Smallest $m_{e,a}$, smallest F_{spring}	$m_{e,a} = 0.43$	$F_a^0 = 0.7$ μN
2. Smallest $m_{e,a}$, and largest F_{spring} for $L > 0$	$m_{e,a} = 0.43$	$F_a^0 = 3.38$ μN
3. Largest F_{spring}, and largest $m_{e,a}$ for $L > 0$	$m_{e,a} = 0.64$	$F_a^0 = 3.37$ μN
4. Smallest F_{spring} , and largest $m_{e,a}$ for $L > 0$	$m_{e,a} = 0.97$	$F_a^0 = 2.23$ μN

Table G.1: Measured apparent zero load adhesion forces F_a^0 and friction coefficients $m_{e,a}$ for the four extreme curves.

From table G.1 it can be concluded that $m_{e,a} = 0.7 \pm 0.3$. A significant friction force at zero load was found, corresponding with an apparent adhesion force
$F_a^0 = F_f\,(L=0) / m_{e,a} = 2.0 \pm 1.3$ μN.

H

Model of the electro-mechanical energy conversion of the lateral motor concept *A* (section 5.2)

A simple expression for the generated force can be found from an energy model of the transducer. This model only contains the electrical energy stored in the gap, the mechanical deformation energy is neglected. Fig. H.1 shows the definitions of variables.

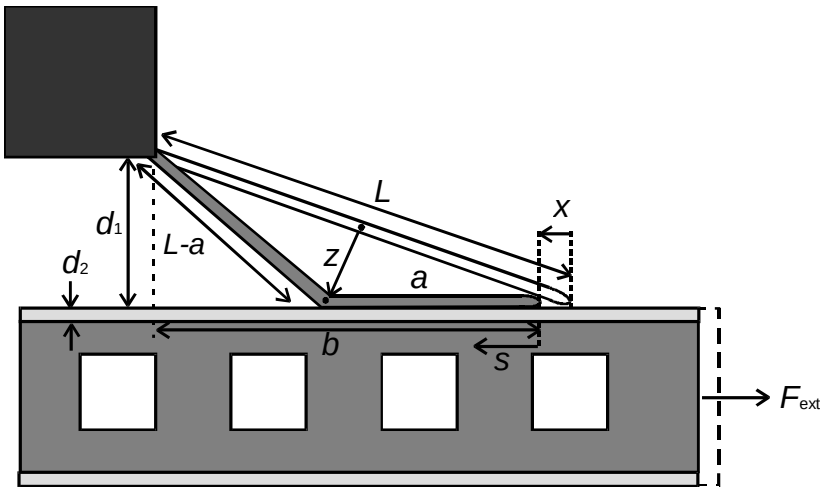

Figure H.1: Definitions of model variables. L is the length of the drive beam, a is the attached length, L - a is the unattached length, d_1 is the size of the air gap between the fixed end of the drive beam and the side-wall of the slider, d_2 is the thickness of the silicon nitride insulator (for the electrical model the silicon nitride on the drive beam is virtually transferred to the shuttle), b projected length of the beam onto the side-wall of the slider, s is the position along the shuttle edge starting at the tip of the beam, x is the displacement of the beam tip by contraction, and F_{ext} is the external force exerted on the shuttle to maintain balance

Fig. H.1 shows the definitions of the variables in the energy model. L is the length of the drive beam, a is the attached length, L - a is the unattached length, d_1 is the size of the air gap between the fixed end of the drive beam and the side-wall of the slider, d_2 is the thickness of the silicon nitride insulator, b projected length of the beam onto the side-wall of the slider, s is the position along the shuttle edge starting at the tip of the beam, x is the displacement of the beam tip by contraction, and F_{ext} is the external force exerted on the shuttle to maintain balance. For reasons of simplicity the insulator of both the beam and the side-wall have been added into one layer. The force F_{ext} under voltage control can be calculated from the derivative of the Legendre transformed energy function $W'(x, U)$. If only the electrical energy is accounted for, the expression for the force becomes:

$$F_{ext} = -\frac{\partial W'(x,U)}{\partial x} = \frac{\partial}{\partial x}[\frac{1}{2}C(a(x))\cdot U^2] = \frac{\partial}{\partial a}[\frac{1}{2}C(a(x))\cdot U^2]\frac{\mathrm{d}a}{\mathrm{d}x} \qquad \text{(H.1)}$$

Where the minus sign has been added because the force is pointing towards $-x$. The capacity $C(a)$ of the gap between the beam and the shuttle is calculated by assuming a small ratio $d_1 / (b - a)$. This implies that the capacitance between the oblique part of the beam and the shuttle can be calculated by integration with respect to s of infinitesimal parallel plate elements with an area $t \cdot \mathrm{d}s$, with t the thickness of the polysilicon (in the direction perpendicular to the paper). The total capacitance is the sum of the capacitance of the attached and the unattached part of the beam:

$$C(a) = \frac{e_1 \cdot t \cdot (b-a)}{d_1} \ln\left|1 + \frac{e_2 \cdot d_1}{e_1 \cdot d_2}\right| + \frac{e_2 \cdot t \cdot a}{d_2} \qquad \text{(H.2)}$$

Where e_1 is the permittivity of the air, and e_2 is the permittivity of the insulator. The relation between a and x follows from simple geometry calculation. The contraction x of the beam is given by:

$$x = L \cdot \left(\sqrt{1 - \frac{d_1^2}{L^2}} - \frac{a}{L} - \sqrt{(1 - \frac{a}{L})^2 - \frac{d_1^2}{L^2}} \right) \cong \frac{d_1^2}{2(L-a)} - \frac{d_1^2}{2L}$$

($d_1 << L$ and $d_1 << (L - a)$) (H.3)

For the (realistic) dimensions L = 400 μm, d_1 = 10 μm and a = 100 μm, a contraction x = 42 nm follows from eq. (H.3). For calculating the produced force, it is necessary to derive $\mathrm{d}a$ / $\mathrm{d}x$:

$$\mathrm{d}a / \mathrm{d}x = 1/ (\mathrm{d}x / \mathrm{d}a) \cong 2(L - a)^2 / {d_1}^2 \qquad \text{(H.4)}$$

Combination with eq. (H.2) yields:

$$F_{ext} = \frac{(L-a)^2}{d_1^2} \cdot \{\frac{e_2 \cdot t}{d_2} - \frac{e_1 \cdot t}{d_1} \ln\left|1 + \frac{e_2 \cdot d_1}{e_1 \cdot d_2}\right|\} \cdot U^2 \qquad \text{(H.5)}$$

I

Lateral pull-in and pull-down of the drive beams of the lateral motor concept *A* (section 5.2)

Pull-down towards the substrate can be calculated using eq. 3.19. For the beam composed of a silicon-silicon nitride sandwich eq. (3.19) changes into:

$$U_{pi} = \sqrt{0.22 \frac{g_n{}^3 \cdot t^3 \cdot (E_1 + E_2 \frac{w_2}{w_1})}{e_0 \cdot L^4}} \qquad \text{(I.1)}$$

Where L is the length of the drive beam, t its thickness (height), E_1 the Young's modulus of the poly silicon, E_2 the Young's modulus of the silicon nitride, w_1 is half the width of the poly silicon part of the beam, and w_2 is the width of the silicon nitride at the side-walls (see fig. I.1). For the lateral pull-in we follow a similar procedure as in paragraph 3.5.1. The difference is that initially the electrodes are non-parallel. Figure I.1 shows the definitions used in the pull-in calculation. The deflection with respect to the initial position is $y(r)$, $y(L)$ is the tip deflection, g is the initial gap at the tip, d_1 is the air gap width at the base of the drive beam, $v(r)$ is the local distance between the drive beam and the shuttle. It is assumed that $d_1 << L$, and therefore L is used for the length as well as the projection of the length. For the capacitance we assume a linear deflection profile (like in fig. 3.9). The capacity is determined by the capacitance of the silicon nitride layer in series with the capacitance of the air gap. Due to the small thickness of the silicon nitride and its higher permittivity the capacitance of this layer can be neglected. The expression for the capacitance becomes:

$$C(v(L)) = \frac{e \cdot w \cdot l}{v(L)} \cdot \ln \left| \frac{d_1}{d_1 - v(L)} \right| \qquad \text{(I.2)}$$

Mechanically, for the deformation we assume the shape with a concentrated load at the tip of the beam. This yields for the mechanical deformation energy:

$$W_m = \frac{45}{30} \frac{EI}{L^3} y^2(L) \qquad \text{(I.3)}$$

Where EI is the flexural rigidity of the silicon-silicon nitride sandwich:

$$EI = \frac{t \cdot w_1^3}{3} \cdot (E_1 - E_2) + \frac{t \cdot (w_1 + w_2)^3}{3} \cdot E_2 \qquad \text{(I.4)}$$

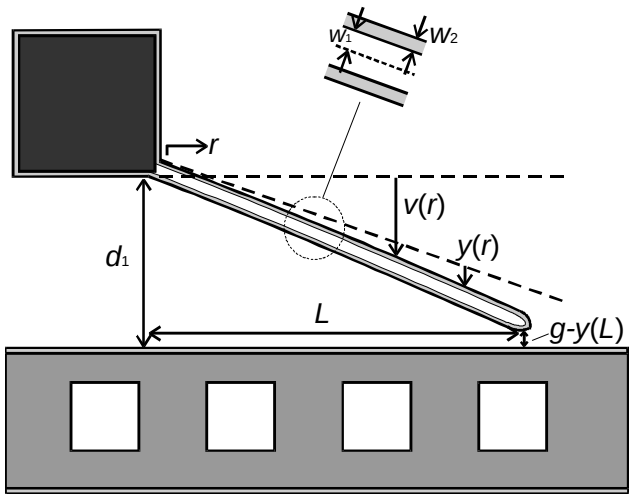

Figure I.1 Definitions of the variables used in the pull-in analysis. The deflection with respect to the initial position is $y(r)$, $y(L)$ is the tip deflection, g is the initial gap at the tip, d_1 is the air gap width at the base of the drive beam, $v(r)$ is the local distance between the drive beam and the shuttle. w_1 is half the width of the poly silicon part of the beam, and w_2 is the width of the silicon nitride at the side-walls of the drive beam. It is assumed that $d_1 << L$, and therefore L is used for the length of the beam as well as the projection of the length.

Following the procedure of section 3.5 we derive an implicit equation for the pull-in tip position $v_{pi}(L)$:

$$g^2 \cdot (v(L) - d_1 + g)\left[\frac{1}{v(L)^3} \cdot \ln\left(\frac{d_1}{d_1 - v(L)}\right) - \frac{1}{v(L)^2 \cdot (d_1 - v(L))} + \frac{1}{2v(L) \cdot (d_1 - v(L))^2}\right] =$$

$$= \frac{g^2}{2 \cdot (v(L) \cdot (d_1 - v(L))} - \frac{g^2}{2v^2} \cdot \ln\left(\frac{d_1}{(d_1 - v(L)}\right)$$

Once the pull-in tip position is known, the pull-in voltage can easily be derived by substitution in $\partial W'(v(L)) / \partial v(L) = 0$:

$$U_{pi} = \sqrt{3 \cdot c \cdot \frac{EI \cdot g^3}{e_0 \cdot t \cdot L^4}} \qquad \text{(I.5)}$$

Where c is a dimensionless constant depending on the geometry:

$$c = \frac{v(L) - d_1 + g}{\frac{g^3}{2 \cdot (v(L) \cdot (d_1 - v(L)))} - \frac{g^3}{2v(L)^2} \cdot \ln\left(\frac{d_1}{d_1 - v(L)}\right)}$$

J

Stiffness Calculations for the Lever, concept *C* (section 5.4)

J.1 Input Stiffness of the Lever

In order to show the feasibility of the implementation of a lever in MEMS in combination with electrostatic actuation, we calculate the input stiffness of a lever with elastic joints

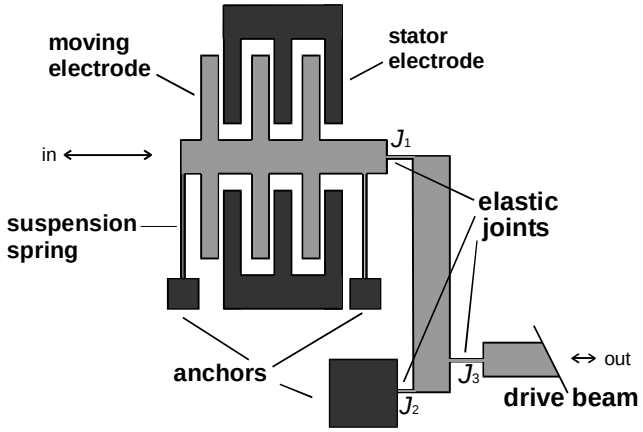

Figure J.1: Lay-out of the propulsion actuator with a lever. The light gray parts are released, and are on the same potential as the substrate. The dark gray parts are fixed to the substrate by insulating silicon oxide. The three elastic joints are indicated by J_1, J_2, J_3.

Fig. J.1 shows the lay-out of an actuator with lever. The definition is of variables used is done in fig. J.2. By choosing the joint lengths l_1 and l_3 large enough, the stiffness in the *y*-direction of joint 2 is largest, and it can therefore be assumed that the center of rotation is located halfway in joint 2. This implies that the transformation ratio $\Delta x_{out} : \Delta x_{in} = l_{out} / L$. The displacement of the lever beam in the *y*-direction is determined by the displacement y_2 of the tip of joint 2, induced by the moment exerted by the lever beam. For small deflections, and neglecting the influence of tensile forces in the joints (in the *x*-direction) linear elastic theory [1], can be applied. For small deflection the following kinematic relations apply:

$$q_1 = q,\ q_2 = q,\ q_3 = -q,\ \ y_3 = y_2 + q \cdot w_{lever},\ y_1 = y_2 - q^2 \cdot L \text{ , and } q = x_{in} \cdot L \quad \text{(J.1)}$$

Where q_j is the tip rotation of joint *j*, positive when tip displacement is in the positive *y*-direction.

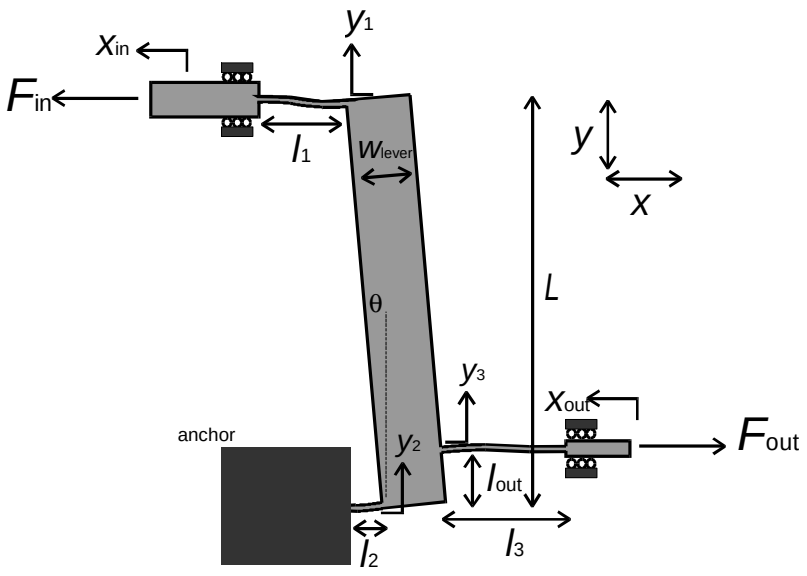

Figure J.2: Definitions of variables for the stiffness analysis of the lever.

Neglecting shear deformation (pure bending condition [**Timoshenko**]), the following relations for the joints apply:

$$M_1=M_1(y_2,\, q_1,\, q)=\frac{(4\cdot l_1\cdot q_1-6\cdot y_1(y_2,q))\cdot E\cdot I_1}{l_1^2} \qquad \text{(J.2a)}$$

$$M_3(y_2,\, q_3,\, q)=\frac{(4\cdot l_3\cdot q_3-6\cdot y_3(y_2,q))\cdot E\cdot I_3}{l_3^2} \qquad \text{(J.2b)}$$

$$M_2(q)=\frac{E\cdot I_2}{l_2}\cdot q \qquad \text{(J.2c)}$$

$$y_2=\frac{q_2\cdot l_2}{2} \qquad \text{(J.2d)}$$

Where $I_j = t\cdot w_j^3 / 12$ is the moment of inertia of joint *j*. The moments are taken positive when deflecting the tip upward. Equilibrium is analyzed by the balance of moments acting on the beam, with respect to the tip of joint 2:

$$M_2 = F_{in}\cdot L + M_3 - M_1 - F_{out}\cdot l_{out} \qquad \text{(J.3)}$$

Where L is the total length of the lever beam. Combination of eq. (J.1-J.3) with the relation $x_{in} = q\cdot L$ the effective stiffness at the input side of the lever due to the bending stiffness of the joints equals:

$$k_{in}=\frac{\partial F_{in}}{\partial x_{in}}=\frac{(4l_1-3\cdot l_2)\cdot E\cdot I_1}{L^2\cdot l_1^2}+\frac{E\cdot I_2}{L^2 l_2}+\frac{(4l_3+3l_2+6w_{lever})\cdot E\cdot I_3}{L^2\cdot l_3^2} \qquad \text{(J.4)}$$

Here we have neglected the q^2 term in the expression for $y_1(y_2,q)$.

J.2 Output Stiffness of the Lever

Bending stiffness of the lever beam
The generated deflection can be lost by bending of the lever beam. The bending stiffness measured at the input is given by:

$$k_{\mathrm{b,in}} = \frac{3E \cdot I_{\mathrm{b}}}{L^3} \tag{J.5a}$$

The stiffness can be transformed to the output, yielding:

$$k_{\mathrm{b}} = \frac{3E \cdot I_{\mathrm{b}}}{L^3} \cdot \frac{(L - l_{out})^2}{l_{\mathrm{out}}^2} \tag{J.5b}$$

Tensile stiffness of the joints
The lengths of joints should be taken not too long, as the output stiffness $F_{\mathrm{out}} / x_{\mathrm{out}}$ (with x_{in} = constant), could become too small. The effective tensile stiffness of the three joints measured at the output is given by:

$$k_{\mathrm{t}} = \frac{1}{\frac{l_{\mathrm{out}}^2}{L^2 \cdot k_{\mathrm{t1}}} + \frac{(L - l_{out})^2}{L^2 \cdot k_{\mathrm{t2}}} + 1/k_{\mathrm{t3}}} = \frac{E \cdot t}{\frac{l_{\mathrm{out}}^2 \cdot l_1}{L^2 \cdot w_1} + \frac{(L - l_{out}) \cdot l_2}{L^2 \cdot w_2} + \frac{l_3}{w_3}} \tag{J.6}$$

Total output stiffness
The total effective output stiffness is given by:

$$k_{out} = \left(\frac{1}{k_{\mathrm{b}}} + \frac{1}{k_{\mathrm{t}}}\right)^{-1} \tag{J.7}$$

J.3 Literature

[1] J.M. Gere, and S.P. Timoshenko,” Mechanics of Materials”, 3rd ed., Chapman & Hall, London, 1991.

Summary

The Micro Walker project ,which is reported in this thesis, focuses on the development of linear micro-motors with a large dynamic range (reach : resolution). The key question for this project is if it is possible to implement walking motion in MEMS, and what can be the performance of linear micromotors employing walking motion. From their potential application in data storage guiding specifications are derived: An output acceleration of a 1 mg load larger than 100 m / s^2, 10 nm resolution, reach larger than 10 μm, a driving voltage below 30 V and a maximum linear size smaller than 1 mm.

The linear micromotors to made in the project, are based on variable capacitance electrostatic actuation and surface micromachining fabrication technology. Electrostatic motors have already been made in the 18^{th} century. The first known variable capacitance motor has been built by Zipernowski in 1889. Different propulsion principles for linear micromotors have been found in literature: Inertial drive, elastic inertial drive, impact drive, traveling field surface drive, scratch drive, zigzag drive, transformation of rotary into linearly motion, and walking motion. The latter principle is implemented in the project.

Controlled friction in clamp feet is necessary for walking. Therefore, microtribology is one of the main topics in this thesis. The focus is on shearing friction in elastic adhesive contacts. Questions to be answered in the project have been collected in section 1.6.

Equilibrium and stability of conservative electrostatic transducers is studied by means of the energy stored in the electrical and mechanical buffers. States of stable equilibrium are found by minimization of a generalized potential with respect to the unconstraint state variables. Electrostatic actuators can become unstable if the effective actuator stiffness becomes negative. This can occur for both fixed charge and fixed voltage. An actuator model has been made that expresses the electrostatic force as the product of the energy density and the active area, which is the derivative of the volume containing the electric field, with respect to the direction of movement. From literature a maximum allowable electric field 2×10^8 V/m in a 2 μm gap in air has been found, limited by breakdown. This corresponds with an energy density of 2×10^5 J/m^3. The energy density is in the same order as can be obtained in magnetic actuators, and which is allowed in commercial PZT piezoelectric actuators. The maximum attainable electrostatic force using surface micromachining design rules, is 0.1 mN with a driving voltage of 30V for both the gap-closing and the comb-drive actuator. This force is large enough to meet our demands, however the stroke of 2 μm is too small. Using walking motion we try to increase the stroke.

Due to the flatness of the surfaces in surface micromachining, large adhesion forces between fabricated structures and the substrate are encountered. Four major adhesion mechanisms have been analysed: Capillary forces, Hydrogen-bridging, electrostatic forces and van der Waals forces. Once contact is made adhesion forces can be stronger than the restoring elastic forces and even short, thick beams will continue to stick to the substrate. Contact, resulting from

drying liquid after release etching, has been successfully reduced. In order to make a fail-safe devices stiction during their operational life-time should be anticipated. Electrostatic forces can cause pull-down of short, stiff structures already at moderate voltages. In particular applications, contact between moving parts is even desired. In order to avoid in-use stiction, adhesion forces should therefore be minimized. This is possible by coating the contacting surfaces with low adhesive materials, by using bumps and side-wall spacers and by increasing the surface roughness at the interface. Capillary condensation should also be taken into account as this can lead to large increases of the effective contact area of roughened surfaces. The stiction reduction by means of robust side-wall spacers has been measured for the first time, yielding a stiction reduction which is slightly larger than the reduction of the geometrical contact area.

Reduction and control of friction is an important issue in MEMS. Using the Greenwood and Williamson elastic contact model, the dependence of static friction on the surface topography is analyzed. Static friction in shearing mode is assumed to be proportional to the real contact area. The real contact area is almost proportional to the load. The mean elastic contact pressure is almost independent of the load. The effect of adhesion is included using Maugis' expansion of the Greenwood and Williamson model. Analysis of low loaded conditions reveals that the statistical models fail, as there can be a too small number of contact points. In particular the adhesive load is underestimated in this case. A discrete contact model is introduced to calculate the friction under low loading conditions, when the number of contact points is too small to use the statistical models. The transition from elastic to plastic contact is analyzed. With increasing roughness the friction coefficient decreases to a lower limit, until the friction coefficient of the plastic contact is reached. Static friction in a polysilicon side-driven friction meter is characterized, and related to the surface topography. The measured friction vs. load fits well the relation found using the discrete contact model with three contact points.

Three different laterally driven motors have been developed and tested. The first design (concept *A*) uses drive beams which attach to the shuttle, and generate motion by contraction of the drive beams due to bending. Electrostatic forces are generated by applying a voltage difference between the drive beams and the shuttle. The experiments show that it is hard to generate a high enough clamping force. The second design (*B*) therefore uses separated clamp and propulsion actuators, which yields more freedom in the generation of clamp and propulsion forces. Using this design static friction in the clamps as a function of the clamp force has been measured. The experiment shows that there is friction with zero applied clamp force. This is caused by adhesion, which has to be added to the externally applied load. The adhesion in is the order of 1 μN, small enough to be overcome by the switchable electrostatic forces in the clamp actuators. Walking motion has been successfully generated with this design. The third design (concept *C*) is based on the second. The difference is that it has been tried to include levers to increase the propulsion force. The most difficult issue in this concept is how to increase the clamp force, and still be able to close the initial 1-2 μm gap between the clamp shoe and the shuttle. Three different solutions have been proposed for the clamping. The one which has been implemented uses a voltage difference between the clamp shoe and

the shuttle (across the side-wall insulator layers) to generate the clamp force. It turned out that this force becomes smaller than required, probably due to an effective air gap caused by surface roughness, which remains during clamping. Walking experiments with this concept have failed, due to the fact that the impact of the incoming second clamp disturbs the clamping of the first, and the displacement generated in the first step is lost. Recommendations are made to improve concept *C*. The focus should be on improving the clamps, possibly by employing a pre-clamp spring.

The shuffle motor is a linear electrostatic walking motor, employing a mechanical transformation to obtain an amplification of forces and reduction of the step size. The motor is normally driven in order to maximize the active electrode area. The motor consists of three polysilicon and two silicon nitride layers and has been fabricated using surface micromachining. An energy model has been made to calculate the step size and the driving voltage as a function of the load force and the motor geometry. In theory the actuator is able to deliver up to 1 mN at 30V driving voltage. Tests show an effective step size of about 85 nm and a produced force of 43 μN at 40V driving voltage. The smaller than expected force is caused by weak clamping, which is the consequence of the modulated AC-voltage drive. The AC-voltage drive was introduced to reduce electrostatic stiction by charging of the silicon nitride insulating layer covering the bottom electrodes. A recommendation is made for a new design of the clamps.

Samenvatting

Het project dat wordt beschreven in dit proefschrift richt zich op de ontwikkeling van lineaire micromotoren met een groot dynamisch bereik (slag : resolutie). The sleutelvraag in dit project is of het mogelijk is om een loopbeweging te realiseren in MEMS (Micro Electro Mechanische Systemen), en wat de prestaties kunnen zijn van lineaire motoren die een loopbeweging maken. Voor de mogelijke toepassing in data-opslagsystemen zijn de volgende specificaties afgeleid voor de motoren: een versnelling aan de uitgang van meer dan 100 m / s^2, een 10 nm resolutie, een aandrijfspanning van minder dan 30 V en afmetingen kleiner dan een millimeter. De lineaire micromotoren die worden gemaakt in het project, maken gebruik van elektrostatische actuatie via variërende capaciteiten, en worden gemaakt met behulp van *surface micromachining*. Elektrostatische motoren werden reeds in de 18de eeuw gemaakt. Zover bekend werd de eerste variable capaciteit motor gebouwd in 1889 door Zipernowski. In de literatuur zijn verschillende aandrijf principes gevonden voor lineaire micromotoren: Inertie aandrijving, elastische inertie aandrijving, botsings aandrijving, aandrijving d.m.v. lopende elektrische velden, *scratch-drive*, zigzag aandrijving, omzetten van roterende in translerende beweging, en lopen. Dit laatste principe is geïmplementeerd in dit project. Om te kunnen lopen is het nodig om wrijving in klemvoeten te kunnen controleren. Daarom is microtribologie een van de belangrijkste onderwerpen in dit proefschrift. We concentreren ons op wrijving door afschuiving in elastische adhesieve contacten. Vragen die beantwoord worden in de loop van het onderzoek zijn verzameld in sectie 1.6. Evenwicht en stabiliteit van conservatieve elektrostatische transducenten wordt bestudeerd door middel van de energie die is opgeslagen in de elektrische en mechanische buffers. Toestanden van stabiel evenwicht worden gevonden door de gegeneraliseerde potentiaal te minimaliseren voor variatie van de vrije toestandsvariabelen. Elektostatische actuatoren kunnen uinstabiel worden als de effectieve actuatorstijfheid negatief wordt. Dit kan zowel bij lading- als bij spanningsturing plaatsvinden. Een actuatormodel is opgesteld dat de gegenereerde kracht als functie van de elektrische energiedichtheid en het actieve oppervlakte uitdrukt. Het actieve oppervlakte is de afgeleide van het volume dat het veld bevat naar de verplaatsing. In de literatuur een maximale veldsterkte van 2×10^8 V/m in een 2 μm luchtspleet is gevonden, begrensd bij doorslag. Dit correspondeerd met een energiedichtheid van 2×10^5 J/m^3. Deze energiedichtheid is even groot als welke mogelijk zijn in magnetische actuatoren en welke toegestaan zijn in commerciëel verkrijgbare PZT piëzoelektrische actuatoren. Uitgaande van *surface micromachinining* ontwerpregels een maximale kracht van 0.1 mN is mogelijk met een aandrijfspanning van 30 V voor zowel de *comb-drive* als de *gap-closing* elektrostatische actuatoren. Deze kracht is groot genoeg, echter de bijbehorende slag van 2 μm is te klein. Door middel van lopen wordt getracht de slag te vergroten.

Door de vlakheid van oppervlakten in *surface micromachining* kunnen er grote adhesiekrachten optreden tussen de gefabriceerde structuren en het substraat. Vier belangrijke

adhesie-mechanismen zijn bestudeerd: Capillaire krachten, waterstof-bruggen, elektrostatische krachten en van der Waals krachten. Zodra contact optreedt kunnen adhesiekrachten groter zijn dan de tegenwerkende elastische krachten en zelfs korte, dikke balkjes kunnen blijven plakken aan het substraat. Contact ten gevolge van capillaire krachten bij het drogen na het vrij etsen is met succes verminderd. Om fout-vrije *devices* te maken moet er op stictie in de operationele periode geanticipeerd worden. Bijvoorbeeld omdat elektrostatische krachten zelfs korte, stijve structuren bij middelmatige spanningen al naar het substraat kunnen trekken. Ook zijn er toepassingen waarbij contact tussen bewegende delen nodig is. Om stictie in deze gevallen te voorkomen dienen de adhesiekrachten geminimaliseerd te worden. Dit is kan door de contacterende oppervlakken te coaten met een laag adhesieve film, door bobbeltjes aan te brengen, door middel van randen die de oppervlakken uit elkaar houden (*side-wall spacers*), en door de oppervlakte ruwheid te vergroten. Ook moet rekening worden gehouden met capillaire condensatie, omdat dit tot vergroting van het effectieve contactoppervlak kan leiden. Voor het eerst is de effectiviteit van side-wall spacers gemeten. De stictie vermindering is iets groter dan op grond van de reductie van het geometrische (schijnbare) contact oppervlak verwacht werd.

Het reduceren en controleren van wrijving is een belangrijk issue in MEMS. Met behulp van het Greenwood & Williamson elastische contactmodel, is de afhankelijkheid van de statische wrijving van de oppervlakte topografie geanalyseerd. We nemen aan dat in de afschuif-modus De statische wrijving proportioneel met het werkelijke contactoppervlak is. Het werkelijke contactoppervlak is op zijn beurt bijna proportioneel met de aangebrachte belasting. The gemiddelde elastische contactdruk is vrijwel onafhankelijk van de belasting. Het effect van adhesie kan door Maugis' uitbreiding van de Greenwood&Williamson theorie in rekening worden gebracht. Uit de analyse van omstandigheden van lage belasting blijkt dat hier de statistische contactmodellen falen, doordat er onder deze omstandigheden een te klein aantal contactpunten kan zijn. In het bijzonder wordt onderdeze omstandigheden de adhesieve belasting onderschat. Om wrijving bij lage belasting te kunnen beschrijven hebben we daarom een discreet contactmodel ingevoerd. De overgang van elastisch naar plastisch contact is geanalyseerd. Bij afschuiven neemt met toenemende oppervlakte ruwheid de wrijvingscoefficient af totdat een ondergrens, de wrijvingscoefficient voor plastisch contact is bereikt. Statische wrijving in een poly-silicium zijwaarts aangedreven wrijvingssensor is gemeten, en gerelateerd aan oppervlakteruwheid. De gemeten relatie tussen wrijving en belasting voldoet goed aan de berekening met het discrete contactmodel met drie contactpunten.

Er zijn drie lateraal aangedreven motoren ontwikkeld en getest. Concept *A* maakt gebruik van aandrijfbalken die aanliggen tegen de *shuttle*, en die een verplaatsing genereren door middel van een contractie ten gevolge van buiging. Elektrostatische krachten worden gegenereerd door een spanningsverschil aan te leggen tussen de *shuttle* en de aandrijfbalken. De experimenten laten zien dat het moeilijk is om een voldoende grote klemkracht op te wekken. Concept *B* maakt gebruik van aparte klem -en aandrijfactuatoren, zodat er meer vrijheid is om de klem -en aandrijfkracht apart te optimaliseren. Met dit ontwerp de wrijving in de klemmen als een functie van de klemkracht is gemeten. De experimenten laten zien dat er wrijvings is

zonder dat er een klemkracht wordt aangebracht. Dit wordt veroorzaakt door de adhesiekrachten in de klem, die opgeteld moeten worden bij de extern aangebrachte klemkracht. The adhesie is in de grootte orde van 1 μN, klein genoeg om te worden overheerst bij de schakelbare elektrostatische klemkrachten. Met dit ontwerp is met succes een loopbeweging gegenereerd.. Het derde ontwerp(concept *C*) is gebaseerd op het tweede. Het verschil is dat er hefbomen zijn geïmplementeerd om de aandrijfkracht te vergroten. Het grootste probleem met dit concept is hoe de klemkracht te vergroten en tevens in staat te zijn om de initiële 1-2 μm opening tussen de klemschoen en de *shuttle* te sluiten. Drie oplossingen zijn voorgesteld voor het klemmen. De oplossing die geïmplementeerd is, maakt gebruik van een spanningsverschil tussen de klemschoen en de *shuttle* (over een isolator op de zijwanden), om de klemkracht op te wekken. Het is gebleken dat deze klemkracht kleiner is dan vereist, waarschijnlijk door een effectieve luchtlaag in de klem ten gevolge van oppervlakte ruwheid en/of niet-parallelliteit van de zijwanden. Loopexperimenten met dit concept zijn mislukt, doordat de botsing van de tweede klem met de *shuttle* het klemmen van de eerste verstoord, en de verplaatsing van de eerste stap verloren gaat. Er zijn aanbevelingen gedaan om concept *C* te verbeteren. Hierbij moet geconcentreerd worden op verbetering van de klemmen, mogelijkerwijs door een voorspan-veer toe te passen.

De *shuffle motor* is een lineaire electrostatische lopende motor, die gebruik maakt van een hefboom om de kracht te vergroten en de stapgrootte te verkleinen. De motor wordt loodrecht op het substraat aangedreven om het actieve elektrode oppervlek te maximaliseren. De motor is opgebouwd uit drie lagen poly-silicium en twee lagen silicium-nitride en is gemaakt met behulp van *surface micromachining*. Een energiemodel is opgesteld om de stapgrootte en de benodigde aandrijfspanning als functie van de belastingskracht en de motor geometrie uit te rekenen. In theorie de actuator kan 1 mN opwekken bij 30V aandrijfspanning. Experimenteel is een effectieve stapgrootte van 85 nm en een gegenereerde kracht van 43 μN bij 40V aandrijfspanning. De kleiner dan verwachte kracht wordt veroorzaakt door gebrekkig klemmen, wat wordt veroorzaakt door de gemoduleerde AC-aandrijfspanning. Deze AC-spanning is geïntroduceerd om de electrostatische stictie te verminderen die het gevolg is van oplading van de silicium-nitride isolator die de onder-electrodes afdekt. Een aanbeveling is gedaan voor een nieuw klemontwerp.

Dankwoord

Graag wil iedereen bedanken die op een of andere manier heeft bijgedragen aan de totstandkoming van dit proefschrift. Allereerst mijn promotoren Miko Elwenspoek en Rien Koster. Miko, jouw benadering van het wetenschappelijk onderzoek spreekt mij aan. De cultuur van vrijheid, en het stimuleren van creativiteit bij de MicMec is uniek. Ik ben je zeer dankbaar voor de steun en het vertrouwen dat je mij gegeven hebt tijdens en na mijn 'dip'. Rien, het was een genoegen met jou te werken. Jouw inzet en betrokkenheid bij het *Micro Walker* project waardeer ik zeer. Wat we van je geleerd hebben op het gebied van mechanisch ontwerpen is van groot belang voor de micromechanica groep. Ook wil ik Jan Fluitman danken voor zijn bijdrage aan de initiatie van het project. Het succes van het *Micro Walker* project is voor een groot deel te danken aan de bijdrage van de afstudeerders die er aan gewerkt hebben. Tonny Sonnenberg, Robert Molenaar, Bart Vogelzang, André Verholen, Jeroen Wissink, Chris Gortemaker, Marko Blom, Coen Lauwerijssen en Sandra Kits jullie bijdrage aan het project is essentieel geweest, en ik heb met veel plezier met jullie gewerkt.
Door de opheffing van de mechanica groep van Philips NatLab halverwege het project kwam formeel de aandacht van Philips voor het project te vervallen. Niettemin ben ik tevreden over samenwerking die we met de overgebleven (electro)mechanici op het NatLab hebben voortgezet. In het bijzonder wil ik mijn contactpersonen Louis Sander en Jan Peter Baartman voor hun aandacht voor en bijdrage aan het project.
Graag wil ik mijn collega's van de micromechanica groep ('MicMec') bedanken voor de prettige en stimulerende werksfeer. De in de MicMec aanwezige expertise is een schier onuitputtelijke bron van inspiratie. Rob legtenberg mij de fijne kneepjes van het MESA surface micromachining process (ook wel 'mijn process' genoemd) bijgebracht. Henri Jansen ben ik zeer dankbaar voor z'n hulp en adviezen op het gebied van actuator-theorie, micro fabricage, en electrostatica. Verder heeft hij een aanzienlijk deel van dit proefschrift gelezen en van commentaar voorzien. De micmec technologie goeroes Erwin Berenschot en Meint de Boer (conditiegetal = 2 x leeftijd) ben ik zeer erkentelijk voor hun adviezen en hulp bij de fabricage van de devices. Met Cheng-Qun Gui heb ik met veel plezier samengewerkt aan de modellering van ruwe adhesieve oppervlakken. Ook de staf van MESA+ wil ik bedanken voor de prettige samenwerking. In het bijzonder wil ik de SEM-mers Bert Otter, Johnny Sanderink en Mark Smithers bedanken voor de fraaie foto's waarvan ik in dit boekje en andere publicaties dankbaar gebruik heb gemaakt.
De dames van het secretariaat en de administratie, Judith, José, Simone en Ingrid wil ik graag bedanken voor de adequate technische en sociale ondersteuning en aangenaam gezelschap. Met veel plezier heb ik de afgelopen jaren kamer 7246 bewoond. Mijn kamergenoten Han Gardeniers en Willem Tjerkstra en ikzelf staan er om bekend dat we gedurende de dag nogal eens onze gemoedstoestand met elkaar deelden. De keywords zijn inmiddels algemeen bekend. Als u bij het betreden van onze kamer heeft gedacht 'ik voel nattigheid', dan klopt dit.
Het grootste gedeelte van mijn studententijd heb ik op Dirty Trix (‡1985-†1998) gewoond. Daar vandaan werd de Drienerlose roei-vereniging Euros op positief kritische wijze ondersteund op velerlei terreinen. Een tijd van veel gezelligheid en vrijheid, lekker (veel) eten

en uitbuiken op de groene bank. Simon, Frank, Olav, Anneke, Jaap, Alan, Robbin, Arum, Age, Evelijn, Ronald, Hedwig, Niels (Teun), Eveline, Pascal, Edwin, Maaike, Wouter, allemaal zeer bedankt! Bij Euros heb ik vele jaren geroeid en gecoached, en heb ik veel vrienden ontmoet. Marinus, het ga jou en Euros goed. Herman, Félippe, Jaap, Kathy, Cornelis, Ida, Niels, Vincent, Alie, Tjalling, Monique, Michiel, Marja, Erik, Anne-Marieke, Huib, Sietske, Gert-Jan. Ik hoop dat we nog vaak Ameland en de Alpen onveilig zullen maken.
Frank, Henri, Johannes, Dragana, Livija, Cristina en Commerijn allemaal hartelijk bedankt voor gezellige en inspirerende uren samen. Michiel en Monique, bedankt voor het aanvaarden van het paranimfschap. Last but not least wil ik mijn familie, en i.h.b. mijn ouders en grootouders, bedanken voor hun voortdurende belangstelling en steun.

Enschede, maart 2000.

Biography

Niels Tas was born in Jutphaas (The Netherlands) on Januari 4th 1970. Starting in 1982 he went for pre-university education (VWO) to *Schoonoord* in Zeist, where he received his diploma in 1988. Starting in 1988 he studied Electrical Engineering at the University of Twente, where he received the M.Sc. degree in 1994. His M.Sc. thesis dealt with modeling, design and fabrication of micro hydraulic systems. In 1995 he started his Ph.D.-project on linear micromotors, which resulted in this Ph.D. thesis. The focus of the project was on electrostatic actuation and micro tribology, for application in micromotors that employ walking motion.
He will continue to work in the MEMS-field, focussing on micro actuators, adhesion in micro structures, micro liquid handling, and flowsensors.
In his spare time he enjoys spending time with friends, reading, travelling and sports. Among his favorite sports are rowing, fitness, cycling, running and inline skating. He enjoys surfing the internet, virtually travelling the world.

ISBN 90-36514355